Losses in high frequency power inductors and transformers.

Augla, Kader Hmood

Award date:
1985

Awarding institution:
University of Bath

LOSSES IN HIGH FREQUENCY POWER INDUCTORS AND TRANSFORMERS

submitted by

KADER HMOOD AUGLA

for the degree of

DOCTOR OF PHILOSOPHY

at the University of Bath

1985

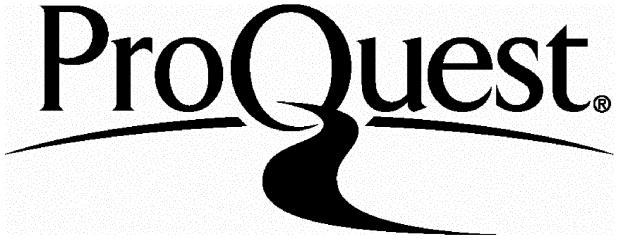

CONTENTS

ABSTRACT

This thesis is concerned with some aspects of losses produced in the inductors and transformers of switched-mode power supplies (SMPS).

The main subject of study is the eddy-current losses due to non-uniform current distribution across foil windings. These are calculated and measured for the cases when the foil constitutes an air-cored inductor, and when it is used as the secondary of a ferrite cored transformer. A coupled circuit model is used in which the foil inductor is subdivided into sets of mutually coupled filament coils. A formal method of solution of the resulting sets of equations is presented, and alternative mathematical methods of calculating self and mutual inductances are also compared.

In addition to this work two other topics are addressed briefly. First, the magnetic fields in and around magnetic cores are measured, and compared with computed results using a 3D magnetostatic package, TOSCA. Secondly, core losses in ferrite cores due to sinusoidal and non-sinusoidal excitation are measured and calculated.

ACKNOWLEDGEMENTS

The author wishes to express his sincere gratitude to his supervisor, Dr. P.D. Evans, for providing the inspiration behind the project, his keen interest, encouragement and advice during the course of the work described in this thesis. Much is owed to him.

A similar expression of thanks is due to Professor J.F. Eastham of the School of Electrical Engineering, University of Bath, for his enlightened guidance and encouragement.

The author is thankful to Mr. R.J. Hill-Cottingham, for his assistance, help and kind cooperation with the experimental work.

Thanks are also given to other members of the staff of the School of Electrical Engineering, including Dr. R.C. Dodson, for their assistance.

Thanks are due to the IRAQI Ministry of Higher Education and Scientific Research for the Scholarship awarded to him.

The author wishes to thank the Science Research Council for the computing facilities.

In addition the author wishes to thank Mrs. A. Balchin for her careful and efficient typing of this thesis.

Finally, the author is grateful to his wife, Amira, for her patience, and the forbearance of his children Nazar, Louy and Nawar.

LIST OF PRINCIPAL SYMBOLS

a	smaller radius of coil
A	larger radius of coil
b	axial length
bw	width of the layer
B	flux density
B_r	radial flux density
B_z	axial flux density
E(k)	complete elliptic integral of second kind
f	operating frequency
F_R	radio of ac resistance to dc resistance
H	magnetic field strength
J	current-density
K(k)	complete elliptic integral of first kind
L	self-inductance
M	mutual-inductance
N	number of turns
nf	number of filaments in each layer
nℓ	number of layers
n_p	number of primary turns
n_s	number of secondary turns
P_C	total core loss
P_e	eddy-current loss density
P_E	total eddy-current loss
P_h	hysteresis loss density
P_H	total hysteresis loss
R_{ac}	ac resistance
R_{dc}	dc resistance
t	thickness of the layer

u	permeability
w	width of filament
ϕ	flux
ρ	resistivity

CHAPTER ONE

INTRODUCTION

Switched-mode power supplies, (SMPS), have developed rapidly during the last ten years or so. A block diagram of a mains operated SMPS is shown in Figure 1.1. The mains supply is rectified and smoothed in a conventional way. The resulting dc voltage is then chopped at high frequency by a power transistor into the primary of a transformer. The secondary voltage from the transformer is rectified and smoothed to give the required dc output. The output voltage is sensed and a control circuit adjusts the switching duty of the transistor to maintain substantially constant dc output irrespective of load current and mains voltage. Clearly this system can also operate from a dc source, such as a battery, if the input rectifier is removed. This type of supply has two main advantages over conventional power supplies. First, the output voltage control mechanism is relatively loss free as the control transistor is operating in a switching mode, so that the efficiency of the supply is good. This is important from the point of view of total heat loss of the power supply. The lower the heat loss the less cooling required and the smaller overall package the equipment can be housed in.

Secondly, the transformer can be operated at a high frequency, typically 20 kHz - 100 kHz and so it is relatively small compared to a 50 Hz transformer. The volume and weight of the transformer is therefore reduced considerably. This reduces cost and allows the

power supply to be housed in a smaller package.

These advantages are offset by greater initial design problems. Amongst these are conducted and radiated RFI and the design of the efficient high frequency transformers and inductors which operate with non sinusoidal waveforms. Whereas a wide range of semiconductor devices and associated components have been developed for SMPS, the design of the wound components is still left in the hands of the circuit designer and this causes one of the main problems of SMPS design. Some specific aspects of high frequency transformer and inductor design are the main topics of this thesis.

A considerable amount of work has already been published on these design aspects. Most notably in the UK is probably the design and application notes produced by Philips (Mullard)[1,2,3,4,5,6,7].

Apart from the usual problems of conventional transformer and inductor design, a significant additional loss mechanism that occurs at high frequency is eddy-current loss in the copper windings, sometimes called proximity loss, which is due to the rapidly alternating leakage flux in the window of the core that is incident transversely on the windings causing eddy-currents in them.

This leads to non-uniform current distribution in them and hence increased losses. This aspect of loss has been analysed by Dowell[8] for round wire conductors.

Strip or foil conductors are also used in transformer secondaries where a few turns are required for low voltage, high

current outputs. They are also used for some inductors.

It is known that non-uniform current distribution is produced across strip conductors by eddy-currents produced by radial fields. This has been studied by a number of authors. Murgatroyd[9] has shown the behaviour of a single turn, air cored foil wound inductor. El-Missiry [10,11] has studied foil conductors in both inductors and transformers using equivalent coupled circuit techniques with special attention to low frequency (around 50 Hz), aluminium foil distribution transformers.

Mullinex[12] has treated similar problems using essentially field-based techniques.

Other authors, for example Reeves[13], Murgatroyd[14] and Walker[15] have considered the foil wound inductor problem where very high frequencies i.e. greater than 100 kHz are employed and the interturn capacitance also becomes significant to the extent that resonant frequencies occur. The present work concerns frequencies below 100 kHz and foil windings of a relatively small number of turns. The essential problem that has been tackled is of computing conductor losses so that efficient inductor and transformer designs can be undertaken.

Chapter Two presents some preliminary aspects of the work where a three-dimensional, magnetostatic computer package (TOSCA[16]) is used to compute the magnetic fields in and around typical ferrite cores that are used in SMPS design. The magnetic fields in the cores themselves are calculated, and when the cores are gapped for use in

the construction of inductors the fields in the region of the airgap are also computed and compared with measurements. Fields in the regions where the windings are situated are also computed. Both axial fields (the conventional window leakage fields) and radial fields, these are the fields that cause the non-uniform current distribution in foil inductors that are calculated for a number of conditions. The effect of the conventional use of 'sandwich' windings to reduce leakage fields is demonstrated. Also, it is found that leakage fields in a transformer do not change greatly when the core is removed, providing that the primary and secondary ampere-turns are equal and opposite in effect.

This result was generally confirmed by loss measurements, and provides the basis of the approximate model developed, in which the presence of the ferrite was neglected for the purpose of calculating the self and mutual inductances in the coupled circuit model.

Chapter Three develops the formal method of specifying and solving the equivalent circuit model used to calculate current distribution in the foil and hence the losses. This equivalent circuit is of the same type as that used by Murgatroyd[9] and El-Missiry[10] in that the foil conductor is assumed to be subdivided into notional filament coils each of sufficiently small cross sectional area that the current distribution across it can be assumed to be uniform. In view of the very large number of equations these produced, by writing down the voltage equation of each filament coil in terms of its own resistance and inductance and its mutual inductance with all the other filaments a formal method of solution was adopted. This employs the tensor-based technique[17] of writing

down the canonical equation for each circuit irrespective of its interconnection. A connection or transformation matrix is used to obtain a transformed set of parameters from which current distribution is calculated. The advantage of this method is that it is the same whether the problem is an inductor or a transformer is concerned, only the content of the connection matrix, a matrix of 0, ±1 which defines the interconnection of the circuits needs to be changed.

Chapter Four investigates possible methods of calculating the self and mutual inductances of co-axial circular filament coils in air. The complete solution for this problem results in elliptic integrals and the methods of solving them, including numerical techniques and truncated series solutions are studied. It is shown that for the conditions required, i.e. with filament coils very close together or with slightly different diameters some techniques are more reliable, or quicker, than others. The techniques of Grover[18] were also investigated here.

Chapter Five contains the comparison of experimental and theoretical results for some examples of multiturn air cored inductors, and transformer with foil wound secondaries. It is shown that reasonable prediction of losses is possible.

Chapter Six departs slightly from the main thesis of the previous work, in that it is a study of losses in ferrite cores themselves. Measurements are compared with predictions for a range of cores and at different temperatures and it is shown that existing equations for predicting core losses can be used over a restricted

range providing that empirical constants and exponents are used in the usual way. Core losses with sinusoidal and square wave excitation are also studied experimentally. The basis of equivalence under which the above mentioned equations can be used for non sinusoidal conditions is also established and explained.

References

1. Jongsma, J.: "Minimum-loss transformer windings for ultrasonic frequencies", Electronic Applications Bulletin 35:146-163, (No.3) and 211-266 (No.4), 1978.
2. Bracke, L.P.M. and Geerlings, F.C.: "High-frequency ferrite power transformer and choke design, Part 1: Switched-mode power supply magnetic component requirements", Electronic Components and Materials (Philips Publication), 1982.
3. Bracke, L.P.M.: "High-frequency ferrite power transformer and choke design, Part 2: Switched-mode power supply magnetic considerations and core selection", Electronic Components and Materials (Philips Publication), September 1982.
4. Jongsma, J.: "High-frequency ferrite power transformer and choke design, Part 3: Transformer winding design", Electronic Components and Materials (Philips Publication), 1982.
5. Jongsma, J. and Bracke, L.P.M.: "High-frequency ferrite power transformer and choke design, Part 4: Improved method of power-choke design", Electronic Components and Materials (Philips Publication), 1982.
6. Bracke, L.P.M.: "Optimizing the configuration of ferrite-core transformers for advanced switched-mode magnetics", Proc. Powercon 9, Power Concepts, Inc., Ventura, California, 1982.
7. Bracke, L.P.M.: "Optimizing the power density of ferrite-cored transformers", Proc. Powercon 9, Power Concepts, Inc., Ventura, California, 1982.
8. Dowell, P.L.: "Effects of eddy-currents in transformer windings", Proc.IEE, Vol.(113), No.(8), 1387-1394, August 1966.

9. Murgatroyd, P.N. and Walker, N.J.: "Frequency-dependent inductance and resistance of foil conductor loops", Proc.IEE, Vol.124, No.5, May 1977, pp.493-496.

10. El-Missiry, M.M.: "Calculations of current distribution and optimum dimensions of foil-wound air-cored reactors", Proc.IEE, Vol.124, No.11, November 1977, pp.1073-1077.

11. El-Missiry, M.M.: "Current distribution and leakage impedance of various types of foil-wound transformer", Proc.IEE, Vol.125, No.10, October 1978, pp.987-992.

12. Mullineux, N., Reed, J.R. and Whyte, I.J.: "Current distribution in sheet- and foil-wound transformers", Proc.IEE, Vol.116, NO.1, January 1969, pp.127.

13. Reeves, R.: "Air-cores foil-wound inductors", Proc.IEE, Vol.125, No.5, May 1978, pp.460-463.

14. Murgatroyd, P.N.: "Field and circuit models for the wound foil inductor", Electrocomponent Science and Technology, Vol.3, pp.97-102, 1976.

15. Walker, N.J.: "Studies of foil wound components", Ph.D. Thesis, Loughborough University of Technology, July 1979.

16. Armstrong, A.G.A.M., Riley, C.P. and Simkin, J.: "TOSCA User Guide, 3D static electromagnetic/electrostatic analysis package, Version 3.1, May 1982.

17. Bewley, L.V.: "Tensor Analysis of Electric Circuits and Machines", The Ronald Press Company, New York, 1961.

18. Grover, F.W.: "Inductance Calculations", (Van Nostrand, 1947).

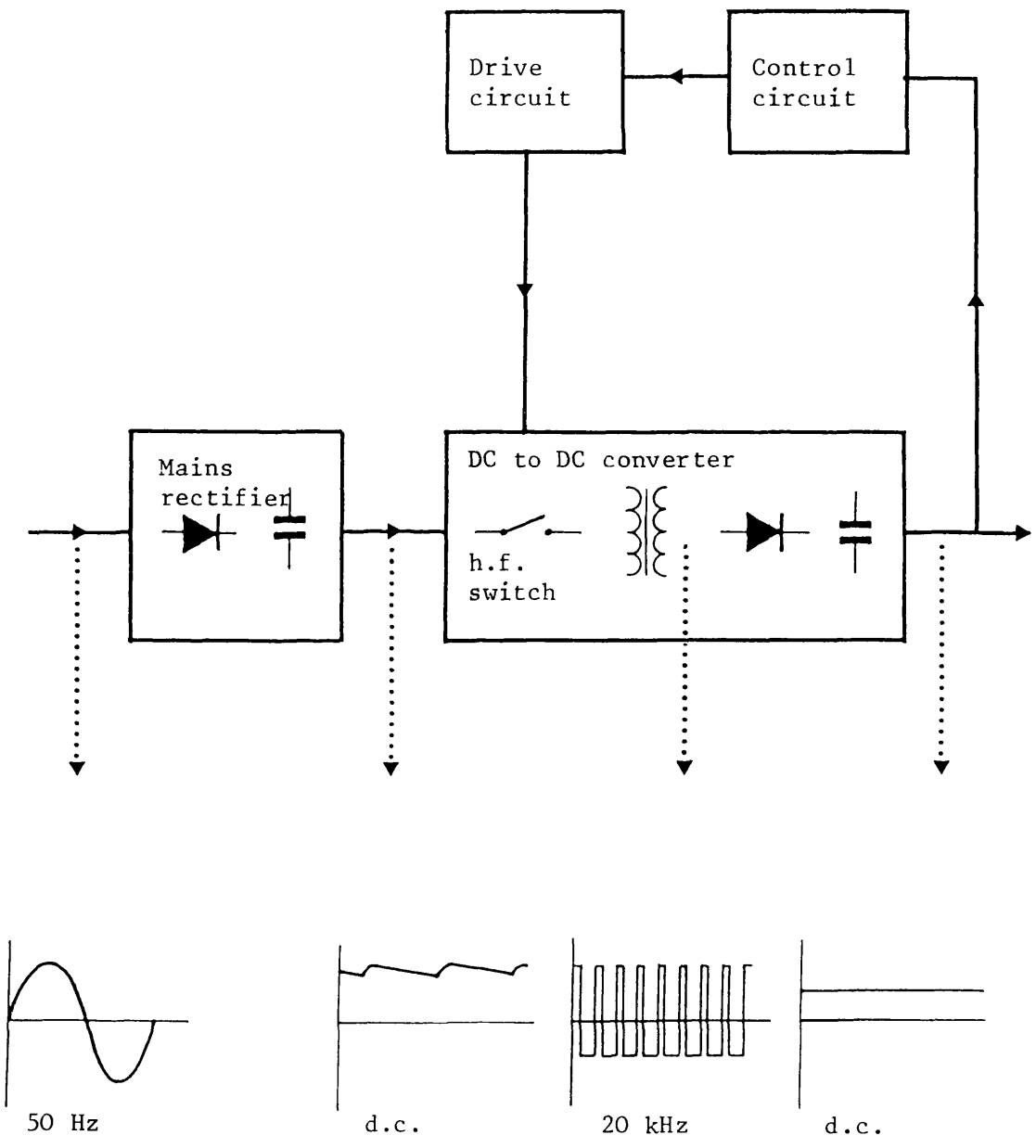

Fig.1.1: Block diagram of a switched-mode power supply

CHAPTER TWO

INVESTIGATION OF SOME MAGNETOSTATIC CONDITIONS OF FERRITE CORES

2.1 Introduction

Some information on the behaviour of ferrite-cored inductors and transformers used in switched-mode power supplies (SMPS) can be obtained from the magnetostatic conditions in and around the ferrite cores themselves. This is because eddy-currents in the ferrite material are generally small at the practical frequencies of operation (20 kHz - 100 kHz), and although eddy-currents in conductors may be relatively severe and disturb the local fields they do not usually have a great effect on the overall field pattern. To start the investigation of these components in SMPS, it is therefore of interest to obtain some practical and theoretical magnetostatic results. These act as a guide to the general field patterns in the ferrite components.

The work reported in this chapter has been undertaken in three parts:

i) Measurement of the B-H and magnetization curves of several cores, selected at random and compared with the data of a typical curve published by Mullard for these cores. This work was carried out at temperatures of 25°C and 100°C.

ii) The 3-dimensional magnetostatic finite-element computer package 'TOSCA'[1] was used to compute the fields in and around typical ferrite cores. These results were compared with measurements to establish that TOSCA was applied

satisfactorily to this type of problem.

iii) With some confidence in TOSCA it was then further applied to field computation in conductor regions. These results were difficult to obtain experimentally but are of importance from the point of view of conductor eddy-current losses.

2.2 B-H Loops for Ferrite Cores FX3750

The possible variation in ferrite property from one core to another was examined briefly by measuring the B-H loops of three cores, type FX3750 (EC70/34/17) selected at random using low frequency (50 Hz) sinusoidal excitation.

This was done in the conventional way, using an excitation coil to excite the core, from which the magnetic field intensity (H) was obtained, and a search-coil connected to a flux meter, from which the flux density (B) was obtained. The basic circuit used to investigate and display B-H loops is shown schematically in Figure 2.1. The results, taken with the core material at a uniform temperature of 25^{o}C and 100^{o}C, are illustrated in Figures 2.2 and 2.3 respectively.

Figures 2.2 and 2.3 (a), (b) and (c) are for the individual cores. Figures 2.2 and 2.3 (d) consist of the three results superimposed. It can be seen that the variation from one core to another is negligible from the point of view of saturation flux density, although there appear to be small differences in loop shapes. There is therefore possibly some variation in hysteresis loss from one core to another, and this is investigated separately in Chapter Six.

The variation in B-H loop with temperature is shown in Figure 2.4. The results in this figure are extracted from Figures 2.2(b) and 2.3(b). The fact that there is a decrease in saturation flux density with temperature can be seen quite clearly.

Magnetisation curves for the ferrite cores, type FX3750, were also measured in the conventional way, using dc excitation. The schematic diagram of the circuit used is given in Figure 2.5. The usual precautions, such as reversing the direction of the field, were taken.

The results of these measurements are given in Figure 2.6. This graph is scaled in flux against ampere-turns, which are parameters dependent upon core dimensions and are therefore particular for the FX3750. In addition, the axes are scaled in flux density, B, against field strength, H, which generalise the results for the ferrite, Ferrox-cube grade 3C8. The change in shape of the characteristics with temperature can be seen quite clearly, the saturation flux density reducing from around 0.35T at 25^{o}C to about 0.28T at 100^{o}C. It can be seen that there is quite good correlation betwen measured results and the data published by Mullard Ltd. for their core.

This gives some reassurance both about the measurement technique and correspondence between the characteristics of randomly chosen cores and published typical data.

2.3 Computation of Magnetic Conditions in Ferrite Cores

2.3.1 Introduction

The geometry of ferrite 'E' cores is relatively complex, in magnetic terms. The particular core under consideration, the FX3750, has complications as shown in Figure 2.7 where the channels in the side limbs to take mounting screws are seen. This is clearly beyond the scope of analytical techniques for 3-dimensional field solution and a numerical technique was therefore adopted. An existing software package known as TOSCA was used. This is a complete 3-dimensional field computation package developed by a group at the Rutherford Appleton Laboratory and mounted on the computers there. It was accessed from a terminal at Bath University via a dedicated telephone link. The package which is described in Appendix A1 contains a pre-processor which allows the physical problem to be defined conveniently and the data to be converted into suitable format for computation, and a post-processor which enables the computed results to be prepared and displayed in a convenient form.

2.3.2 Representation of FX3750 core on TOSCA

The symmetry of the core was utililsed to minimise the amount of ferrite that had to be modelled in the program. TOSCA allows symmetry conditions to be defined in this way in order to save computer time and space. In the present problem it was necessary to define one-eighth of the core only, as shown in Figure 2.8. In the field model the core is assumed to be situated in space of unity relative permeability, the boundaries of which are set at a equipotential, and they are so remote from the core that they have negligible effect on the field solution.

Circular coils for excitation of the core may also be defined in TOSCA, and one example is given in Fig.2.9.

2.3.3 Computed flux density conditions in FX3750 ferrite cores

Flux densities in the ferrite material of the FX3750 were computed using TOSCA. These computations were made for the conditions summarised below.

i) Core temperatures of 25°C and 100°C.

ii) The B-H curves provided by the core manufactured (Fig.2.6) were used in TOSCA, which was consequently operated in its non-linear mode.

iii) Magnetising AT of 6, 10 and 40 AT.

These are indicated in Fig.2.6 where they can be seen to represent unsaturated conditions (6 AT, H = 42 AT/m), slightly saturated conditions (10 AT, H = 69 AT/m) and highly saturated conditions (40 AT, H = 278 AT/m). The computed results are illustrated pictorially in Figures 2.10 to 2.15 inclusive. The conditions are tabulated below:

Fig. No.	Temperature (°C)	Magnetising AT (AT)
2.10	25	40
2.11	25	10
2.12	25	6
2.13	100	40
2.14	100	10
2.15	100	6

Each figure has four components so that flux density components may be examined. These are as follows:

a) $|B|$

b) B_x

c) B_y

d) B_z

The coordinate axes are indicated in each figure. All the figures contain detailed information relating to the precise conditions. The general patterns are similar, however, and are discussed briefly below:

a) $|B|$ - This produces the expected pattern where the flux is confined to the E core shape and is substantially zero elsewhere.

b) B_x - Is the flux density component in the cross arms which join the centre and outer limbs. The redistribution of flux density as the flux changes direction is indicated. The contours of $B_x = 0$ are shown in the middle of the centre pole and side limbs.

c) B_y - This is the flux density component in the centre pole and side limbs and follows the expected pattern, with the $B_y = 0$ again being indicated. It can be seen here that the ratio of centre limb to outer limb flux density is 1.86, which corresponds very closely to the nominal area ratio of 1.83.

d) B_z - Although the z-component of flux density would ideally be zero, it can be seen that there are components, of roughly half the maximum $|B|$, which occur where there are changes of ferrite core cross section, especially from the round centre limb to the

rectangular cross arms. The main results from these computations are set out in Table 2.1 below, where they are compared with measured and specified data.

Temp (°C)	Ampere Turn (AT)	Computed (TOSCA) (T)	Measured (Fig.2.6) (T)	Specified Mullard Typical Data (T)
25	40	0.42	0.41	0.43
25	10	0.34	0.32	0.34
25	6	0.24	0.21	0.23
100	40	0.32	0.33	0.34
100	10	0.30	0.29	0.3
100	6	0.28	0.24	0.25

Table 2.1: Central ferrite flux densities

It can be seen that the computed results agree quite well with measured and specified data, especially under saturated conditions, where agreement is typically within 8%.

This speaks well for TOSCA under non-linear conditions. At low flux densities the agreement is typically within about 15%.

2.3.4 Computed flux densities in window region of FX3750

Although the main flux associated with power transfer is confined within the ferrite core, nevertheless some stray fields are also produced by the windings. The leakage fields which appear within the window area in which the windings are situated produce high frequency proximity losses in the windings. Although this problem is dealt with in detail in section 2.4 below, some preliminary results were obtained at an early stage to establish that these fields could be predicted with some precision. Computations

were therefore compared with measurements as shown in Figures 2.17 and 2.18. In this case the flux densities were measured directly, using a fluxmeter and Hall Probe, at the positions indicated in Figure 2.16.

A single coil excitation was used for these results so that ampere-turns driving the leakage flux is less than in a transformer.

It can be seen quite clearly that there is very close agreement between measured and computed results in this region.

2.3.5 Representation of gapped ferrite core FX3751 on TOSCA

Gapped ferrite cores are widely used to make inductors in high frequency power electronics equipment such as the output filter choke in the forward converter and the coupled inductor in flyback converter type switched-mode power supplies (SMPS). The magnetic aspects of the design of these cores required that the magnetic loading of the ferrite is satisfactory, and that a reliable estimate of the effective inductance can also be made. These conditions are significantly affected by the presence of fringe flux around the airgap. This flux increases by a significant margin the total flux above that which would be estimated from simple magnetic circuit considerations. This has the effect of increasing the inductance above that which might be expected.

Therefore, in designing a magnetic system with an airgap, it is necessary to make allowance for fringing of magnetic flux around the edges of the airgap which has the effect of increasing the effective airgap cross section area[2]. In flyback converters, currents in the

windings of the coupled inductor are varying rapidly. The fringe flux, where it impinges on the windings, therefore also produces eddy-current losses of the same type as the proximity losses. These losses can be particularly severe in foil screens. The shape of fringe fields around the airgap is therefore of interest from this point of view.

The FX3751 is a version of the FX3750 in which there is a total airgap of 5 mm situated symmetrically in the middle of the centre pole. This was used as a test piece for measurements and computation.

General results are shown in Figure 2.19 where the four diagrams (a), (b), (c) and (d) represent |B| and B_x, B_y and B_z, as before. The patterns produced are as expected, the components of flux density around the airgap being of particular interest.

Figure 2.21 illustrates the computed and measured results at different positions and the same conditions as indicated in Figure 2.20. It is clear that the measured and computed results in Figure 2.21 are very close to each other. From the previous sections, the good agreement between computed and measured results gives some confidence in the prediction method 'TOSCA'. Hence 3D, magnetostatic computation can be used for producing further details about the behaviour of the flux density in transformer windings as discussed in the following sections.

2.4 Flux Density Distribution in Winding Regions

2.4.1 Introduction

The leakage inductance of transformer windings due to the leakage flux in the window region is well known, and can be calculated by conventional methods, as for example, described by Langsdorf[3] or Snelling [4]. The mmf producing the leakage flux is usually shown as in Figure 2.22. Figure 2.22(a) is for a "simple" winding where the primary and secondary windings are each a single coil. Fig.2.22(b) represents a "sandwich" winding in which, for example, the primary winding is made in two sections which are placed on either side of the secondary coil. The corresponding leakage mmf diagrams indicate clearly that the leakage flux is less in the 'sandwich' winding which is usually the reason for employing the more complicated design.

The terms "simple" and "sandwich" will be used below to denote the two types of winding shown in Fig.2.22. Windings with further subdivision and sandwiching of the coils are clearly possible but are not considered further in the present work. The mmf diagrams of Fig.2.22 clearly assume that the magnetizing current is zero, which is the usual assumption made for this aspect of a transformer behaviour.

So far, the model assumes that low frequency conditions are operative, and that current distribution within the wire of the coils is uniform.

In high frequency applications this is not the case, as the leakage flux, which is incident transversely on the windings,

produces eddy-currents in them. The current distribution is consequently non-uniform and the copper loss is higher than would be the case for low frequency operation. This additional loss is often called "proximity loss" and is characterised by means of an ac resistance, R_{ac}. An analysis of these effects has been performed by Dowell[5], who assumes somewhat idealised conditions, i.e. mmf and components in the direction indicated in Fig.2.22 are the only ones that exist.

In practice other components of leakage flux exist and these have significant effects on foil conductors especially. This is considered from the point of view of inductor losses in Chapter Three below. In the present section the flux density components in the window region have been examined under magnetostatic conditions to give some appreciation of the actual form. "Simple" and "sandwich" windings have been treated. Also results along two core axes have been produced, together with results for the coils situated in air with ferrite core removed.

For the present work a new core, the ETD44, has been used. This is shown in Fig. 2.23. This was one of a new range of ferrite cores introduced during the course of the research.

The finite-element model of one-eighth of the core that was defined in TOSCA is shown in Fig.2.24. The coordinate axes X, Y and Z are the global coordinates in which the problem was most conveniently defined.

An example of the simple coil arrangement is shown in Fig. 2.25.

The output data was presented in a "local" polar coordinate system where the Z-direction is along the centre pole as indicated in Fig.2.26. The radial direction, R, is also shown here.

The positions at which Z and R components of flux density were computed are indicated in Fig.2.26.

2.4.2 Flux density components in winding region with "simple" transformer windings

As described above B_Z is the usual component of leakage flux density. Computed results for B_Z are illustrated in Fig.2.27 at two positions. These are for R varying from 0.75 cm to 1.65 cm with Z = 0, along the central line of symmetry of the core and at Z = 1.55 cm at the edge of the windings, close to the cross limb of the core. These positions are labelled (A) and (C) in Fig.2.26. The results are also plotted along two radial trajectories, $\theta = 10^{\circ}$ and $\theta = 90^{\circ}$. The former is close to the centre limb, but was used instead of the precise $\theta = 0^{\circ}$ line so that the results obtained were away from the edge of the model. $\theta = 90^{\circ}$ produces the fields to which the windings are exposed when not precisely within the ferrite window. A third set of results is for the case when the ferrite is absent, i.e. the same coils are situated in air.

A number of observations can be made on the results displayed in Fig.2.27.

i) They are generally of the expected shape rising linearly to a maximum, due to the primary mmf, remaining constant over the space between the primary and secondary coils and reducing linearly to zero again due to the opposite mmf produced by the secondary.

ii) Taking the $\theta = 10^{o}$, Z = 0 case with the ferrite core present, then the maximum B_z is 5.5×10^{-3}T. This is the value to be expected with the total primary AT (145AT) driving flux across the 33 mm space between the cross limbs, according to the simple model in Fig.2.28, i.e.

$$B_z = \frac{\mu_o NI}{b}$$

$$= \frac{\mu_o . 145}{33 \times 10^{-3}}$$

$$= 5.5 \times 10^{-3} \text{ T } (= 55 \text{ Gauss})$$

iii) The case for $\theta = 90^{o}$, Z = 0 is for all purposes identical to the $\theta = 10^{o}$ case, as would generally be expected.

iv) More surprisingly perhaps if the ferrite is removed completely, B_z reduces by a small amount only, less than 10%.

v) for the three cases, treated with Z = 1.55 cm there is again considerable similarity in the magnitudes, although in this case they are all around one-half of the Z = 0 results. This reduction is symptomatic of the fact that the simple model in Fig.2.28 is not precise, and this model is the one used by Dowell[5] and is discussed further in Chapter Three. Of particular interest is the fact that the removal of the ferrite makes very little difference.

The radial flux density, B_r as defined in Fig.2.26, is illustrated in Fig.2.29 at three positions. These positions are labelled (A), (B) and (C) in Fig.2.26. The computed results are plotted for the same three conditions as before, i.e. the purpose of these results was to examine the variation in radial flux density occurring in winding region with and without ferrite.

It is clear from the Figure 2.29 that B_r along the central line of symmetry of the model is approximately zero, as would be expected, but B_r increases towards the end of the coil as shown by the results for Z = 1.4 cm and Z = 1.55 cm. The maximum B_r is 1.8 x 10^{-3}T (18 Gauss) and it is around one-half of the B_z component in the same position.

The B_r component therefore has significant magnitude as shown in Fig.2.29 especially near the edges of the windings.

Fig.2.30 (a), (b) and (c) illustrates the comparison between B_r and B_z components in different positions. It is clear that B_z reduces by about 50 per cent from the centre to the ends of the windings, while B_r increases and is around one-half of B_z at the ends, Fig.2.30(c). Therefore, it is clear that B_r exists and has significant effects.

Computed results are also presented for Z varying from 0.0 to 1.65 cm at fixed value of R, as indicated by (D), (E), (F), (G) and (H) in Fig.2.26.

Fig.2.31 shows both B_z and B_r at the inner edge, (D), and the middle, (E), of the primary coil. For Fig.2.31(a) the B_r characteristics are similar in shape, the magnitude of B_r with no ferrite being approximately the average of the $\theta = 10^o$ and $\theta = 90^o$ results with ferrite. This has possible implications which are discussed in Chapter Three below. The B_z characteristics appear to be very different, B_z being much smaller when ferrite is present. The actual magnitude of B_z along the inner edge of the primary coil is however very small, around 0.5×10^{-3}T (5 Gauss) which is less than 10% of the magnitude determined in Fig.2.27. For Fig.2.31(b) the same comments as for Fig.2.31(a) apply for B_r. The value of B_z with no ferrite is smaller than the other two cases, but B_z for $\theta = 90^o$ falls off to approach it near the end of the coil.

Fig.2.32 illustrates the variation of B_r and B_z at the middle of the small gap between the primary and secondary coils. B_r is very small in this region, as would be expected from symmetry and the B_z characteristics show the similarity expected from Fig.2.27.

Fig.2.33 shows B_r and B_z at the middle, (G), and the end, (H), of the secondary coil. These are in general similar to the shapes in Fig.2.31 and the same comments apply. Note that in this case B_r has the opposite sign, i.e. is negative, as would be anticipated.

The cusp like shape in the B_z characteristics in Fig.2.33(b) when there is no ferrite is thought to be a numerical effect of trying to obtain results along the precise edge of the coil.

2.4.3 Flux density components in winding region with "sandwich" transformer windings

As shown in Fig.2.22b, the leakage flux is less in the "sandwich" winding than in the "simple" winding. This reduction of flux density is caused by dividing the primary winding into equal parts and it is known to be of importance from the point of view of conductor eddy curent losses. The results already presented for the "simple" winding in Figure 2.27 and 2.29–2.33 have therefore been repeated for the case of the "sandwich" winding.

The same finite-element model by which the space is divided up was used to investigate B_z and B_r in the winding region. Fig.2.34 illustrates the sandwich coil arrangement which was specified in the model. The positions at which B_z and B_r components of the flux density were computed are indicated in Fig.2.35 and the results obtained are presented and discussed below. The computed results for B_z component are shown in Fig.2.36, at the three positions (A), (B) and (C) of Fig.2.35.

Results are plotted at $\theta = 10^{o}$, $\theta = 90^{o}$ and for the case when the ferrite core is removed as before. The results are generally of the expected shape. The mmf is zero in the middle of the secondary coil, so it may be considered to be in two equal sections. As discussed before the similarity in the magnitudes of B_z in the three cases are clearly shown in the figure. B_z in this case is however nearly one-half of the value with the "simple" winding, i.e. about $0.25–0.3 \times 10^{-3}$T (25–30 Gauss).

Fig.2.37 represents the radial flux density B_r at the winding region at position Z = 0.0, 1.4, 1.55 cm ((A), (B) and (C)). B_r is again zero at Z = 0.0, and increases towards the ends of the coils.

It is now most severe in the region of the secondary winding but is nevertheless considerably reduced (approximately halved) compared to the simple winding case.

Fig.2.38 represents both B_z and B_r at the positions labelled (A), (B) and (C) in Fig.2.35. It can again be seen that B_r increases from a very small value at Z = 0 and becomes the same order of magnitude as B_z at the ends.

The computed results for Z varying from 0.0 cm to 1.65 cm for different constant values of R are also presented in the Figures 2.39, 2.40 and 2.41 to show both B_z and B_r in the first half and second half of the primary and at the secondary coil and again labelled (D), (E), (F), (G), (H), (I) and (J) in Fig.2.35. These results follow the same general patterns already noted for the simple winding and are therefore not discussed further

2.4.4 Comparison between the flux densities

The flux density components in the winding region in the two cases "simple" and "sandwich" coils were computed and were discussed separately in previous sections using 3D magnetostatic computation 'TOSCA'. In this section the flux density components for the two types of winding are compared. No new results are presented, the purpose of Fig.2.42-2.47 is to give direct comparison of magnitude for the two cases.

Figures 2.42, 2.43 and 2.44 present the B_z component at Z = 0.0, 1.4, 1.55 cm at the case $\theta = 10^o$, 90^o and without ferrite core respectively.

It is clear that the B_z reduces by one-half in the case of "sandwich" coils in the expected manner. Similarly Figures 2.45, 2.46 and 2.47 illustrate the B_r component. It seems that although the sandwiched coil now sees the highest B_r components it is still less than in the simple coil case.

2.5 Conclusions

This chapter has described the magnetostatic conditions in and around ferrite cores, and has given some results from the measurement of the B-H loops and magnetisation curves of several cores.

The good correlation between measured and published data gives some reassurance both about the measurement technique and correspondence between the characteristics of randomly chosen cores and published typical data. Also, the 3-dimensional magnetostatic finite-element computer package 'TOSCA' was used to compute the fields at some conditions in and around the ferrite core and these results were compared with measured results. Good agreement was obtained. This agreement gives some confidence in the application of TOSCA to this work. TOSCA was then applied to the field computation in conductor regions, of ferrite cores which are of importance from the point of view of conductor eddy-current losses in high frequency transformers and inductors.

The flux density components were investigated in the winding regions of both "simple" and "sandwich" coils, with and without ferrite core being present. These results examined the Z directed components of flux density which were found to be as predicted. The radial components were also examined and these are more difficult to estimate analytically. The radial components were however found to be of the same order of magnitude as the Z components. The significance of these results is discussed more fully in Chapter Three where the conductor eddy-current losses due to leakage fields are examined.

2.6 References

1. Armstrong, A.G.A.M., Riley, C.P. and Simkin, J.:
   TOSCA User Guide, 3D Static Electromagnetic/Electrostatic Analysis Package, Version 3.1, May 1982.
2. Evans, P.D. and Saied, B.M.:
   "Calculation of the effective inductance of gapped ferrite cores", International Conference on Power Electronics and Variable-Speed Drives, 1-4 May 1984.
3. Langsdorf, A.S.:
   "Theory of Altenating Current Machinery", McGraw-Hill Book Company Inc., (1955 - Second Edition).
4. Snelling, E.C.:
   "SoftFerrites, Properties and Applications", Butterworths, London, 1969.
5. Dowell, P.L.:
   "Effects of eddy-currents in transformer windings", Proc.IEE, Vol.(113), No.(8), 1387-1394, August 1966.

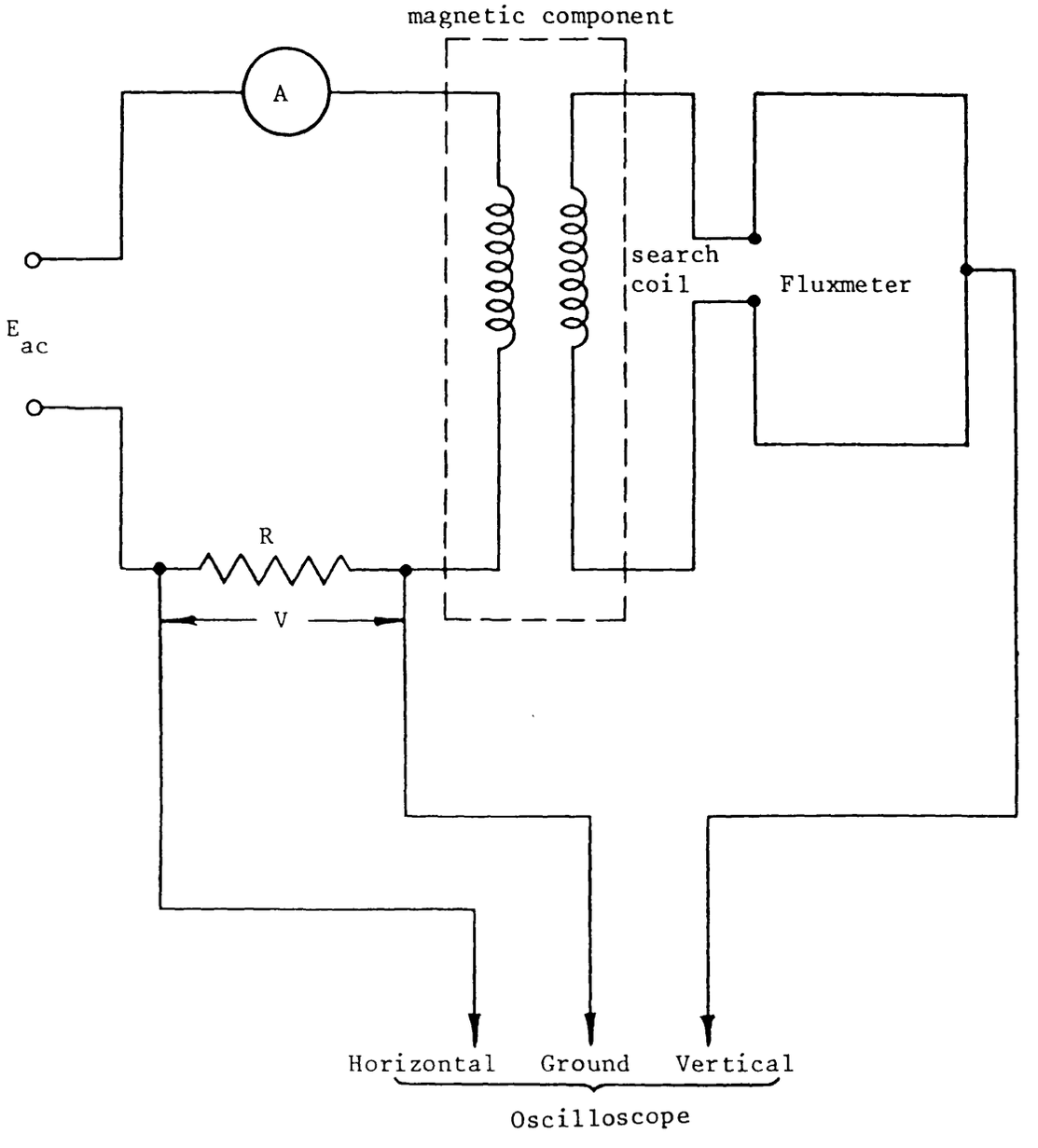

Fig.2.1: B-H loop test circuit

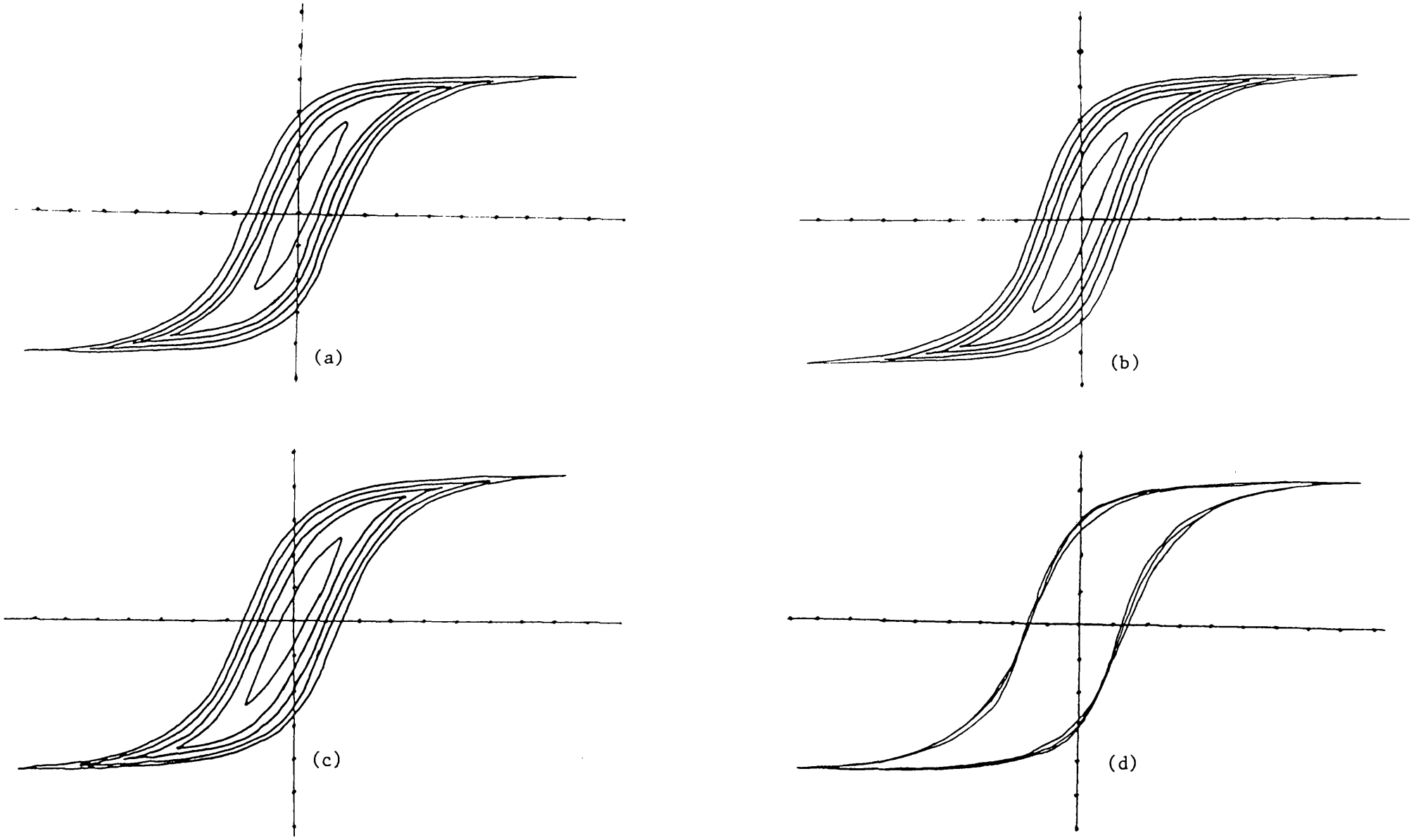

Fig.2.2: BH loops for 3 cores FX3750 at 25°C

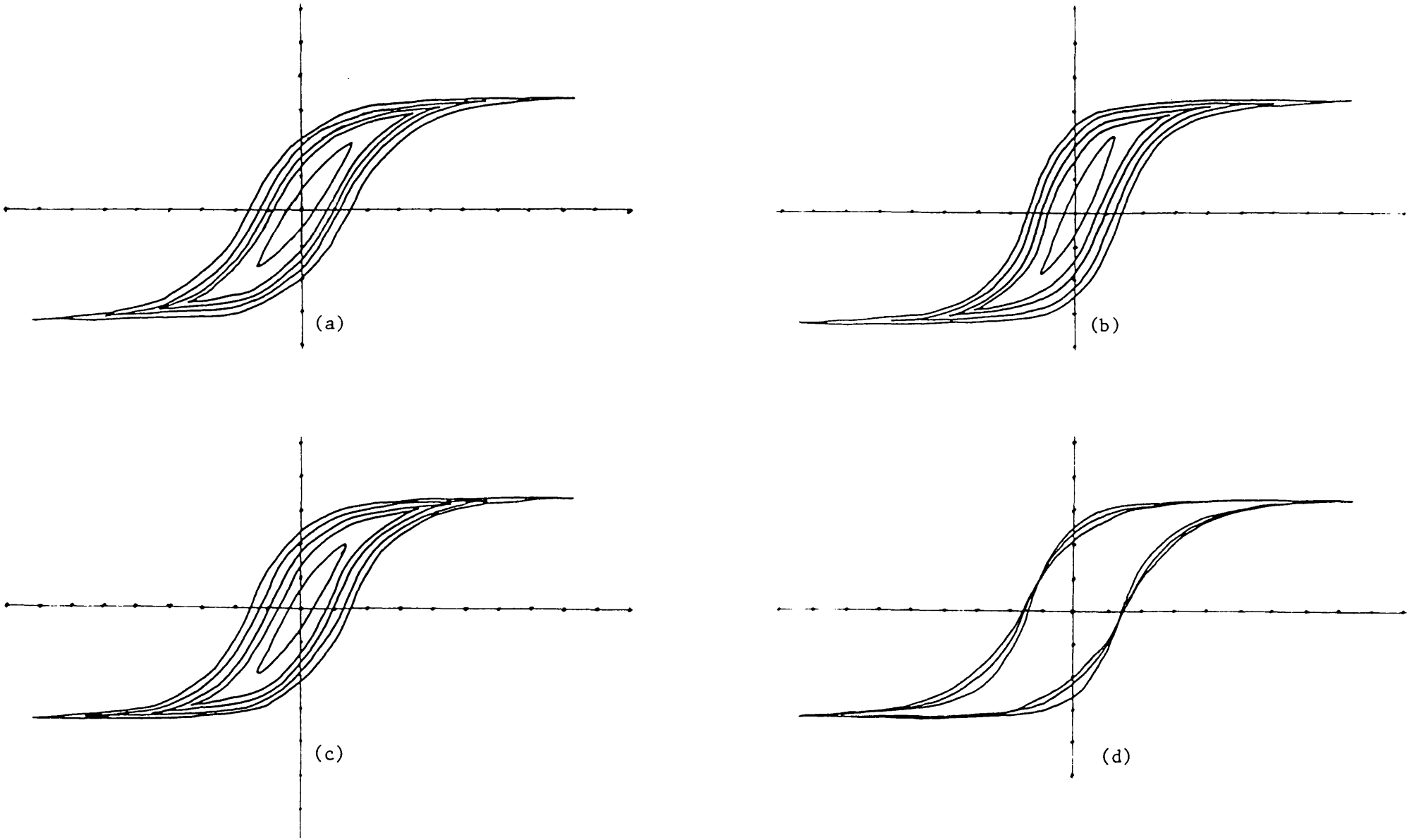

Fig.2.3: BH loops for 3 cores FX3750 at $100^{o}C$

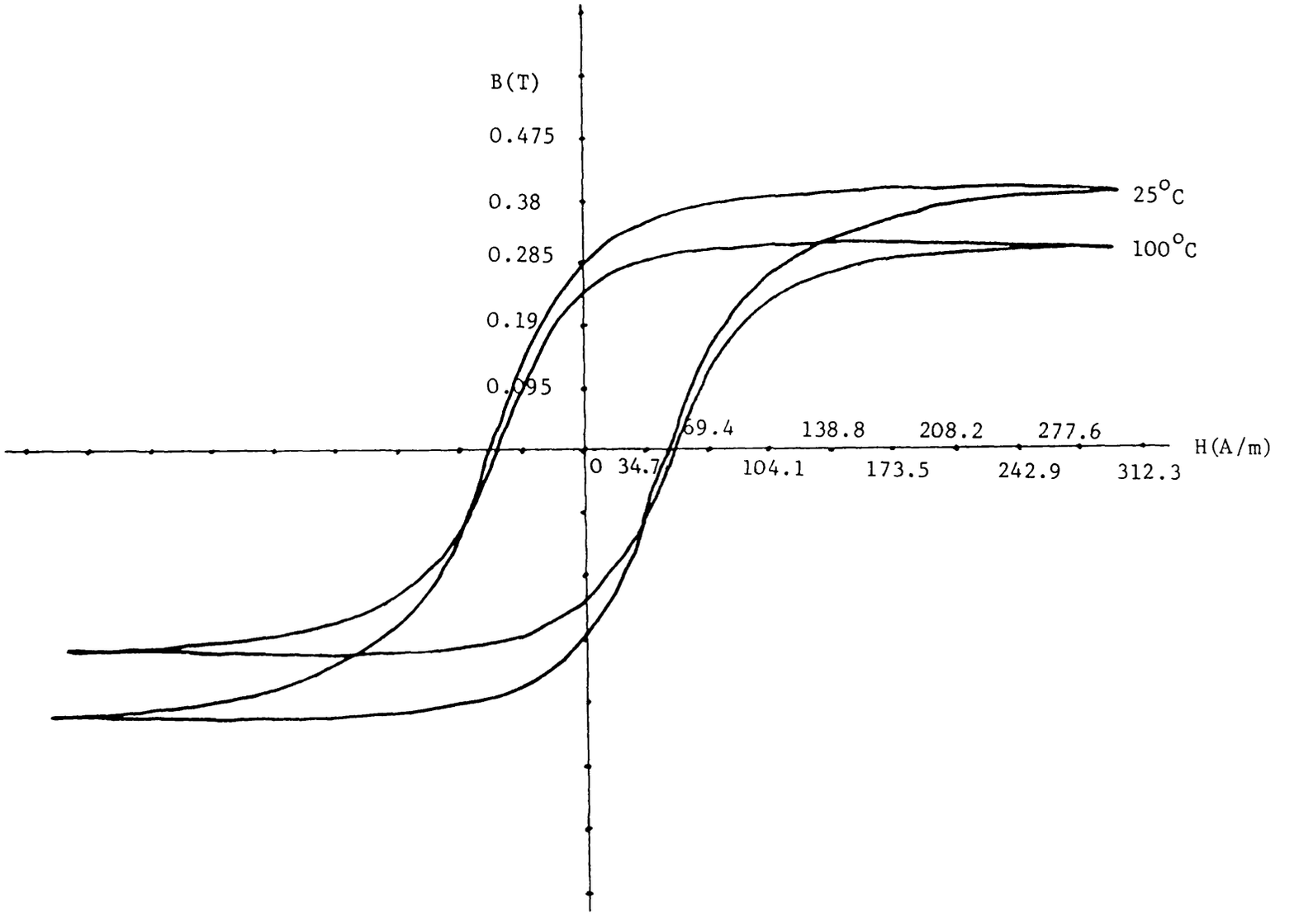

Fig.2.4: Variation in BH loops with temperature

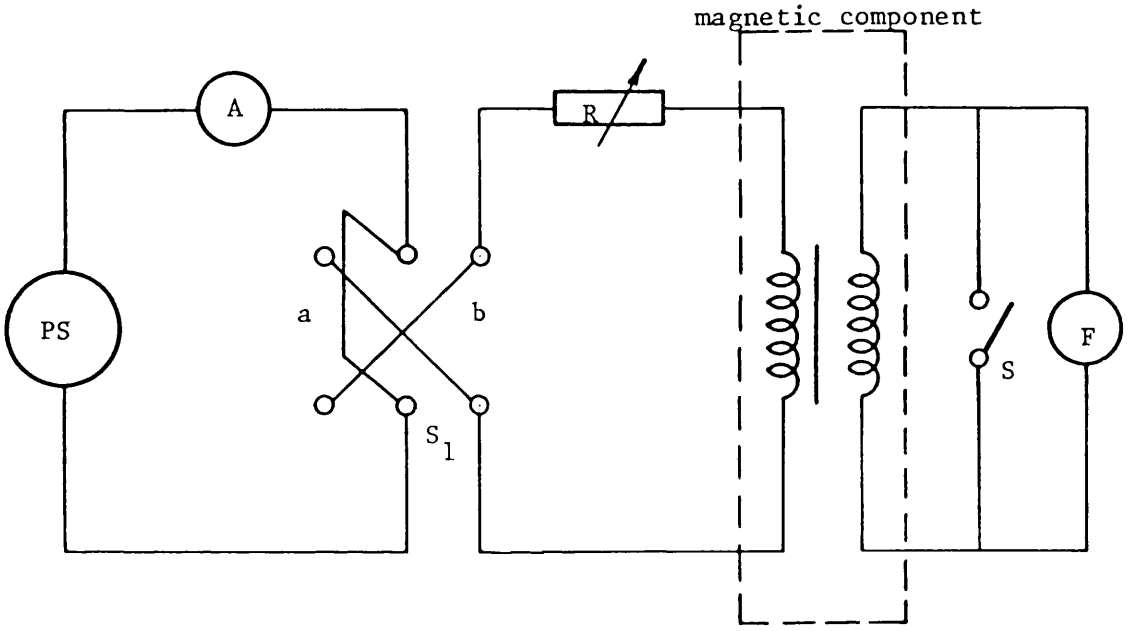

Fig.2.5: Circuit used for magnetization curves measurement

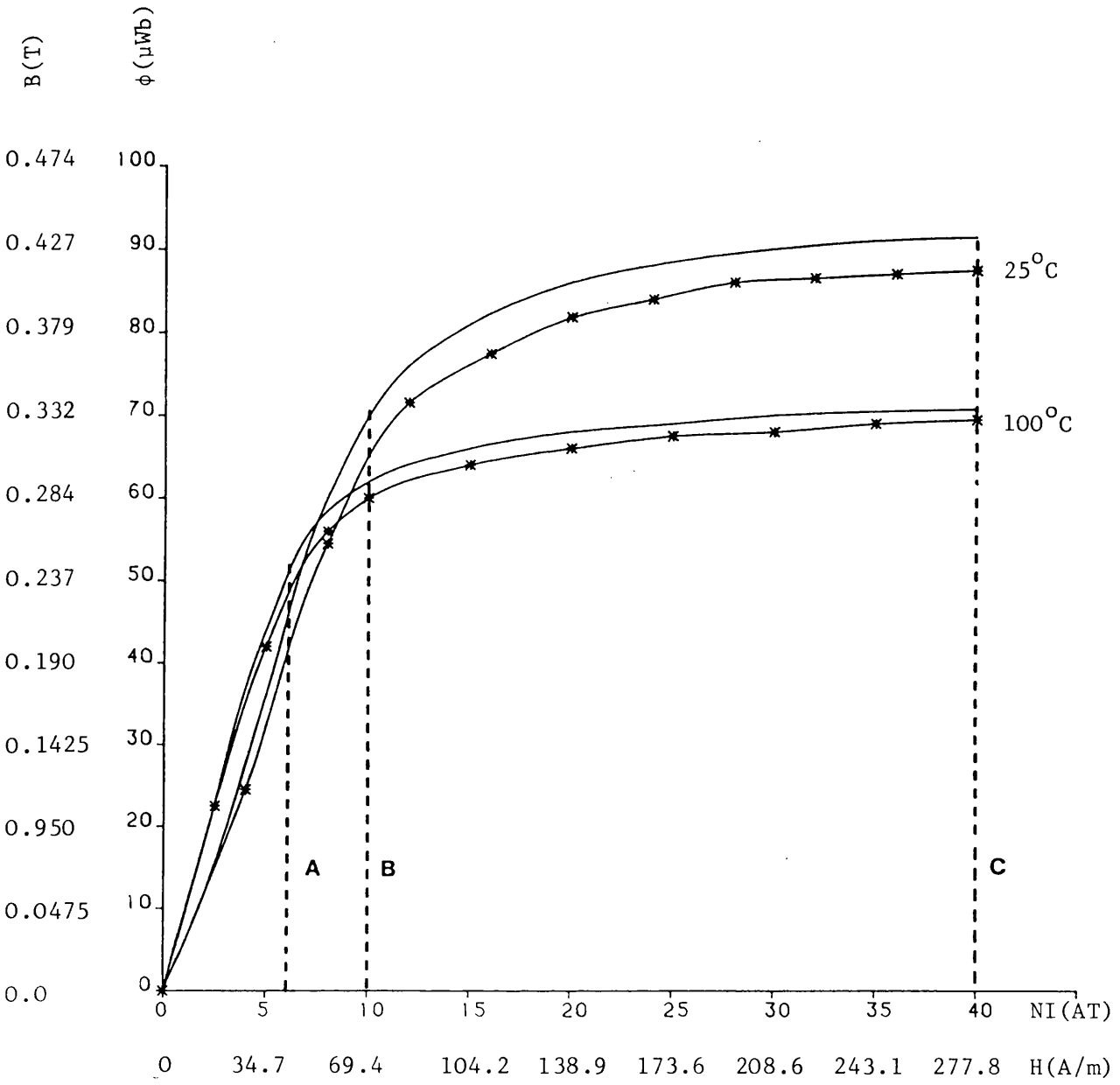

Fig. 2.6: Magnetization curves of FX3750 core

——— Mullard data sheet

--* Measurement results

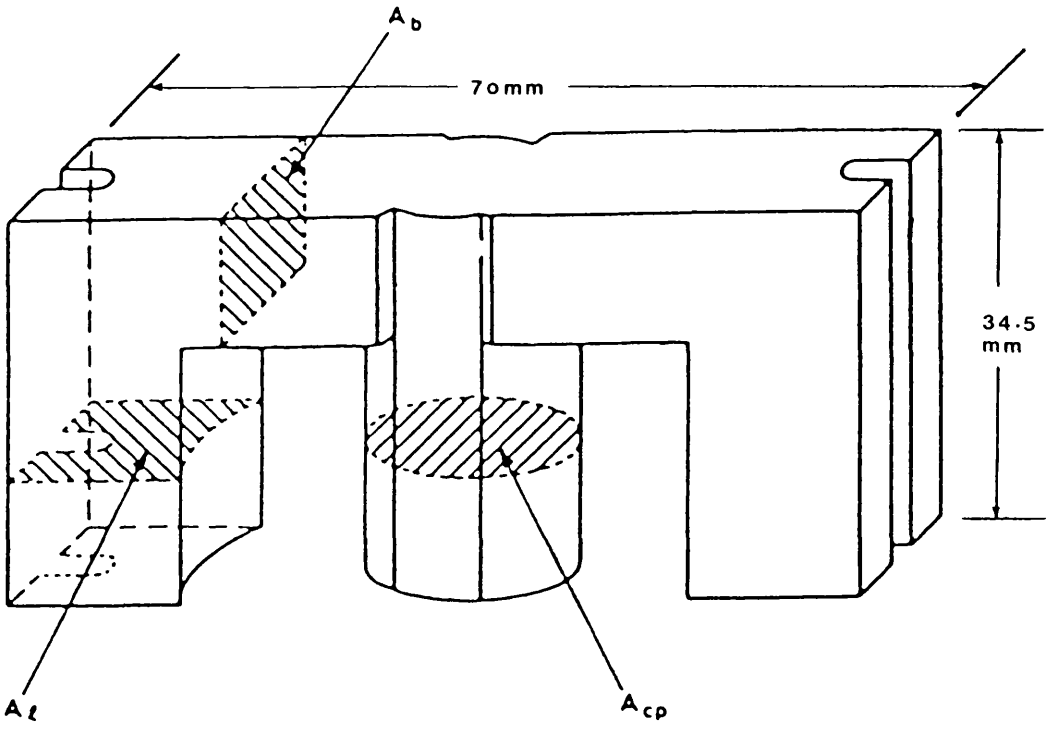

Fig.2.7: Dimensions of FX3750 core

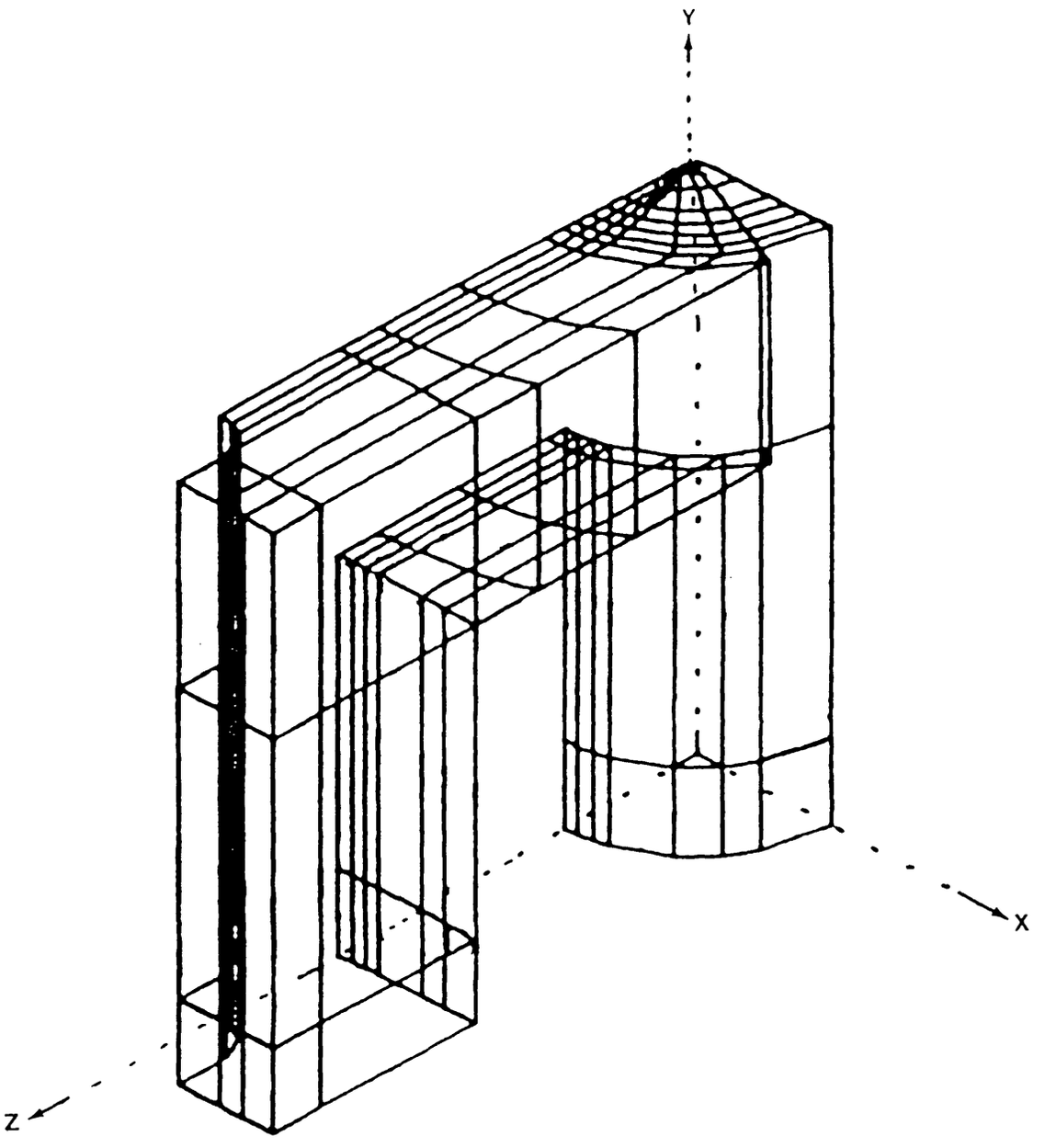

Fig.2.8: Model of FX3750 core on TOSCA

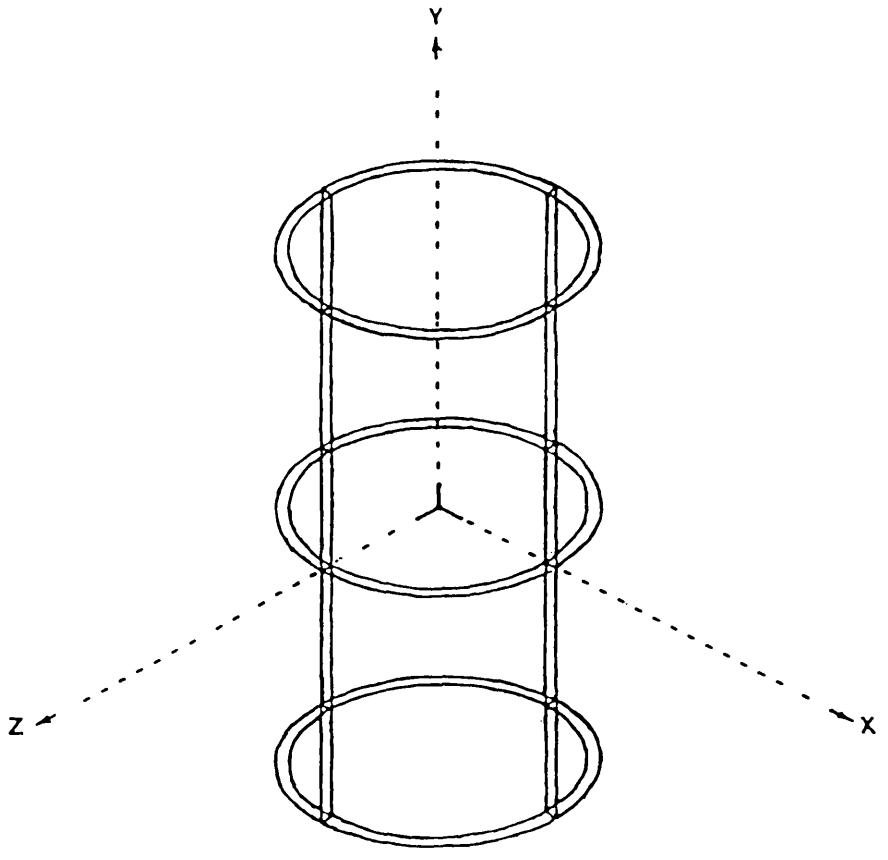

Fig.2.9: Representation of the coil on TOSCA

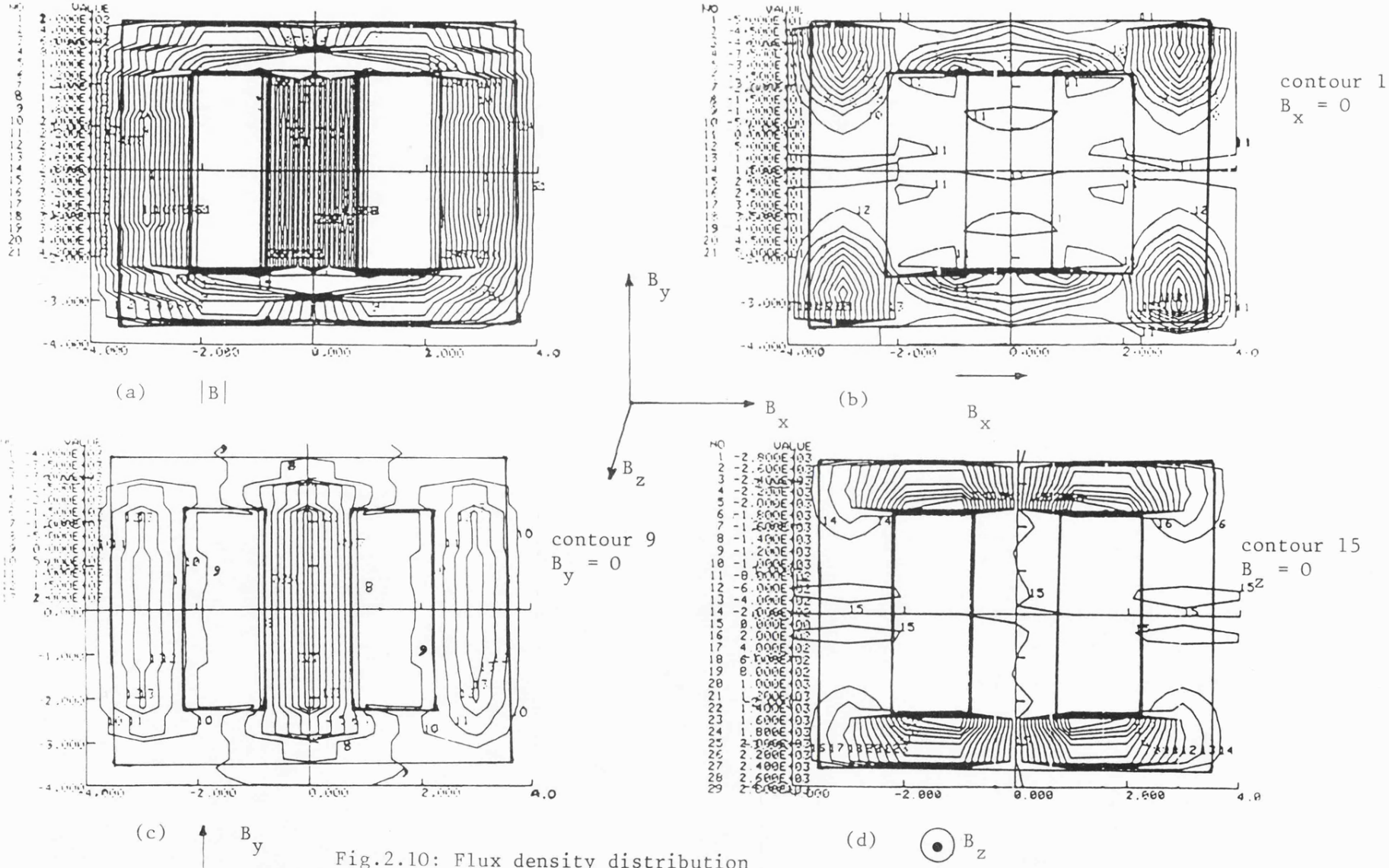

Fig.2.10: Flux density distribution at 25°C and NI = 40 AT

(a) |B| (c) B_y

(b) B_x (d) B_z

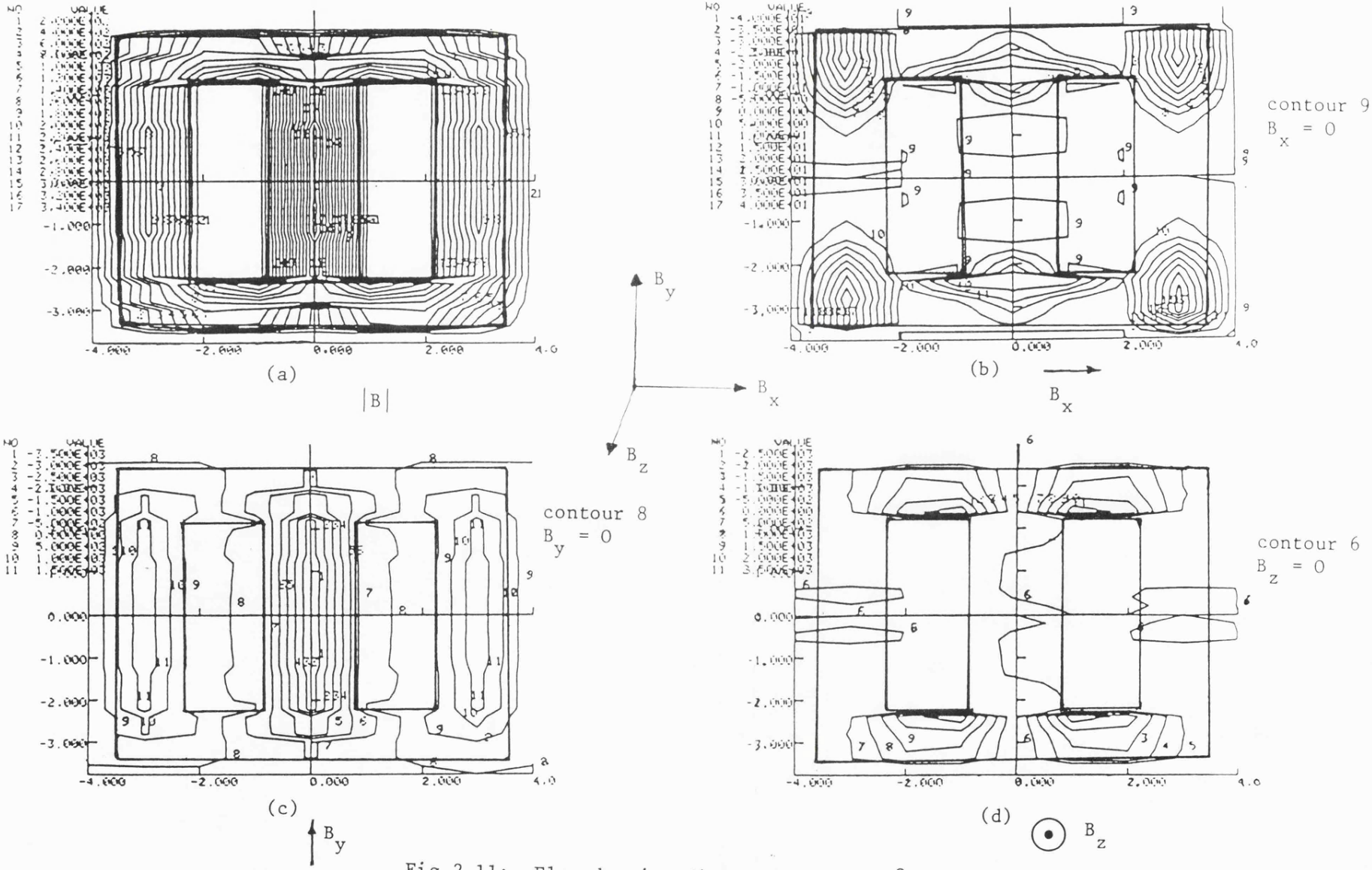

Fig.2.11: Flux density distribution at 25°C and NI = 10 AT

(a) |B| (c) B_y

(b) B_x (d) B_z

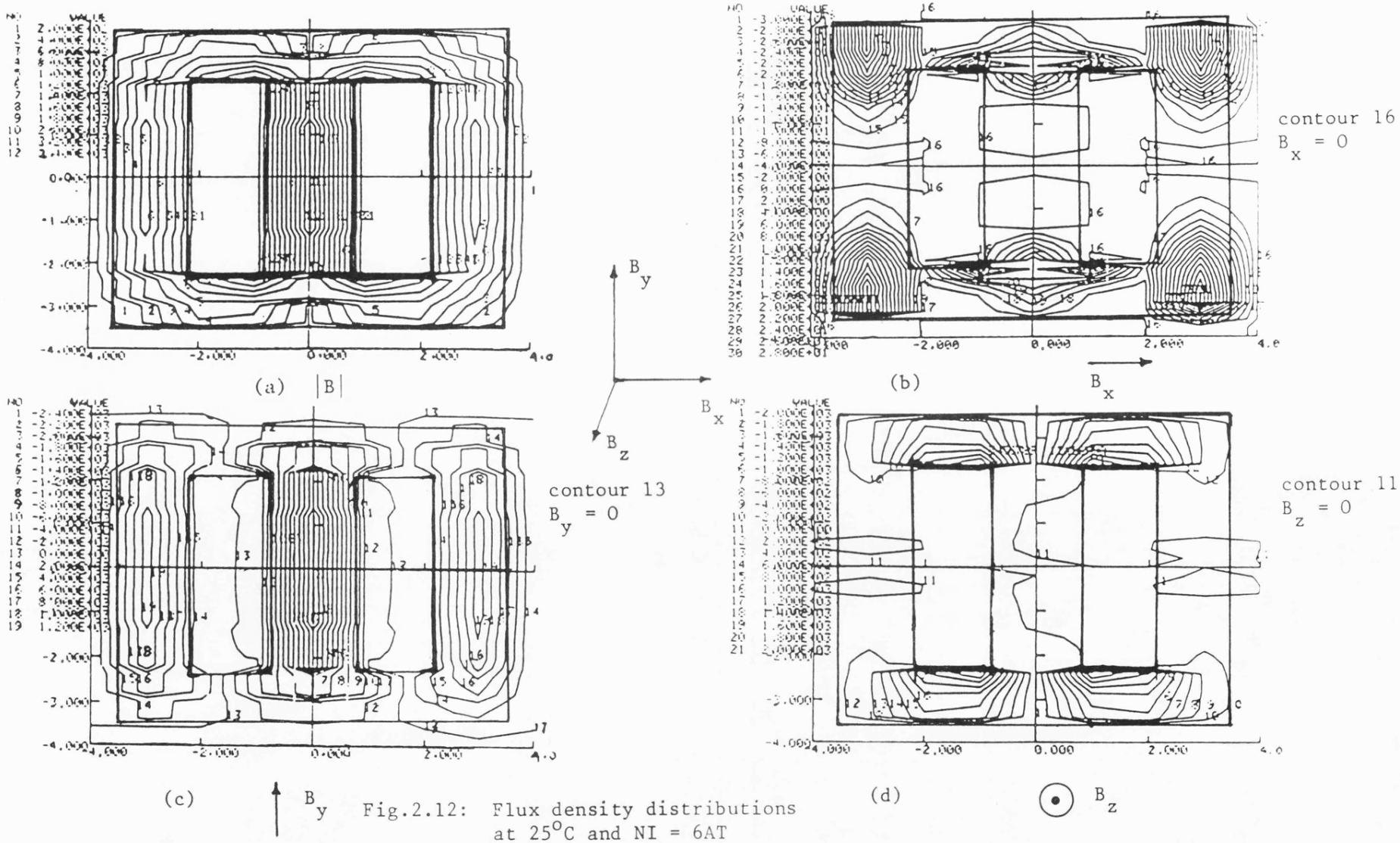

Fig.2.12: Flux density distributions at 25°C and NI = 6AT

(a) |B| (c) B_y

(b) B_x (d) B_z

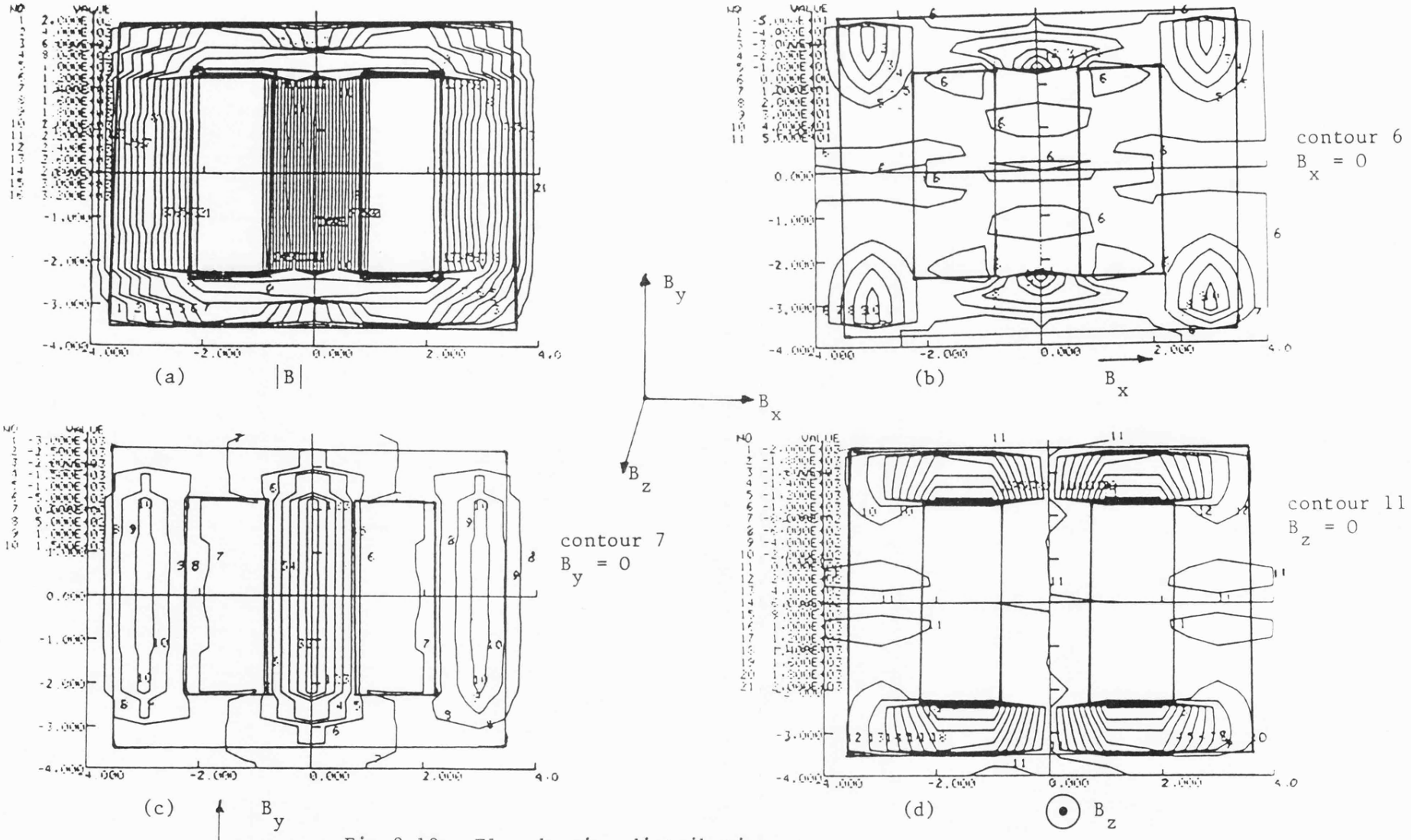

Fig.2.13: Flux density distribution at 100°C and NI = 40AT

(a) |B| (c) B_y

(b) B_x (d) B_z

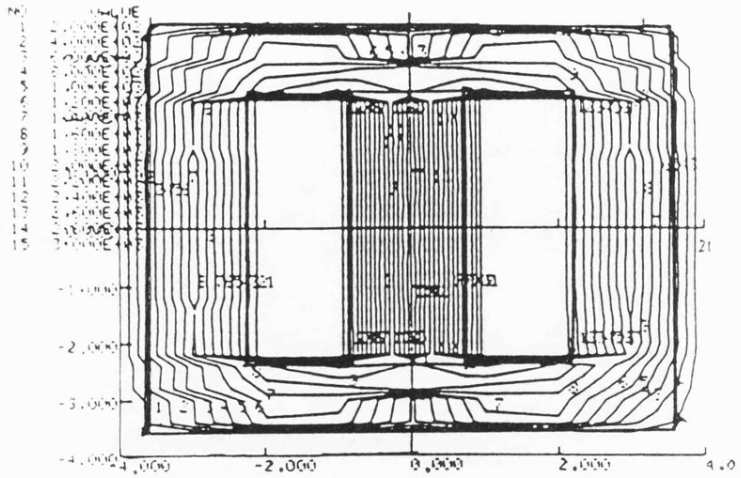

(a) $|B|$

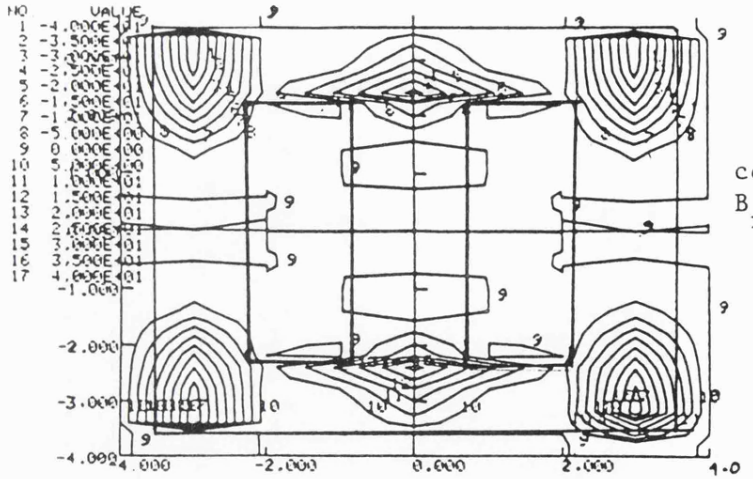

contour 9
$B_x = 0$

(b) B_x

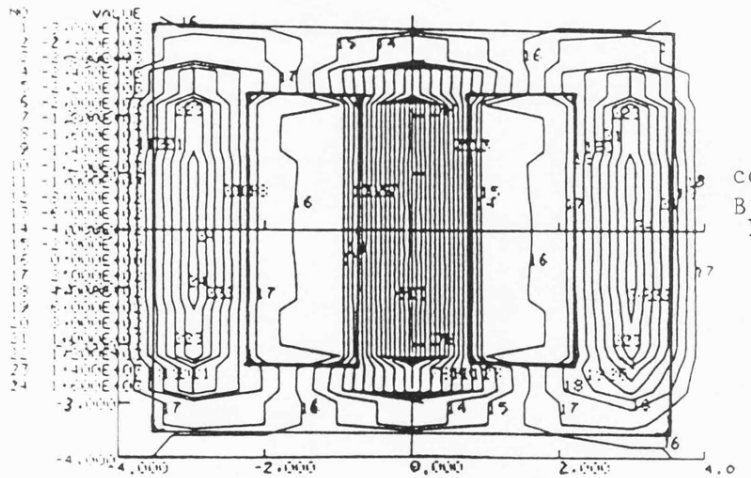

contour 16
$B_y = 0$

(c) B_y

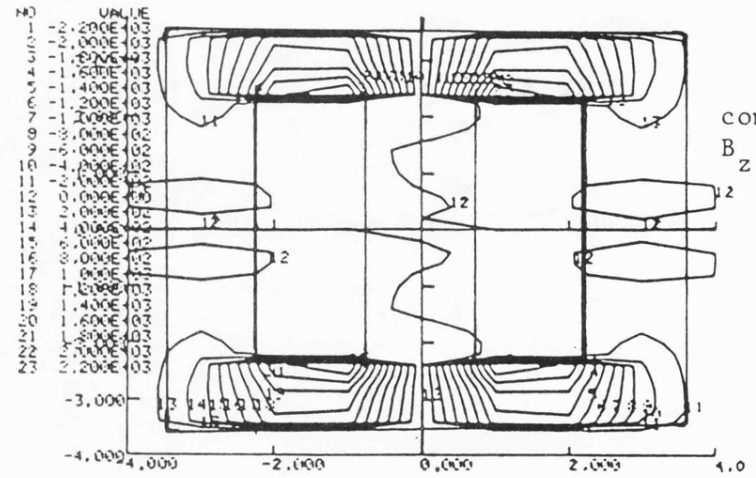

contour 12
$B_z = 0$

(d) B_z

Fig.2.14: Flux density distribution at 100°C and NI = 10AT

(a) $|B|$ (c) B_y

(b) B_x (d) B_z

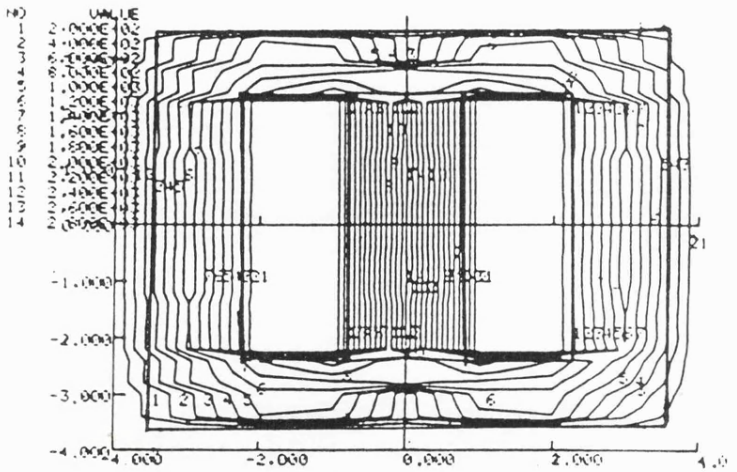

(a) $|B|$

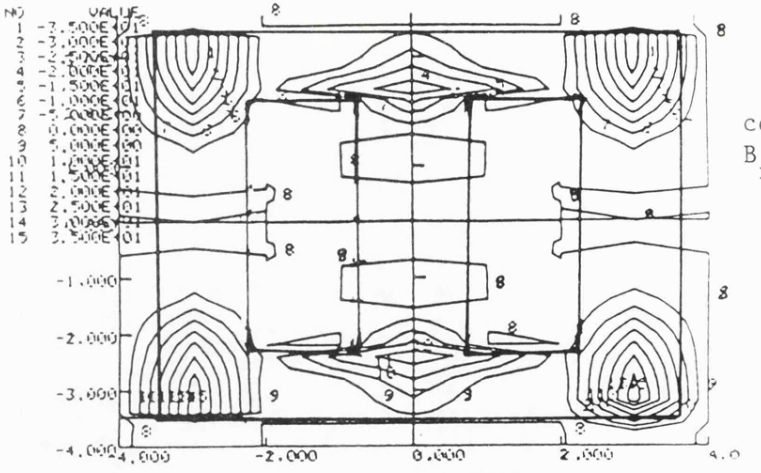

(b) B_x

contour 8
$B_x = 0$

B_y

B_x

B_z

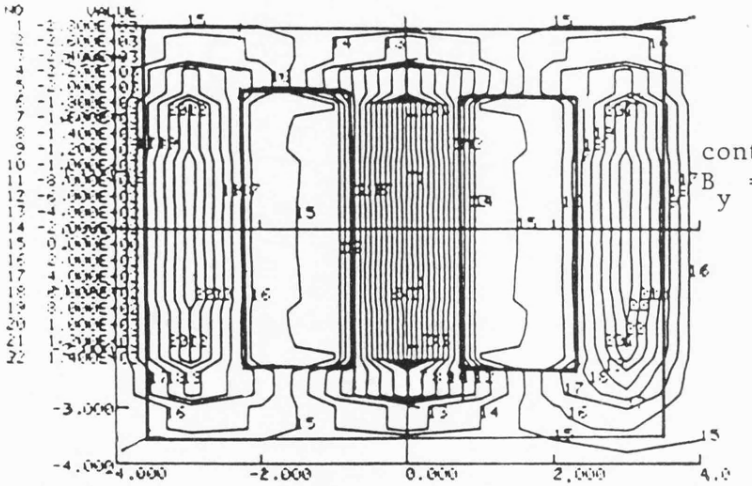

(c) B_y

contour 15
$B_y = 0$

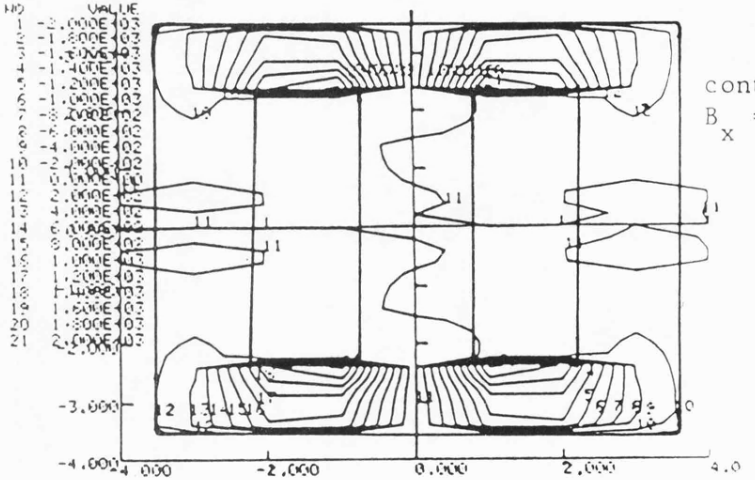

(d) B_z

contour 11
$B_x = 0$

Fig.2.15: Flux density distribution at 100°C and NI = 6AT

(a) $|B|$ (c) B_y

(b) B_x (d) B_z

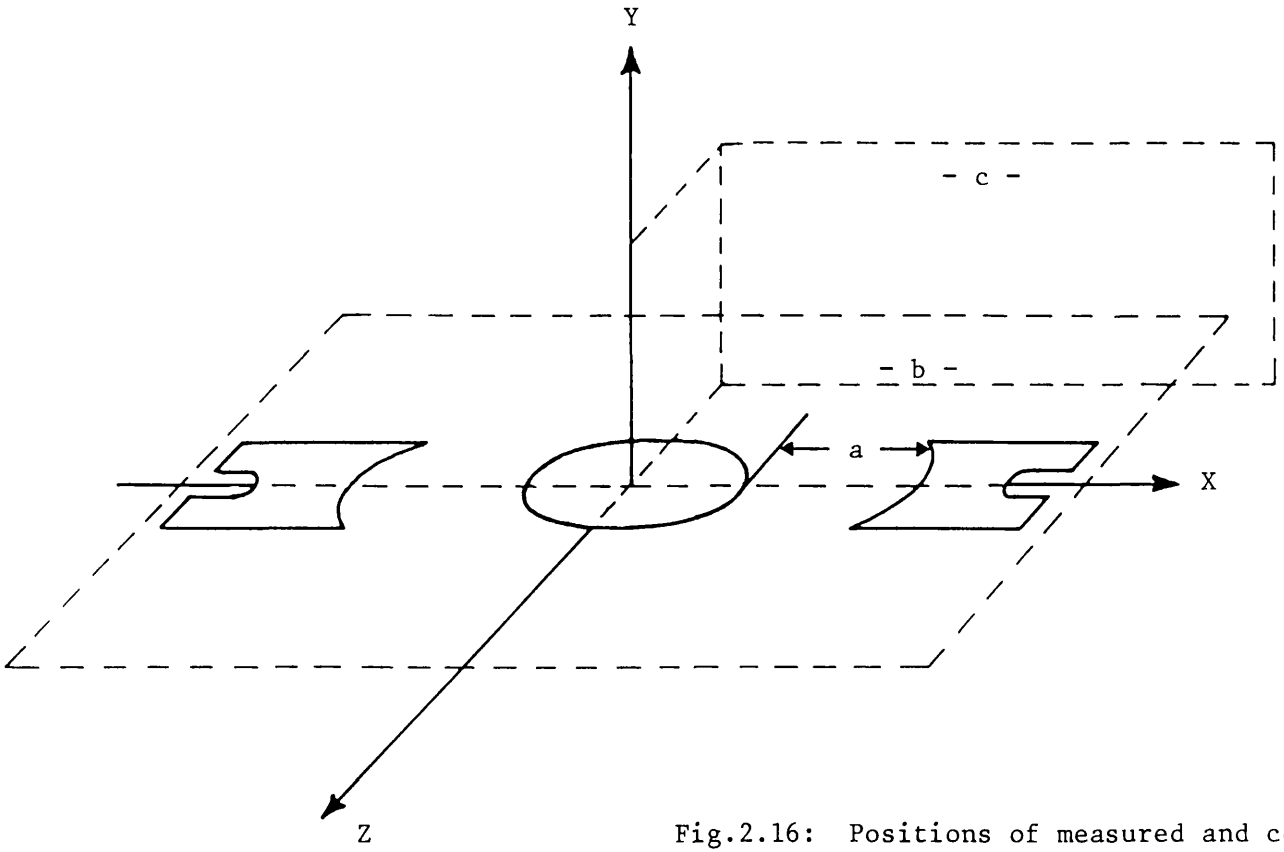

Fig.2.16: Positions of measured and computed results

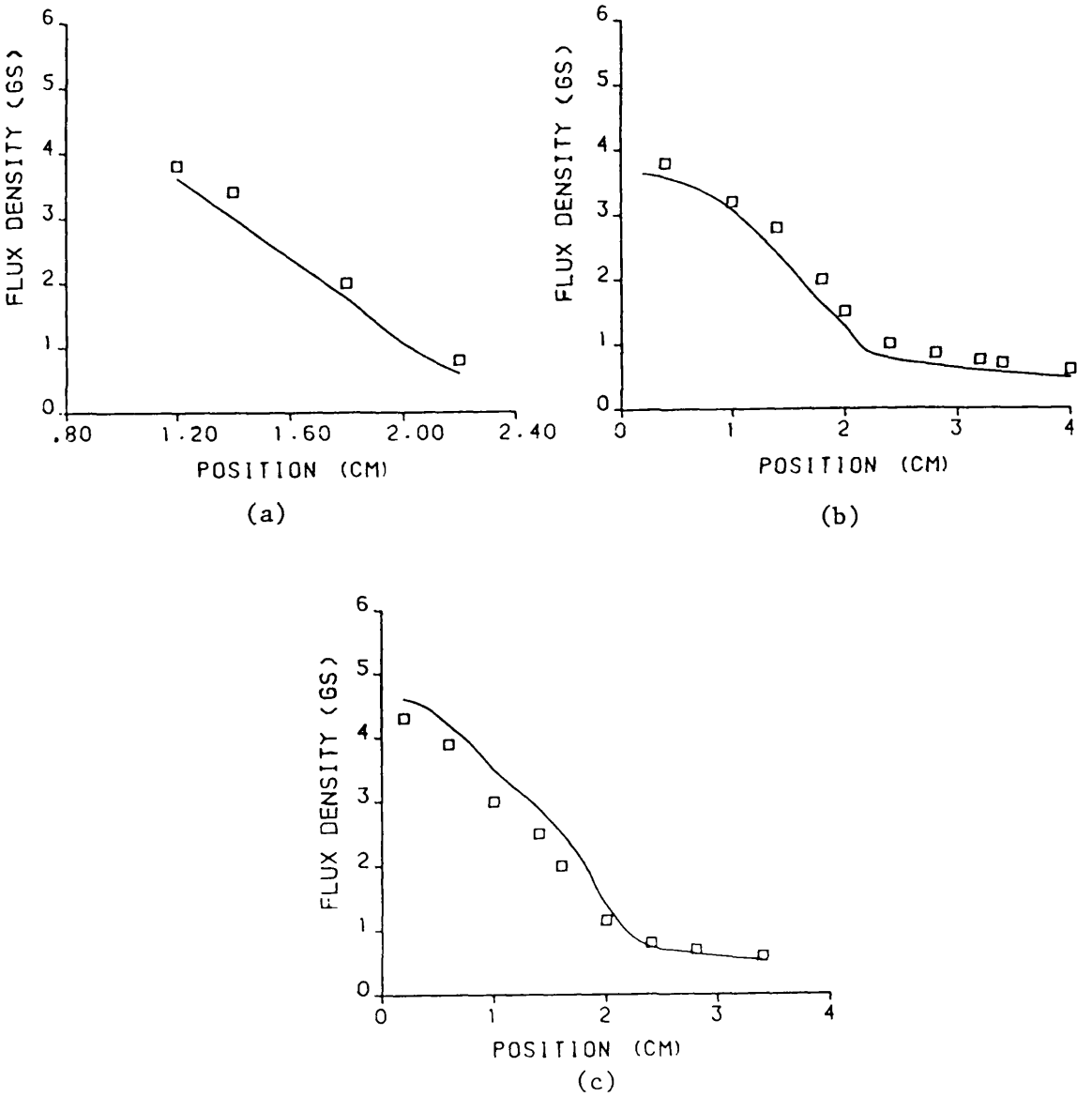

Fig.2.17: Distribution of flux density at NI = 40 AT

(a) at window area (x = 0, y = 0)
(b) outside the core (x = 1.4 cm, y = 0.0 cm)
(c) outside the core (x = 1.4 cm, y = 1.0 cm)

——— computed results using TOSCA

□ □ □ experimental results

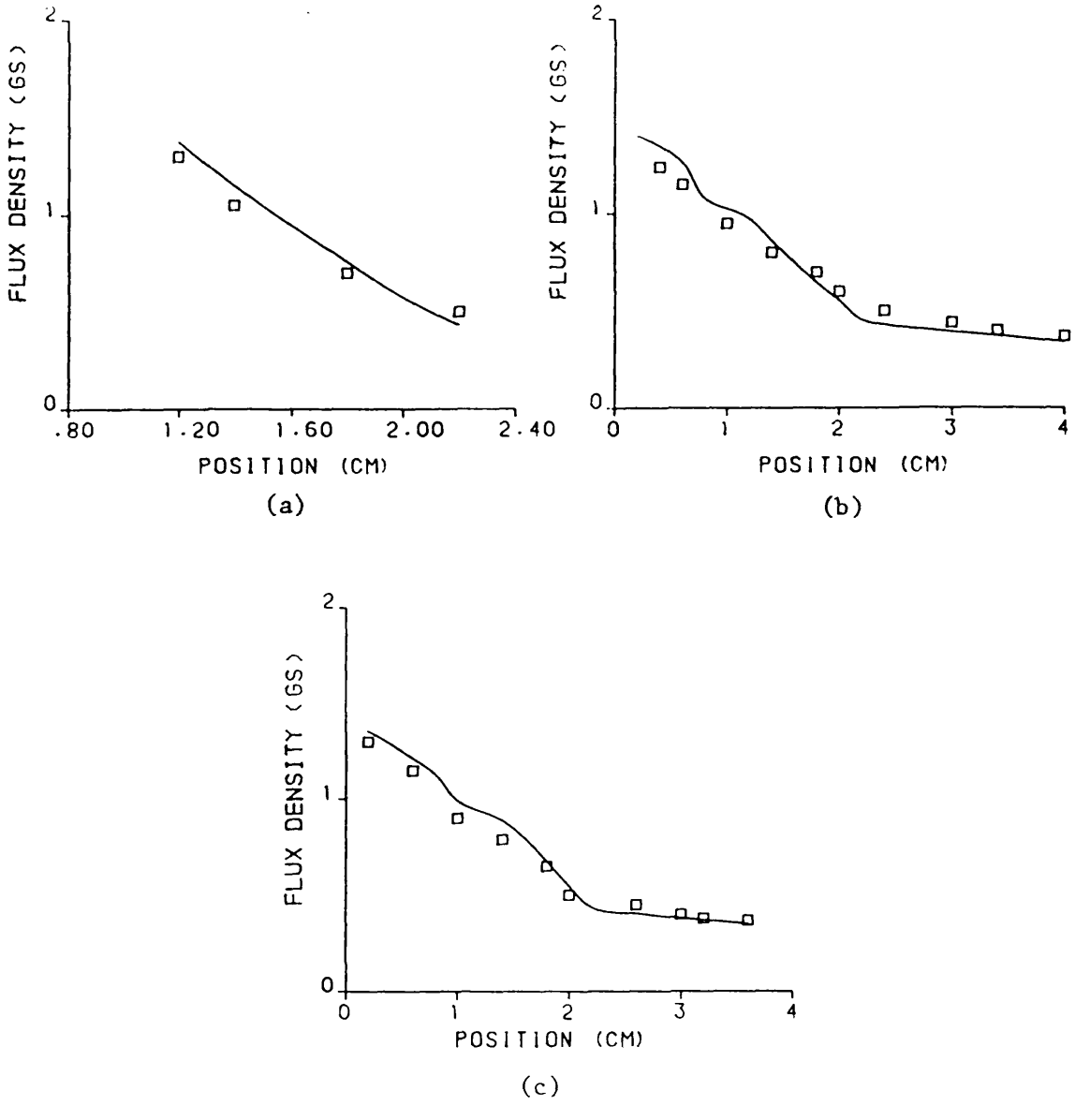

Fig.2.18: Distribution of flux density
at NI = 10 AT

(a) at window area at (x = 0, Y = 0 cm)
(b) outside the core at (x = 1.4 cm, y = 0.0)
(c) outside the core at (x = 1.4, y = 1.0)

——— computed results using TOSCA

□ □ □ experimental results

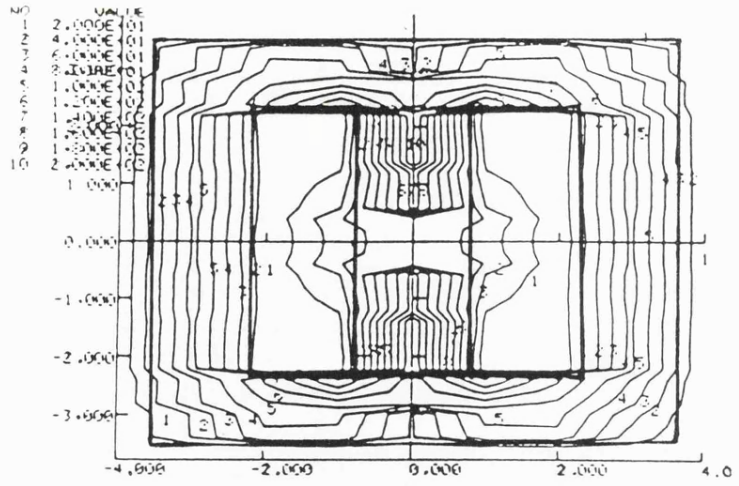

(a) |B|

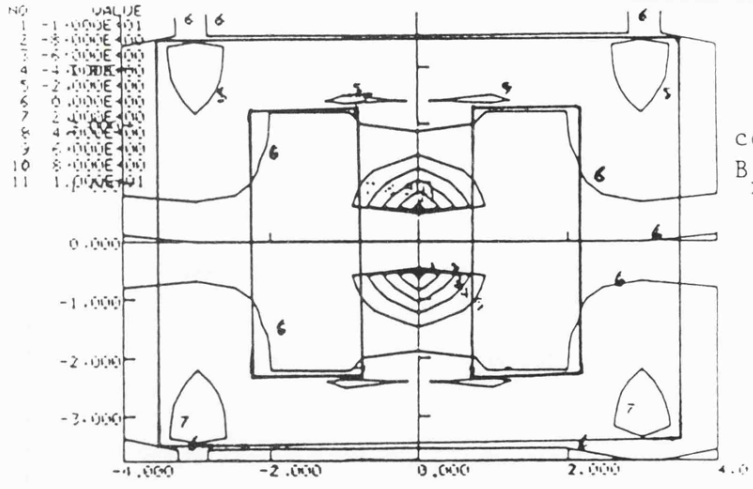

contour 6
$B_x = 0$

(b)

B_x

B_y

B_z

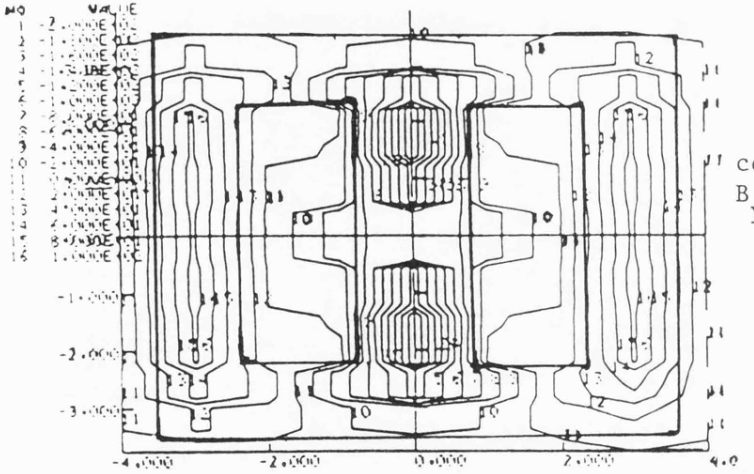

contour 11
$B_y = 0$

(c)

B_y

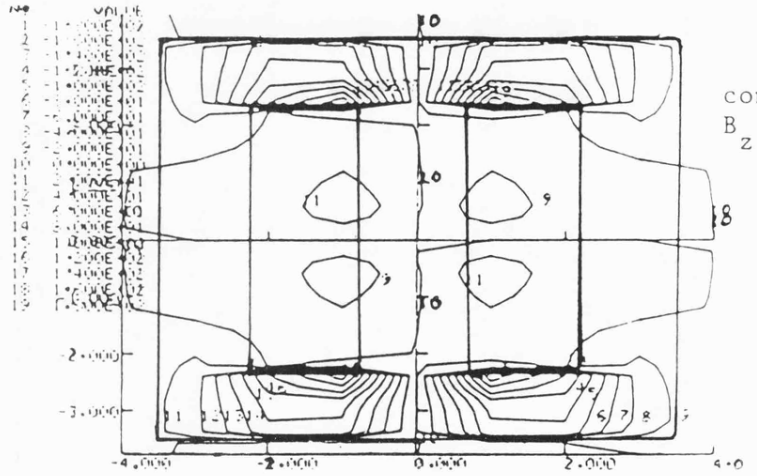

contour 10
$B_z = 0$

(d)

B_z

Fig.2.19: Flux density distribution at 25°C and NI = 40AT

(a) |B| (c) B_y

(b) B_x (d) B_z

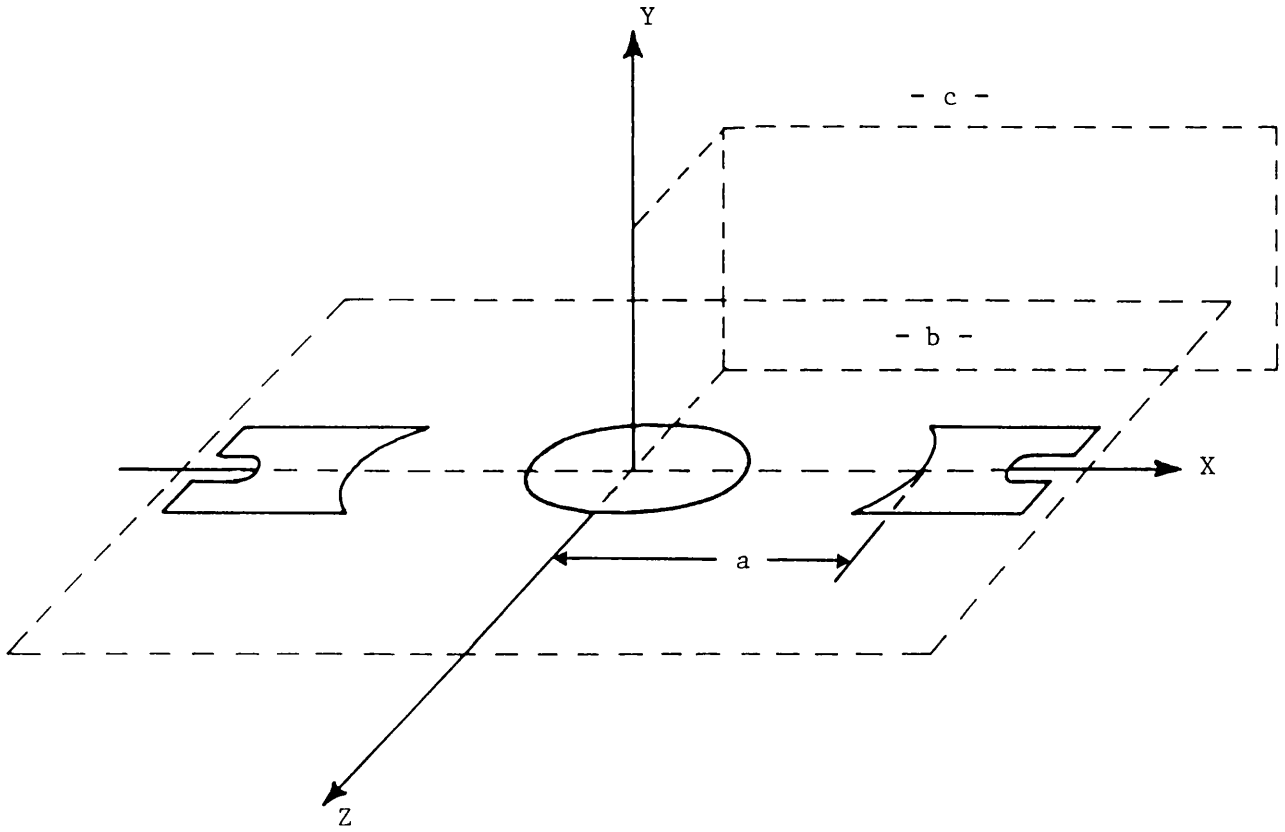

Fig.2.20: Positions of measured and computed results

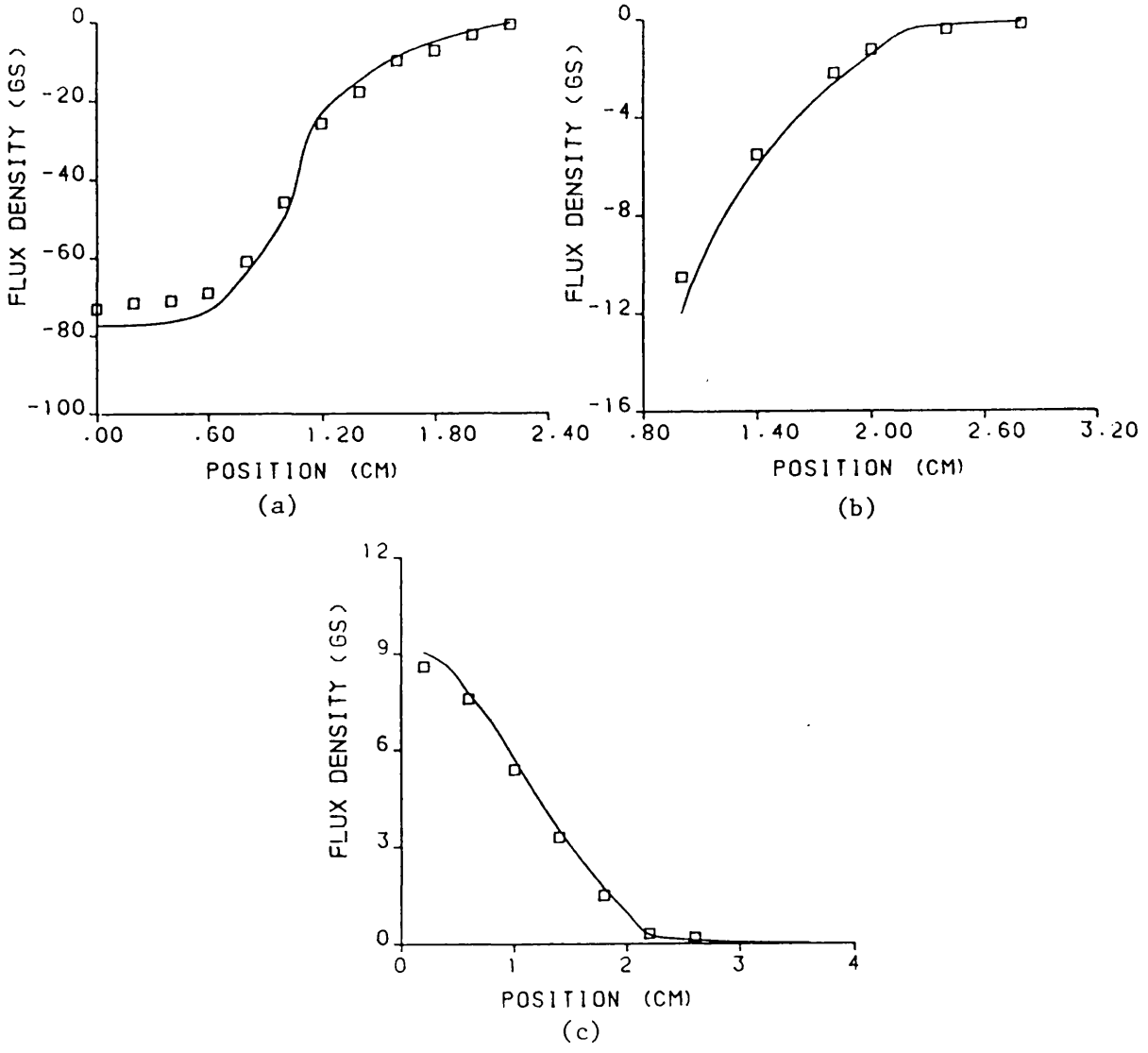

Fig.2.21: Distribution of flux density using gapped core at NI = 40 AT

(a) at the centreof the core at (x = 0.0, y = 0.0)
(b) outside the core at (x = 1.4, y = 0.0)
(c) outside the core at (x = 1.4, y = 1.4)

——— computed results using TOSCA

□ □ □ experimental results

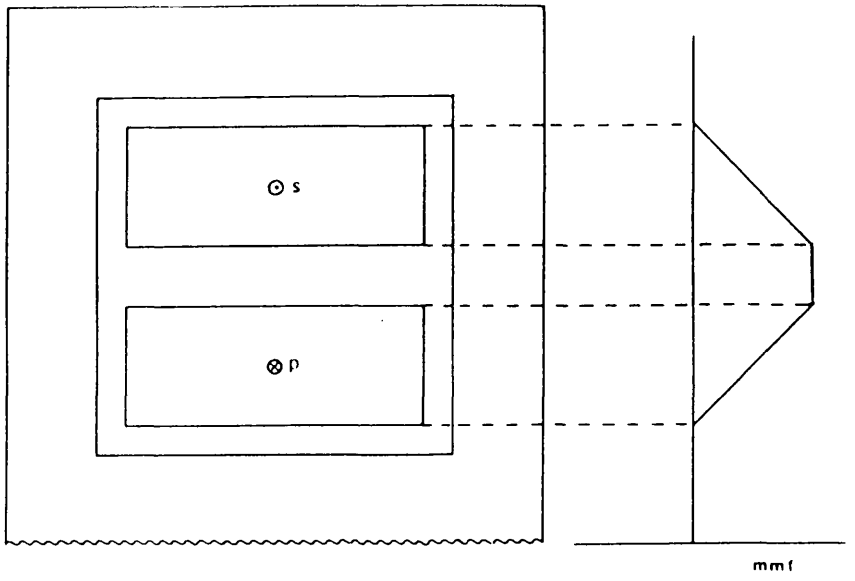

a

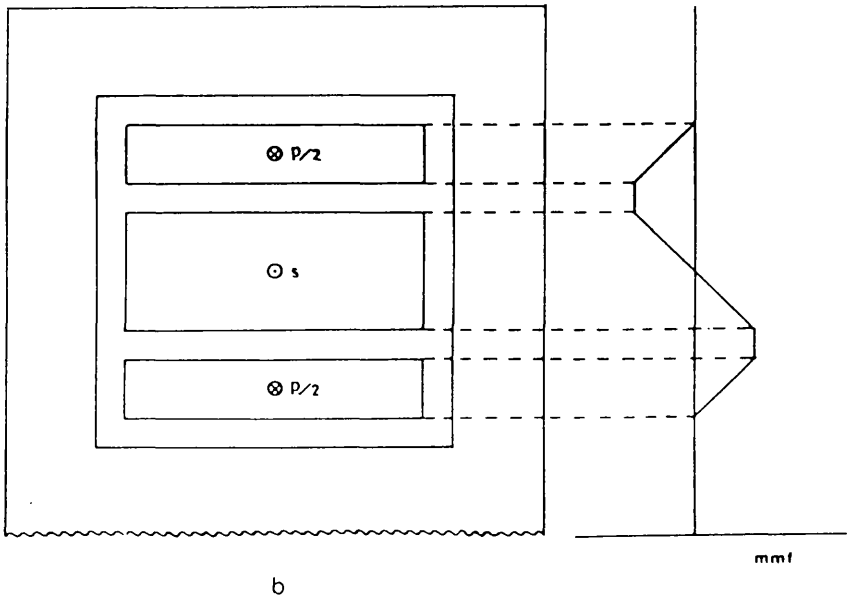

b

Fig.2.22: Transformer winding arrangement and the corresponding mmf diagrams

(a) 'simple' winding

(b) 'sandwich' winding

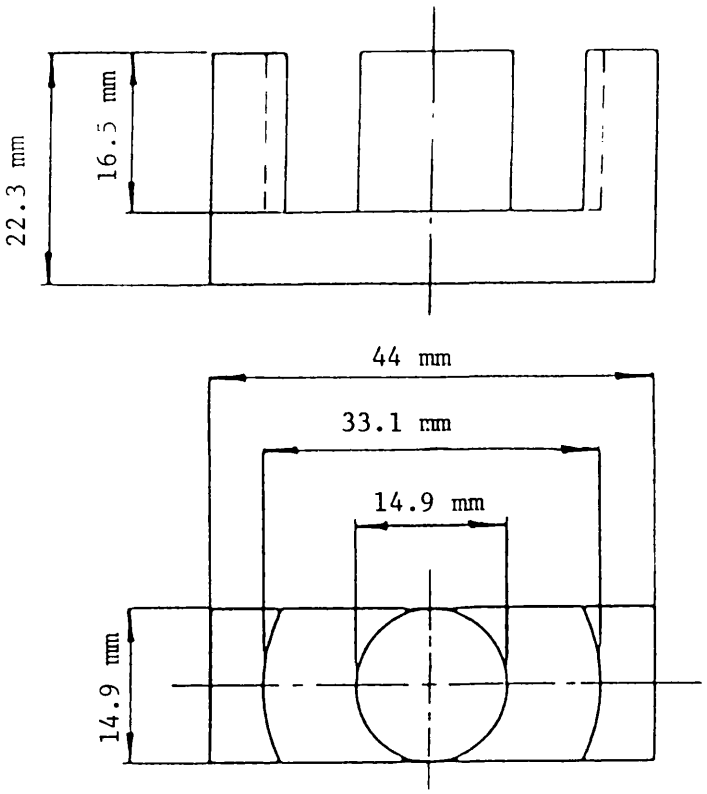

(a)

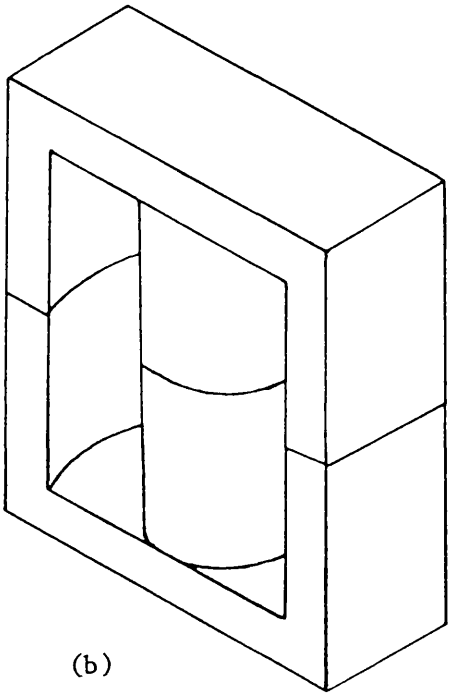

(b)

Fig.2.23: ETD44 core and winding
(a) dimensions of fully-wound core
(b) core

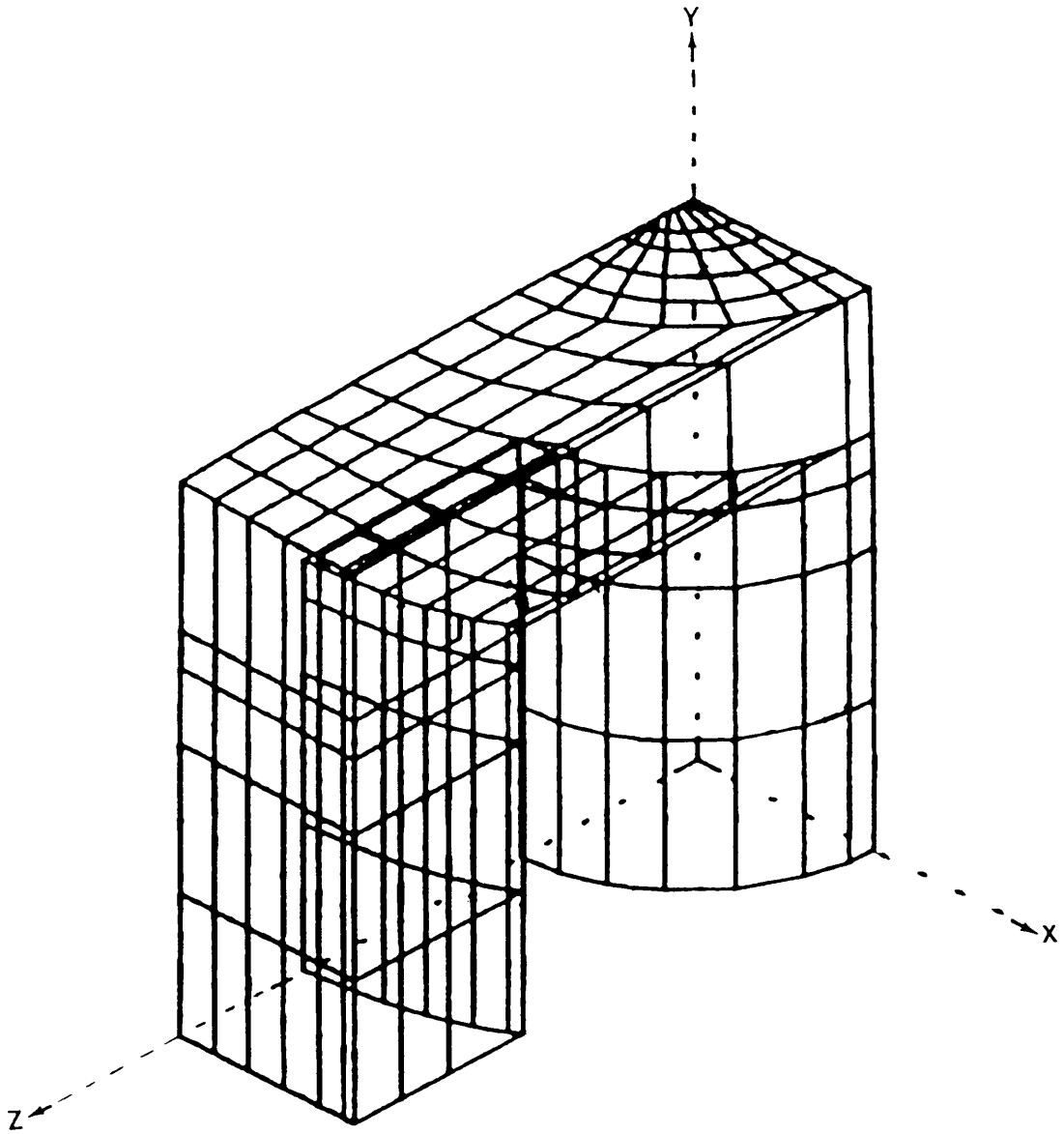

Fig.2.24: Model of ETD44 core

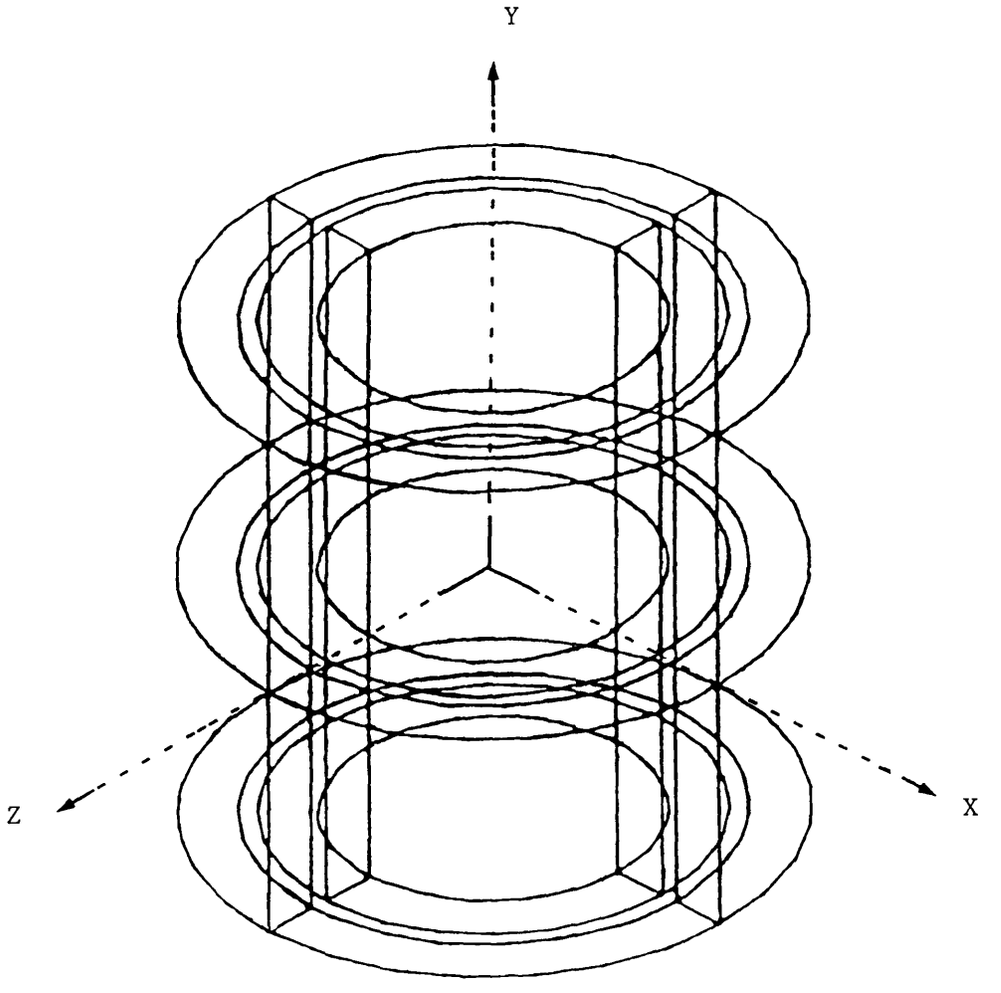

Fig.2.25: Representation of the coils on TOSCA

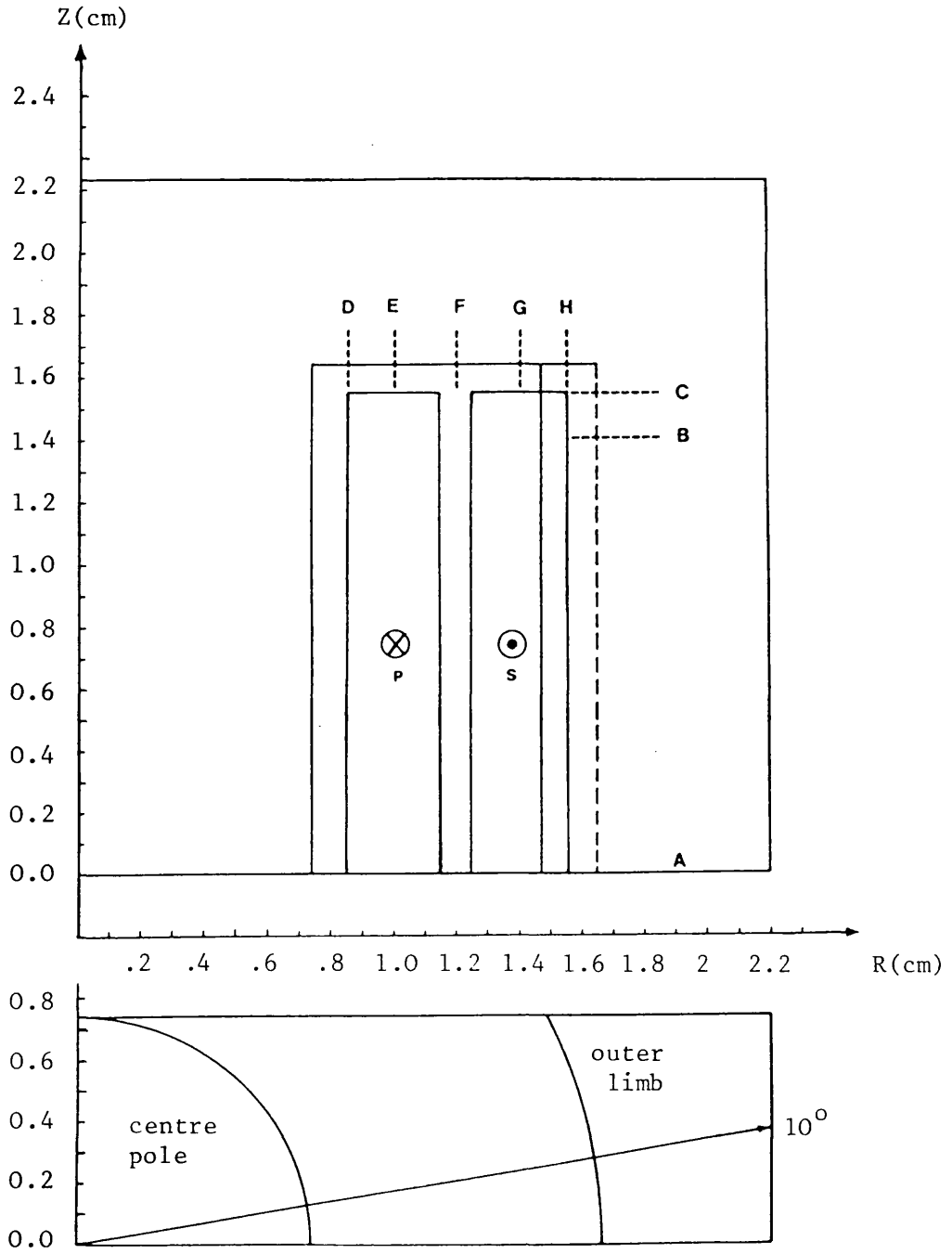

Fig.2.26: Quarter core polar coordinate with 'simple' winding

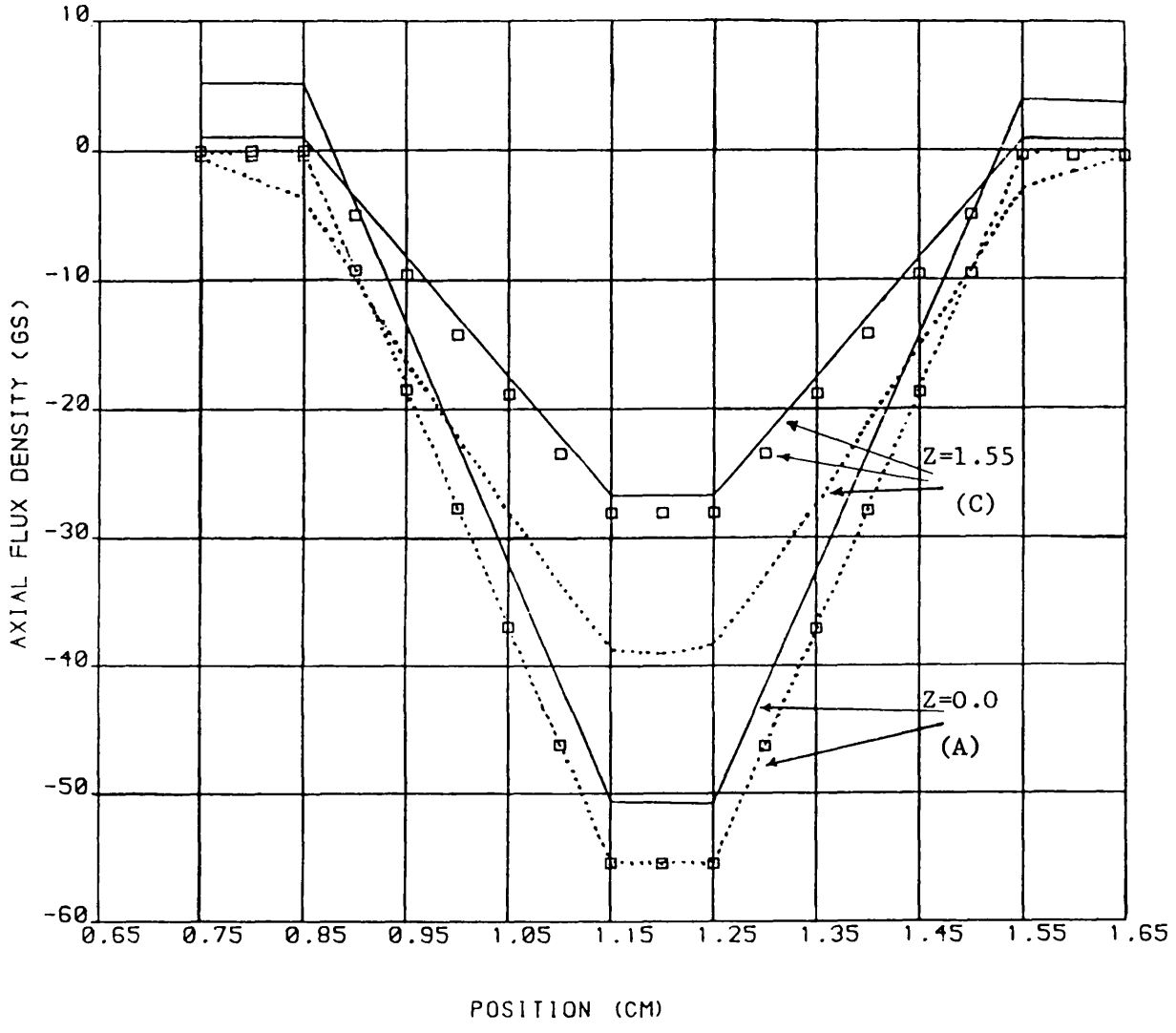

Fig.2.27: Axial flux density at position Z = 0.0(A) and Z = 1.55(C)

——— Model ETD44 without ferrite core

. . . Model ETD44 with ferrite core at $\theta = 10^{o}$

□ □ □ Model ETD44 with ferrite core at $\theta = 90^{o}$

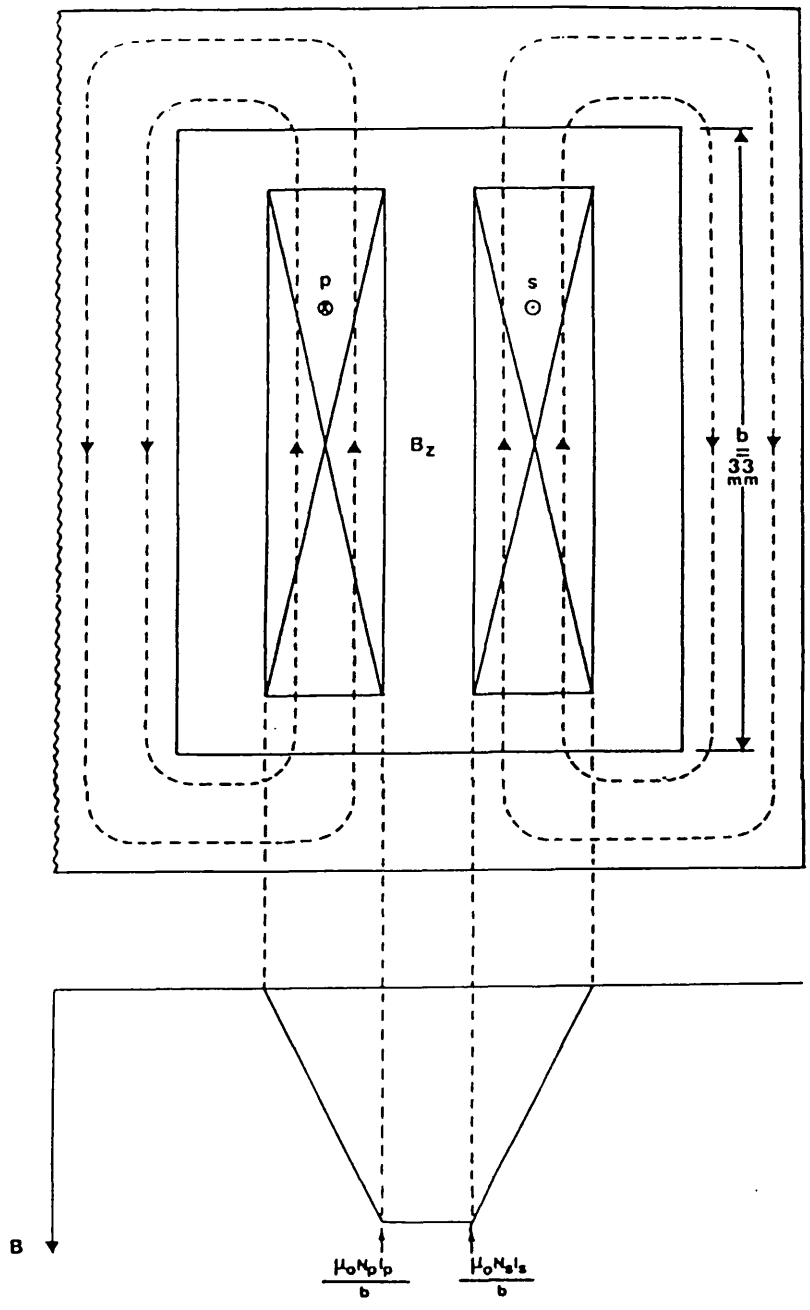

Fig.2.28: Leakage flux paths in 'simple' transformer winding and flux density distribution

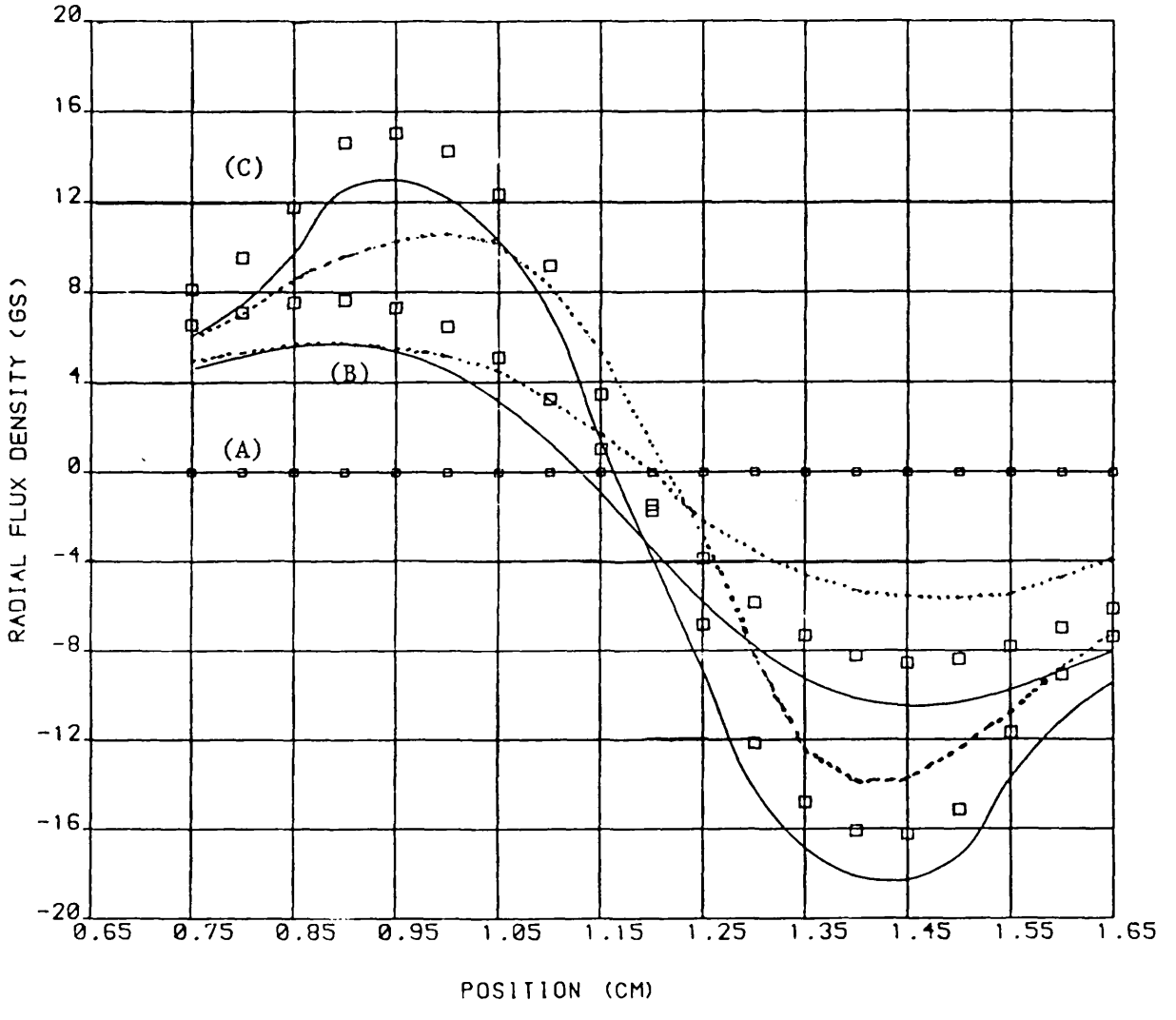

Fig.2.29: Radial flux density at positions Z = 0.0(A), Z = 1.4 cm(B) and Z = 1.55 cm(C)

——— Model ETD44 without ferrite core

. . . Model ETD44 with ferrite core at $\theta = 10^{o}$

□ □ □ Model ETD44 with ferrite core at $\theta = 90^{o}$

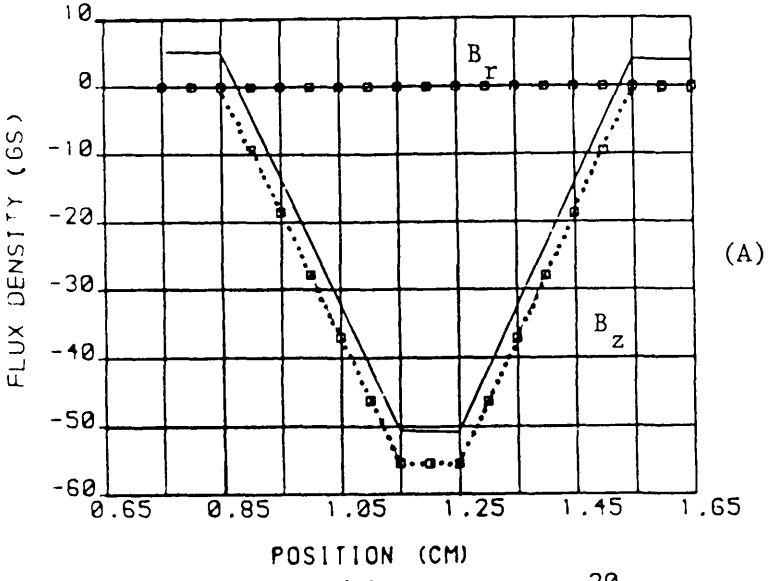

(a)

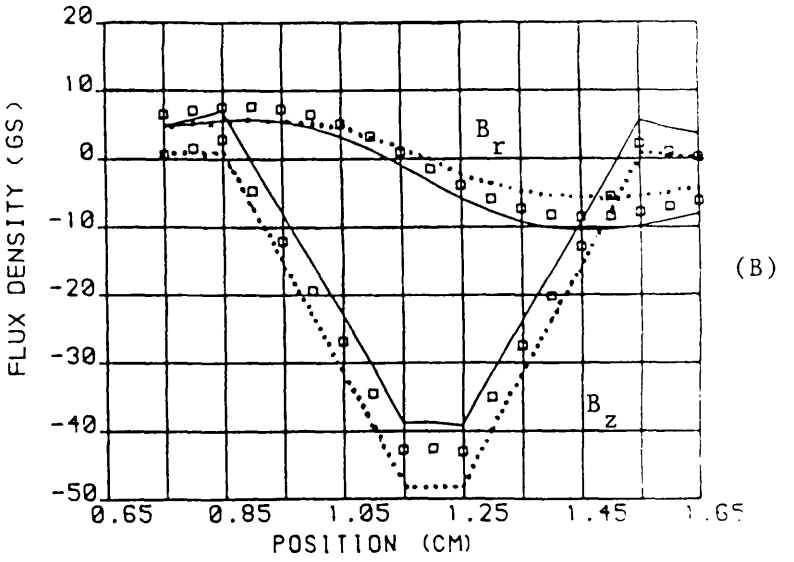

(b)

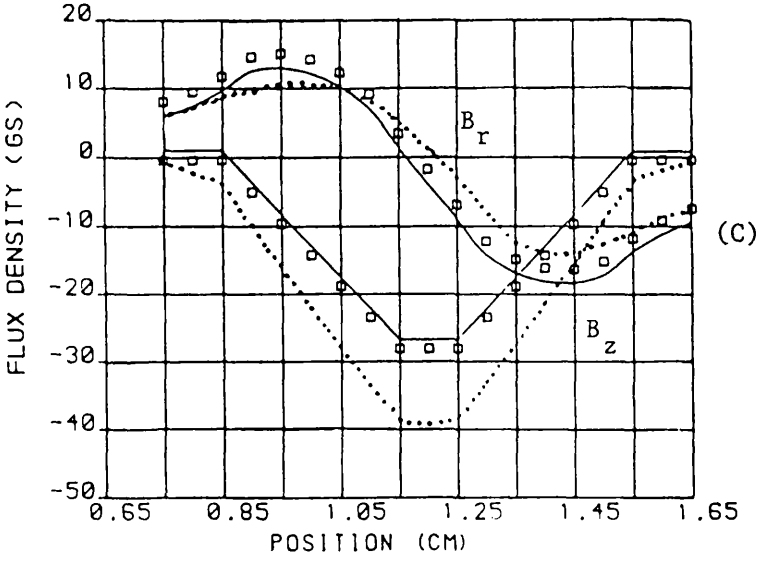

(c)

Fig.2.30: Comparison between B_r and B_z flux density

(a) B_r and B_z at Z = 0.0(A)

(b) B_r and B_z at Z = 1.4 cm(B)

(C) B_r and B_z at Z = 1.55 cm(C)

——— without ferrite core

. . . with ferrite core at $\theta = 10^{\circ}$

□ □ □ with ferrite core at $\theta = 90^{\circ}$

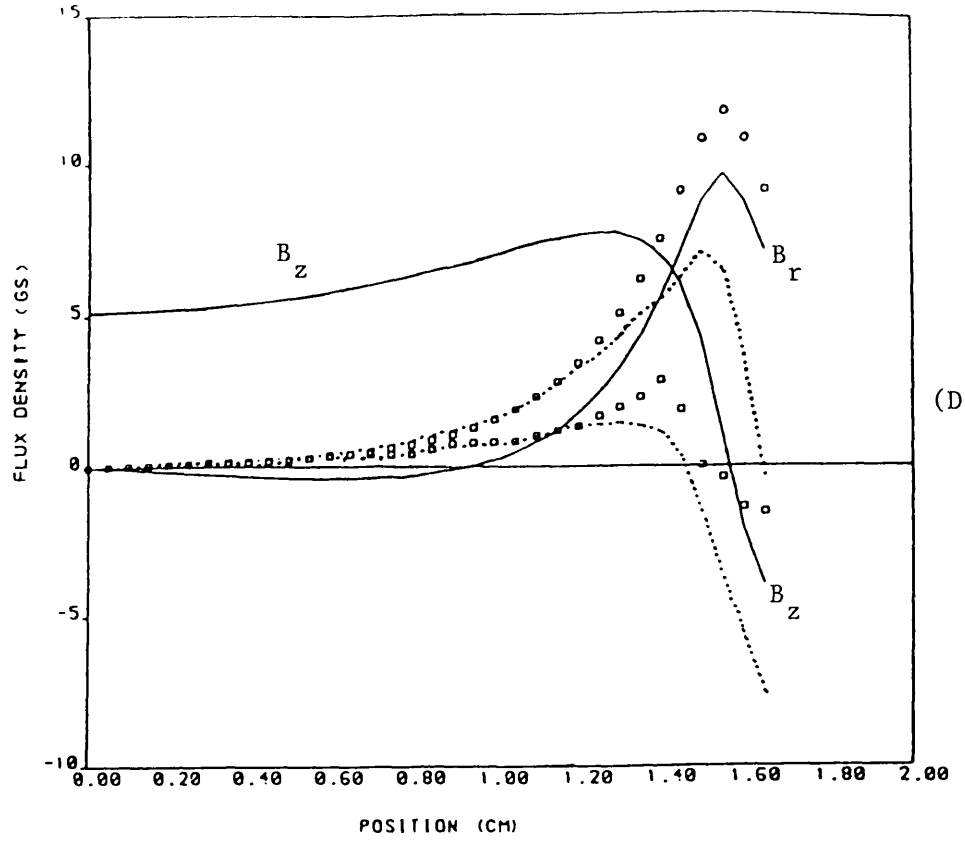

(D)

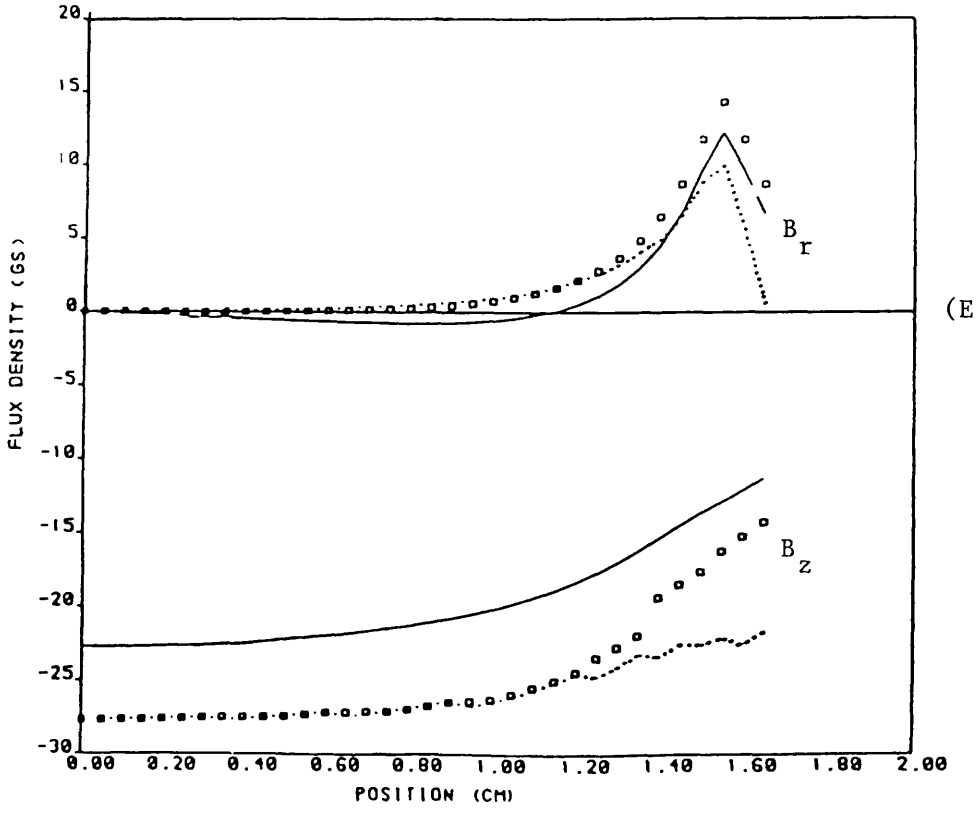

(E)

Fig.2.31: Distribution of flux density B_r and B_z

(a) R = 0.85 cm (D)
(b) R = 1.0 cm (E)

——— B_r and B_z without ferrite core (Air)

. . . B_r and B_z with ferrite core at $\theta = 10^o$

□ □ □ B_r and B_z with ferrite core at $\theta = 90^o$

(F)

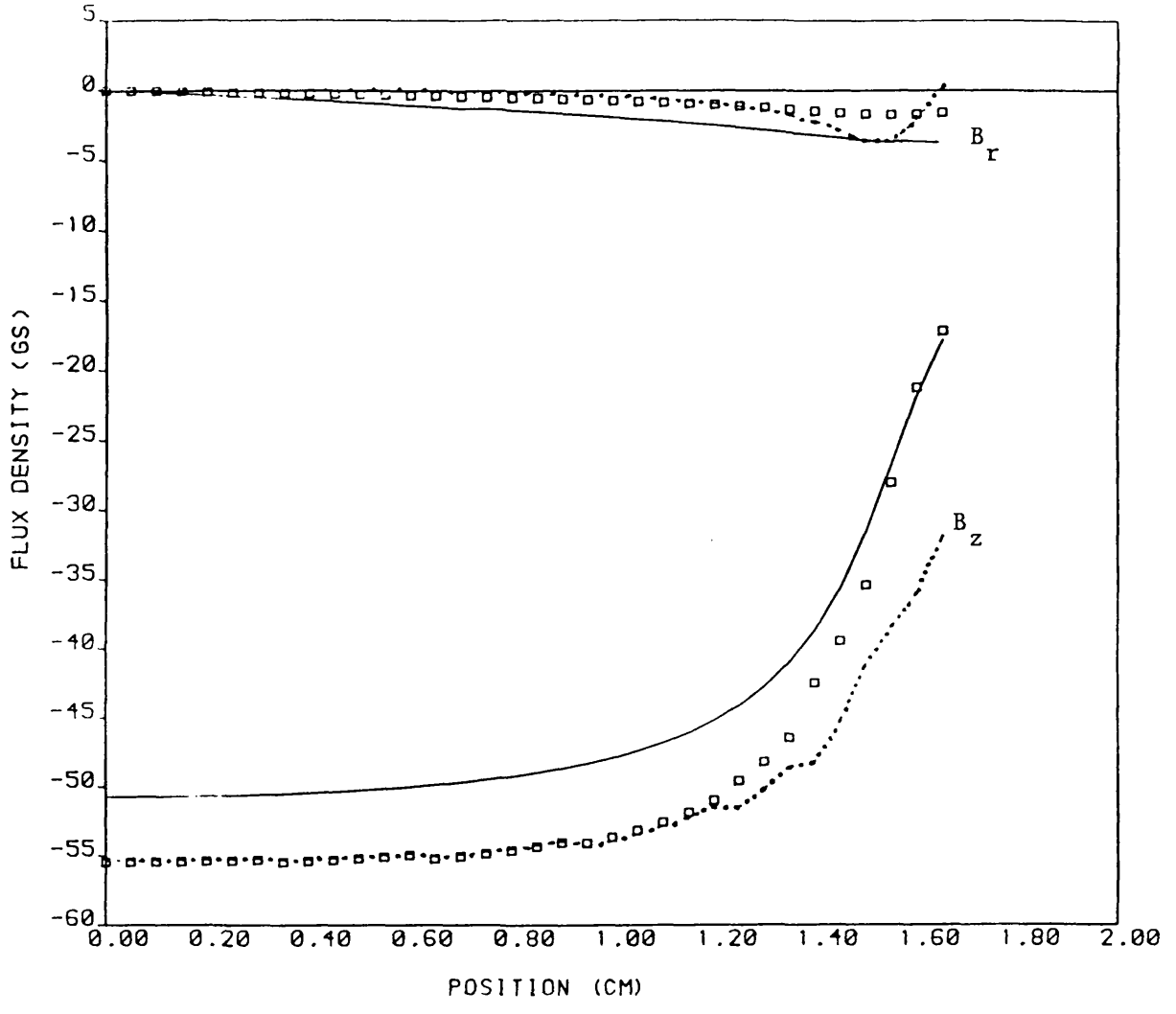

Fig.2.32: Distribution of flux density B_r and B_z
R = 1.2 cm (F)

——— B_r and B_z without ferrite (Air)
. . . B_r and B_z with ferrite at $\theta = 10^o$
□ □ □ B_r and B_z with ferrite at $\theta = 90^o$

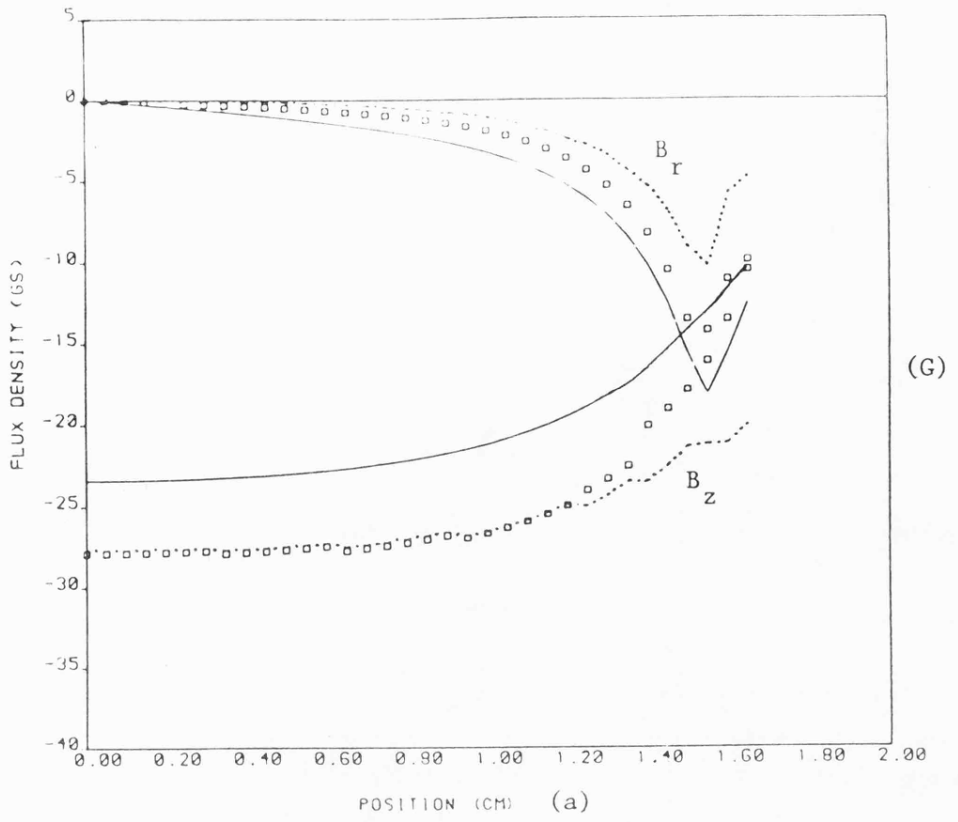

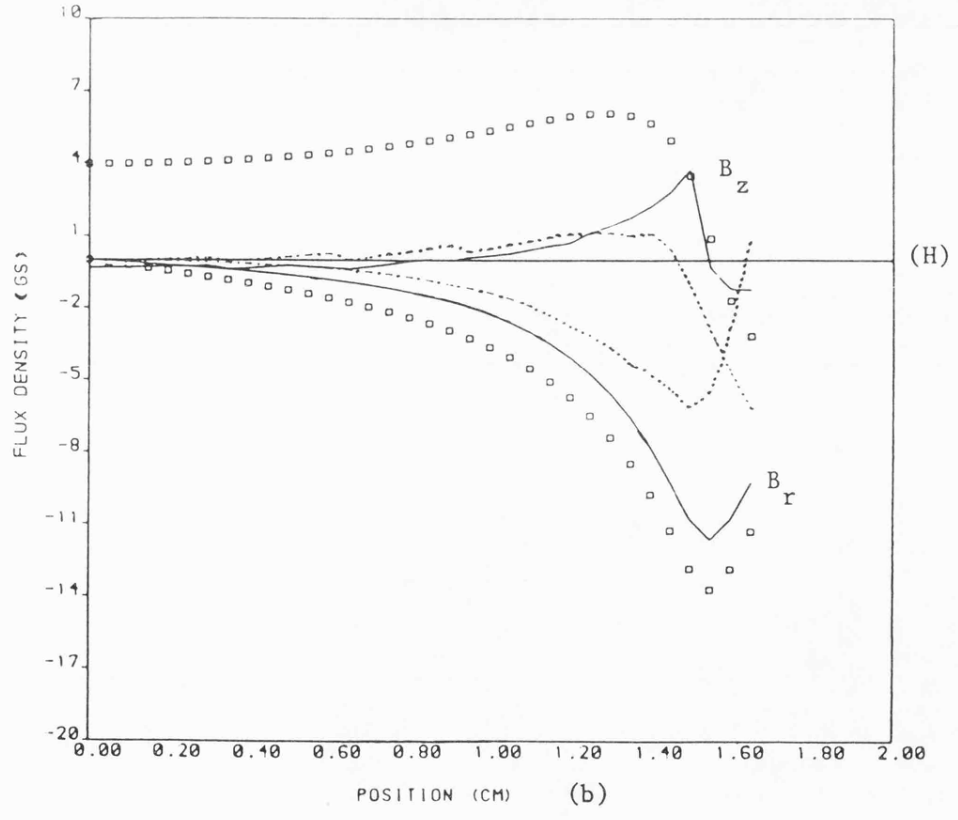

Fig.2.33: Distribution of B_r and B_z at
(a) R = 1.4 cm (G)
(b) R = 1.55 cm (H)

——— B_r and B_z without ferrite (Air)

. . . B_r and B_z with ferrite core at $\theta = 10^o$

□ □ □ B_r and B_z with ferrite core at $\theta = 90^o$

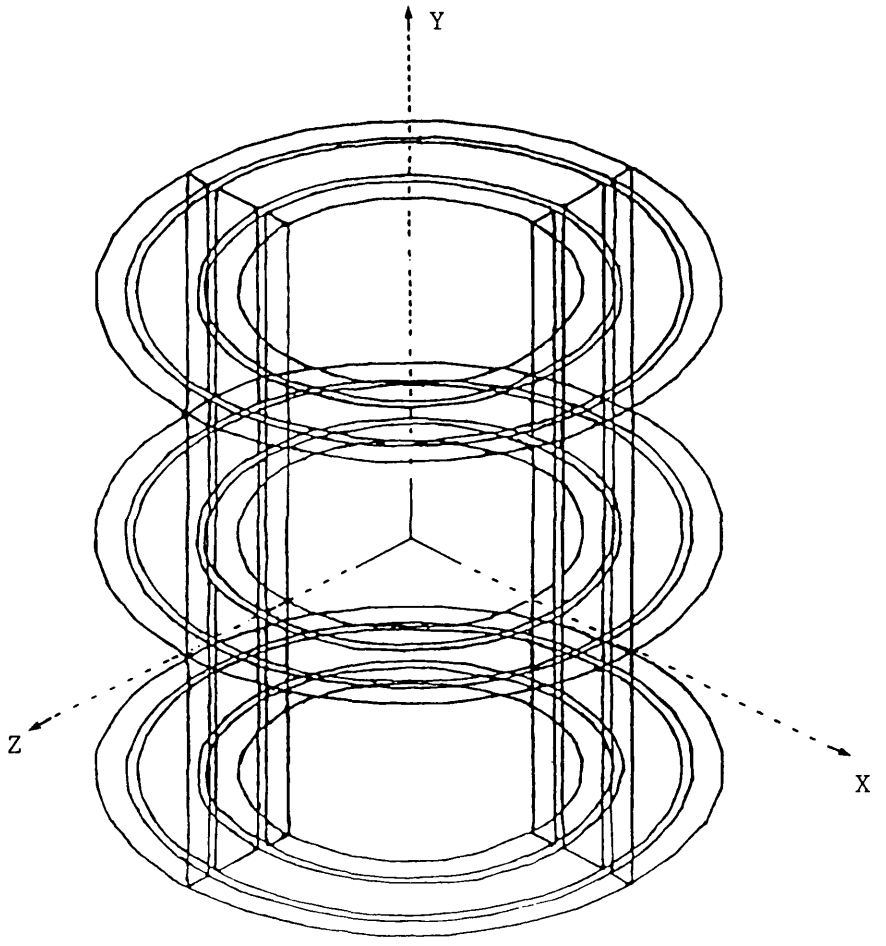

Fig.2.34: Representation of coils on TOSCA

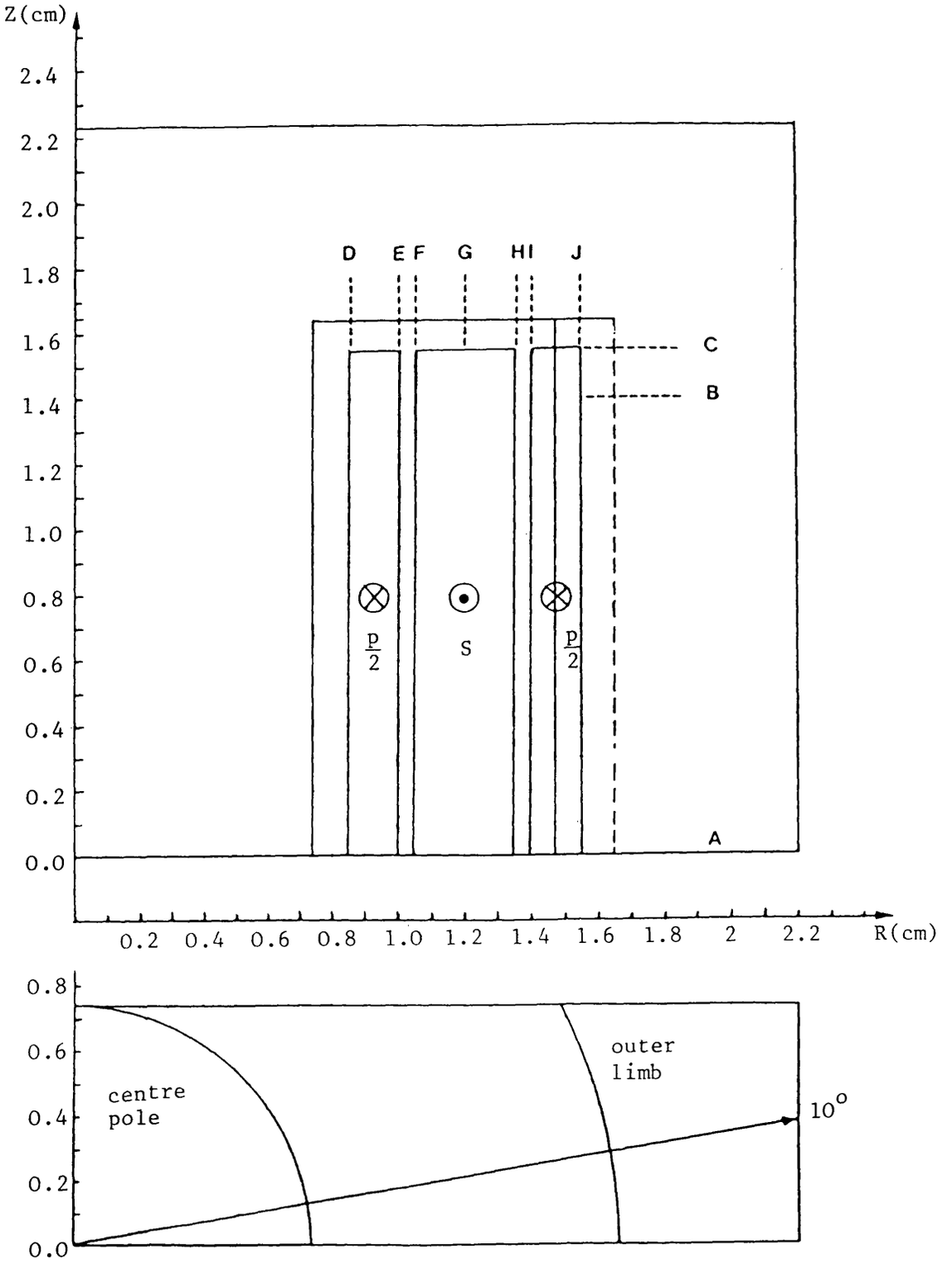

Fig.2.35: Quarter core polar coordinate with 'sandwich' winding

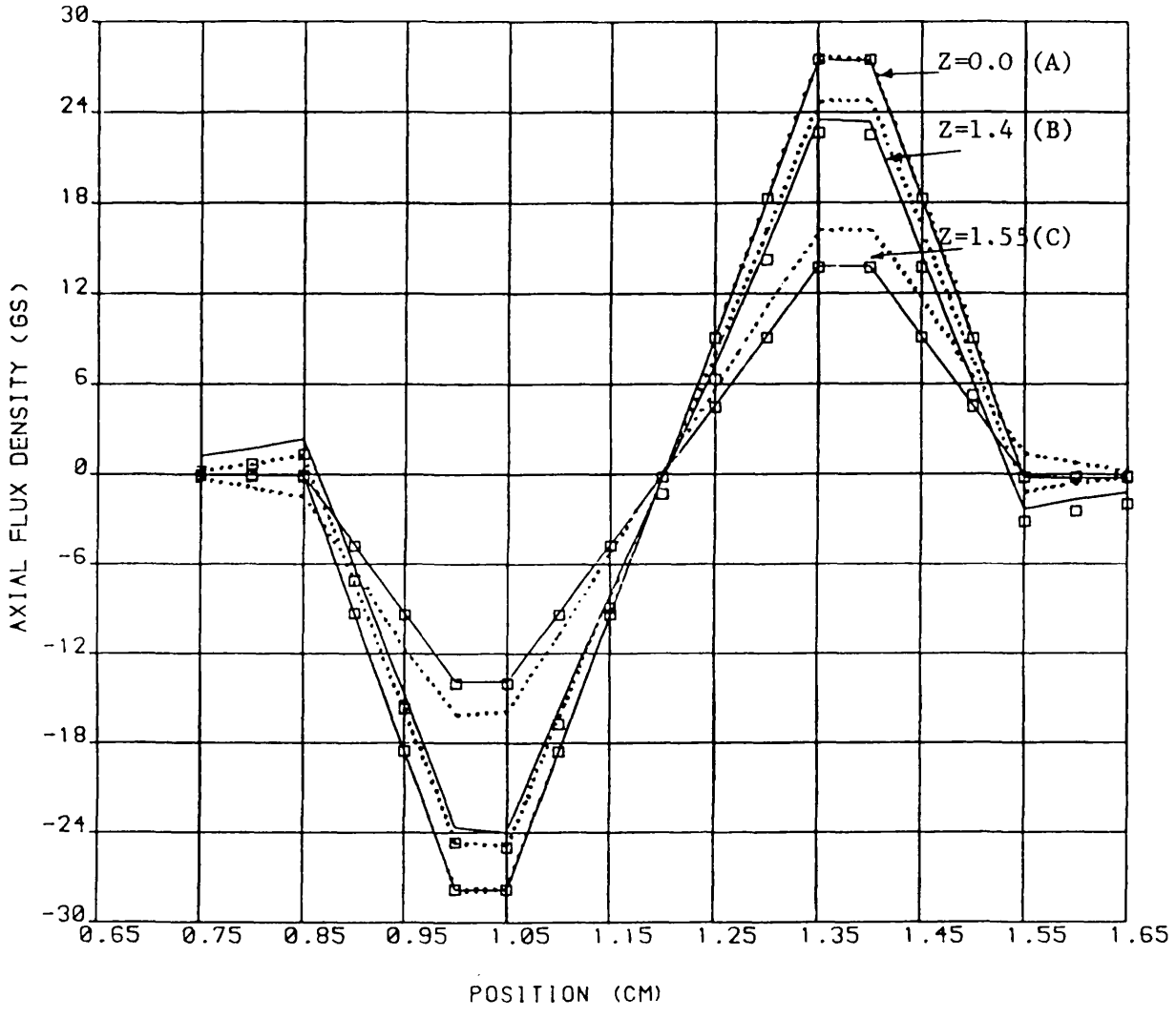

Fig.2.36: Axial flux density distribution at positions Z = 0.0 (A), Z = 1.4 (B) and Z = 1.55 (C)

——— Model ETD44 without ferrite core

. . . Model ETD44 with ferrite core at $\theta = 10^{o}$

□ □ □ Model ETD44 with ferrite core at $\theta = 90^{o}$

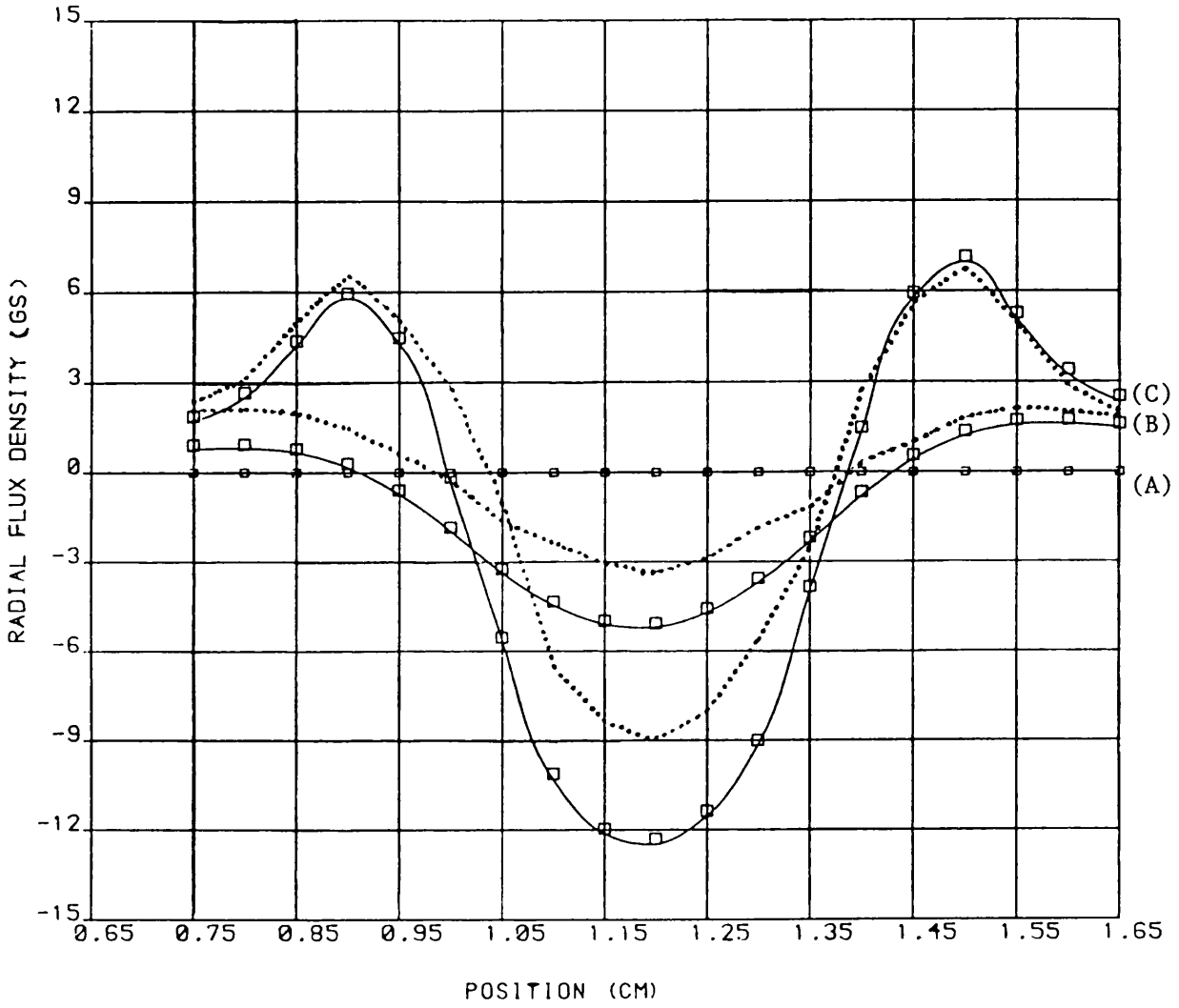

Fig.2.37 : Radial flux density distribution at positions Z = 0.0 (A), Z = 1.4 (B) and Z = 1.55 (C)

——— Model ETD44 without ferrite core

. . . Model ETD44 with ferrite core at $\theta = 10^{o}$

□ □ □ Model ETD44 with ferrite core at $\theta = 90^{o}$

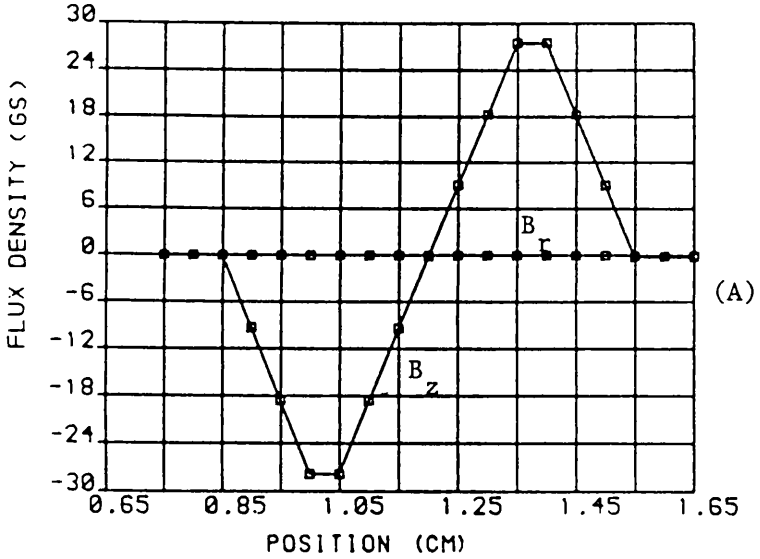

(a)

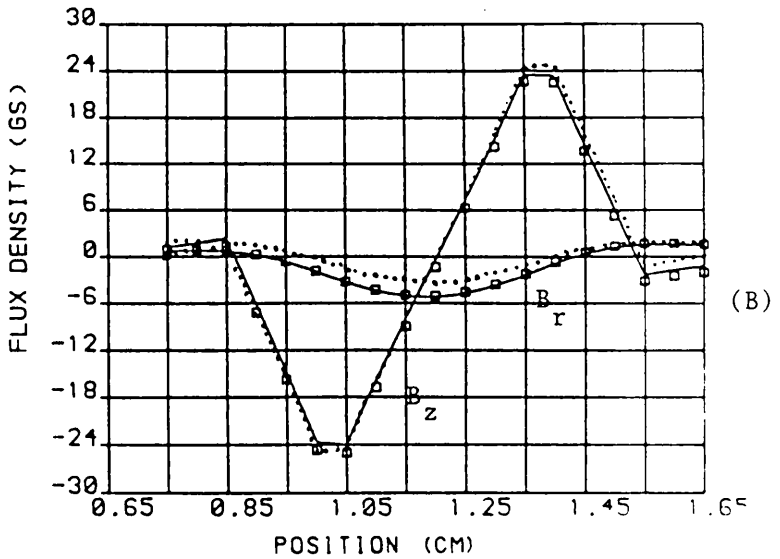

(b)

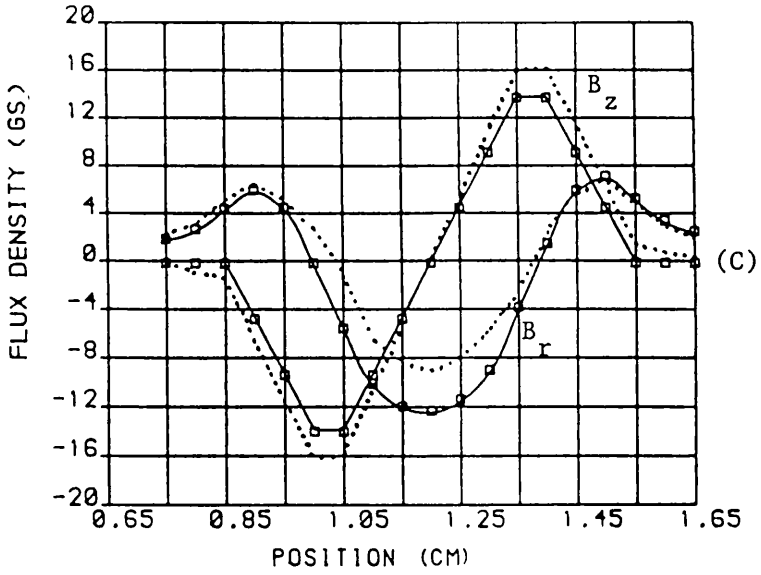

(c)

Fig.2.38: Comparision between B_r and B_z flux density

(a) B_r and B_z at Z = 0.0 cm (A)

(b) B_r and B_z at Z = 1.4 cm (B)

(c) B_r and B_z at Z = 1.55 cm (C)

——— without ferrite core

. . . with ferrite core at $\theta = 10^{o}$

□ □ □ with ferrite core at $\theta = 90$

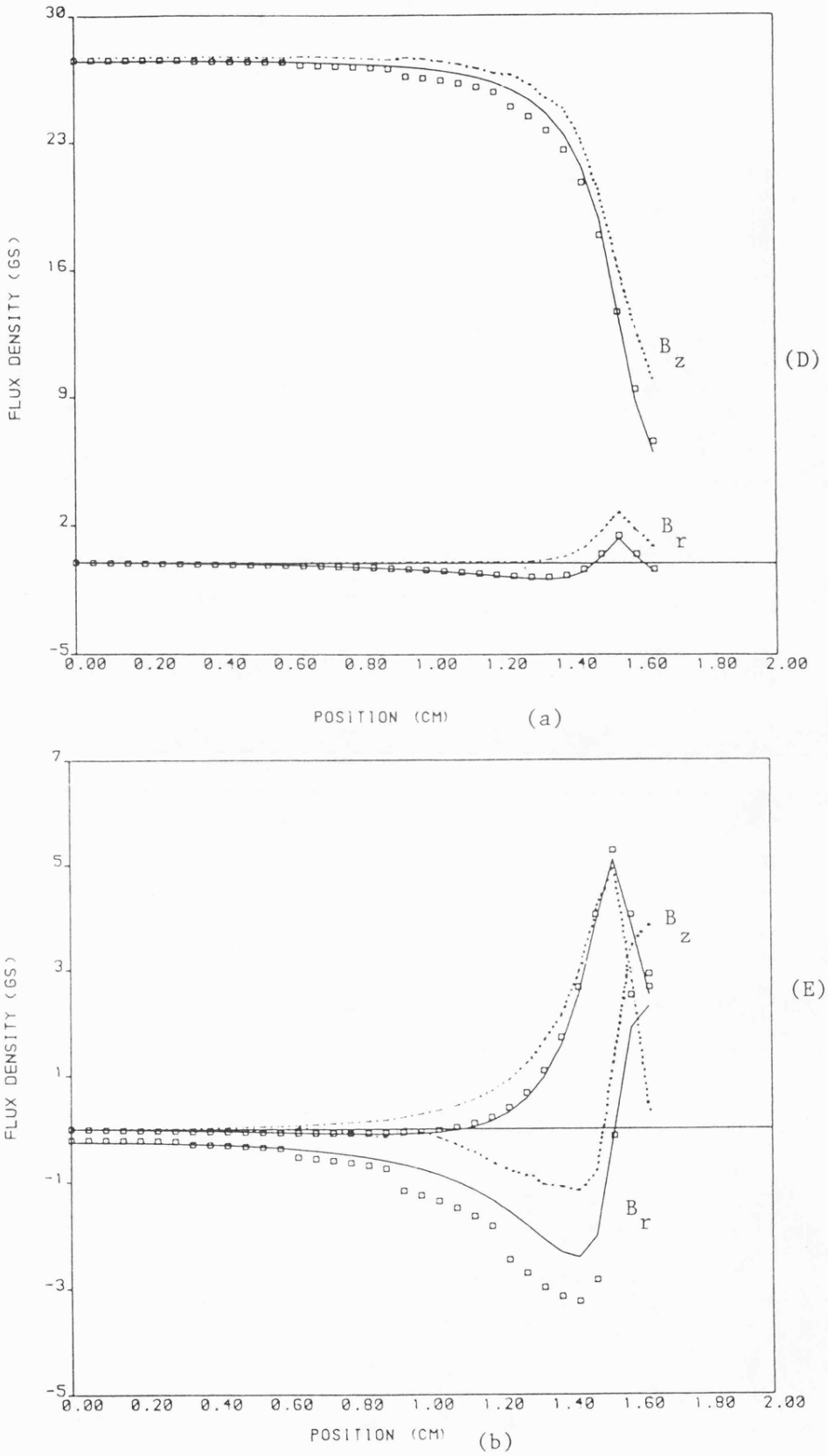

Fig.2.39: Distribution of B_r and B_z at
(a) R = 0.85 cm (D)
(b) R = 1.0 cm (E)

——— B_r and B_z without ferrite (Air)

. . . B_r and B_z with ferrite at $\theta = 10^o$

□ □ □ B_r and B_z with ferrite at $\theta = 90^o$

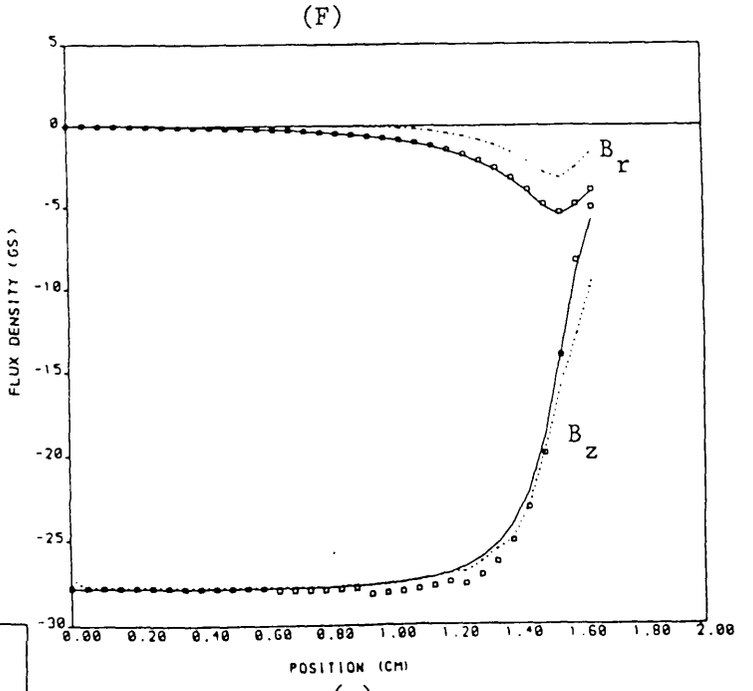

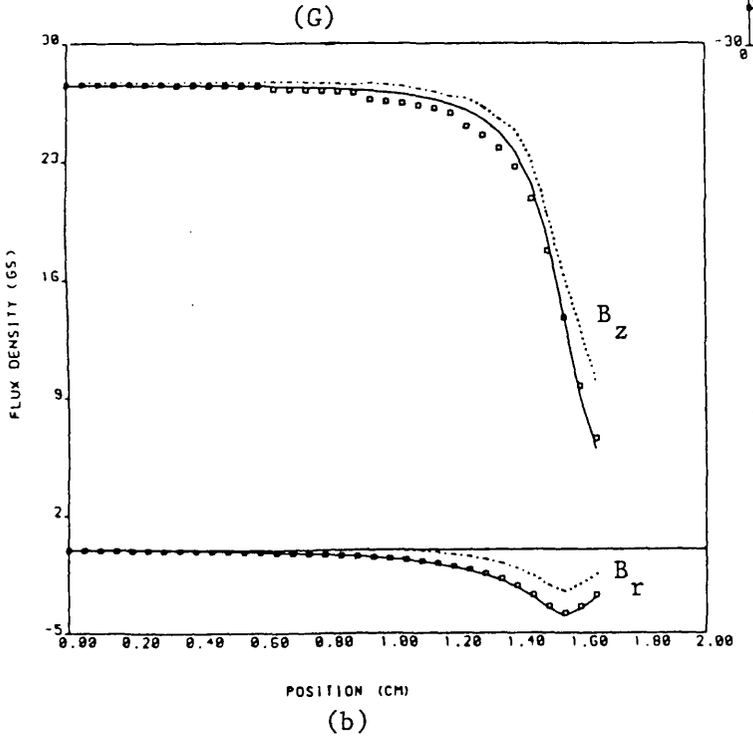

Fig.2.40: Distribution of B_r and B_z at
(a) R = 1.05 cm (F)
(b) R = 1.35 cm (G)
(c) R = 1.2 cm (H)

——— B_r and B_z without ferrite (Air)

. . . B_r and B_z with ferrite at $\theta = 10^o$

□ □ □ B_r and B_z with ferrite at $\theta = 90^o$

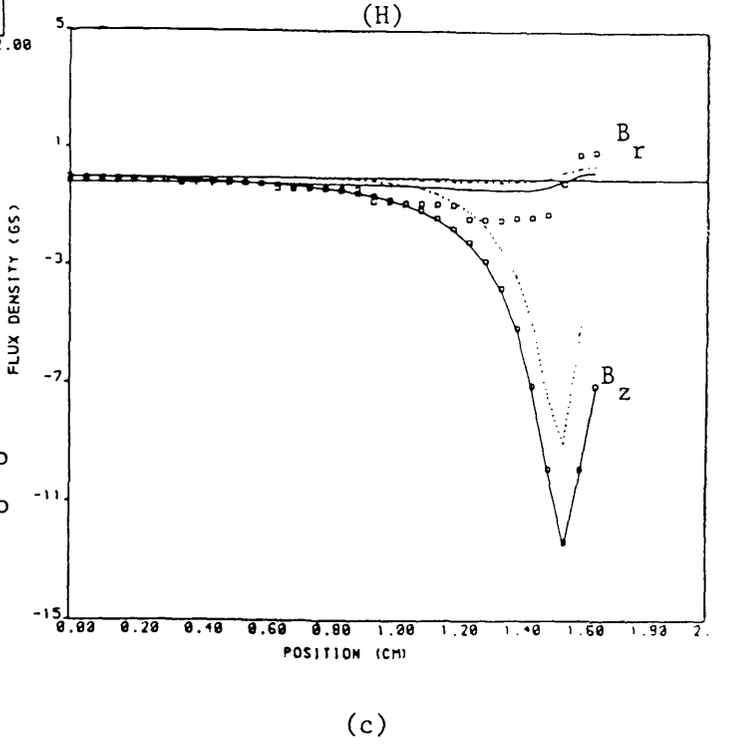

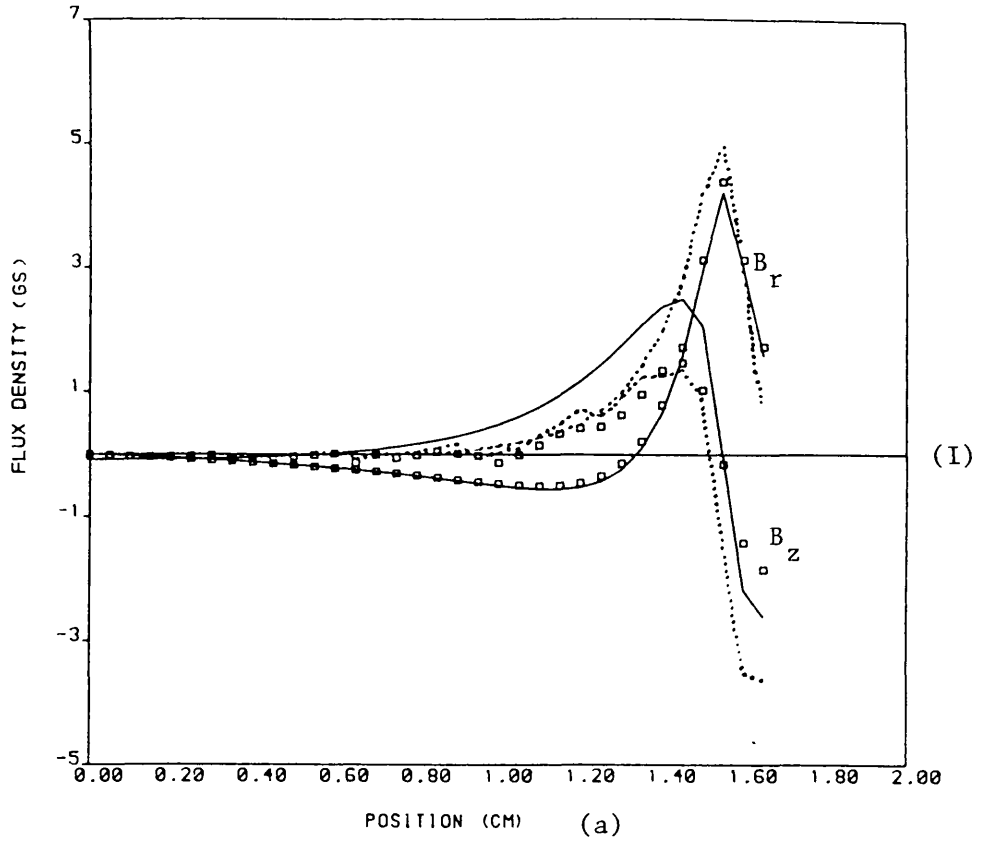

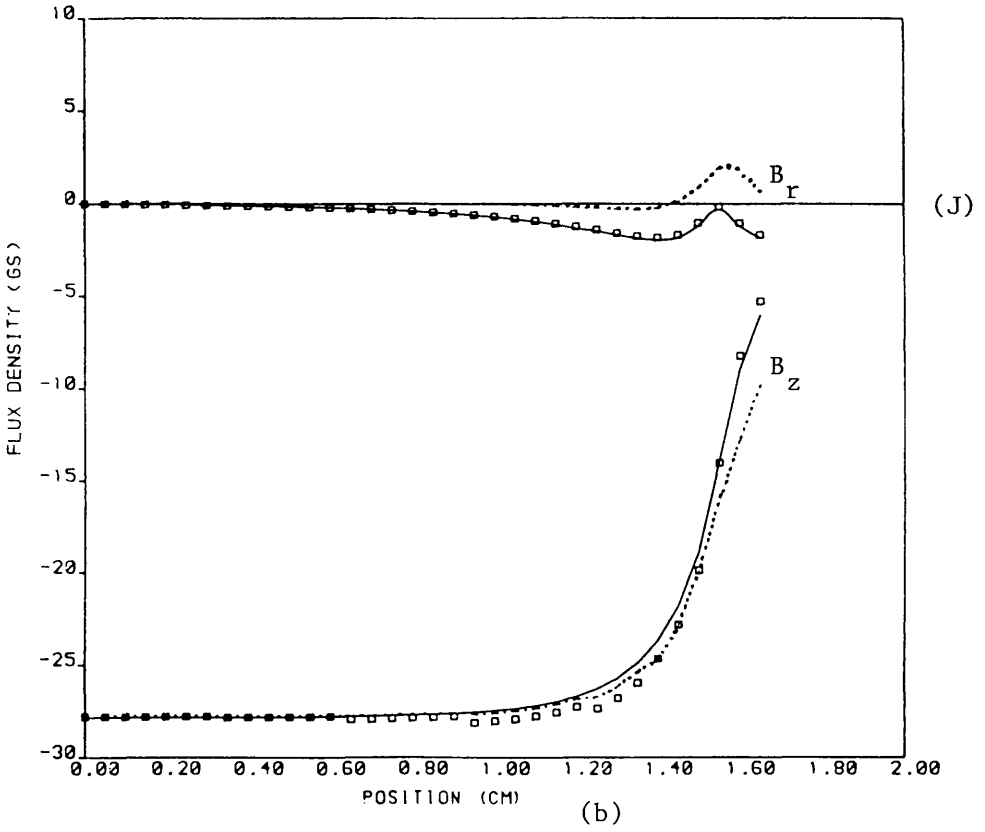

Fig.2.41: Distribution of B_r and B_z at
(a) R = 1.4 cm (I)
(b) R = 1.55 cm (J)

——— B_r and B_z without ferrite (Air)
. . . B_r and B_z with ferrite at $\theta = 10^o$
□ □ □ B_r and B_z with ferrite at $\theta = 90^o$

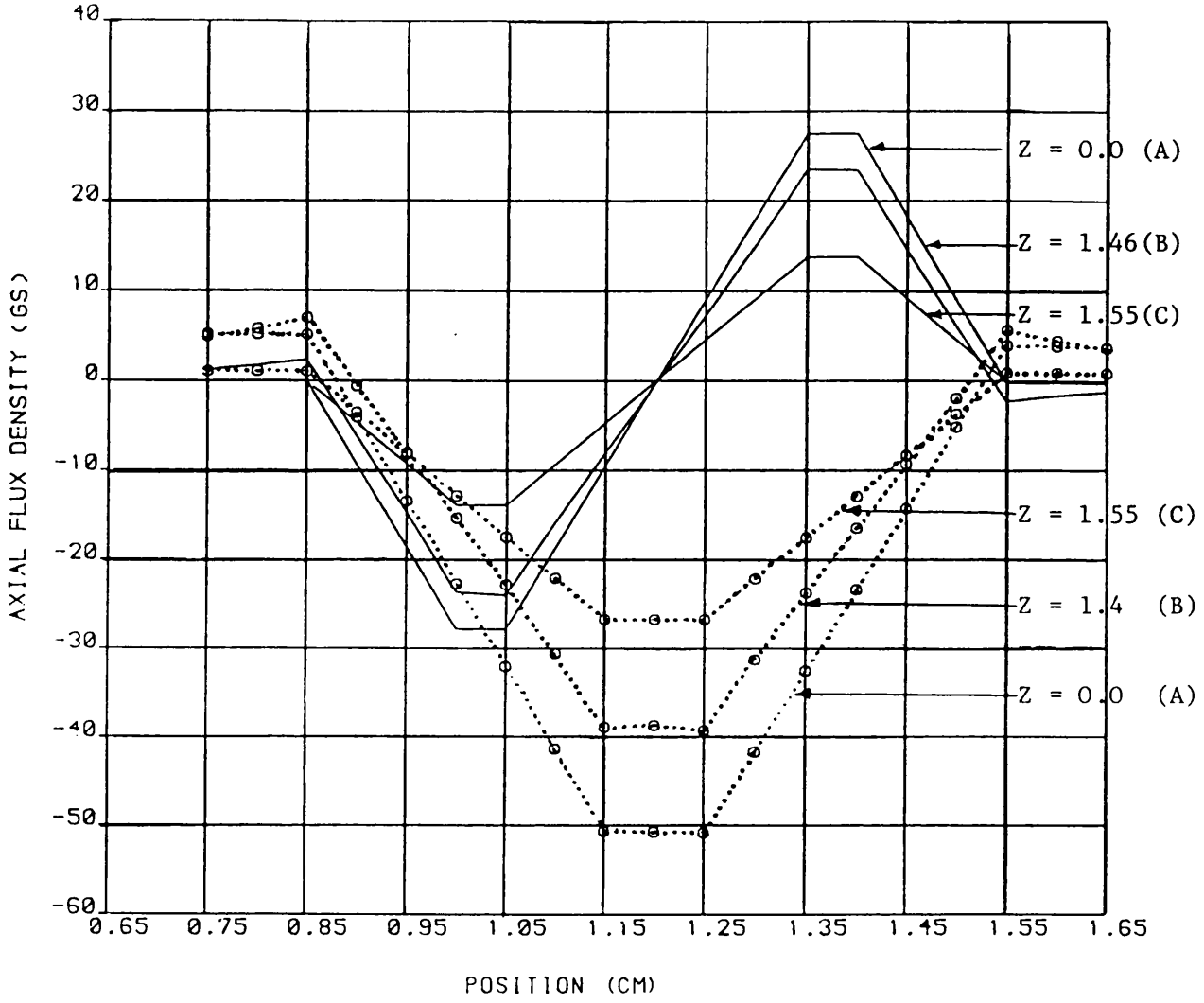

Fig.2.42: Comparison between B_z component "without ferrite core (Air)"

o..o..o 'simple' transformer winding

——— 'sandwich' transformer winding

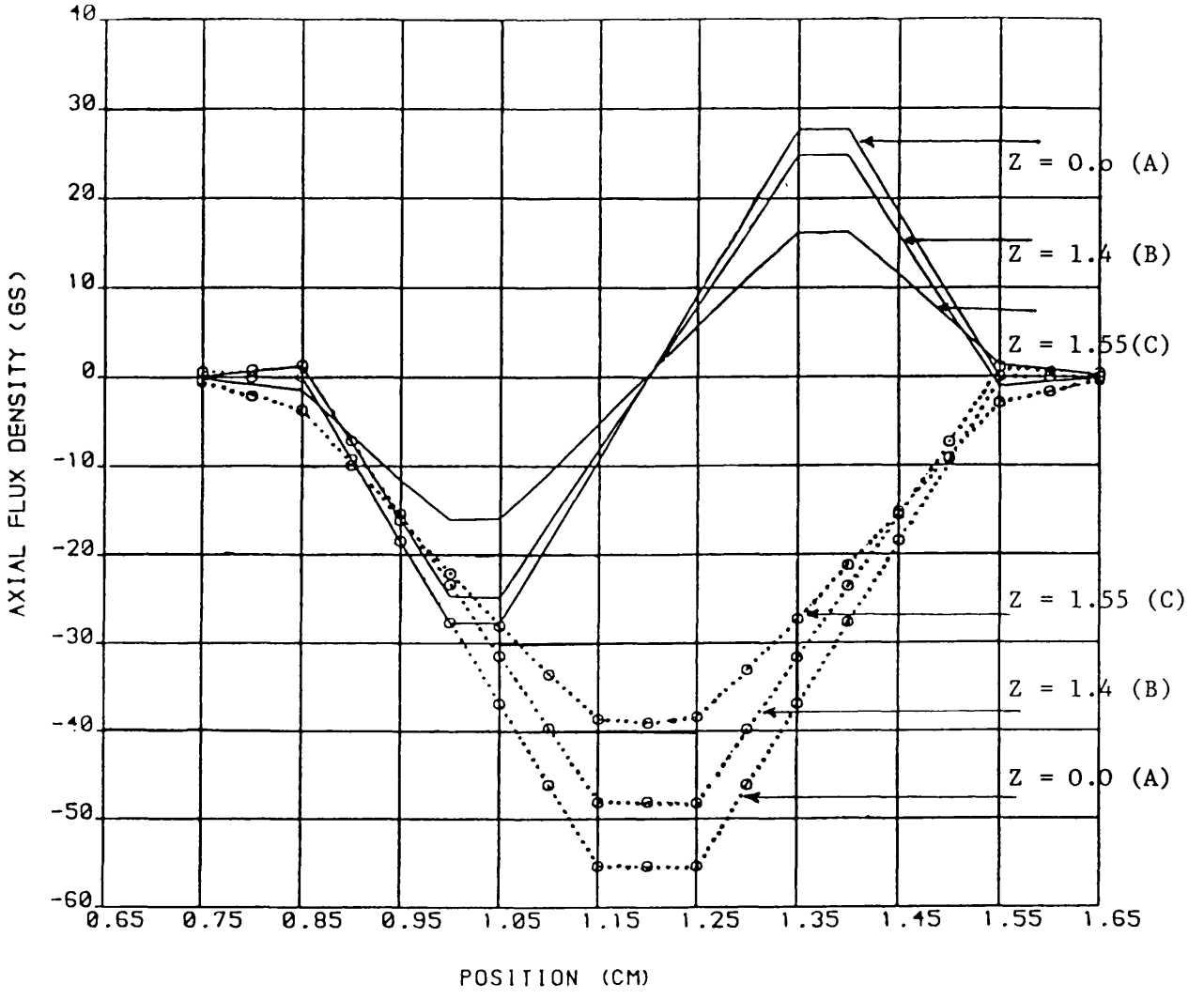

Fig.2.43: Comparison between B_z component "with ferrite core at $\theta = 10^{o}$"

o..o..o 'simple' transformer winding

——— 'sandwich' transformer winding

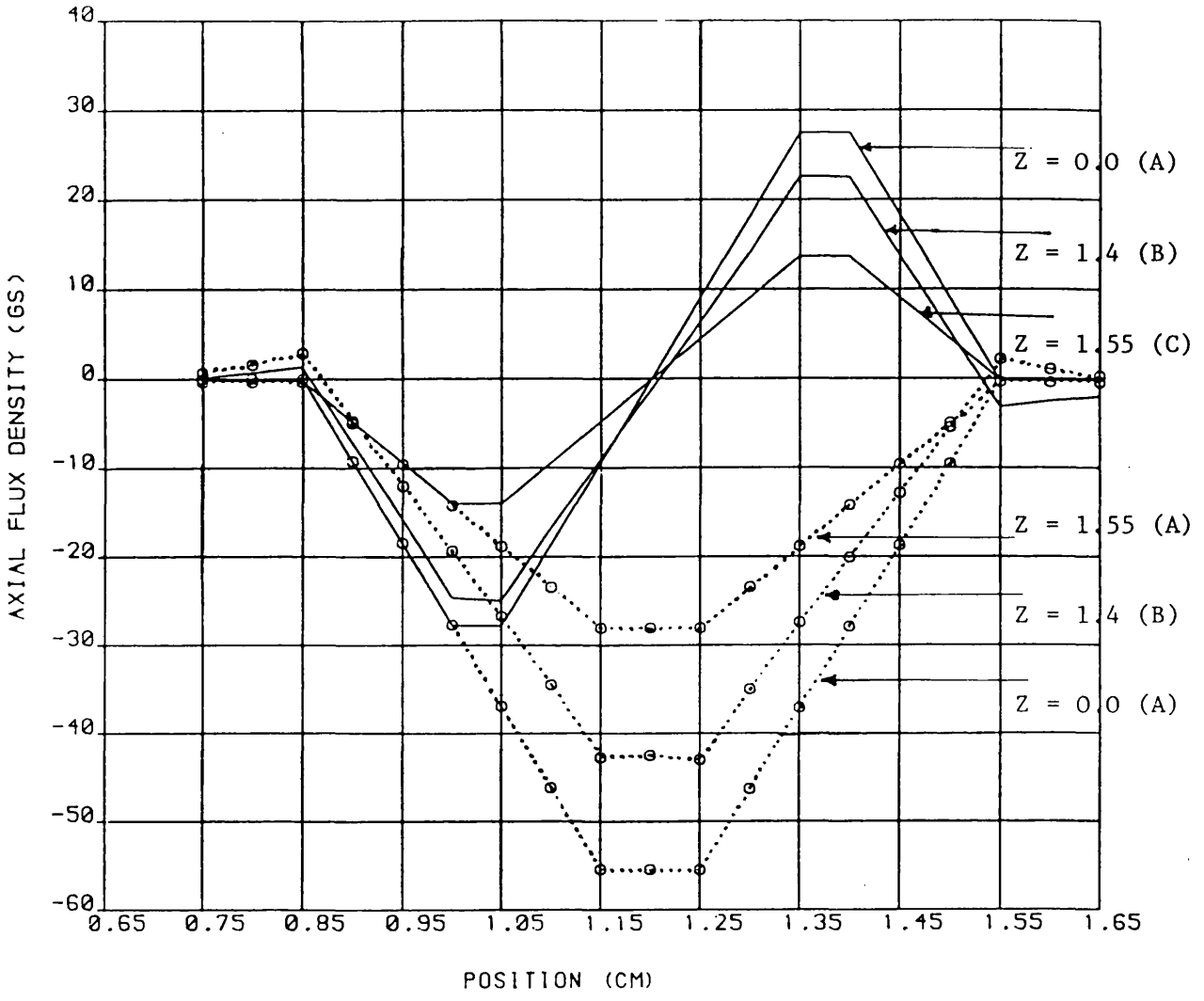

Fig.2.44: Comparison between B_z component
'with ferrite core at $\theta = 90^o$'

o..o..o 'simple' transformer winding

——— 'sandwich' transformer winding

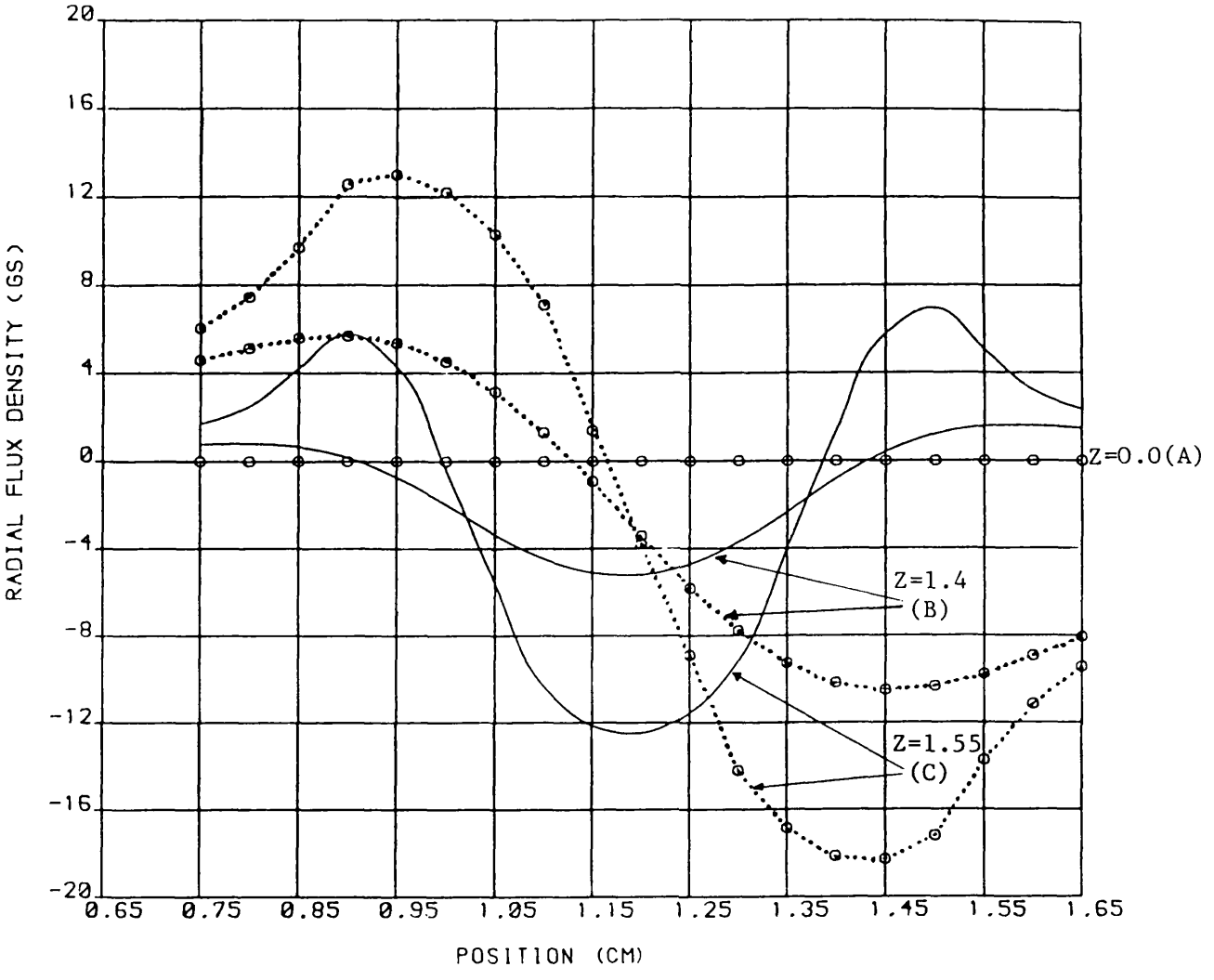

Fig.2.45: Comparison between B_r component
'without ferrite core (Air)

o..o..o..o 'simple'transformer winding

———— 'sandwich' transformer winding

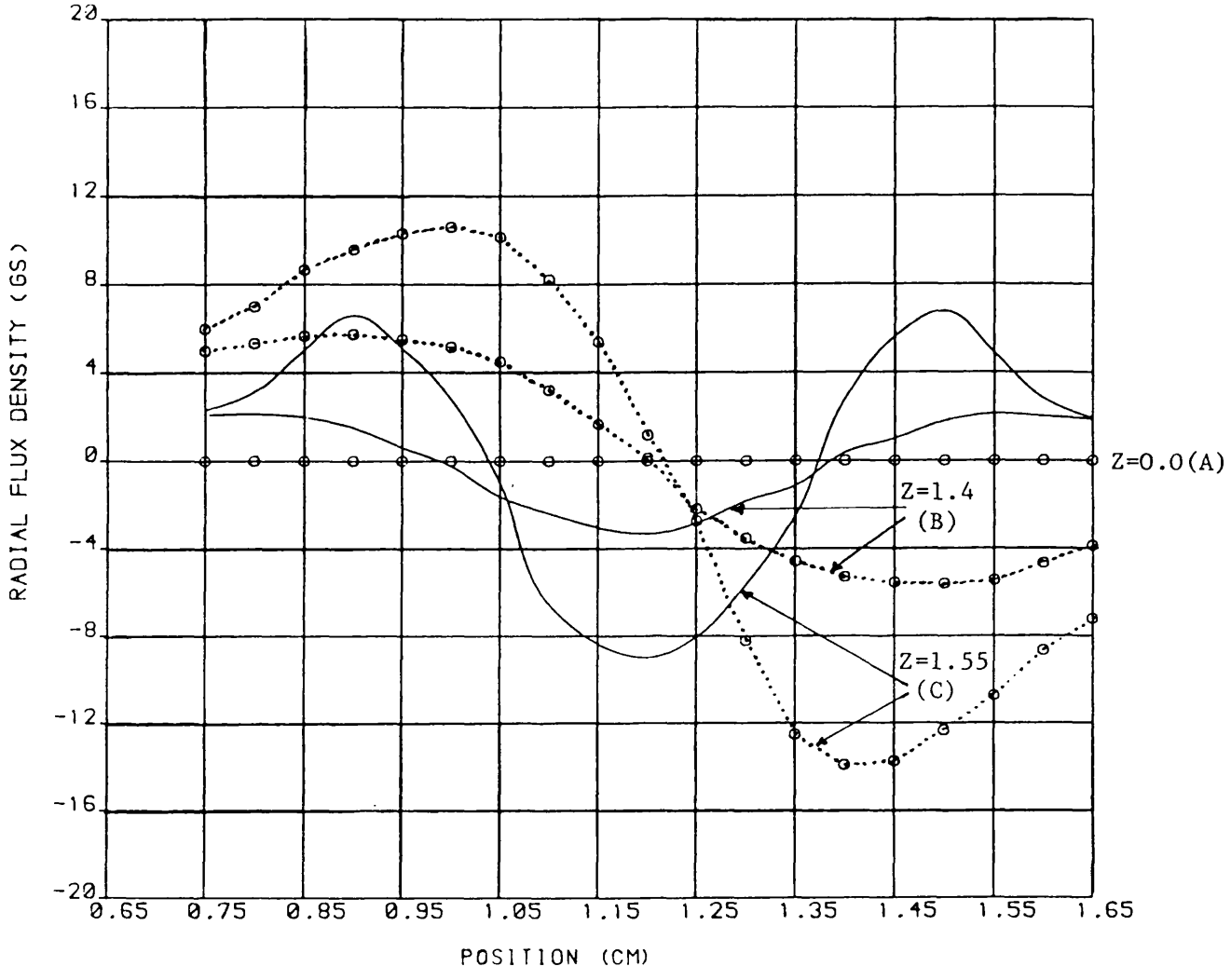

Fig.2.46: Comparison between B_r component
'with ferrite core at $\theta = 10^{o}$

o..o..o..o 'simple' transformer winding

———— 'sandwich' transformer winding

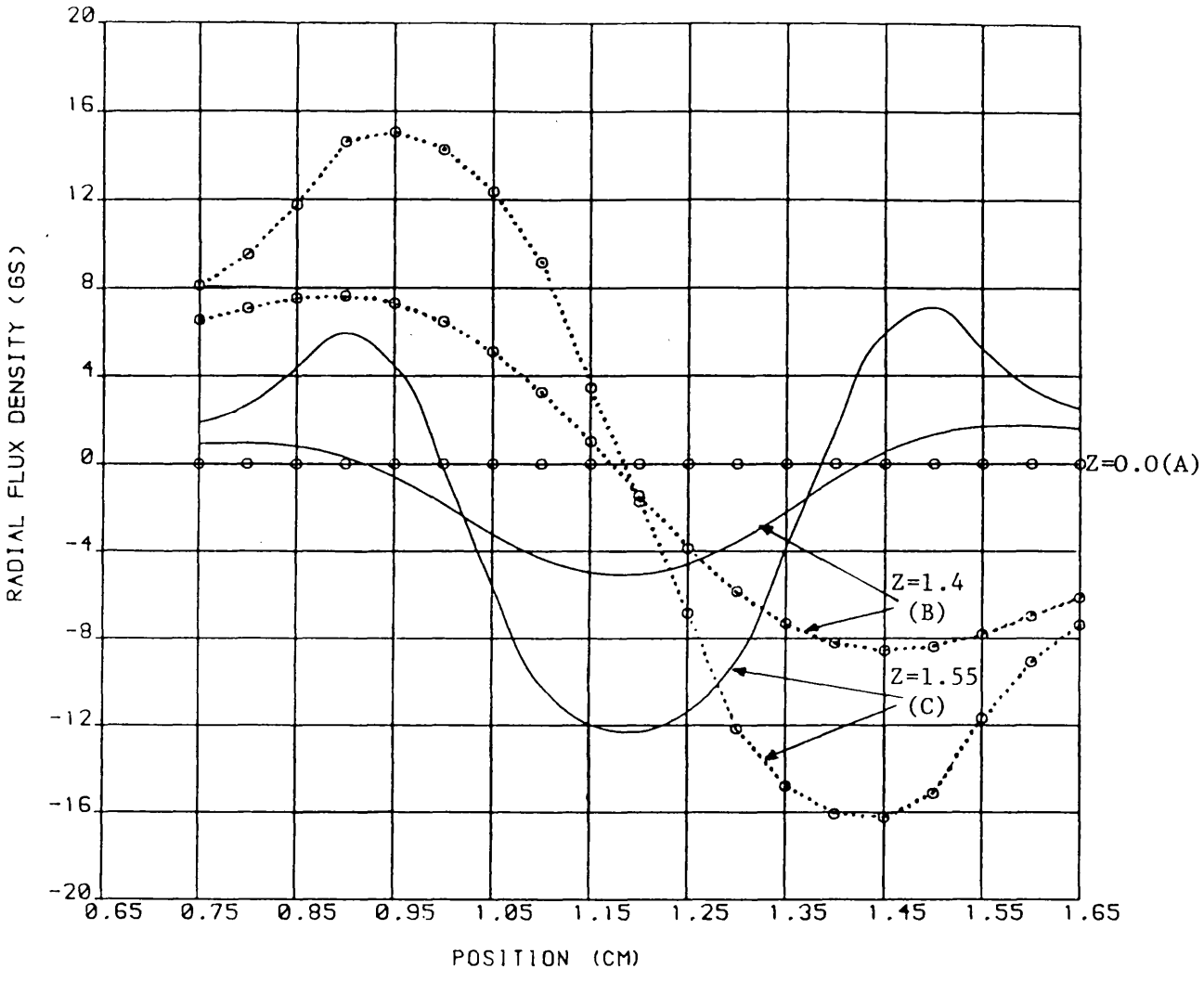

Fig.2.47: Comparison between B_r component
'with ferrite core at $\theta = 90^o$

o..o..o..o 'simple' transformer winding

———— 'sandwich' transformer winding

CHAPTER THREE

CALCULATION OF LOSSES IN FOIL CONDUCTORS

3.1 Introduction

Strip or foil conductors are used in inductor and transformer windings in a number of applications. For example, formerly strip aluminium conductors were used in the low voltage high current secondaries of distribution transformers. At present copper foil and strip conductors are used in inductors in power electronics equipment and in the transformers of switched-mode power supplies. It is well known that in these conductor shapes the current distribution tends to be non-uniform due to the eddy currents produced by leakage fluxes, and this has the effect of increasing the losses.

Several methods of calculating these conditions have been proposed, for example Mullineux[1] gives an expression for the current density in a foil winding in a mathematical model of a 2-winding transformer. The mathematical model is set up for such transformers, and the current density is obtained as the solution to integral equations. This model cannot be applied to the problem in the present chapter because:

i) The model is a simplified form for the sole case of a transformer; the inner winding was of foil and the outer of wire.

ii) The effects of the yoke and the curvature of the winding were neglected, so that the model is 2-dimensional only.

iii) The current density is assumed invariant throughout the radial thickness of the winding.

Murgatroyd and Walker[2] have shown how the effective resistance and inductance of a single foil turn, respectively, rise and fall with increasing frequency. Figure 3.1(a) shows the single foil turn with equipotential connecting bars. Using a circuital model, by considering the turn as a number of narrow filament coils in parallel, is shown in Figure 3.1(b). Each filament is represented by a constant resistance in series with an inductance, each filament coil is sufficiently narrow for current distribution to be uniform. Hence the dc resistance of a filament is given by

$$R = \frac{2\pi a \rho}{wt} \qquad 3.1$$

and the dc resistance of the complete turn is $R_o = R/N$. The inductance of a filament is given by Grover[3].

$$L = \mu_o a \left[\log_e \frac{8a}{w} - \frac{1}{2} \right] \qquad 3.2$$

which is calculated on the assumptions of t negligible and uniform current density within w . The mutual inductance between any pair of filaments can be calculated[3] using the formula for coaxial circular filaments as discussed in Chapter Four. It has the form

$$M_{\alpha,\beta} = \mu_o a G_{\alpha,\beta} \qquad 3.3$$

where $G_{\alpha\beta}$ is a dimensionless factor dependent on the ratio d_α, where d is the axial separation of the filaments denoted by subscripts α and β.

Figure 3.2 represents the equivalent circuit of the complete foil turn. They analysed the equivalent circuit as follows:

The total current I_o is the sum of the filament currents I_α:

$$I_o = \sum_{\alpha=1}^{\alpha=N} I_\alpha \qquad 3.4$$

The total circuit impedance is given by

$$Z_o = \frac{V_o}{I_o} \qquad 3.5$$

The currents are found by solving the N simultaneous equations

$$V_o = I_\alpha R + j\omega L I_\alpha + \sum_{\beta\neq\alpha} j\omega I_\beta M_{\alpha\beta} \qquad 3.6$$

They are assuming all filaments have equal width and hence equal R and L.

They solved the equations by reducing the problem to dimensionless form as follows. A generalised frequency ζ is defined by

$$\zeta = \frac{\omega L}{R} \qquad 3.7$$

and a generalised admittance for filament α:

$$t_\alpha = \frac{RI_\alpha}{V_o} \qquad 3.8$$

Also, the matrix of mutual inductance $M_{\alpha\beta}$ is replaced by a matrix of coupling coefficients $K_{\alpha\beta}$ where

$$K_{\alpha\beta} = \frac{M_{\alpha\beta}}{L} \qquad 3.9$$

With the above transformations the equations become

$$t_\alpha (1 + j\zeta) + j\zeta \sum_{\beta\neq\alpha} t_\beta K_{\alpha\beta} = 1 \qquad 3.10$$

and the complete foil admittance will be given by

$$S(\zeta) = \frac{1}{R} \sum_{\alpha=1}^{N} t_\alpha \qquad 3.11$$

These equations are solved using a numerical technique on a digital computer. The most severe problem is calculation of the self and mutual inductances.

The effective overall resistance and inductance of the foil turn are calculated from the real and imaginary parts, respectively, of the equations 3.11 and the current distribution is obtained from the filament currents.

Also, Reeves[4] has published a paper on air-cored coil-wound inductors. He noted that the foil inductance decreases by about 10%, as the frequency increases and that foil inductors have substantial ac resistance because of current redistribution across the foil width. His analysis is based on an equivalent circuit approach and the results agree with experiment and Murgatroyd results. El-Missiry[5,6] has also tackled the problem for both inductors and transformers and his methods follow, but with significant extensions, the equivalent circuit approach of Murgatroyd.

The problem addressed in the present work concerns losses in foil conductors used in the inductors and transformers of switched-mode power supplied (SMPS). These operate at high repetition frequencies typically (20-100 kHz) but are relatively low power, up to 100 watts for flyback converters and up to 500-1000 watts for forward converters.

The wound ferrite components are therefore usually relatively small in physical size, and it is important that losses can be estimated in order to ensure satisfactory operating temperatures.

The main source of additional copper loss is due to 'proximity effect'. This is the result of high frequency variation of leakage flux on the windings, so that eddy currents are produced within the thickness of the conductors. This problem has been treated by Dowell[7], and his model is described briefly below.

The model consists in dividing the transformer winding into portions to calculate the variation of winding resistance and leakage inductance with frequency for transformers with single-layers, multilayer and sectionalised windings.

Dowell explained that the leakage flux crossing conductor in a particular layer depends on the mmf due to the currents in that layer and the other layer between that layer and the next point of zero mmf.

The leakage flux varies from layer to layer, but is constant over the breadth of each layer as shown in Figure 2.22, Chapter Two.

The proximity effect is greatest in the layers at both sides of the gap between primary and secondary, where the leakage flux density is greatest (i.e. at the edge where the mmf is greatest).

In order to make the model analytically tractable Dowell assumed leakage flux components were z directed only (as defined in Figure 2.28, Chapter Two).

The magnetostatic results in Chapter Two, section 2.4, showed that this was not precisely the case, radial components also being

present.

While to some extent the presence of radial components would not be thought to be a worry with wire conductors, the wire in effect being 'laminated' in two directions, with foil conductors this would not be the case.

Radial components impinging on foil would be expected to produce large eddy currents. Although the Dowell model could therefore, in principle, be applied to both wire and foil conductors, good results would be anticipated with wire, but not with foil.

Some preliminary measurements were therefore made in order to assess the position.

First, two 'transformer windings' were constructed to suit the ETD44 core, and their details are shown in Figure 3.3. One used round wire for both primary and secondary, the other used foil for both primary and secondary.

Both transformers were tested in the same way, that is to say, the primary winding connected in series opposition with the secondary winding. Sinusoidal excitation was applied by means of a signal generator, a power amplifier type 240L from ENI and a matching transformer. Measurement of electrical power into the transformer under test was accomplished using a two-beam digital storage oscilloscope (Nicolet, Explorer II, Type 2090-II) which was connected via an IEEE bus to a microcomputer (Commodore CBM Model 8032). See Appendix A2 for description of experiment equipment used.

Transformer current and voltage were monitored and connected to the two channels of the oscilloscope. Stored results of V and i vs time were read into the microcomputer. Instantaneous values of power dissipation were calculated by multiplying corresponding pairs of points together. Average power consumption was then obtained by averaging instantaneous values over a complete cycle. The transformer was also tested with the core removed from the windings.

The results are shown in Figure 3.4 and 3.5. There are a number of points to observe from these results.

i) For both types of windings the losses with and without the ferrite core are the same to within about 10%. In fact the losses were also measured with the central limb of ferrite only being present, the cross- and side-limbs having been removed. The losses measured in this case were intermediate between the two other results. Although these results seem surprising in isolation, the magnetostatic results in Chapter Two, section 2.4, which show that leakage fluxes are not substantially affected by the presence of the ferrite, tend to support the finding.

ii) Although Dowell predicts quite well the round wire case it is clearly unsatisfactory for the foil conductors. This is attributed to the radial components of flux density which were discussed above. They are ignored by Dowell but have been shown to be significant.

iii) While in the application of Dowell to the round wire case, it would be expected that the width of the core would be used to calculate the effective winding length exposed to the leakage flux. In practice it has been found[8] that the mean turn length should be taken, which was the case for the theoretical results in Figure 3.4 and 3.5. Again, this is surprising initially, although the magnetostatic computations in Chapter Two, section 2.4, indicated the reason.

These results indicate that the eddy currents losses in foil conductors may be calculated under the special conditions of the ferrite being absent, providing that the primary and secondary ampere-turns are the same. This means that an equivalent circuit type of model can be developed which involves only the calculation of the self and mutual inductances of filament coils, situated in air. This is still a relatively complex problem, although simpler than having to allow for the presence of ferrite cores.

The general principle of the model is introduced in the next section, by describing the simple case of a single layer foil inductor. The model is closely related to those of Murgatroyd[2] and El-Missiry[5] in that an equivalent electrical circuit was used.

3.2 Single layer model

A single foil layer with equipotential connecting busbars is shown in Figure 3.1(a). It is made from material of uniform thickness (t), width (bw) formed to mean radius (a). The layer is subdivided into theoretical filaments in the axial direction. It is

convenient to have (nf) filaments of equal width (w) so that

$$bw = nf \times w \qquad 3.12$$

The complete foil turn is represented by the equivalent circuit as shown in Figure 3.2. Each filament is represented by a constant (dc value) resistance in series with an inductance and all the inductances are mutually coupled together.

3.2.1 Voltage equations for the filament coils

The purpose of subdividing each layer into a set of filament coils was to calculate the current in each filament coil, and then to use the filament coil currents to represent the distribution of current across the flat bar conductors of the winding loops. The filament coil currents can be calculated by writing down the voltage equation for each of the parallel connected filaments in terms of resistance and inductance. Thus, for say five filament (nf = 5) the voltage equations can be written in the form:

$$\begin{aligned}
v_1 &= i_1R_1 + j\omega i_1L_{11} + j\omega(i_2M_{12} + i_3M_{13} + i_4M_{14} + i_5M_{15}) \\
v_2 &= i_2R_2 + j\omega i_2L_{22} + j\omega(i_1M_{21} + i_3M_{23} + i_4M_{24} + i_5M_{25}) \\
v_3 &= i_3R_3 + j\omega i_3L_{33} + j\omega(i_1M_{31} + i_2M_{32} + i_4M_{34} + i_5M_{35}) \qquad 3.13 \\
v_4 &= i_4R_4 + j\omega i_4L_{44} + j\omega(i_1M_{41} + i_2M_{42} + i_3M_{43} + i_5M_{45}) \\
v_5 &= i_5R_5 + j\omega i_5L_{55} + j\omega(i_1M_{51} + i_2M_{52} + i_3M_{53} + i_4M_{54})
\end{aligned}$$

where

$$v_1 = v_2 = v_3 = v = v = \ldots \; Vnf$$

because all the filaments are assumed to be connected in parallel by equipotential end bars and excited from the same voltage source.

Equations (3.13) can be written in matrix form:

$$\begin{bmatrix} v_1 \\ v_2 \\ v_3 \\ v_4 \\ v_5 \end{bmatrix} = \begin{bmatrix} R_1 + j\omega L_{11} & j\omega M_{12} & j\omega M_{13} & j\omega M_{14} & j\omega M_{15} \\ j\omega M_{21} & R_2 + j\omega L_{22} & j\omega M_{23} & j\omega M_{24} & j\omega M_{25} \\ j\omega M_{31} & j\omega M_{32} & R_3 + j\omega L_{33} & j\omega M_{34} & j\omega M_{35} \\ j\omega M_{41} & j\omega M_{42} & j\omega M_{43} & R_4 + j\omega L_{44} & j\omega M_{45} \\ j\omega M_{51} & j\omega M_{52} & j\omega M_{53} & j\omega M_{54} & R_5 + j\omega L_{55} \end{bmatrix} \begin{bmatrix} i_1 \\ i_2 \\ i_3 \\ i_4 \\ i_5 \end{bmatrix} \qquad 3.14$$

or as

$$[v] = [i][z] = [R][i] + j\omega[M][i] \qquad 3.15$$

The resistance matrix [R] contains terms on the major diagonal only, and the inductance matrix [M] is symmetrical about the major axis, for $M_{12} = M_{21}$. The dc resistance of each filament is the same, i.e.

$$R_1 = R_2 = R_3 = R_4 = R_5 = \ldots R_{nf}$$

where the R_{nf} can be calculated as in equation 3.1. Also, the self inductance of each filament is the same

$$L_{11} = L_{22} = L_{33} = L_{44} = L_{55} = L_{nf,nf}$$

where L_{nf} is obtained from Grover[3] as in section 3.1, equation 3.2.

Equation (3.15) can be solved by assuming an arbitrary voltage level for the voltage matrix and using conventional matrix inversion techniques. This model was checked by inserting in it the parameters used by Murgatroyd. Identical results were obtained as shown in Figure 3.6, thus showing that the method and its implementation is satisfactory.

For real systems multilayer inductors and transformer secondaries are used. This problem is considerably more severe than the single layer case and is described below.

3.3 Multilayer model

When a foil winding consists of more than one turn, whether in an inductor or transformer, the problem of calculating current distribution across the turns of the foil becomes more complicated. This is because the current distribution is not in general the same from one layer to the next. Under some conditions, most especially for coils where the ratio of outer to inner diameter is not great, it may be possible to make the approximation that current distribution is the same for all layers. In this case the method of section 3.2 above can be used, with all resistances and inductances calculated for 'N' turns, and the radius being the mean radius of the coil.

In general, however, the allowance must be made for the current distributed across each turn to be different. This is because the flux linking notional filament coils will change from one layer to the next as will the resistance with increasing diameter, so that the balance of the 'iR' and 'di/dt' voltage components will change. As only the total voltage across the windings is likely to be known, the voltage drops across the layers of the winding are unknown and in general not the same.

The model used to allow for these effects is indicated in Figure 3.7. Each layer of the coil is subdivided into a set of filament coils, as in the single layer case in section 3.2. But each layer is terminated by an equipotential so that current can redistribute itself from one layer to the next.

This is similar to the model used by El-Missiry[5]. It contains all filament coils as circular and concentric so that their self and

mutual inductances may be calculated with relative ease. A more complicated model, which may be more precise would involve subdividing the filaments into a "fishing net" type of equivalent circuit as sketched in Figure 3.8. This would increase the number of circuits to be handled, would make calculation of the self and mutual inductances more complicated and was not thought to be justified in terms of improved results that might be obtained.

The type of model adopted, as illustrated in Fig.3.9, leads to a considerable increase in the size of the mathematical problem to be handled and computed compared to the single layer case. For example, take a very simple two layer, three filament case the equations are written out below. The total voltage across all the layers is equal to the sum of the voltage in each layer, i.e.

$$V = \sum_{n=1}^{n=n\ell} v_n \qquad 3.16$$

Since the filaments are connected in parallel the voltage across each filament remains constant, also the resistance of each filament in the same layer is equal, i.e.

$R_{11} = R_{12} = R_{13}$ for the first layer

and for the second layer

$R_{21} = R_{22} = R_{23}$

The dc resistance of a filament depends on the radius of each layer as below:

$$R_n = \rho \frac{2\pi\, a_n}{t.bw/nf}$$

$$R_n = \rho nf \frac{2\pi a_n}{t\ bw} \qquad 3.17$$

where

R_n = dc resistance of nth filament

nf = number of filament in each layer

t = thickness of the layer

bw = width of the layer

a_n = radius of the nth layer

ρ = resistivity of the material

Similarly the self inductance of each filament in the same layer is equal, i.e.

$L_{11,11} = L_{12,12} = L_{13,13}$ for the first layer

and for the second layer

$L_{21,21} = L_{22,22} = L_{23,23}$

and in general $L_{n\ell nf,n\ell nf}$ represents the self inductance of (nℓ) and (nf) filament. Also $M_{n\ell nf,n\ell nf}$ represents the mutual inductance of the circuit whose voltage is being calculated. Therefore, the equations of the voltage and currents of three filaments and two layers are as in Equ. (3.18) and these equations can be rewritten in matrix form as in Equ. (3.19).

It is clear that a formal method of notation and calculation is required to handle the size of problem that is to be encountered where up to 10 layers, each with a 100 or more filaments may be utilised. An approach which uses simple form of tensor notations and analysis was therefore adopted, and this is described below.

$$V_{11} = I_{11}R_{11} + j\omega(i_{11}L_{11,11} + i_{12}M_{11,12} + i_{13}M_{11,13} + i_{21}M_{11,21} + i_{22}M_{11,22} + i_{23}M_{11,23})$$

$$V_{12} = I_{12}R_{12} + j\omega(i_{11}M_{12,11} + i_{12}L_{12,12} + i_{13}M_{12,13} + i_{21}M_{12,21} + i_{22}M_{12,22} + i_{23}M_{12,23})$$

$$V_{13} = I_{13}R_{13} + j\omega(i_{11}M_{13,11} + i_{12}M_{13,12} + i_{13}L_{13,13} + i_{21}M_{13,21} + i_{22}M_{13,22} + i_{23}M_{13,23}) \quad (3.18)$$

$$V_{21} = I_{21}R_{21} + j\omega(i_{11}M_{21,11} + i_{12}M_{21,12} + i_{13}M_{21,13} + i_{21}L_{21,21} + i_{22}M_{21,22} + i_{23}M_{21,23})$$

$$V_{22} = I_{22}R_{22} + j\omega(i_{11}M_{22,11} + i_{12}M_{22,12} + i_{13}M_{22,13} + i_{21}M_{22,21} + i_{22}L_{22,22} + i_{23}M_{22,23})$$

$$V_{23} = I_{23}R_{23} + j\omega(i_{11}M_{23,11} + i_{12}M_{23,12} + i_{13}M_{23,13} + i_{21}M_{23,21} + i_{22}M_{23,22} + i_{23}L_{23,23})$$

$$
\begin{bmatrix} V_{11} \\ V_{12} \\ V_{13} \\ V_{21} \\ V_{22} \\ V_{23} \end{bmatrix} = \begin{bmatrix} R_{11} + j\omega L_{11,11} & j\omega M_{11,12} & j\omega M_{11,13} & j\omega M_{11,21} & j\omega M_{11,22} & j\omega M_{11,23} \\ j\omega M_{12,11} & R_{12} + j\omega L_{12,12} & j\omega M_{12,13} & j\omega M_{12,21} & j\omega M_{12,22} & j\omega M_{12,23} \\ j\omega M_{13,11} & j\omega M_{13,12} & R_{13} + j\omega L_{13,13} & j\omega M_{13,21} & j\omega M_{13,22} & j\omega M_{13,23} \\ j\omega M_{21,11} & j\omega M_{21,12} & j\omega M_{21,13} & R_{21} + j\omega L_{21,21} & j\omega M_{21,22} & j\omega M_{21,23} \\ j\omega M_{22,11} & j\omega M_{22,12} & j\omega M_{22,13} & j\omega M_{22,21} & R_{22} + j\omega L_{22,22} & j\omega M_{22,23} \\ j\omega M_{23,11} & j\omega M_{23,12} & j\omega M_{23,13} & j\omega M_{23,21} & j\omega M_{23,22} & R_{23} + j\omega L_{23,23} \end{bmatrix} \begin{bmatrix} i_{11} \\ i_{12} \\ i_{13} \\ i_{21} \\ i_{22} \\ i_{23} \end{bmatrix}
$$

(3.19)

$$
\begin{aligned}
V_{a1} &= i_{a1}R_{a1} + j\omega(i_{a1}L_{a1,a1} + i_{a2}M_{a1,a2} + \ldots) + \underbrace{(i_{b1}M_{a1,b1} + i_{b2}M_{a1,b2} + \ldots)}_{Z_{ab}} + \underbrace{(i_{n\ell 1}M_{a1,n\ell 1} + i_{n\ell 2}M_{a1,n\ell 2} + \ldots)}_{Z_{an\ell}} \\
V_{a2} &= i_{a2}R_{a2} + j\omega(i_{a1}M_{a2,a1} + i_{a2}L_{a2,a2} + \ldots) + \underbrace{(i_{b1}M_{a2,b1} + i_{b2}M_{a2,b2} + \ldots)}_{Z_{ab}} + \underbrace{(i_{n\ell 1}M_{a2,n\ell 1} + i_{n\ell 2}M_{a2,n\ell 2} + \ldots)}_{Z_{an\ell}} \\
V_{b1} &= i_{b1}R_{b1} + j\omega(i_{a1}M_{b1,a1} + i_{a2}M_{b1,a2} + \ldots) + \underbrace{(i_{b1}L_{b1,b1} + i_{b2}M_{b1,b2} + \ldots)}_{Z_{bb}} + \underbrace{(i_{n\ell 1}M_{b1,n\ell 1} + i_{n\ell 2}M_{b1,n\ell 2} + \ldots)}_{Z_{bn\ell}} \\
V_{b2} &= i_{b2}R_{b2} + j\omega(i_{a1}M_{b2,a1} + i_{a2}M_{b2,a2} + \ldots) + \underbrace{(i_{b1}M_{b2,b1} + i_{b2}L_{b2,b2} + \ldots)}_{Z_{bb}} + \underbrace{(i_{n\ell 1}M_{b2,n\ell 1} + i_{n\ell 2}M_{b2,n\ell 2} + \ldots)}_{Z_{bn\ell}} \\
V_{n\ell 1} &= i_{n\ell 1}R_{n\ell 1} + j\omega(i_{a1}M_{n\ell 1,a1} + i_{a2}M_{n\ell 1,a2} + \ldots) + \underbrace{(i_{b1}M_{n\ell 1,b1} + i_{b2}M_{n\ell 1,b2} + \ldots)}_{Z_{n\ell b}} + \underbrace{(i_{n\ell 1}L_{n\ell 1,n\ell 1} + i_{n\ell 2}M_{n\ell 1,n\ell 2} + \ldots)}_{Z_{n\ell n\ell}} \\
V_{n\ell 2} &= i_{n\ell 2}R_{n\ell 2} + j\omega(i_{a1}M_{n\ell 2,a1} + i_{a2}M_{n\ell 2,a2} + \ldots) + \underbrace{(i_{b1}M_{n\ell 2,b1} + i_{b2}M_{n\ell 2,b2} + \ldots)}_{Z_{n\ell b}} + \underbrace{(i_{n\ell 1}M_{n\ell 2,n\ell 1} + i_{n\ell 2}L_{n\ell 2,n\ell 2} + \ldots)}_{Z_{n\ell n\ell}}
\end{aligned}
\tag{3.20}
$$

3.4 Generalised multilayer equations

First the circuit equations may be rewritten as in Equ.(3.20), for the case of $n\ell$ layers and nf filaments per layer, as shown in Figure 3.10.

The set of equations (3.20) can be rewritten in matrix form.

$$\begin{bmatrix}[V_a]\\ [V_b]\\ [V_c]\\ \vdots\\ [V_{n\ell}]\end{bmatrix} = \begin{bmatrix}[R_a] & [o_b] & [o_c] & \cdots & [o_{n\ell}]\\ [o_a] & [R_b] & [o_c] & \cdots & [o_{n\ell}]\\ [o_a] & [o_b] & [R_c] & \cdots & [o_{n\ell}]\\ & & & & \\ [o_a] & [o_b] & [o_c] & \cdots & [R_{n\ell}]\end{bmatrix} \begin{bmatrix}[i_a]\\ [i_b]\\ [i_c]\\ \vdots\\ [i_{n\ell}]\end{bmatrix}$$

$$+ \begin{bmatrix}[Z_{aa}] & [Z_{ab}] & [Z_{ac}] & \cdots & [Z_{an\ell}]\\ [Z_{ba}] & [Z_{bb}] & [Z_{bc}] & \cdots & [Z_{bn\ell}]\\ [Z_{ca}] & [Z_{cb}] & [Z_{cc}] & \cdots & [Z_{cn\ell}]\\ \vdots & & & & \\ [Z_{n\ell a}] & [Z_{n\ell b}] & [Z_{n\ell c}] & \cdots & [Z_{n\ell n\ell}]\end{bmatrix} \begin{bmatrix}[i_a]\\ [i_b]\\ [i_c]\\ \vdots\\ [i_{n\ell}]\end{bmatrix} \qquad 3.21$$

where the resistance matrix can be written by inspection as:

$$[R_a] = \begin{bmatrix}R_{a1} & 0 & 0 & \cdots & 0\\ 0 & R_{a2} & 0 & \cdots & 0\\ 0 & 0 & R_{a3} & \cdots & 0\\ \vdots & & & & \\ 0 & 0 & 0 & \cdots & R_{anf}\end{bmatrix}$$

$$[R_b] = \begin{bmatrix}R_{b1} & 0 & 0 & \cdots & 0\\ 0 & R_{b2} & 0 & \cdots & 0\\ 0 & 0 & R_{b3} & \cdots & 0\\ \vdots & & & & \\ 0 & 0 & 0 & \cdots & R_{bnf}\end{bmatrix}$$

$$[R_{n\ell}] = \begin{bmatrix} R_{n\ell 1} & 0 & 0 & \cdots & 0 \\ 0 & R_{n\ell 2} & 0 & \cdots & 0 \\ 0 & 0 & R_{n\ell 3} & \cdots & 0 \\ \vdots & & & & \\ 0 & 0 & 0 & \cdots & R_{n\ell nf} \end{bmatrix}$$

and the matrices

$[o_a]$, $[o_b]$, $[o_c]$ ..... and $[o_{n\ell}]$

being null matrices each having zero elements.

The inductance matrices can be written as below:

$$[Z_{aa}] = \begin{bmatrix} Z_{a1,a1} & Z_{a1,a2} & Z_{a1,a3} & \cdots & Z_{a1,anf} \\ Z_{a2,a1} & Z_{a2,a2} & Z_{a2,a3} & \cdots & Z_{a2,anf} \\ \vdots & \vdots & \vdots & & \vdots \\ Z_{anf,a1} & \vdots & \vdots & \cdots & Z_{anf,anf} \end{bmatrix}$$

$$[Z_{n\ell,n\ell}] = \begin{bmatrix} Z_{n\ell 1,n\ell 1} & Z_{n\ell 1,n\ell 2} & Z_{n\ell 1,n\ell 3} & \cdots & Z_{n\ell 1,n\ell nf} \\ Z_{n\ell 2,n\ell 1} & Z_{n\ell 2,n\ell 2} & Z_{n\ell 2,n\ell 3} & \cdots & Z_{n\ell 2,n\ell nf} \\ \vdots & \vdots & \vdots & & \vdots \\ Z_{n\ell nf,n\ell 1} & Z_{n\ell nf,n\ell 2} & Z_{n\ell nf,n\ell 3} & \cdots & Z_{n\ell nf,n\ell nf} \end{bmatrix}$$

The matrices $[Z_{aa}]$, $[Z_{bb}]$, ... and $[Z_{n\ell n\ell}]$ are symmetrical within themselves.

Also, the voltages and currents matrices can be written as below:

$$[V_a] = \begin{bmatrix} V_{a1} \\ V_{a2} \\ V_{a3} \\ \vdots \\ V_{anf} \end{bmatrix} \quad \cdots\cdots \text{ and } [V_{n\ell}] = \begin{bmatrix} V_{n\ell 1} \\ V_{n\ell 2} \\ V_{n\ell 3} \\ \vdots \\ V_{n\ell nf} \end{bmatrix}$$

Hence, the voltage across each filament in the same layer is equal

(i.e. $V_{a1} = V_{a2} = V_3 = \cdots\cdots V_{anf} = V_a$

and $V_{n\ell 1} = V_{n\ell 2} = V_{n\ell 3} = \cdots\cdots V_{n\ell nf} = V_{n\ell}$)

The current matrices can be written as below:

$$[i_a] = \begin{bmatrix} i_{a1} \\ i_{a2} \\ i_{a3} \\ \cdot \\ \cdot \\ i_{anf} \end{bmatrix} \quad \ldots\ldots \text{ and } [i_{n\ell}] = \begin{bmatrix} i_{n\ell 1} \\ i_{n\ell 2} \\ i_{n\ell 3} \\ \cdot \\ \cdot \\ i_{n\ell nf} \end{bmatrix}$$

The total current in each layer can redistribute itself from one layer to the next.

Equation 3.21 can be written in general in matrix format:

$$[V] = [Z][i] \qquad 3,22$$

where

Z is impedance matrix

and hence

$$Z = R + j\omega M$$

The solution of equation 3.22 is described below.

3.5 Solution for equation systems

A general set of equations was developed in the previous section for the notional filament coils into which the layers of a foil inductor, or the foil secondary of a transformer were subdivided for the purpose of calculating the current distribution across the foil. This set of equations consists simply of the coupled circuit equation for each filament coil taken in turn. There are two problems to be dealt with in the solution of these equations. First there is the fundamental problem that the set consists of ($n\ell$ x nf) equations while there are $n\ell$ x nf + $n\ell$ unknowns (i.e. $n\ell$ x nf unknown currents and $n\ell$ unknown voltages). The second problem is one of organization, in that real problems may introduce a very large number of equations

which make solution inconvenient. Both these problems are overcome by using a formal method of solution based on tensor analysis and a suitable transformation which is implemented by the use of a "connection matrix".

The set of equations in the previous section constitutes the "canonical equations". These are the equations for each notional circuit taken in turn. The connection matrix contains the information on how the circuits are interconnected and in effect provides the extra $n\ell$ equations which make solution of the set of equations possible. The advantage of this formal solution technique from the organization point of view is quite clear. A computer program can be constructed to handle the general problem. It is simply a matter of changing the contents of the connection matrix, to change the application of the equations.

The canonical equations have the form as below:

$$V_j = Z_{jk} i^k \qquad 3.23$$

where (j,k = a,b,c ... $n\ell$)

or in the following form:

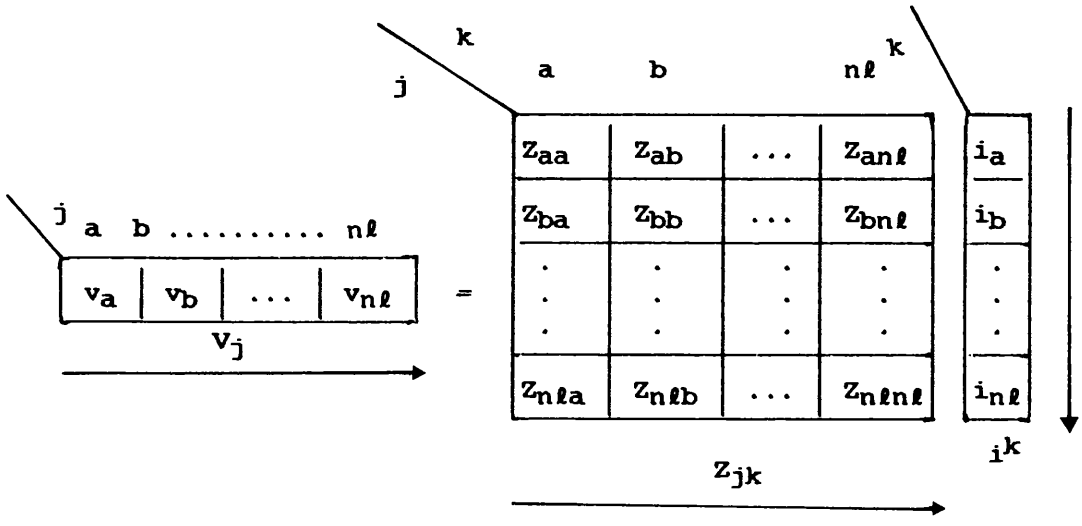

The arrows in each matrix indicate how the multiplication is carried out. The rows of Z_{jk} are to be multiplied with column of i^k.

The concepts employed and the steps in the formulation and solution of tensor equations are illustrated [9] below:

1. Set up the canonical equations of a set simultaneous equation such as

$$V_j = Z_{jk} i^k$$

and this equation the same as equation 3.22 in previous section.

2. Establish the equations of transformation

$$i^k = C^k_{k'} \, i^{k'} \qquad 3.24$$

3. Specify the invariancy of power (the power or energy in the network is the same regardless of the particular set of variables - currents and voltages - used in its description).

$$P = V_j i^j = V_{j'} i^{j'}$$

$$\therefore \quad V_j C^j_{j'} i^{j'} = V_{j'} i^{j'}$$

$$\therefore \quad V_{j'} = C^j_{j'} V_j \qquad 3.25$$

$$\therefore \quad V_j = C^{j'}_j V_{j'} \qquad 3.26$$

Evidently the voltages transform in an inverse fashion from the currents, since $C^{j'}_j$ is the inverse of $C^j_{j'}$.

4. Preserve the invariancy of form in the equation of performance, in passing from the "old" variables v_j, i^k to the "new" variables $V_{j'}$, $i^{k'}$.

$$V_j = Z_{jk} i^k = Z_{jk} C^k_{k'} i^{k'}$$

$$V_{j'} = C^j_{j'} V_j$$

$$V_{j'} = C^j_{j'} Z_{jk} C^k_{k'} i^{k'}$$

$$V_{j'} = Z_{j'k'} i^{k'} \qquad 3.27$$

5. Solve for the new currents by multiplying by the inverse $(Z_{j'k'})^{-1}$ of the impedance matrix

$$i^{k'} = (Z_{j'k'})^{-1} . V_{j'} \qquad 3.28$$

6. The "old" currents can be found in terms of the "new" currents (Eq.3.24).

$$i^k = C^k_{k'} i^{k'} = C^k_{k'} (Z_{j'k'})^{-1} V_{j'} \qquad 3.29$$

7. The old voltages (Eq.3.22) can be found as below

$$V_j = Z_{jk} i^k = Z_{jk} C^k_{k'} (Z_{j'k'})^{-1} V_{j'} \qquad 3.30$$

Thus all quantities have been found in a routine fashion. The seven steps outlined above are always sufficient. Several applications of this method to the present problem are discussed below.

3.5.1 Single layer without symmetry

In section 3.2, the single layer model was discussed and a set of equations were provided. Figure 3.11 presents the electrical circuit of one layer foil subdivided into five filament and the old currents in each filaments are i_1, i_2, i_3, i_4 and i_5, the respective new currents are i'_1, i'_2, i'_3, i'_4 and i'_5. Also the total current is I'_o.

Therefore the relation between the old and new currents are given:

$$i_1 = i'_1$$

$$i_2 = i'_2$$

$$i_3 = I'_o - (i'_1 + i'_2 + i'_4 + i'_5)$$

$$i_4 = i'_4$$

$$i_5 = i'_5$$

Using these relations with equation (3.24) the transformation [c] can be determined as below

$$\begin{bmatrix} i_1 \\ i_2 \\ i_3 \\ i_4 \\ i_5 \end{bmatrix} = \begin{bmatrix} 0 & 1 & 0 & 0 & 0 \\ 0 & 0 & 1 & 0 & 0 \\ 1 & -1 & -1 & -1 & -1 \\ 0 & 0 & 0 & 1 & 0 \\ 0 & 0 & 0 & 0 & 1 \end{bmatrix} \begin{bmatrix} I'_o \\ i'_1 \\ i'_2 \\ i'_4 \\ i'_5 \end{bmatrix}$$

The transpose $[C_t]$ of the above transformation matrix [C] is given

$$[C_t] = \begin{bmatrix} 0 & 0 & 1 & 0 & 0 \\ 1 & 0 & -1 & 0 & 0 \\ 0 & 1 & -1 & 0 & 0 \\ 0 & 0 & -1 & 1 & 0 \\ 0 & 0 & -1 & 0 & 1 \end{bmatrix}$$

The new impedance matrix is then evaluated as below.

$$[Z'] = [C_t][Z][C]$$

The new voltage can be obtained as below.

$$[V'] = [C_t][V]$$

$$[V'] = \begin{bmatrix} 0 & 0 & 1 & 0 & 0 \\ 1 & 0 & -1 & 0 & 0 \\ 0 & 1 & -1 & 0 & 0 \\ 0 & 0 & -1 & 1 & 0 \\ 0 & 0 & -1 & 0 & 1 \end{bmatrix} \begin{bmatrix} V_1 \\ V_2 \\ V_3 \\ V_4 \\ V_5 \end{bmatrix} = \begin{bmatrix} V_3 \\ 0 \\ 0 \\ 0 \\ 0 \end{bmatrix}$$

The voltage across each filament is the same (i.e. $V_1 = V_2 = V_3 = V_4 = V_5$), because the filaments are connected in parallel by equipotential end bars and excited from the same voltage source. Using these new voltages, new currents are obtained as below.

$$[i'] = [Z']^{-1}[V']$$

Further, the old currents are

$$[i] = [C][i']$$

The old voltage across the filaments, using the old currents can be obtained

$$[v] = [Z][i]$$

3.5.2 Multilayer without symmetry

For multilayer configuration, the technique may be applied in the following way, with reference to Figure 3.12. Thus the first layer current transformation:

$$i_{11} = i'_{11}$$

$$i_{12} = I'_o - (i'_{11} + i'_{13})$$

$$i_{13} = i'_{13}$$

Similarly for the second layer

$$i_{21} = i'_{21}$$

$$i_{22} = I'_o - (i'_{21} + i'_{23})$$

$$i_{23} = i'_{23}$$

From these sets of identities the transformation matrix is determined as

$$\begin{bmatrix} i_{11} \\ i_{12} \\ i_{13} \\ i_{21} \\ i_{22} \\ i_{23} \end{bmatrix} = \begin{bmatrix} 0 & 1 & 0 & 0 & 0 \\ 1 & -1 & -1 & 0 & 0 \\ 0 & 0 & 1 & 0 & 0 \\ 0 & 0 & 0 & 1 & 0 \\ 1 & 0 & 0 & -1 & -1 \\ 0 & 0 & 0 & 0 & 1 \end{bmatrix} \cdot \begin{bmatrix} I'_o \\ i'_{11} \\ i'_{13} \\ i'_{21} \\ i'_{23} \end{bmatrix}$$

Then, the transpose $[c_t]$ of the transformation matrix [c] is

$$[C_t] = \begin{bmatrix} 0 & 1 & 0 & 0 & 1 & 0 \\ 1 & -1 & 0 & 0 & 0 & 0 \\ 0 & -1 & 1 & 0 & 0 & 0 \\ 0 & 0 & 0 & 1 & -1 & 0 \\ 0 & 0 & 0 & 0 & -1 & 1 \end{bmatrix}$$

Also the new impedance Z' can be calculated by

$$[Z'] = [c_t][z][c]$$

Thus, the inverse of new impedance matrix is $[Z']^{-1}$.

The new voltage can be obtained as below.

$$[V'] = [c_t][v]$$

$$[V'] = \begin{bmatrix} 0 & 1 & 0 & 0 & 1 & 0 \\ 1 & -1 & 0 & 0 & 0 & 0 \\ 0 & -1 & 1 & 0 & 0 & 0 \\ 0 & 0 & 0 & 1 & -1 & 0 \\ 0 & 0 & 0 & 0 & -1 & 1 \end{bmatrix} \cdot \begin{bmatrix} V_1 \\ V_1 \\ V_1 \\ V_2 \\ V_2 \\ V_2 \end{bmatrix} = \begin{bmatrix} V_1+V_2 \\ 0 \\ 0 \\ 0 \\ 0 \end{bmatrix}$$

The important feature to note here is that in the transformed voltage matrix only the total voltage across all layers is required, i.e.

$V_1 + V_2 = V =$ the applied voltage

Using these new voltages, new currents are obtained.

Thus

$$[i'] = [Z']^{-1}.[V']$$

Further, the old currents are

$$[i] = [C][i']$$

The old voltage across each layer can be obtained by using the old current and impedance as below.

$$[v] = [z][i]$$

In general the number of equations depends on the number of layer nℓ and the number of filaments nf in each layer.

The general impedance matrix has (n x n) elements and is reduced slightly to [m x m] elements by the transformation, where

$n = nf \times n\ell$

$m = (nf + 1)/2 \times n\ell + 1$

For practical purposes the matrices of the equivalent circuit easily become too large for convenience. This is mainly because the time taken to invert a matrix is very closely proportional to the order cubed. Hence while a (100 x 100) problem may run very rapidly on a computer, taking say 30 seconds, a (1000 x 1000) problem will take 10^4 times as long. Thus it is very important that the program is well organised, and the use of symmetry can also be employed to half the number of equations that need to be considered explicitly. Some examples of the use of symemtry are given below.

There are two slightly different symmetrical conditions depending upon whether an odd or even number of filaments is chosen. They are both described briefly below.

3.5.3 Multilayer with odd symmetry

In this case, each layer is divided into an odd number of filaments. Hence the odd symmetry is used to reduce the number of equations so that the time of calculation and size of memory required for computation are reduced. It is important to know how the use of odd symmetry in multilayer winding is reducing the magnitude of the computation involved. As shown in Figure 3.12 and described in the previous section, the relations between the new and old currents are given below.

For the first layer

$$i_{11} = i'_{11}$$

$$i_{12} = I'_o - (i'_{11} + i'_{13})$$

$$i_{13} = i'_{13}$$

Using symmetry the following relations are obtained

$$i'_{11} = i'_{13}$$

Therefore

$$i_{12} = I'_o - 2i'_{11}$$

Similarly for the second layer

$$i_{21} = i'_{21}$$

$$i_{22} = I'_o - 2i'_{21}$$

The transformation matrix of the current is below

$$\begin{bmatrix} i_{11} \\ i_{12} \\ i_{21} \\ i_{22} \end{bmatrix} = \begin{bmatrix} 0 & 1 & 0 \\ 1 & -2 & 0 \\ 0 & 0 & 1 \\ 1 & 0 & -2 \end{bmatrix} \begin{bmatrix} I'_o \\ i'_{11} \\ i'_{21} \\ \end{bmatrix}$$

The transpose $[c_t]$ of the above transformation is given

$$[c_t] = \begin{bmatrix} 0 & 1 & 0 & 1 \\ 1 & -2 & 0 & 0 \\ 0 & 0 & 1 & -2 \end{bmatrix}$$

Also the new impedance Z' can be calculated by

$$[Z'] = [c_t][z][c]$$

The problem can be seen in calculating the new voltage matrix where

$$[V'] = [c_t][v]$$

$$[V'] = \begin{bmatrix} 0 & 1 & 0 & 1 \\ 1 & -2 & 0 & 0 \\ 0 & 0 & 1 & -2 \end{bmatrix} \begin{bmatrix} V_1 \\ V_1 \\ V_2 \\ V_2 \end{bmatrix} = \begin{bmatrix} V_1+V_2 \\ -V_1 \\ -V_2 \end{bmatrix}$$

Therefore, in this case, the new voltage matrix is unknown and the formal method cannot apply to the odd symmetry. For this reason and others the even symmetry is used in the model calculations as described below.

3.5.4 Multilayer with even symmetry

The even symmetry is adopted for multilayer because of its simplicity and it reduced the number of equations more than the same thing obtained with odd symmetry.

For example, assuming the number of layer two and number of filaments four in each layer, the equivalent electrical circuit is drawn in Figure 3.13. The voltage equations are given in matrix form as shown on the following page.

$$\begin{bmatrix} V_1 \\ V_1 \\ V_1 \\ V_1 \\ V_2 \\ V_2 \\ V_2 \\ V_2 \end{bmatrix} = \begin{bmatrix} R_{11}+j\omega L_{1111} & j\omega M_{1112} & j\omega M_{1113} & j\omega M_{1114} & j\omega M_{1211} & j\omega M_{1212} & j\omega M_{1213} & j\omega M_{1214} \\ j\omega M_{1121} & R_{12}+j\omega L_{1122} & j\omega M_{1123} & j\omega M_{1124} & j\omega M_{1221} & j\omega M_{1222} & j\omega M_{1223} & j\omega M_{1224} \\ j\omega M_{1131} & j\omega M_{1132} & R_{13}+j\omega L_{1133} & - & - & - & - & j\omega M_{1234} \\ j\omega M_{1141} & j\omega M_{1142} & - & R_{14}+j\omega L_{1144} & - & - & - & j\omega M_{1244} \\ j\omega M_{2111} & j\omega M_{2112} & - & - & R_{21}+j\omega L_{2211} & - & - & j\omega M_{2214} \\ j\omega M_{2121} & j\omega M_{2122} & - & - & - & R_{22}+j\omega L_{2222} & - & j\omega M_{2224} \\ j\omega M_{2131} & j\omega M_{2132} & - & - & - & - & R_{23}+j\omega L_{2233} & j\omega M_{2234} \\ j\omega M_{2141} & j\omega M_{2142} & - & - & - & - & - & R_{24}+j\omega L_{2244} \end{bmatrix} \cdot \begin{bmatrix} i_{11} \\ i_{12} \\ i_{13} \\ i_{14} \\ i_{21} \\ i_{22} \\ i_{23} \\ i_{24} \end{bmatrix}$$

(3.31)

Applying the even symmetry a reduced form of the matrix is obtained.

$$\begin{bmatrix} V_1 \\ V_1 \\ V_2 \\ V_2 \end{bmatrix} = \begin{bmatrix} R_{11} + j\omega(L_{1111} + M_{1114}) & j\omega(M_{1112} + M_{1113}) & j\omega(M_{1211} + M_{1214}) & j\omega(M_{1212} + M_{1213}) \\ j\omega(M_{1121} + M_{1124}) & R_{12} + j\omega(L_{1122} + M_{1123}) & j\omega(M_{1221} + M_{1224}) & j\omega(M_{1222} + M_{1223}) \\ j\omega(M_{2111} + M_{2114}) & j\omega(M_{2112} + M_{2113}) & R_{21} + j\omega(L_{2211} + M_{2214}) & j\omega(M_{2212} + M_{2213}) \\ j\omega(M_{2121} + M_{2124}) & j\omega(M_{2122} + M_{2123}) & j\omega(M_{2221} + M_{2224}) & R_{22} + j\omega(L_{2222} + M_{2223}) \end{bmatrix} \cdot \begin{bmatrix} i_{11} \\ i_{12} \\ i_{21} \\ i_{22} \end{bmatrix}$$

(3.32)

Using the transformation, the old and new current relations for the first and second layer are given below.

For first layer

$$i_{11} = i'_{11}$$

$$i_{13} + i_{12} = I'_o - (i'_{11} + i'_{14})$$

$$i_{14} = i'_{14}$$

Hence

$$i_{14} = i'_{14} = i'_{11}$$

$$i_{12} = i_{13}$$

Therefore

$$i_{12} = \frac{1}{2} I'_o - i'_{11}$$

Similarly for the second layer

$$i_{21} = i'_{21}$$

$$i_{22} = \frac{1}{2} I'_o - i'_{21}$$

because

$$i_{23} = i_{22}$$

$$i_{24} = i_{21}$$

From these sets of identities the transformation matrix is determined as

$$\begin{bmatrix} i_{11} \\ i_{12} \\ i_{21} \\ i_{22} \end{bmatrix} = \begin{bmatrix} 0 & 1 & 0 \\ \frac{1}{2} & -1 & 0 \\ 0 & 0 & 1 \\ \frac{1}{2} & 0 & -1 \end{bmatrix} \cdot \begin{bmatrix} I'_o \\ i'_{11} \\ i'_{21} \end{bmatrix}$$

Then, the transpose $[C_t]$ of the transformation matrix [c] is

$$[c_t] = \begin{bmatrix} 0 & \frac{1}{2} & 0 & \frac{1}{2} \\ 1 & -1 & 0 & 0 \\ 0 & 0 & 1 & -1 \end{bmatrix}$$

Also, the new impedance Z' can be calculated by

$$[Z'] = [C_t][Z][C]$$

The new voltage can be obtained as below

$$[V'] = [C_t][V]$$

$$[V'] = \begin{bmatrix} 0 & \frac{1}{2} & 0 & \frac{1}{2} \\ 1 & -1 & 0 & 0 \\ 0 & 0 & 1 & -1 \end{bmatrix} \begin{bmatrix} V_1 \\ V_1 \\ V_2 \\ V_2 \end{bmatrix} = \begin{bmatrix} \frac{1}{2} V_1 + \frac{1}{2} V_2 \\ 0 \\ 0 \end{bmatrix}$$

The important feature to note here is that in the transformed voltage matrix only the half of the total voltage across all layers is required, i.e.

$$\frac{1}{2} V_1 + \frac{1}{2} V_2 = 0.5\ V$$

The new currents therefore can be obtained as below.

$$[i'] = [z']^{-1}.[v']$$

Further, the old currents and voltages can be obtained as below.

$$[i] = [c][i']$$

$$[v] = [z][i]$$

Hence, the current transformation and new impedance matrices have the number of elements as below.

$$[c] = [n \times m] \quad \text{and} \quad [z'] = [m \times m]$$

where $n = \frac{nf}{2} \times n\ell$

$$m = \left[\frac{nf - 2}{2}\right] \times n\ell + 1$$

3.5.5 Transformer model

As discussed in section 3.1 above, the field conditions in the winding region of a transformer are approximately the same whether or not the ferrite core is present, providing that the primary ampere-turns are equal to the secondary ampere-turns. This does not mean that an iron cored transformer behaves in the same way as a ferrite cored transformer, and the present approach does not allow a generally valid model of a ferrite cored transformer to be made. However, the particular problem of calculating the losses in a foil wound secondary can be undertaken. This is done in the following way:

i) For a transformer with n_s secondary turns of foil, it is assumed that the notional primary turns, n_p, is equal to n_s, whatever the actual number of turns.

ii) It is assumed that the notional primary turns are spread out to occupy the full primary winding space and that the current is distributed uniformly in each turn.

iii) In a real primary which has many turns of thin round wire there will usually be some localised redistribution of current within each turn due to proximity effect in the usual way. However viewed from the secondary windings the primary current distribution is approximately uniform so

that the field in the region of the secondary is approximately the same for both the real or notional primary winding arrangement.

iv) The canonical equations of each of the windings may be set up in the usual way and the self and mutual inductances computed for air cored coils. There will clearly be n_p equations for the primary, where n_p is the notional number of primary turns, and n_s x nf equations for the secondary, where n_s is the actual number of secondary turns of foil and nf is the number of filaments into which each turn is subdivided in order to calculate the current distribution across each foil turn.

v) The transformation matrix can then be formulated in the usual way, to include the fact that the primary and secondary windings are in series opposition.

vi) Losses in the foil can be calculated in the usual way from the filament currents so that R_{ac}/R_{dc} for the secondary is obtained. Results from the primary data are substantially meaningless. Losses in the real primary winding still need to be calculated via Dowell's Method[7] in the usual way.

The method of implementing this procedure mathematically is described below.

A typical transformer illustrated in Figure 3.14(a), is replaced by the model in Figure 3.14(b) where the notional primary turns are

indicated. There are $n_p + n_s$ x nf canonical equations, which could be reduced to $n_p + n_s$ x nf/2 by using even symmetry for the foil equations as described in section 3.5.4 above. These are written down for each discrete notional circuit in the usual way without regard to the pattern of interconnection. At this point therefore the general method of solution adopted in section 3.5 above does not distinguish between inductors or transformers except in so far as the geometries from which the self and mutual inductances of the notional circuit may differ.

Equations in the form defined in Equation 3.20 above are therefore produced, although they might be considered to be partitioned as follows.

$$\begin{bmatrix} [V_p] \\ [V_s] \end{bmatrix} = \begin{bmatrix} [Z_{pp}] & [Z_{ps}] \\ [Z_{sp}] & [Z_{ss}] \end{bmatrix} \begin{bmatrix} [i_p] \\ [i_s] \end{bmatrix} \qquad 3.33$$

where p and s denote primary and secondary quantities respectively.

The equivalent circuit, when the windings have been interconnected in series opposition is illustrated in Figure 3.15 and from this the transformation or connection matrix [c] needs to be deduced.

The procedure has been written out in full below for a simple case of two foil turns, each subdivided into three filaments, with consequently two notional primary turns. This arrangement and its interconnection is illustrated in Figure 3.15.

The relationships between the current parameters in the canonical equations i_{p1}, i_{p2}, i_{s11}, i_{s12}, i_{s13}, i_{s21}, i_{s22} and i_{s23} and the transformed currents I'_0, i'_{s11}, i'_{s13}, i'_{s21} and i'_{s23} are as follows

$$i_{p1} = I'_0$$

$$i_{p2} = I'_0$$

$$i_{s11} = - i'_{s11}$$

$$i_{s12} = - (I'_0 - i'_{s11} - i'_{s13})$$

$$i_{s13} = - i'_{s13}$$

$$i_{s21} = - i'_{s21}$$

$$i_{s22} = - (I'_0 - i'_{s21} - i'_{s23})$$

$$i_{s23} = - i'_{s23}$$

Hence the connection matrix, [c] becomes

$$[i] = [c][i']$$

where

$$\begin{bmatrix} i_{p1} \\ i_{p2} \\ i_{s11} \\ i_{s12} \\ i_{s13} \\ i_{s21} \\ i_{s22} \\ i_{s23} \end{bmatrix} = \begin{bmatrix} 1 & 0 & 0 & 0 & 0 \\ 1 & 0 & 0 & 0 & 0 \\ 0 & -1 & 0 & 0 & 0 \\ -1 & 1 & 1 & 0 & 0 \\ 0 & 0 & -1 & 0 & 0 \\ 0 & 0 & 0 & -1 & 0 \\ -1 & 0 & 0 & 1 & 1 \\ 0 & 0 & 0 & 0 & -1 \end{bmatrix} \begin{bmatrix} I'_0 \\ i'_{s11} \\ i'_{s13} \\ i'_{s21} \\ i'_{s23} \\ \\ \\ \end{bmatrix}$$

The transformed voltage matrix [V'] is derived from

$$[V'] = [C_t][V]$$

$$[V'] = \begin{bmatrix} 1 & 1 & 0 & -1 & 0 & 0 & -1 & 0 \\ 0 & 0 & -1 & 1 & 0 & 0 & 0 & 0 \\ 0 & 0 & 0 & 1 & -1 & 0 & 0 & 0 \\ 0 & 0 & 0 & 0 & 0 & -1 & 1 & 0 \\ 0 & 0 & 0 & 0 & 0 & 0 & 1 & -1 \end{bmatrix} \begin{bmatrix} V_{p1} \\ V_{p2} \\ V_{s1} \\ V_{s1} \\ V_{s1} \\ V_{s2} \\ V_{s2} \\ V_{s2} \end{bmatrix}$$

$$= \begin{bmatrix} V_{p1} + V_{p2} - V_{s1} - V_{s2} \\ 0 \\ 0 \\ 0 \\ 0 \end{bmatrix}$$

$$= \begin{bmatrix} V \\ 0 \\ 0 \\ 0 \\ 0 \end{bmatrix}$$

Bearing in mind the sense in which the voltages across each turn of primary and secondary winding are summed when the windings are connected in series opposition the term appearing in the transformed voltage matrix, $V_{p1} + V_{p2} - V_{S1} - V_{s2}$, is in fact the total voltage applied across the winding.

The connection matrix [C] can be seen above to have a pattern which depends upon the number of primary and secondary turns, and the number of notional filaments into which the secondary foil is

subdivided.

It is a relatively simple matter to generate this matrix within a computer programme, having specified the numbers of turns and filaments.

Solution of these equations can take place in the usual way in order to compute filament currents in the foil from which current distribution, foil loss and R_{ac}/R_{dc} are readily calculated.

For transformers with sandwich windings, i.e. where the secondary foil turns are sandwiched between two primary sections as described in Chapter Two, section 2.4.3, the connection matrix is identical to that given above. Only the dimensions and positions from which all the self and mutual inductances are calculated must be taken into account.

The techniques of symmetry described in section 3.5.4 above can be incorporated into the present transformer work, where appropriate.

The method described so far for treating the transformer assumes that the self and mutual inductance parameters relating to the primary turns, assume that these conductors are relatively large in cross sectional area, and that the current distribution in them is uniform. As explained in Chapter Four, section 4.2 below, a high level of confidence could not be placed in the existing methods of calculating inductances with conductors of this type. The use of filament coils of infinitely small cross sectional area was found to be most reliable from the point of view of calculating inductances

values.

For the present case, however, when a small number of large area turns is required to represent the primary winding the use of a single filament coil at the centre of each conductor would appear intuitively to be an inadequate representation, and was also found in practice to be unsuitable.

A modified method can be used however where each primary turn is assumed to consist of a number of small turns, small enough to be represented by filaments in the limit. These could sensibly be equal in size to the filament used to respresent the secondary foil - and the connection matrix then adapted so that the same current is forced through each filament, together with the same voltage existing across it.

The 2 layer, three filament example dealt with above and illustrated in Figure 3.15, becomes as shown in Figure 3.16.

The connection matrix is then designed to set so that all primary filaments share current equally. i.e.

$$i_{p11} = I_o'/3$$

$$i_{p12} = I_o'/3$$

$$i_{p13} = I_o'/3$$

$$i_{p21} = I_o'/3$$

$$i_{p22} = I_o'/3$$

$$i_{p23} = I_o'/3$$

and

$$\begin{bmatrix} i_{p11} \\ i_{p12} \\ i_{p13} \\ i_{p21} \\ i_{p22} \\ i_{p23} \\ i_{s11} \\ i_{s12} \\ i_{s13} \\ i_{s21} \\ i_{s22} \\ i_{s23} \end{bmatrix} = \begin{bmatrix} 1/3 & 0 & 0 & 0 & 0 \\ 1/3 & 0 & 0 & 0 & 0 \\ 1/3 & 0 & 0 & 0 & 0 \\ 1/3 & 0 & 0 & 0 & 0 \\ 1/3 & 0 & 0 & 0 & 0 \\ 1/3 & 0 & 0 & 0 & 0 \\ 0 & -1 & 0 & 0 & 0 \\ -1 & 1 & 1 & 0 & 0 \\ 0 & 0 & -1 & 0 & 0 \\ 0 & 0 & 0 & -1 & 0 \\ -1 & 0 & 0 & 1 & 1 \\ 0 & 0 & 0 & 0 & -1 \end{bmatrix} \cdot \begin{bmatrix} I_o' \\ i_{s11}' \\ i_{s13}' \\ i_{s21}' \\ i_{s23}' \\ \\ \\ \\ \\ \\ \\ \end{bmatrix}$$

This carries into the transformed voltage matrix so the only voltage information required is the total voltage across primary and secondary, as before.

3.6 Conclusions

The problems of calculating eddy-current losses in foil conductor is often approached by subdividing the conductors into notional filament coils, such that the current distribution in a filament can be assumed to be uniform.

In principle the method involves writing down the voltage equation for each filament, which includes the effects of its coupling with all other filaments, and then solving these equations simultaneously.

In practice, a very large number of equations often has to be dealt with and a formal method solution for them has been described in this chapter. It uses elementary tensor analysis techniques. That is to say the canonical equations are first written down. In this case these are the set of voltage equations for each filament which is independent of the configuration in which they are electrically interconnected. The connection, or transformation, matrix provides this additional information and allows the equations to be solved.

The advantage of this method is that it is flexible and general, the only difference between using it for an inductor or for a transformer, say, being a different transformation matrix. The method has been explained by writing out in full the equations for a simple problem. The actual calculations were all performed by a Fortran computer programme which was able to treat the general problem when any numbers of turns and subdivisions of turns would be specified as input parameters. These programmes are summarized in Appendix A3.

3.7 References

1. Mullineux, N., Reed, J.R. and Whyte, I.J.: "Current distribution in sheet- and foil-wound transformers", Proc.IEE, Vol.116, No.1, January 1969, pp.127.
2. Murgatroyd, P.N. and Walker, N.J.: "Frequency-dependent inductance and resistance of foil conductor loops", Proc.IEE, Vol.124, No.5, May 1977, pp.493-496.

3. Grover, F.W.: "Inductance Calculations" (Van Nostrand 1947), Chapters 11 and 16.

4. Reeves, R.: "Air-cored foil-wound inductors", Proc.IEE, Vol.125, No.5, May 1978, pp.460-463.

5. El-Missiry, M.M.: "Calculations of current distribution and optimum dimensions of foil-wound air-cored reactors", Proc.IEE, Vol.124, No.11, November 1977, pp.1073-1077.

6. El-Missiry, M.M.: "Current distribution and leakage impedance of various types of foil-wound transformer", Proc.IEE, Vol.125, No.10, October 1978, pp.987-992.

7. Dowell, P.L.: "Effects of eddy currents in transformer windings.", Proc.IEE, Vol.113, No.8, August 1966, pp.1387-1394.

8. Jongsma, J.: "Minimum-loss transformer windings for ultrasonic frequencies", Electronic Applications Bull 35(3), 1978.

9. Bewley, L.V.: "Tensor Analysis of Electric Circuits and Machines", (The Ronald Press Company, New York, 1961).

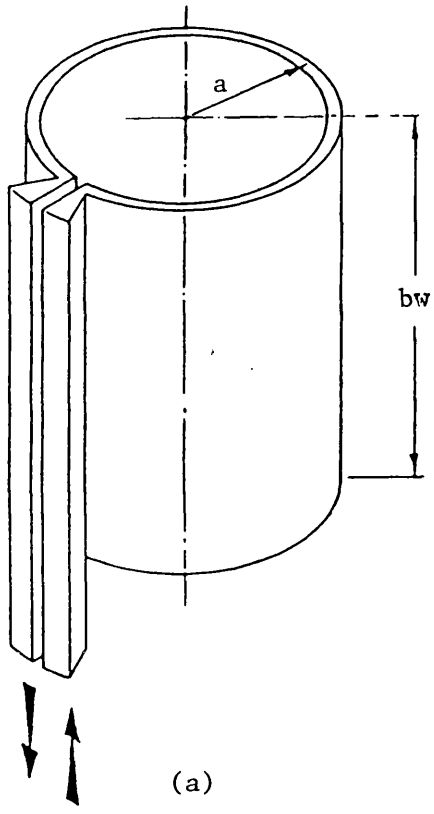

(a)

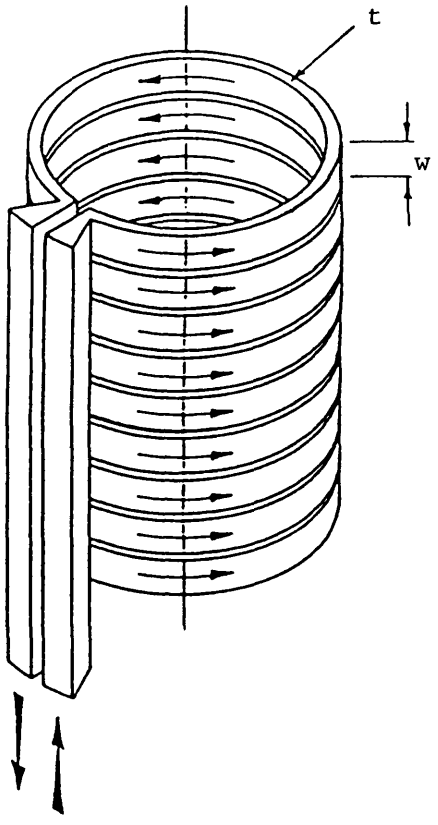

(b)

Fig.3.1: (a) Single foil turn with equipotential connecting bars
(b) Single foil turn divided into equal parallel filaments

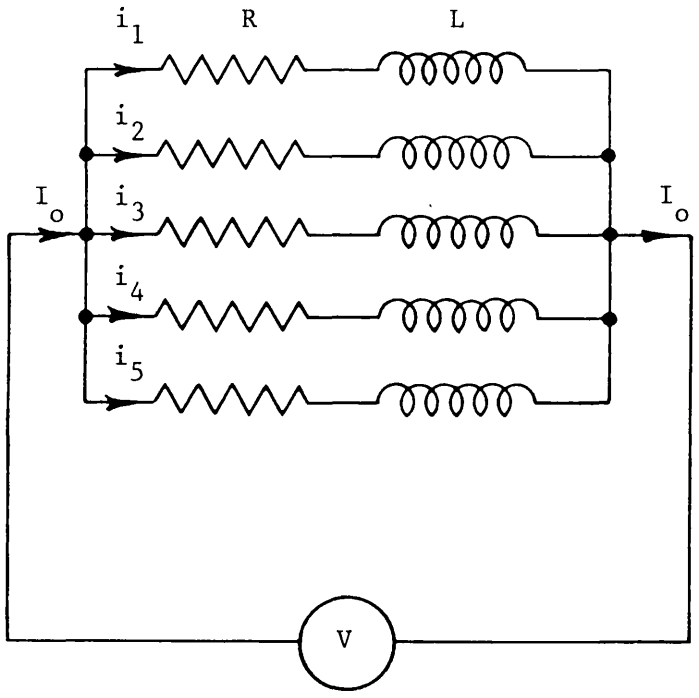

Fig.3.2: Equivalent circuit of single layer

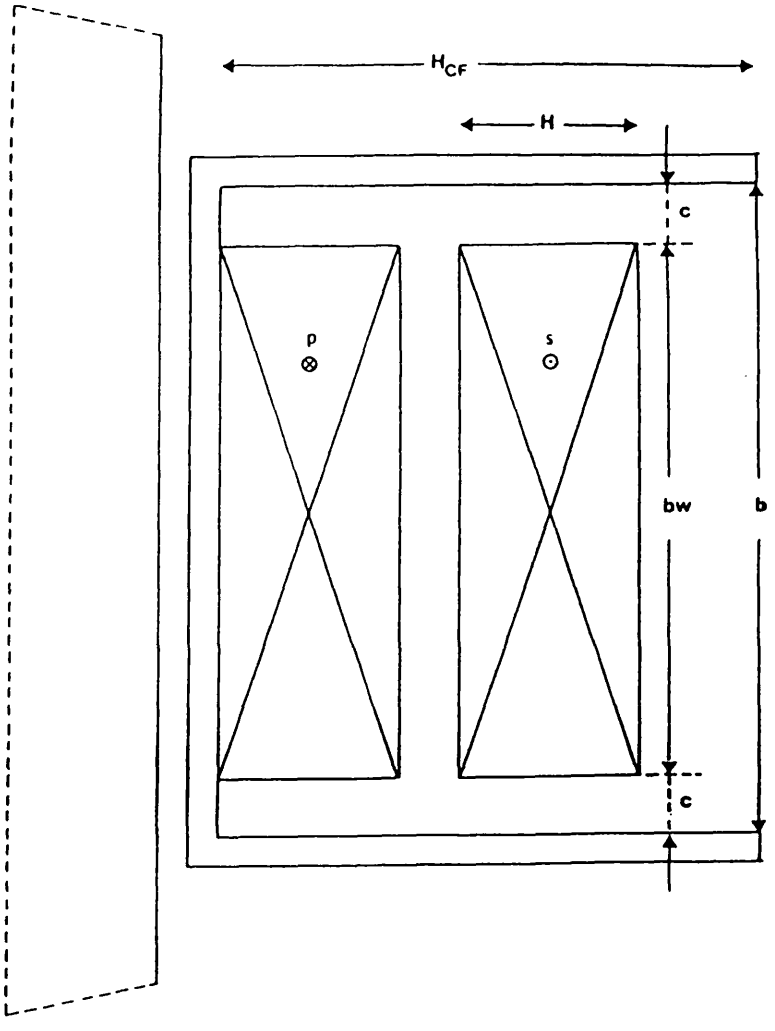

Fig.3.3: Definitions of coil former and winding dimensions

bw = actual winding breadth (30 mm)

b = winding window breadth (33 mm)

H_{CF} = height of winding portion

c = creepage distance

Transformer winding 'wire'	Transformer winding 'strip'
Number of turns = 75	Number of layers = 20
Wire diameter = 1 mm	Copper foil thickness = 0.073 mm

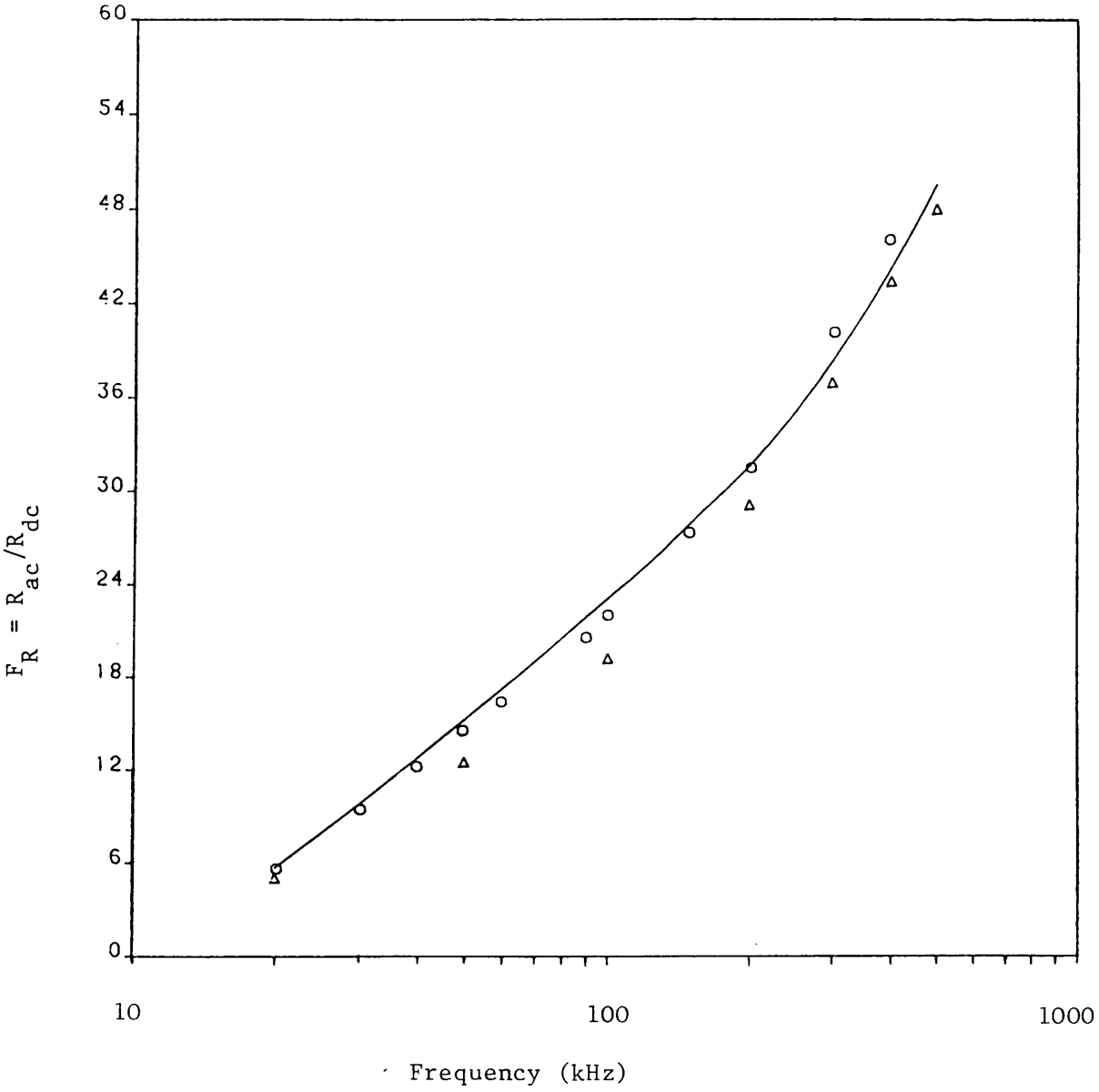

Fig.3.4: Losses in transformer winding 'wire'

——— Theory using Dowell's method

o o o Experimental results with core

Δ Δ Δ Experimental results without core

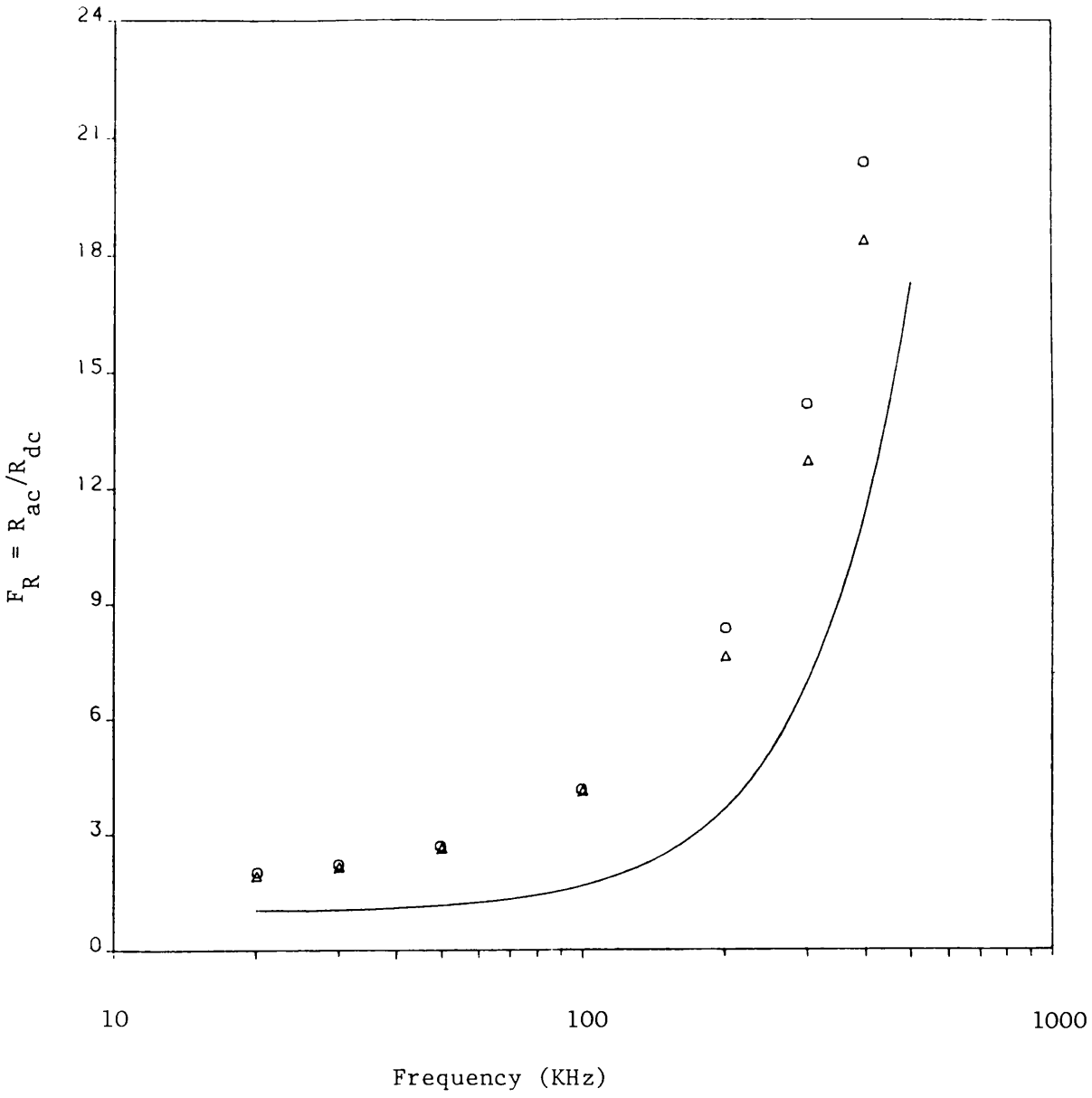

Fig.3.5: Losses in transformer winding 'strip'

——— Theory using Dowell's method

o o o Experimental results with core

Δ Δ Δ Experimental results without core

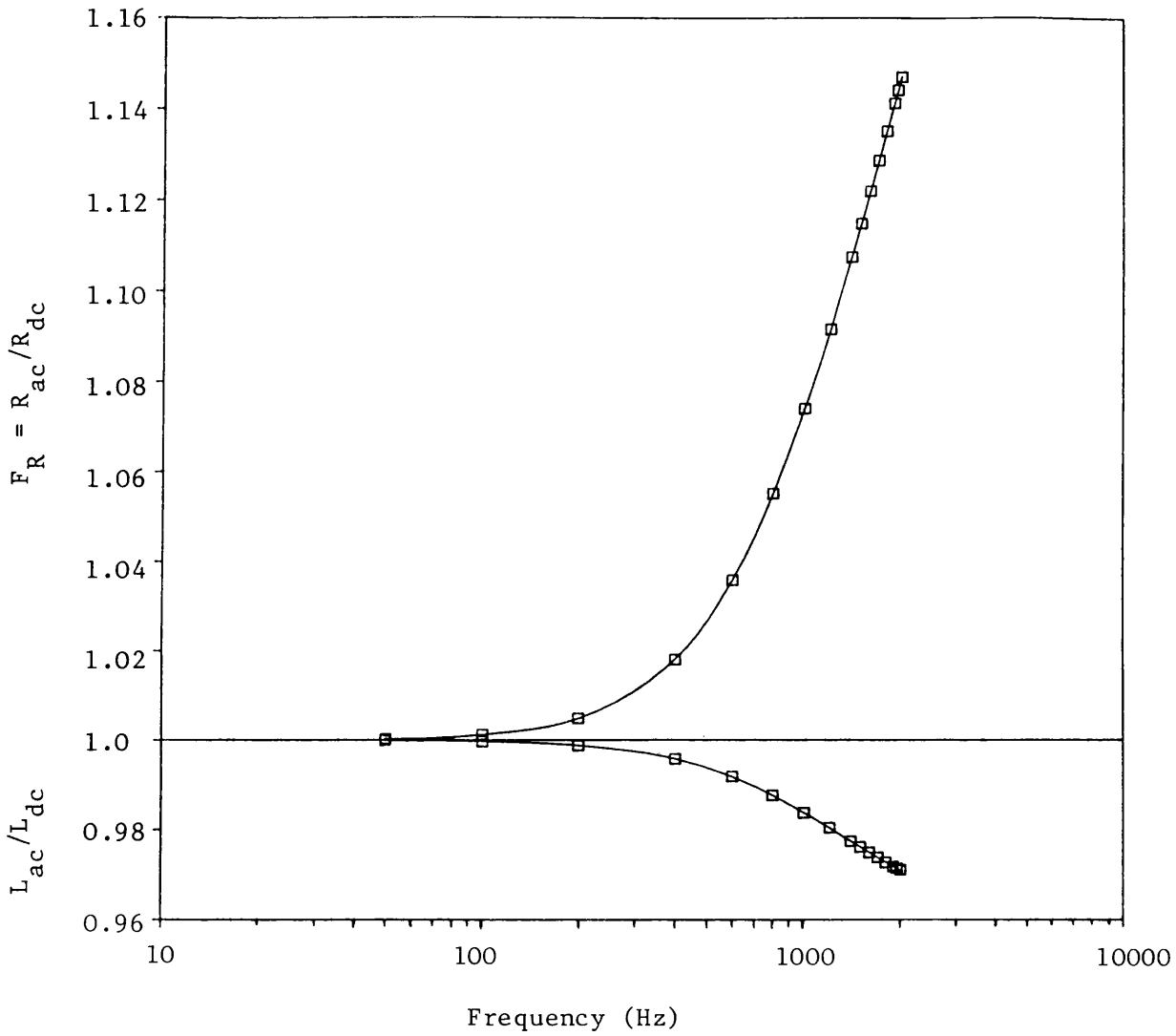

Fig.3.6: Frequency dependence of resistance and inductance for a single foil turn

——— Murgatroyd results

□ □ □ Computed results

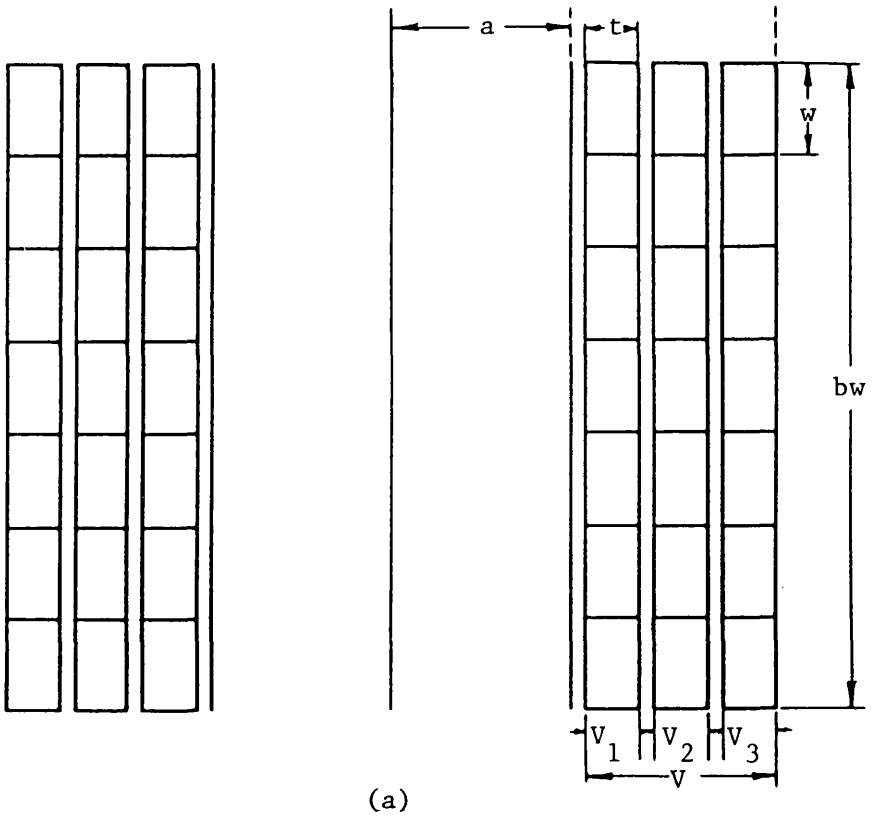

Fig.3.7: Coil and mathematical model

(a) coil
(b) mathematical model

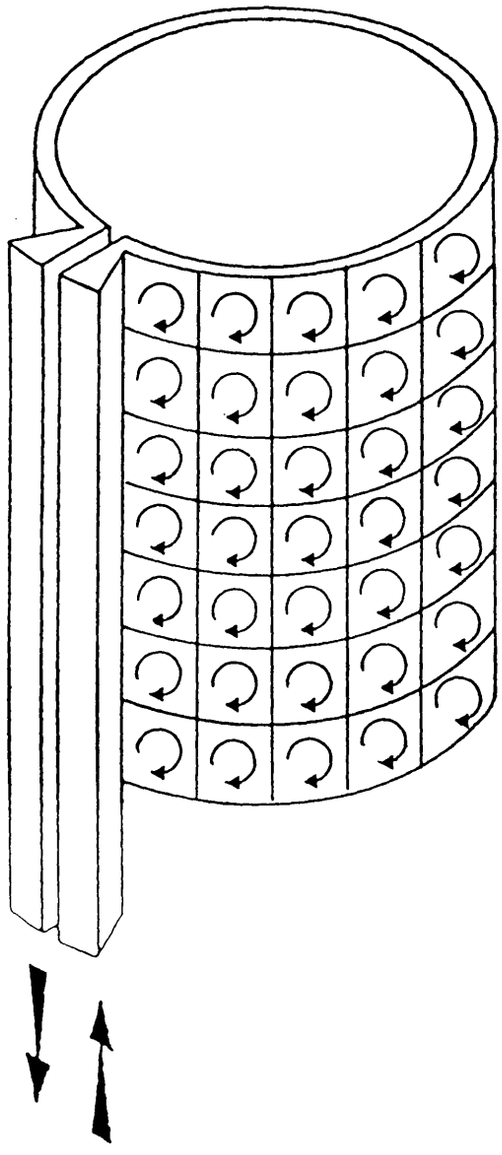

Fig.3.8: Equivalent circuit of subdivided filaments
(Fishing net)

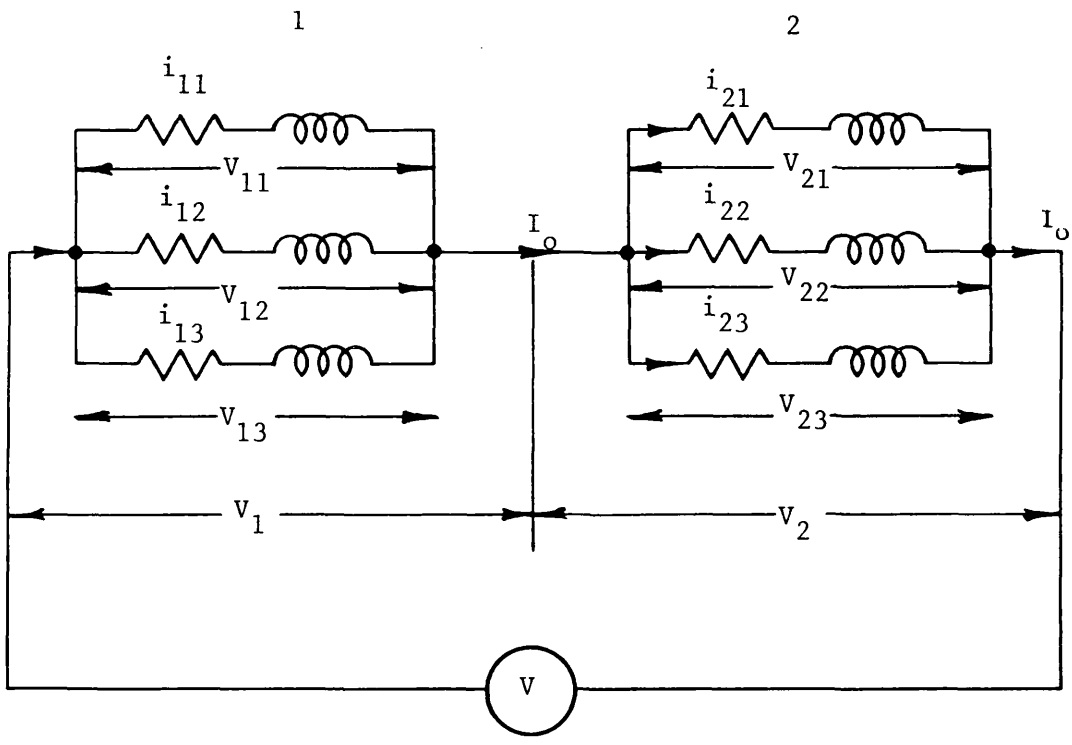

Fig.3.9: Equivalent circuit of multilayer model with 2 layers and 3 filaments

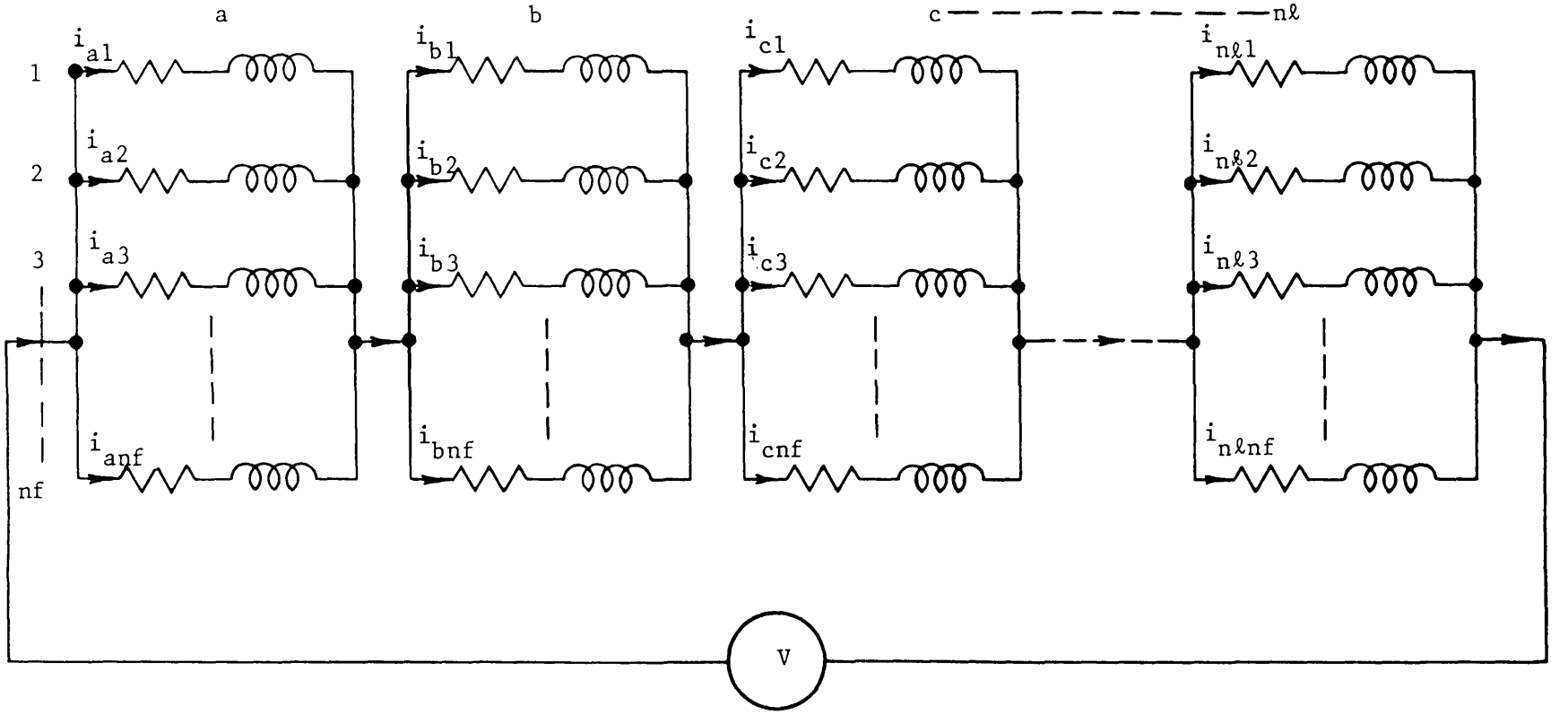

Fig.3.10: Equivalent circuit of multilayer model with nℓ layers and nf filaments

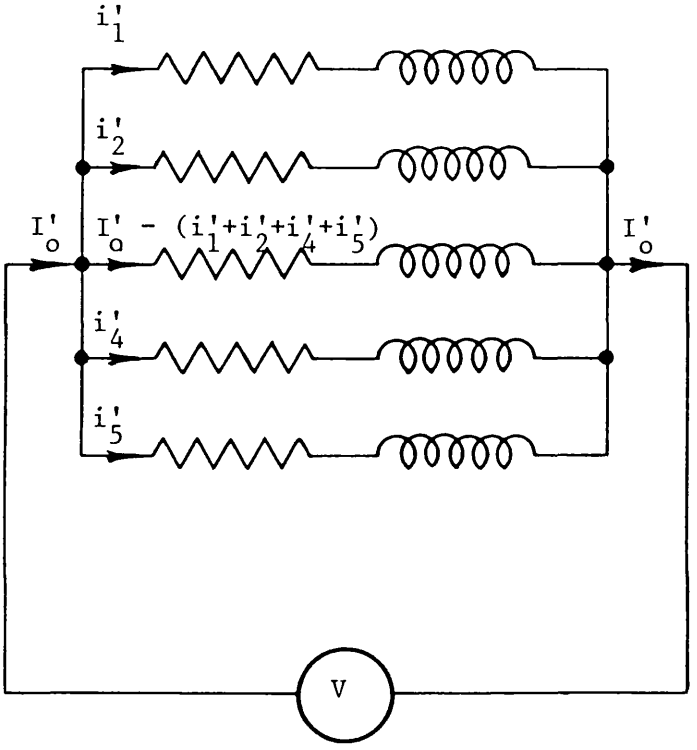

Fig.3.11: Single layer with presentation of the new current

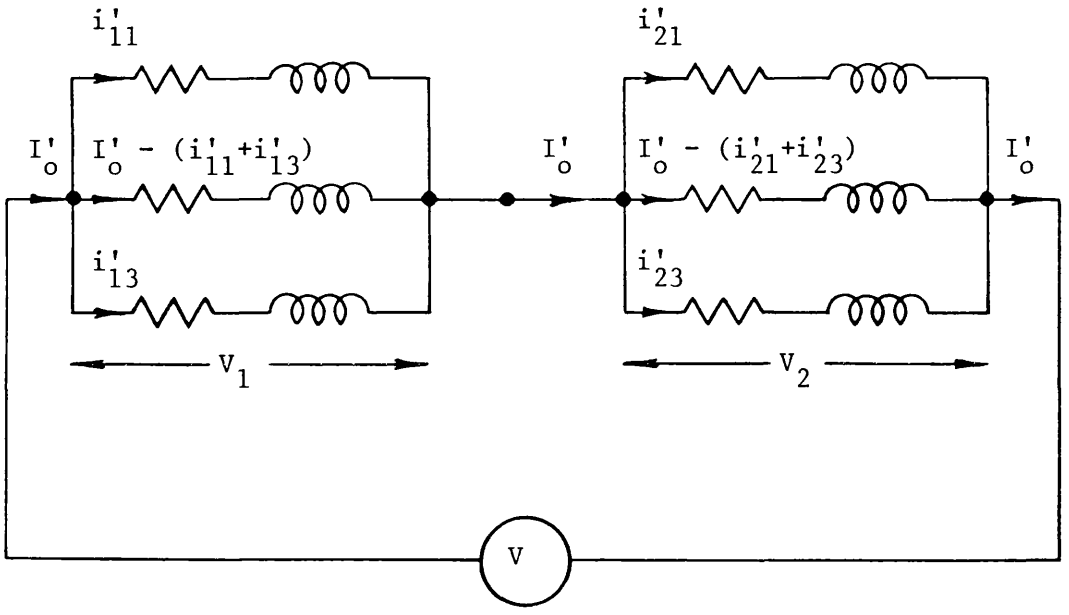

Fig.3.12: Two layer and three filament with presentation of the new current

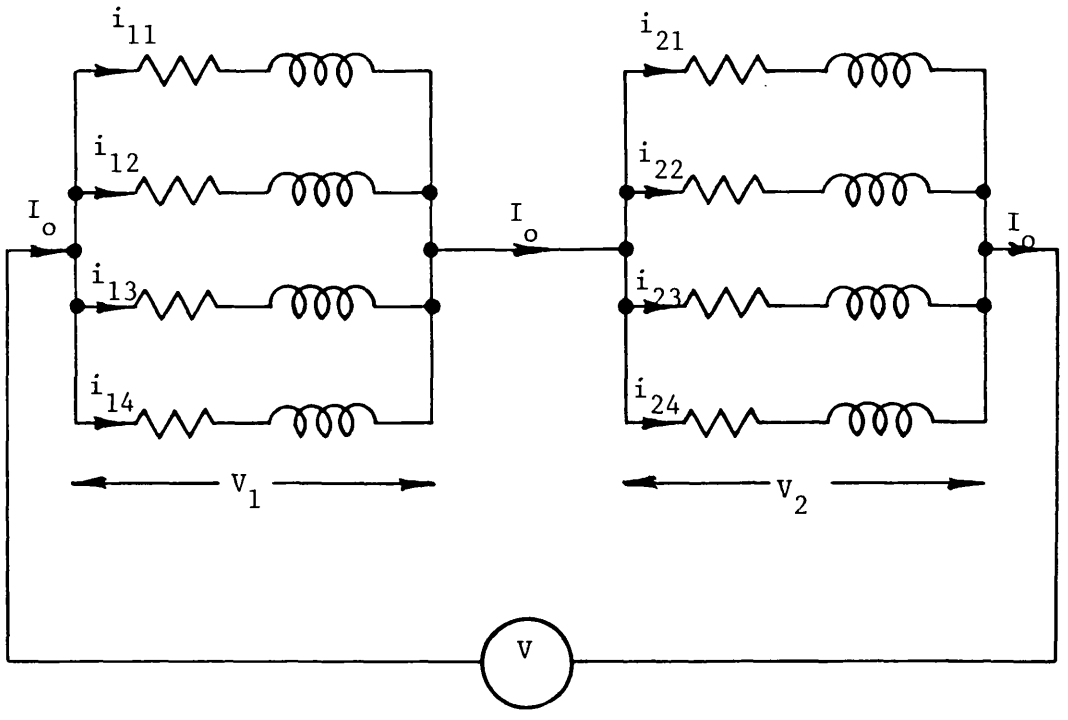

Fig.3.13: Two layer four filament

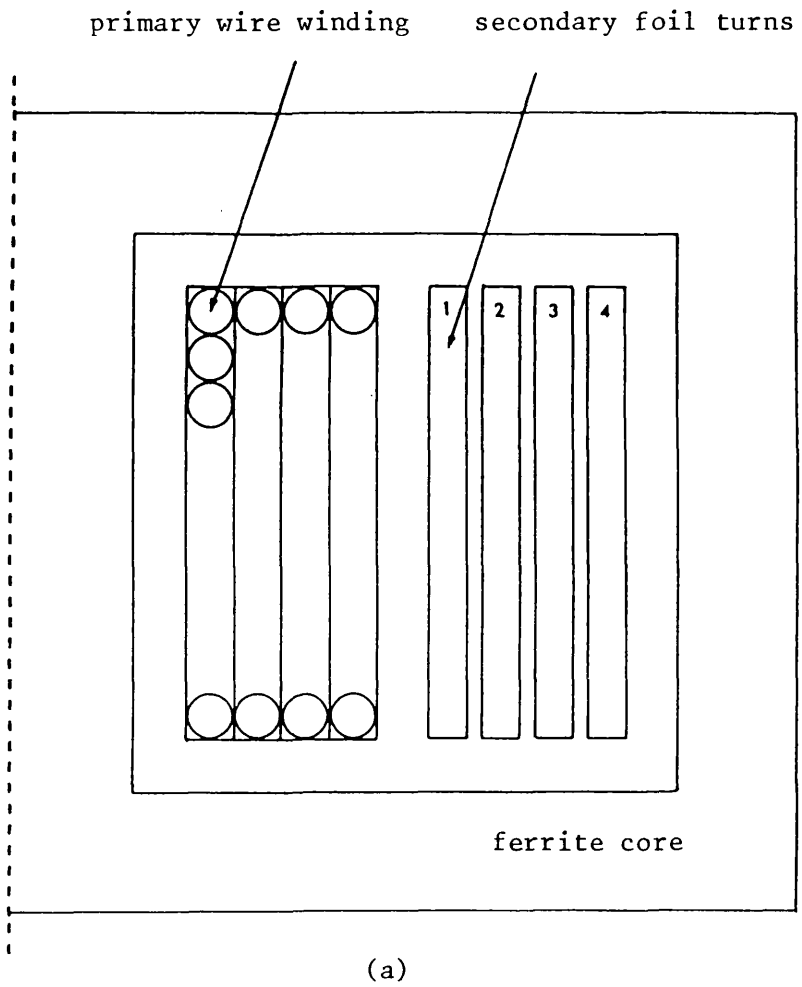

(a)

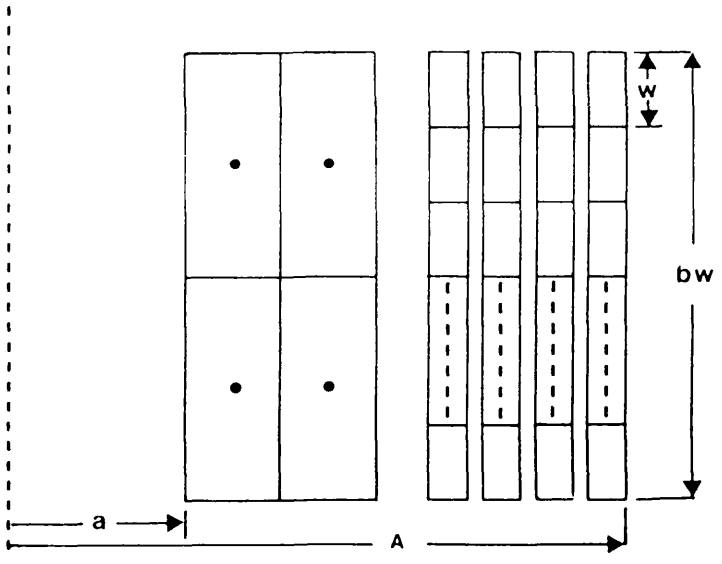

(b)

Fig.3.14: (a) Transformer winding
(b) Transformer model

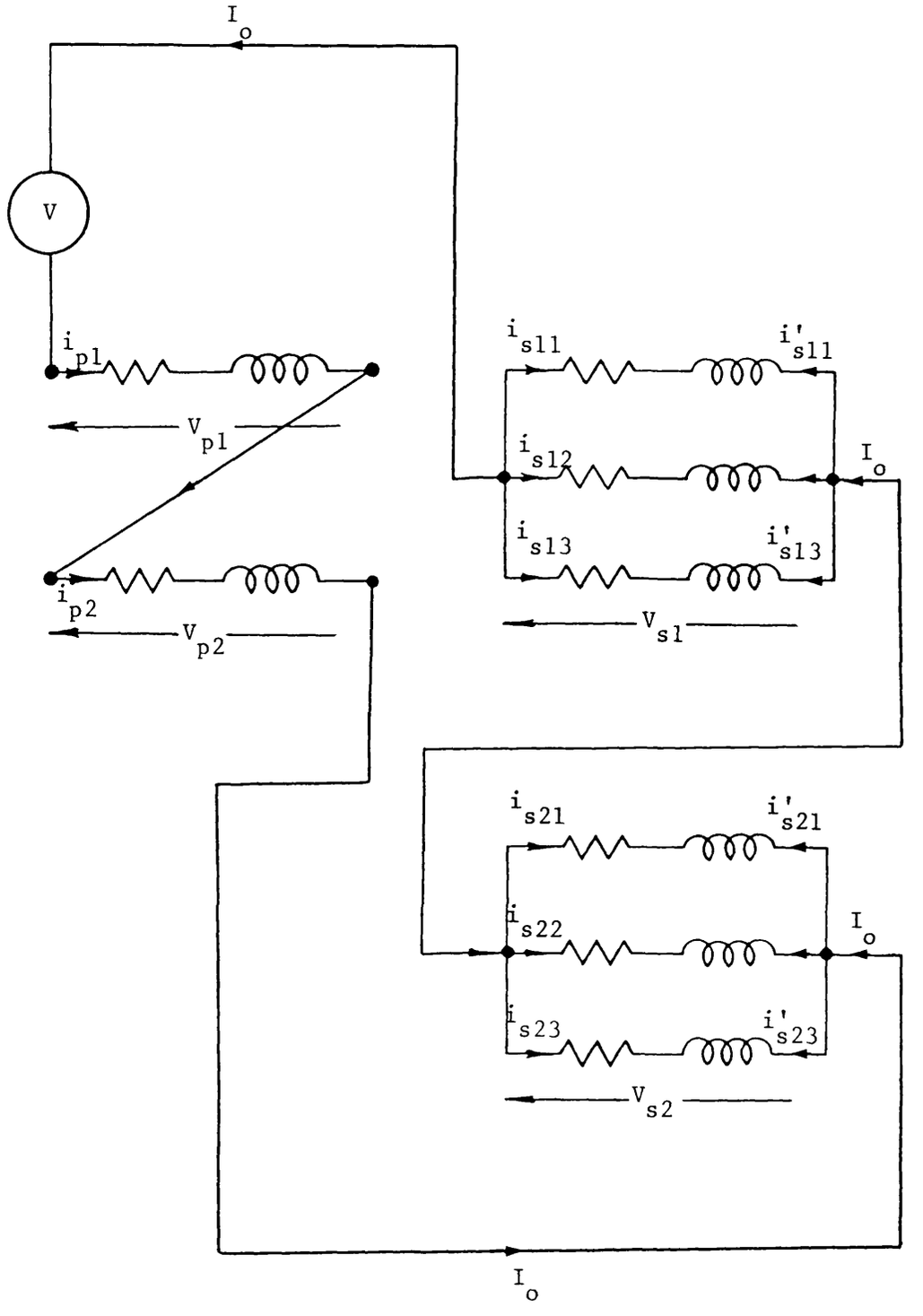

Fig.3.15: Transformer winding connection

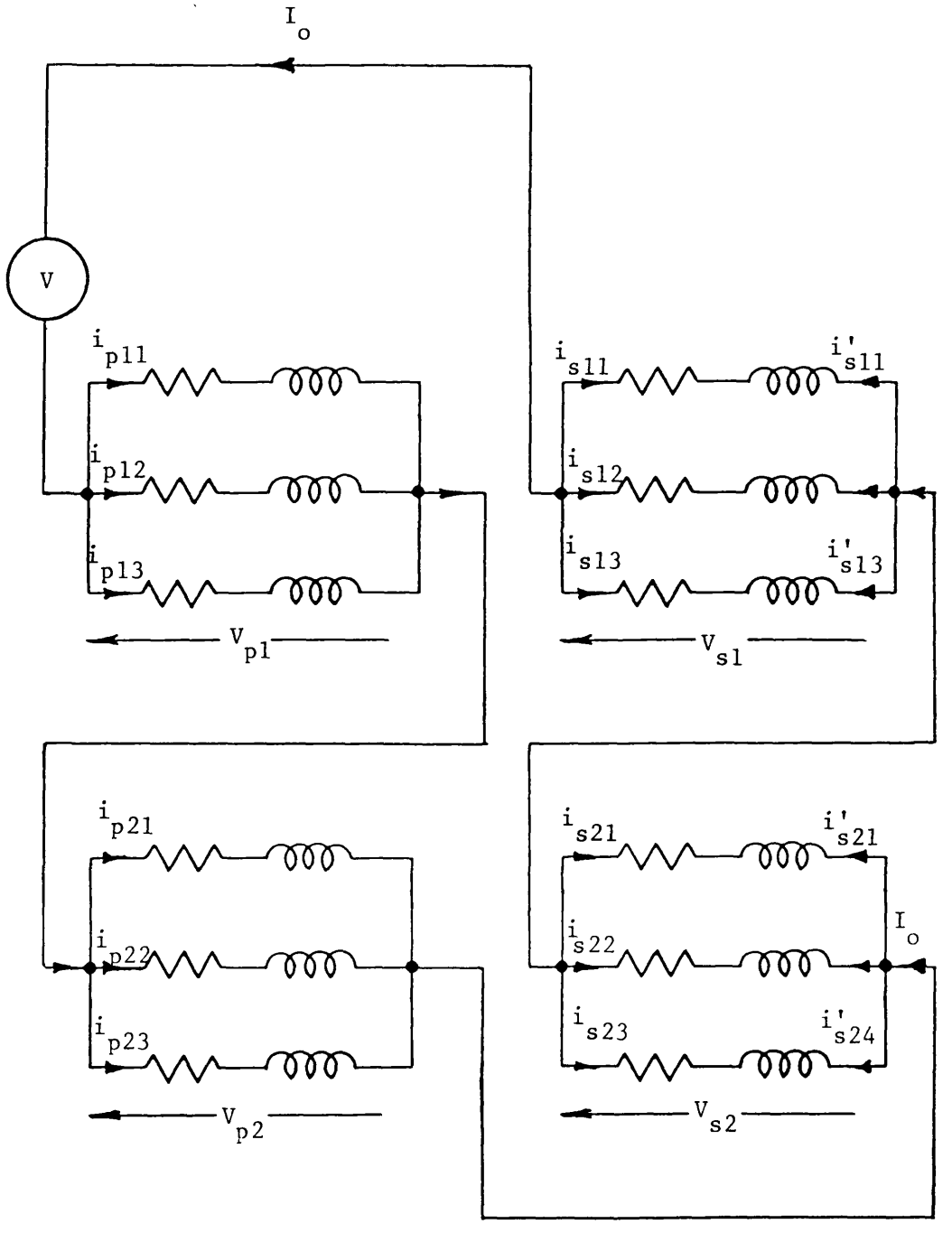

Fig.3.16: Transformer with primary modified

CHAPTER FOUR

INDUCTANCE CALCULATIONS

4.1 Introduction

The previous chapter has formulated the equations for the circuit model which is to be used for analysis of current distribution and losses in foil conductors. The formal method by which these sets of equations may be solved has also been described. The equations were expressed in terms of the self and mutual inductances between the notional filament coils. The problem remains therefore of calculating these inductances so that the equation systems may be used. This is an important part of the work as the quality of the overall results obtained can be no better than the qualities of the parameters used. A number of alternative methods of calculating inductance was therefore examined in order to ensure confidence in the results. The model used consists of circular coaxial coils situated in air and the general problem is therefore to calculate first of all the self-inductance of a circular coil of known dimensions, and secondly to calculate the mutual inductance between two such coils coaxially placed. These geometries are sketched in Figure 4.1. The problems of calculating these inductances were more severe than might be expected and the alternative approaches that were examined are described and discussed below.

4.2 Mutual Inductance

A number of alternative methods of calculating the mutual inductances were derived around the beginning of this century, Maxwell[1], Nagaoka[2], Jones[3], Olshausen[4], Cohen[5], Rosa[6],

Dwight[7], Lyle[8] and Grover[9].

The methods are described briefly below.

4.2.1 Analytical methods for filament coils

Maxwell has derived a formula which is applied only to circular filaments of negligible cross section. This method is described briefly below.

For two circuit elements, the mutual inductance is given, according to the Neumann[10] formula by

$$M = \frac{\mu_o}{4\pi} \iint \frac{\cos \epsilon}{r} \, ds \, ds' \qquad 4.1$$

The double integrations are performed about the two circuits (1) and (2) with ds and ds' representing the differential elements, where ϵ is the angle between the element ds and ds', and (r) the distance between the two. In general it is not possible to perform these integrations.

Figure 4.2 shows the particular problem of the two coaxial circles of the radii (a) and (A) and the distance between the element ds and the projection of ds' on to the plane of circle (1) is given by

$$r_{12} = \sqrt{a^2 + A^2 - 2aA \cos(\theta - \theta')}$$

Therefore the distance (r) between the ds and the ds' follows directly.

$$r = \sqrt{d^2 + r_{12}^2} = \sqrt{a^2 + A^2 + d^2 - 2aA \cos(\theta - \theta')}$$

where

$$\epsilon = \theta - \theta'$$

$$ds = a d\theta$$

$$ds' = A d\theta'$$

Therefore

$$M = \frac{\mu_o}{4\pi} \int_0^{2\pi} \int_0^{2\pi} \frac{aA \cos(\theta - \theta') \, d\theta d\theta'}{\sqrt{a^2 + A^2 + d^2 - 2aA \cos(\theta - \theta')}}$$

By substituting $\theta = \pi - 2\phi$ and

$$k^2 = \frac{4aA}{d^2 + (a + A)^2}$$

The integral then will be found to become[10]

$$M = \mu_o \sqrt{aA} \, k \int_0^{\pi/2} \frac{(2 \sin^2 \phi - 1) d\phi}{\sqrt{1 - k^2 \sin^2 \phi}} \qquad 4.2$$

This equation can be solved by digital computer directly, using "NAG FORTRAN MARK 10 LIBRARY" Subroutine 'D02PAF', on the Multics (Honeywell) system[11]. Alternatively equation 4.2 can be broken into two integrals:

$$M = \mu_o \sqrt{aA} \left[\left[\frac{2}{k} - k \right] \int_0^{\pi/2} \frac{d\phi}{\sqrt{1 - k^2 \sin^2 \phi}} - \frac{2}{k} \int_0^{\pi/2} \sqrt{1 - k^2 \sin^2 \phi} \, d\phi \right]$$

$$= \mu_o \sqrt{aA} \left[\left[\frac{2}{k} - k \right] K(k) - \frac{2}{k} E(k) \right] \qquad 4.3$$

where

$$K(k) = \int_0^{\pi/2} \frac{d\phi}{\sqrt{1 - k^2 \sin^2 \phi}} \qquad 4.4$$

$$E(k) = \int_0^{\pi/2} \sqrt{1 - k^2 \sin^2 \phi} \, d\phi \qquad 4.5$$

The definite integrals (4.4) and (4.5) are tabulated in tables[12] as functions of k and are called complete elliptic integrals of the first and second kinds respectively. Thus

$$M = \mu_o \sqrt{d^2 + (a + A)^2} \left[\left(1 - \frac{k^2}{2}\right) K(k) - E(k) \right] \qquad 4.6$$

where

a = smaller radius

A = larger radius

K(k) = complete elliptic integral of first kind

E(k) = complete elliptic integral of second kind and

$$k = 2 \sqrt{\frac{aA}{d^2 + (a + A)^2}}$$

and d is the distance between the planes of the filaments.

Assuming that the equation 4.6 is to be solved by computer, numerical calculation of elliptic integrals by the technique suggested by Bulirsch[13] was found to be most satisfactory. Both approaches (i.e. using 'NAG' subroutine and numerical technique) were attempted and the latter method was found to be considerably faster than the former methods but under the same conditions identical results were obtained by both methods.

A further method of solution was suggested by Rosa and Cohen[14] who extended Maxwell's Series solution method as described below.

The Maxwell's Series formula is well known for the mutual inductance between two circles, whose radii (a) and (A), and distance apart is (d). The formula gives the mutual inductance when the coils or filaments are near each other.

$$M = \mu_o a \left[\log_e \frac{8a}{r} \left(1 + \frac{c}{2a} + \frac{c^2 + 3d^2}{16a^2} - \frac{c^3 + 3cd^2}{32a^3} + \ldots\right) - \left(2 + \frac{c}{2a} - \frac{3c^2 - d^2}{16a^2} + \frac{c^3 - 6cd^2}{48a^3}\right)\right] \qquad 4.7$$

where

$$c = A - a$$

$$r = \sqrt{d^2 + c^2}$$

r is the least distance from one circle to the other, as shown in Figure 4.3. Rosa and Cohen expanding the terms of equation 4.3 in series and substituting these series in equation 4.3. The integral K(k) and E(k) can be calculated directly, without using elliptic integrals, expanding K(k) and E(k) in terms of complementary modules (k'), where

$$k' = \sqrt{1 - k^2}$$

The expressions for K(k) and E(k) are

$$K(k) = \log_e \frac{4}{k'} + \frac{1}{2^2} k'^2 \left(\log_e \frac{4}{k'} - 1\right) + \ldots$$

$$E(k) = 1 + \frac{1}{2}\left[\log_e \frac{4}{k'} - \frac{1}{2}\right] k'^2 + \ldots$$

Therefore the mutual inductance becomes

$$M = \mu_o a \left[\left(\log_e \frac{8a}{r}\left(1 + \frac{c}{2a} + \frac{3d^2 + c^2}{16a^2} - \frac{3d^2c + c^3}{32a^3} - \frac{15d^4 - 42d^2c^2 - 17c^4}{1024\,a^4} + \frac{45d^4c - 30d^2c^3 - 19c^5}{2048\,a^5} + \ldots\right) - \left(2 + \frac{c}{2d} + \frac{d^3 - 3c^2}{16a^2} - \frac{6d^3c - c^3}{48a^3} - \frac{93d^4 - 534d^2c^2 - 19c^4}{6144a^4} + \frac{1845d^4c - 3030d^2c^3 - 379c^5}{61440a^5} + \ldots\right)\right] \qquad 4.8$$

4.2.2 Tabulated results for inductance

The book by Grover [9] is well known and presents equations for inductance calculations together with tabulated parameters which allow the equations to be used to calculate inductance. For the problem under consideration, the method is presented in chapter 11 of Grover[9] and is described briefly below.

The circular filaments are shown in Figure 4.4, they have radii (a) and (A), where (A) is the larger radius, and the distance between their planes is denoted by (d). Grover presents tables which when used in conjunction with a single formula give the mutual inductance. The mutual inductance depends in this method upon the normalised parameters a/A and d/A, while for pairs of circles having the same parameter values, the mutual inductance is proportional to the corresponding radius.

$$M = f\sqrt{aA} = fA\sqrt{\frac{a}{A}} \quad \mu H \qquad 4.9$$

where f, in this case, is a function of variable k'^2. The values of f are given against k'^2 in tabular form, where

$$k'^2 = \frac{(A-a)^2 + d^2}{(A+a)^2 + d^2} = \frac{\left[1 - \frac{a}{A}\right]^2 + \frac{d^2}{A^2}}{\left[1 + \frac{a}{A}\right]^2 + \frac{d^2}{A^2}}$$

For circular filament coils which are very close together and very far apart, there are Auxiliary Tables to find the value of (f). For circles of equal radii (a), the tabulation of (f) made conveniently with respect to the parameter.

If a = A then f, in this case, is a function of

$$\delta = \frac{\text{distance}}{\text{diameter}} = \frac{d}{2a} \quad \text{or} \quad \Delta = \frac{\text{diameter}}{\text{distance}} = \frac{2a}{d}$$

and it given by Grover in a tabular form.

From equation 4.9

$$M = fa \quad \mu H \qquad 4.10$$

The tables make clear how rapidly the mutual inductance increases as the distance between circles is decreased. Therefore it is highly important to critically examine and compare the previous methods, and to ascertain which are most accurate and convenient to solve the problems.

4.2.3 Computed results

The methods of calculating the mutual inductances of circular coaxial filaments were discussed in previous sections, therefore in this section preliminary theoretical results are presented to ensure confidence in the methods. The computations were carried out using the three methods at different conditions as described below.

i) Computed results of mutual inductance between circular filaments of equal radius as the separation between them increases. The computed results are plotted in Figures 4.5 and 4.6. It is clear from the figures that the mutual inductances decrease as the distance increases in an expected fashion. Good agreement is obtained from Maxwell's method (i.e. analytical method) and Grover's method (i.e. tabulated method) over the whole range, but the series solution is clearly unreliable at large distances, d.

ii) Computed results of mutual inductances between circular filaments with different radii as the separation between them increases. Figures 4.7 and 4.8 show the computed results at different radii as indicated in each figure. There is clearly now some disparity between all three methods. The Series Solution method again shows the unreliability of large values of d where mutual inductances are predicted by it to increase.

The other two methods (analytical method and tabulated method) agree in general trend, but there is some difference in actual values.

Bearing in mind that the Grover's method results rely upon tabulated and interpolated factors, it is thought that the Maxwell, the analytical, method is the more reliable. This was confirmed by comparing it with measurements as shown in section 4.2.5 below.

4.2.4 Mutual inductance of coaxial circular coils of finite cross section

The methods of calculating mutual inductance considered above have all assumed filament coils of zero cross sectional area. It seems possible that improvements in terms of computing time might be achieved by using filament coils of finite cross sectional area - assuming of course uniform current density over the area - so that a reduced number of filaments could be considered, without any reduction in precision.

The first step in examining this therefore was taken by considering mutual inductance between filament coils of zero

thickness but finite length as presented by Grover[9] in Chapter 15, and as illustrated in Figure 4.9 which also shows the parameters used in the calculation.

The method suggested by Grover[9] is described below.

The mutual inductance of coaxial circular coils has been found by Nakaoka[2], Olshausen[4] and Cohen[5]. These formulas involve elliptic integral of four integrations, each of which depends upon one of the four axial distances between the end planes of one of the coils and those of the other. These distances are:

$$x_1 = d + \frac{p + s}{2} \quad , \quad x_3 = d - \left[\frac{p - s}{2}\right]$$

$$x_2 = d + \frac{p - s}{2} \quad , \quad x_4 = d - \left[\frac{p + s}{2}\right]$$

The general formula is given below, used in conjunction with tables, it is based on one given by Clem[15]. The four corresponding diagonals r_n are calculated by the relations

$$r_1 = \sqrt{A^2 + x_1^2} \qquad r_3 = \sqrt{A^2 + x_3^2}$$

$$r_2 = \sqrt{A^2 + x_2^2} \qquad r_4 = \sqrt{A^2 + x_4^2}$$

And the mutual inductance of the coaxial coils is given by the general formula

$$M = \frac{2\pi^2 a^2 n_1 n_2}{10^9} \left[r_1B_1 - r_2B_2 - r_3B_3 + r_4B_4\right] \qquad 4.11$$

where

a = smaller radius of a coil

A = larger radius of A coil

n_1 = winding density of a coil

n_2 = winding density of A coil

s = length of a coil

p = length of A coil

In the case of concentric coils d = 0, and since only the numerical values of the x_n are required, $X_4 = X_1 = (p + s)/2$ and $X_3 = X_2 = |(p - s)/2|$, so that for this special case,

$$M = \frac{4\pi^2 a^2 n_1 n_2}{10^9} (r_1 B_1 - r_2 B_2) \qquad 4.12$$

The quantities B_n are functions of the radii and the spacing of the coils and tables of these are provided by Grover. Two parameters are required for their specification i.e.

$$\alpha = \frac{a}{A} \quad \text{and} \quad \rho_n^2 = \frac{A^2}{r_n^2}$$

each of which must lie always between the limits zero and unity. To use the tables a double interpolation is, in general, necessary. Mutual inductance calculated by this method was compared with calculations by the earlier method for filament coils. Figures 4.10 and 4.11 present the computed results from both methods under conditions as indicated in the figures. Results from the present method were found to be erratic and this was thought to be a problem of interpolation from the tables. A successful method of improving the interpolation was not found. When these erratic results were in fact employed to calculate current distribution in foil wound

inductors, they produced erratic current densities. They were consequently not pursued any further, and the analytical method of Maxwell (section 4.2.1) already discussed above was used for all subsequent calculation.

4.2.5 Comparison between experimental and computed results

As discussed in previous sections, the most accurate method to calculate the mutual inductances of two coaxial filament coils of any size at any distance was thought to be the formula in elliptic integrals given by Maxwell (i.e. equation 4.3). Therefore the mutual inductance was calculated according to this method and the results are compared with those obtained experimentally to ensure confidence in the results.

The measurement of the mutual inductances was carried out at high frequency and different diameters of the coil were used, the method is described below. The coils were constructed on a nylon former such that one would be moved with respect to the other to give repeatable settings. The nylon former is sketched in Figure 4.12. The coil was immersed in oil to maintain constant temperature, and connected to the digital storage oscilloscope (Nicolet, Explorer II, Type 2090 II). This was connected via an IEEE bus to the microcomputer (Commodore CBM Model 8032) to calculate the mutual inductance at various settings of the moving coil.

There are two sets of results obtained. First, the mutual inductance between the circular filaments of equal radius as shown in Figure 4.13 and 4.14, secondly, the mutual inductance between the circular filaments with different radii as shown in Figures 4.15,

4.16 and 4.17. Also shown on these figures are the computed results. It can be seen that they are generally close to measurements and confirm the validity of the computed method. This method, i.e. analytical method, was therefore used for all subsequent calculations.

4.3 Calculation of Self-inductance

Two alternative methods of calculating the self-inductance are discussed and described briefly below.

4.3.1 Nagaoka's formula and tables

Nagaoka[14] has derived formulas and tables by which the self-inductance of a circular filament may be calculated. Nagaoka's formula is

$$L = \mu_o \pi a^2 N^2 K$$

or in the form

$$L = \frac{\mu_o}{2} \pi a \left[\frac{2a}{b}\right] N^2 K \qquad 4.13$$

where

a = mean radius

b = axial length

N = number of turns

And (K) is the factor that takes account of the effect of ends. Nagaoka gave tables of value of (K) as a function of the shape ratio 2a/b = diameter/length or as a function of b/2a. The tables are reproduced by Grover[9] in Chapter 16. In the case, however, when it becomes necessary to obtain a more accurate value of (K) than can be

obtained from these tables, or in a portion where the function is changing so rapidly as to make interpolation difficult, the following series may be used to calculate (K) directly.

$$K = \frac{2\beta}{\pi}\left[\left[\log_e \frac{4}{\beta} - \frac{1}{2}\right] + \frac{\beta^2}{8}\left[\log_e \frac{4}{\beta} + \frac{1}{2}\right] - \frac{\beta^4}{64}\left[\log_e \frac{4}{\beta} - \frac{2}{3}\right] + \frac{5}{1024}\beta^6\left[\log_e \frac{4}{\beta} - \frac{109}{120}\right]\ldots\right] \qquad 4.14$$

where

$$\beta = \frac{b}{2a}$$

For very small values of β, such as encountered in the present work, this series may be truncated after the first term. Consequently

$$K = \frac{2\beta}{\pi}\left[\log_e \frac{4}{\beta} - \frac{1}{2}\right]$$

$$= \frac{2}{\pi}\frac{b}{2a}\left[\log_e \frac{8a}{b} - \frac{1}{2}\right]$$

and substituting this into equation 4.13 gives

$$L = \mu_o a N^2 \left[\log_e \frac{8a}{b} - \frac{1}{2}\right] \qquad 4.15$$

4.3.2 Self-inductance in terms of elliptic integrals

Lorenz[16] gave an exact formula for the self-inductance in terms of complete elliptic integrals of the first and second kind. Also Coffin[16] derived an expression for self-inductance which is equivalent to Lorenz's formula.

This formula is:

$$L = \frac{32}{3} \frac{\pi^2 N^2 a^2}{b^2} \left[\frac{2k^2 - 1}{k^3} E + \frac{1 - k^2}{k^3} K - 1 \right] \qquad 4.16$$

where a is the radius, b the length of the coil and

$$k^2 = \frac{4a^2}{4a^2 + b^2}$$

For the geometries involved in the present work identical results were obtained by equations 4.13, 4.15 and 4.16. For simplicity, and to avoid using the tables or elliptic integrals, equation 4.15 was adopted. Computed results are compared with experimental results in Figures 4.13 and 4.14, and good agreement can be observed. Equation 4.15 was therefore used for all subsequent calculations.

4.4 Conclusions

Reliable calculation of the self and mutual inductances is vital to the coupled circuit model proposed for the present work. Calculation of these parameters is remarkably difficult for circular filament coils in air, where the flux paths are not well defined and numerous methods and simplification of them have been proposed in the past.

Several of these methods have been compared, and theoretical results produced by them have been tested against measurements. A single method each for self and mutual inductance calculations has therefore been found which combines accuracy of prediction over the range of geometries involved with simplicity of computation.

4.5 References

1. Maxwell, J.C.: "A Treatise on Electricity and Magnetism", (Oxford, 1904, 3rd ed.) Pt.II.
2. Nagaoka, H.: "The inductance coefficients of solenoids", J. Coll. Sci. Tokyo, Japan, 27, Art.6 (1909).
3. Jones, J.V.: "Calculation of the coefficient of mutual induction of a circle and a coaxial helix", Proc. Roy. Soc. (London) 63, 192 (1898).
4. Olshausen, G.R.: "Absolute formula for the mutual inductance of coaxial solenoids", Phys. Rev. 31, 617 (1910), B. of S .Sci. Paper 169, 73.
5. Cohen, L.: "An exact formula for the mutual inductance of coaxial solenoids", Bull. Bur. Stand., 3, p.295, 1907.
6. Rosa, E.B.: "Mutual inductance of coaxial coils", Bull. Bur. Stand., Vol.2, No.3 (1906).
7. Dwight, H.B.: "Some new formulas for reactance coils", J. AIEE (1919).
8. Lyle, T.R.: "On the self inductance of circular coils of rectangular section", Philos. Trans. Roy. Soc., 1913, 213, p.421.
9. Grover, F.W.: "Inductance Calculations", (Van Nostrand, 1947).
10. Ramo, S., Whinnery, J.R.: "Fields and Waves in Modern Radio", 2nd ed., John Wiley & Sons Inc., New York.
11. Numerical Algorithms Group. NAG FORTRAN Library Manual, Mark 10, Vol.2, 1983.
12. Beyer, W.H.: "Standard Mathematical Tables", 25th Ed. CRC Press Inc., 1978.
13. Bulirsch, R.: "Numerical calculations of elliptic integrals and elliptic functions", Numer. Math. 7, 78-90, (1965).

14. Rosa, E.B. and Cohen, L.: "The mutual inductance of two circular coaxial coils of rectangular section", Bull. Bur. Stand., Vol.2, No.3, (1906).

15. Clem, J.: "Mechanical forces in transformers", J. AIEE, Vol.46, p.814, August, (1927).

16. Stratton, S.W.: "Bulletin of the Bureau of Standards, Vol.8, p.118, 1912.

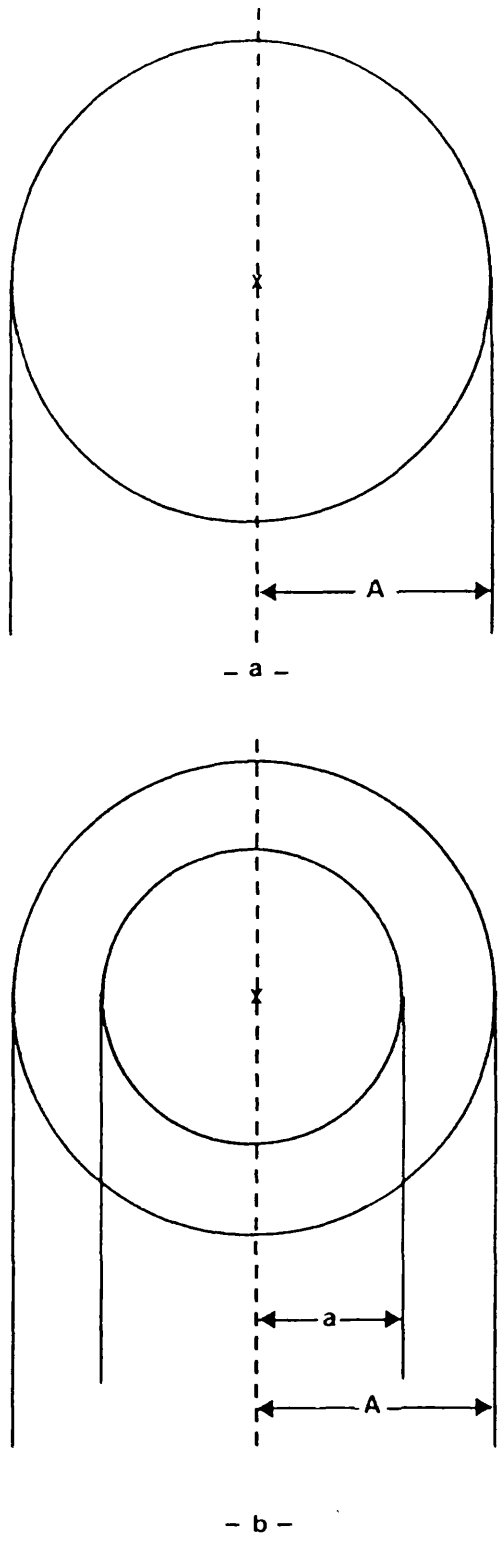

Fig.4.1: (a) Self-inductance of coil in air

(b) Mutual-inductance between two coaxial coils in air

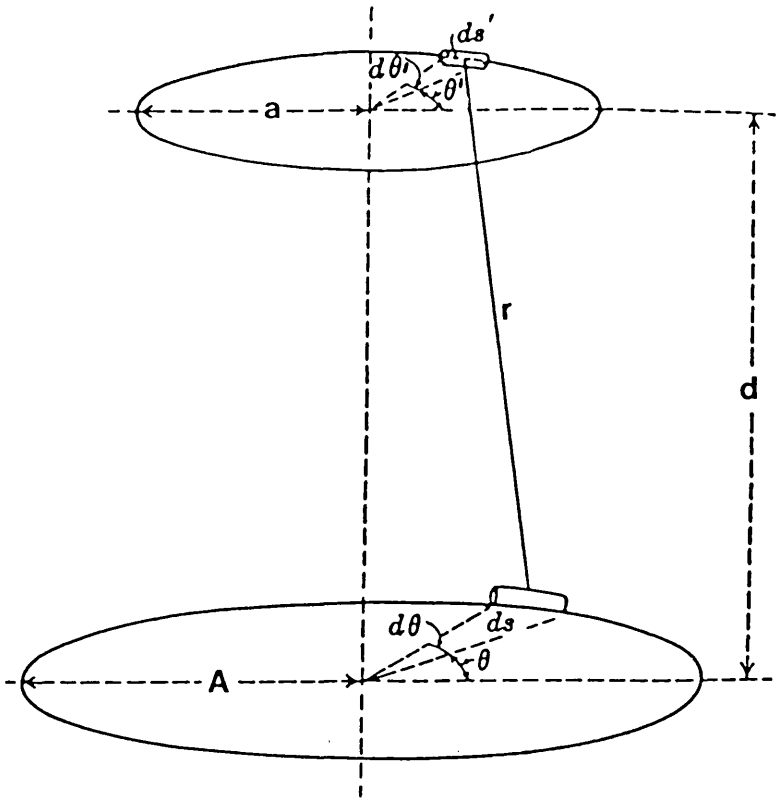

(a)

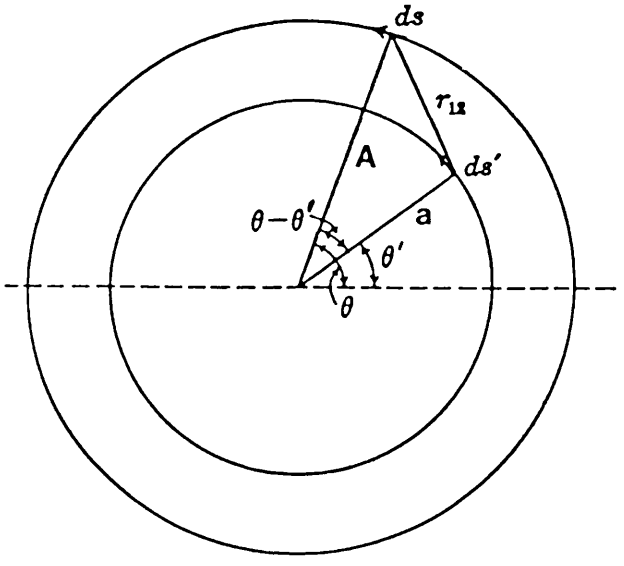

(b)

Fig.4.2: (a) Coaxial circles

(b) Construction for determining r_{12} for coaxial circles

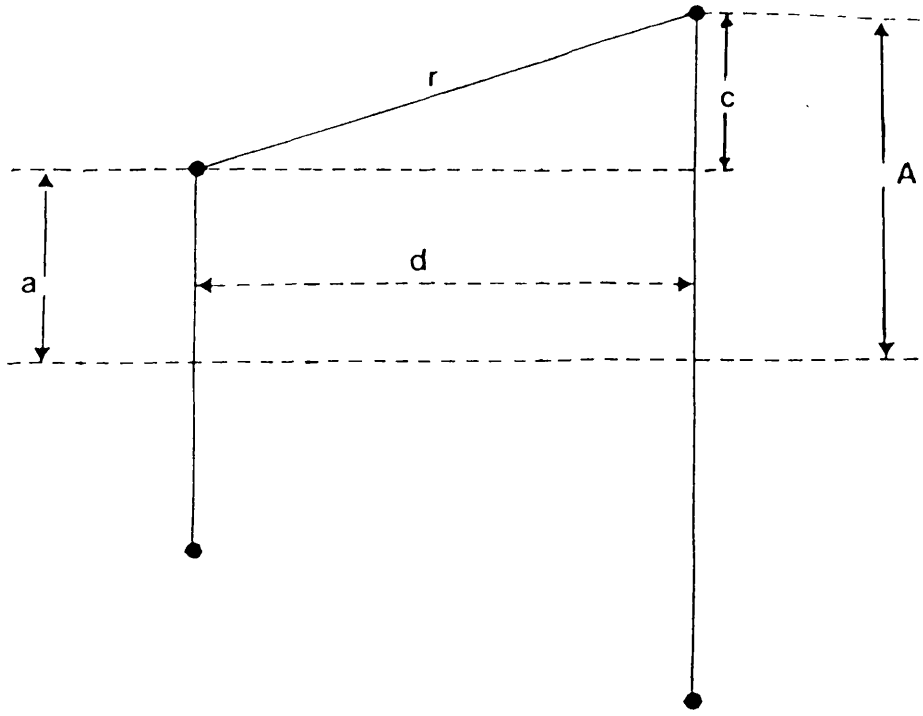

Fig.4.3:

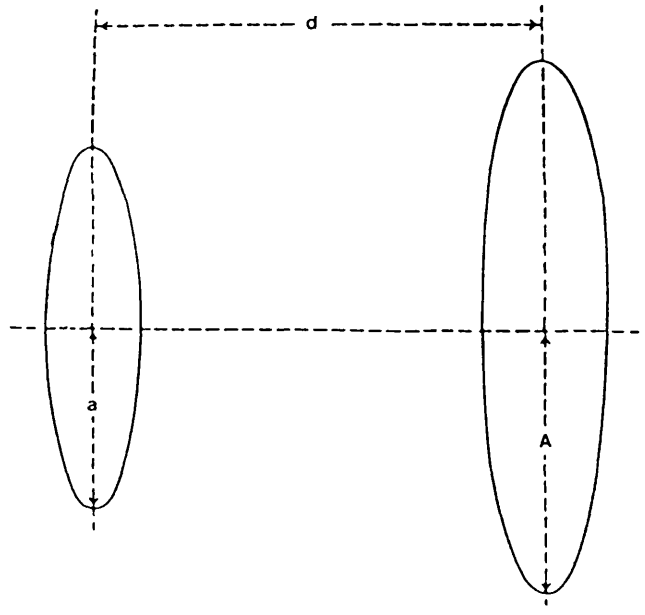

Fig.4.4: Coaxial circular filaments

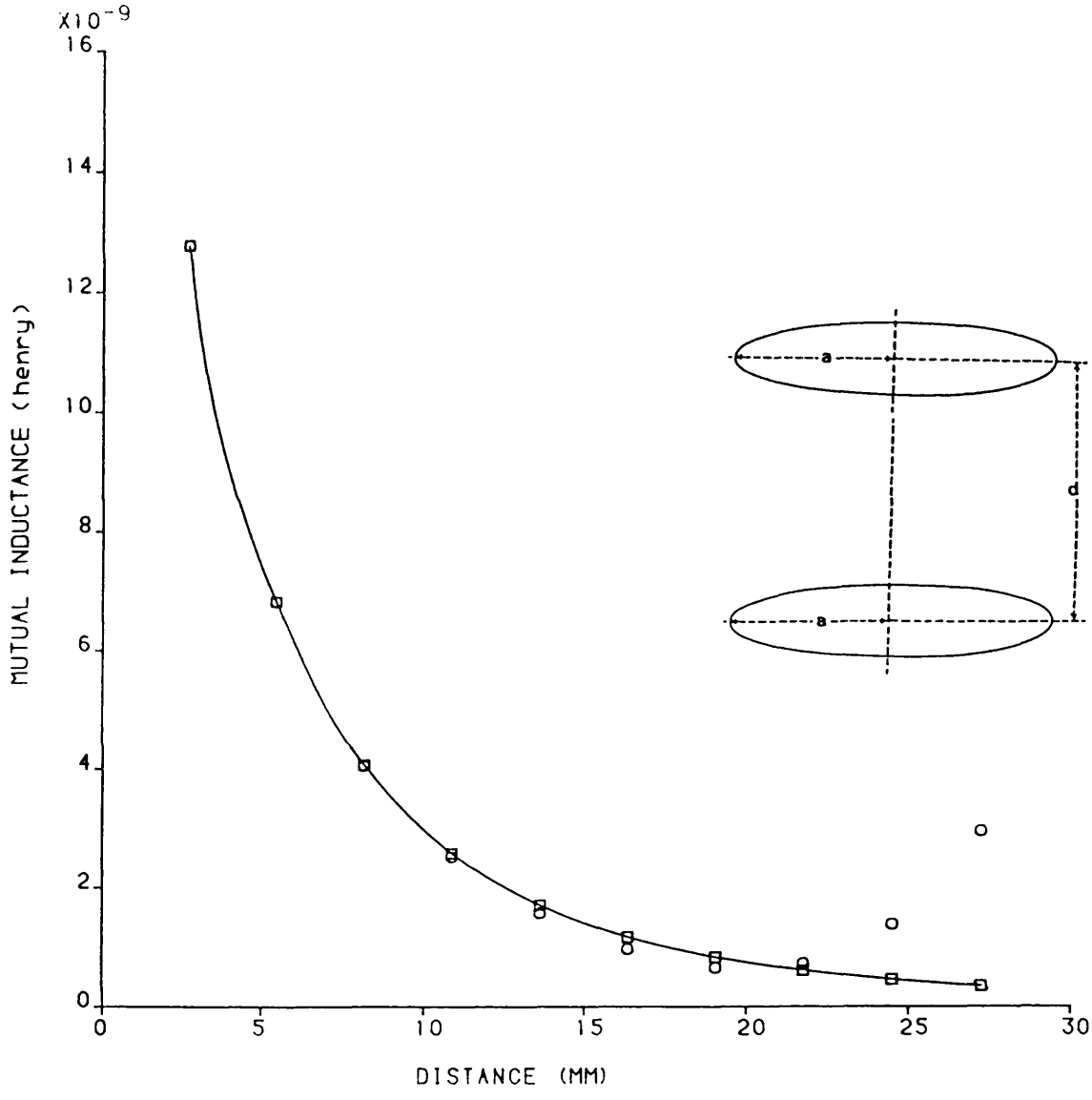

Fig.4.5: Mutual inductance between two circular filament with equal radius
a = 8.2 mm
max.d = 30 mm

——— Analytical method

o o o Series method

□ □ □ Tabulated method

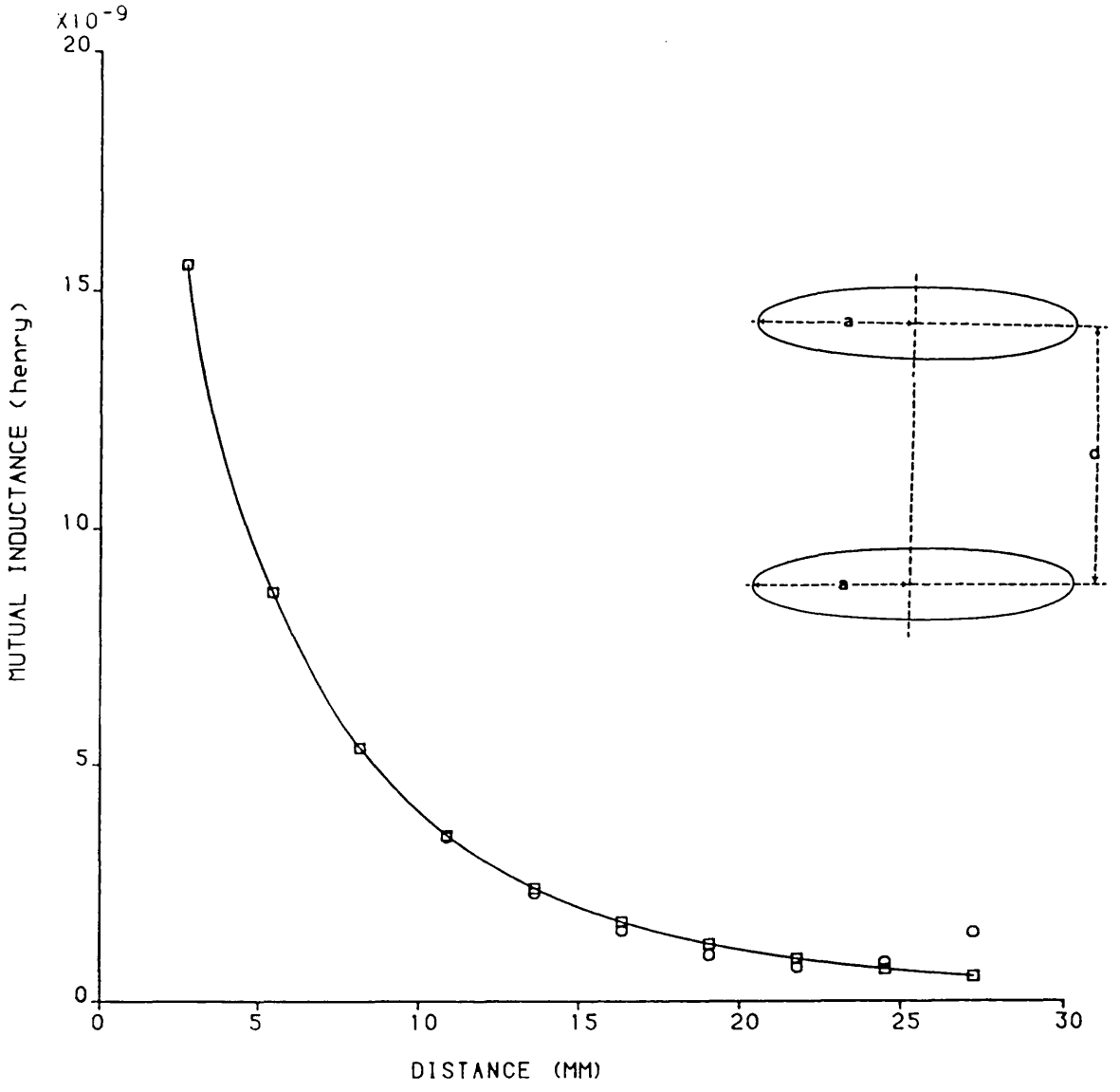

Fig.4.6: Mutual inductance between two circular filament with equal radius

a = 9.2 mm
max. d = 30 mm

——— Analytical method

o o o Series method

□ □ □ Tabulated method

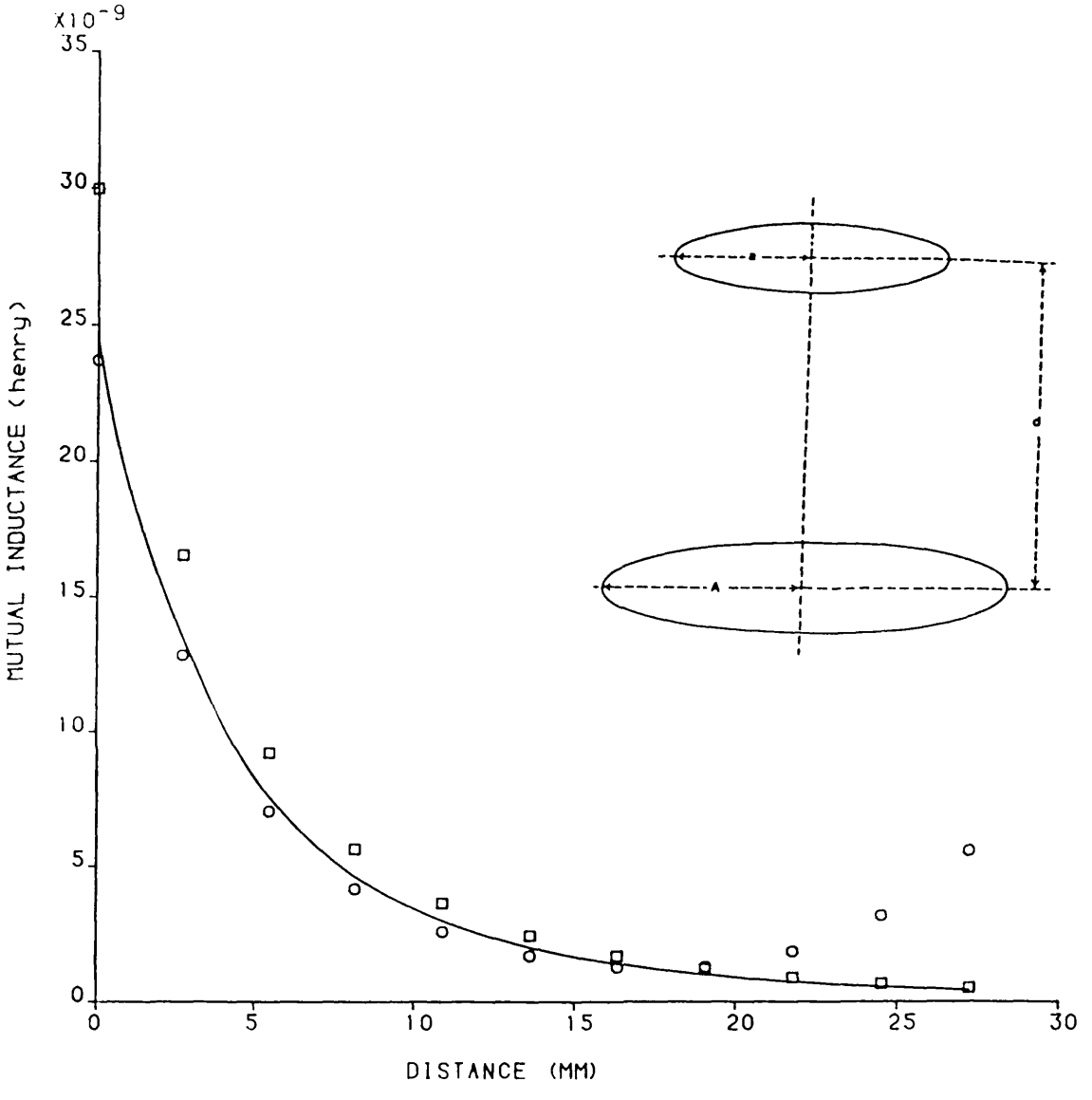

Fig.4.7: Mutual inductance between two coaxial filament

a = 8.2 mm
A = 9.2 mm
max. d = 30 mm

——— Analytical method

o o o Series method

□ □ □ Tabulated method

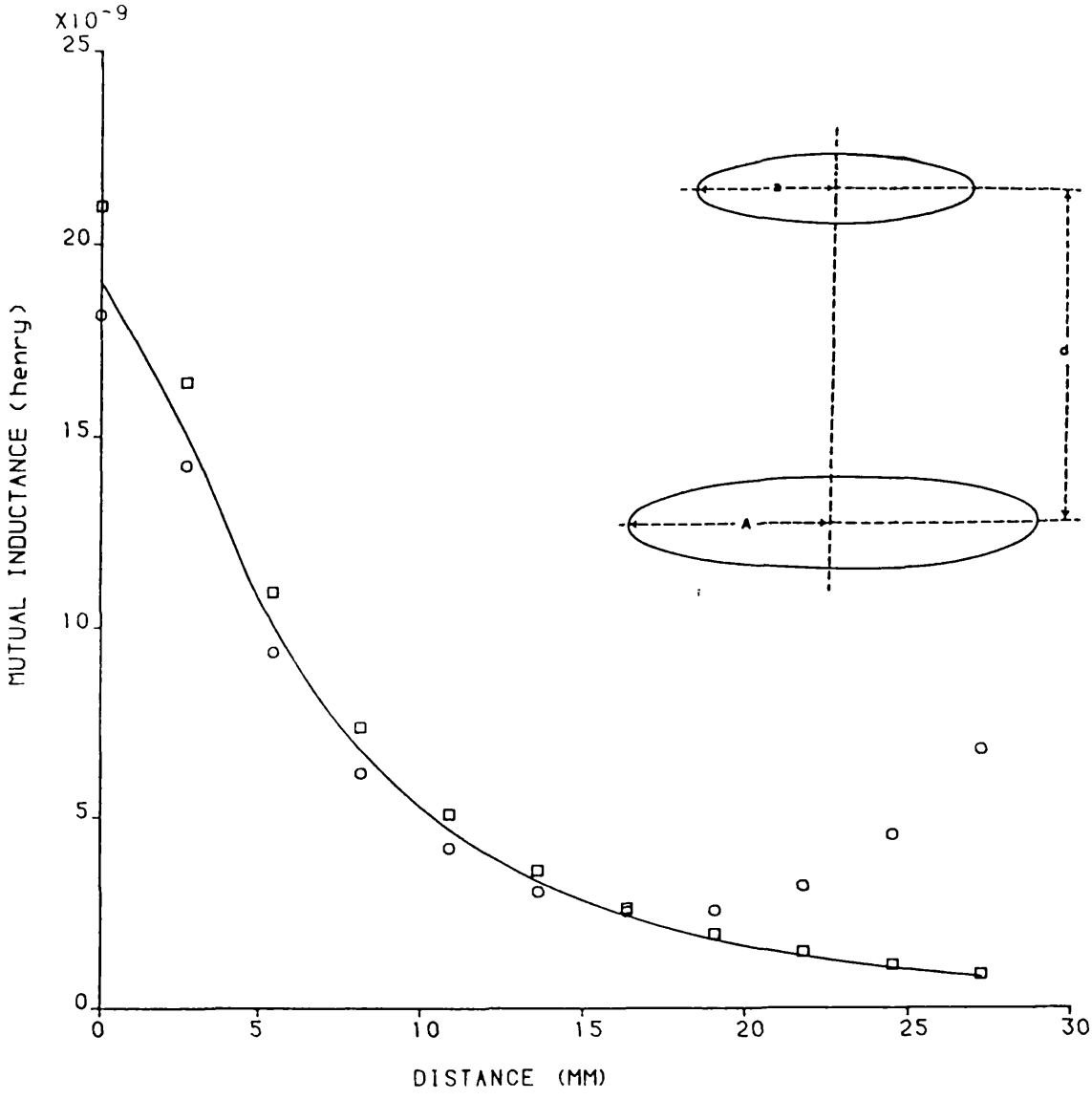

Fig.4.8: Mutual inductance between two coaxial circular filament

a = 9.2 mm
A = 12 mm
max. d = 30 mm

——— Analytical method

o o o Series method

□ □ □ Tabulated method

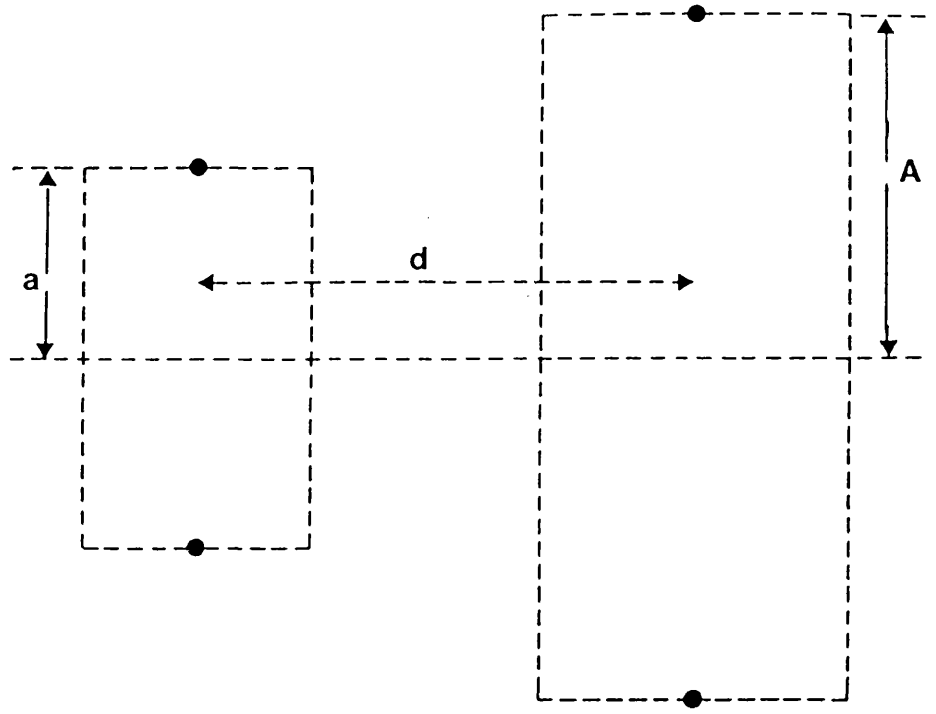

(a)

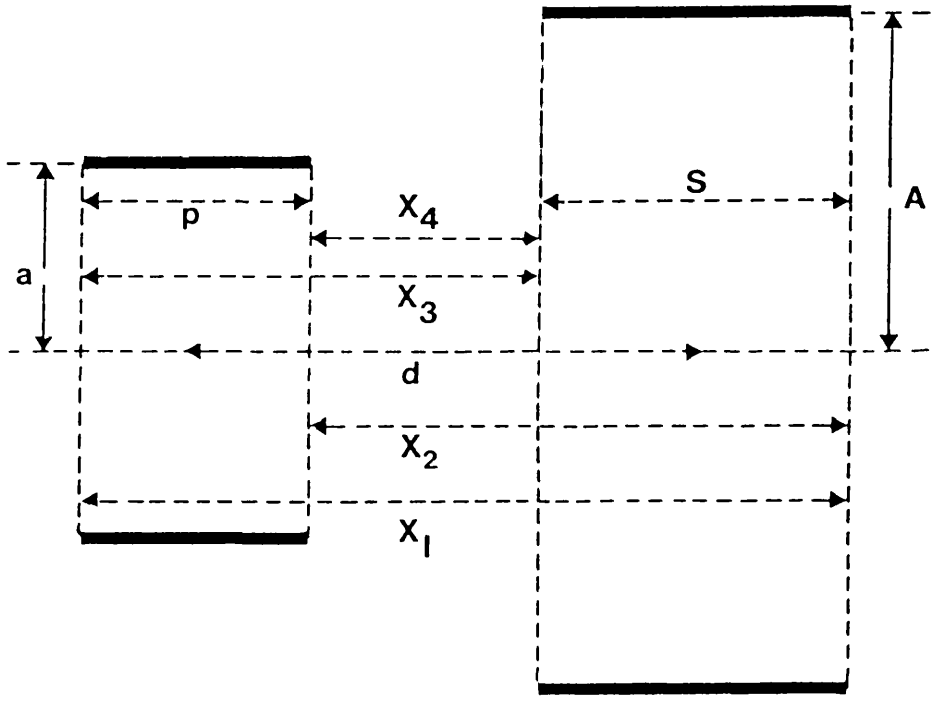

(b)

Fig.4.9: (a) Coaxial circular filament with zero cross section area

(b) Coaxial circular filament with finite length

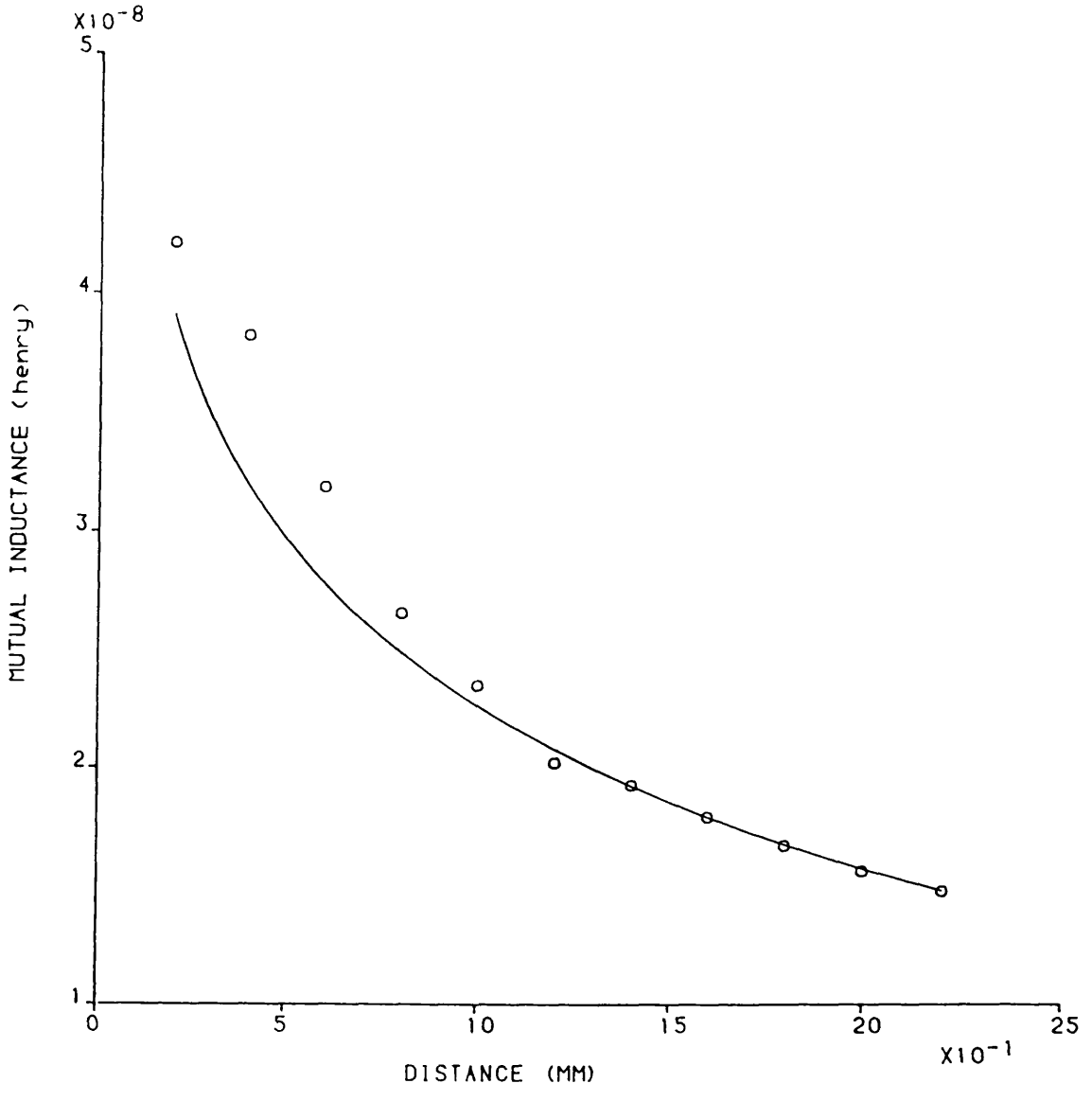

Fig.4.10: Mutual inductance between coaxial circular coils with equal radius and length 0.2 mm

——— Analytical method

o o o Grover method

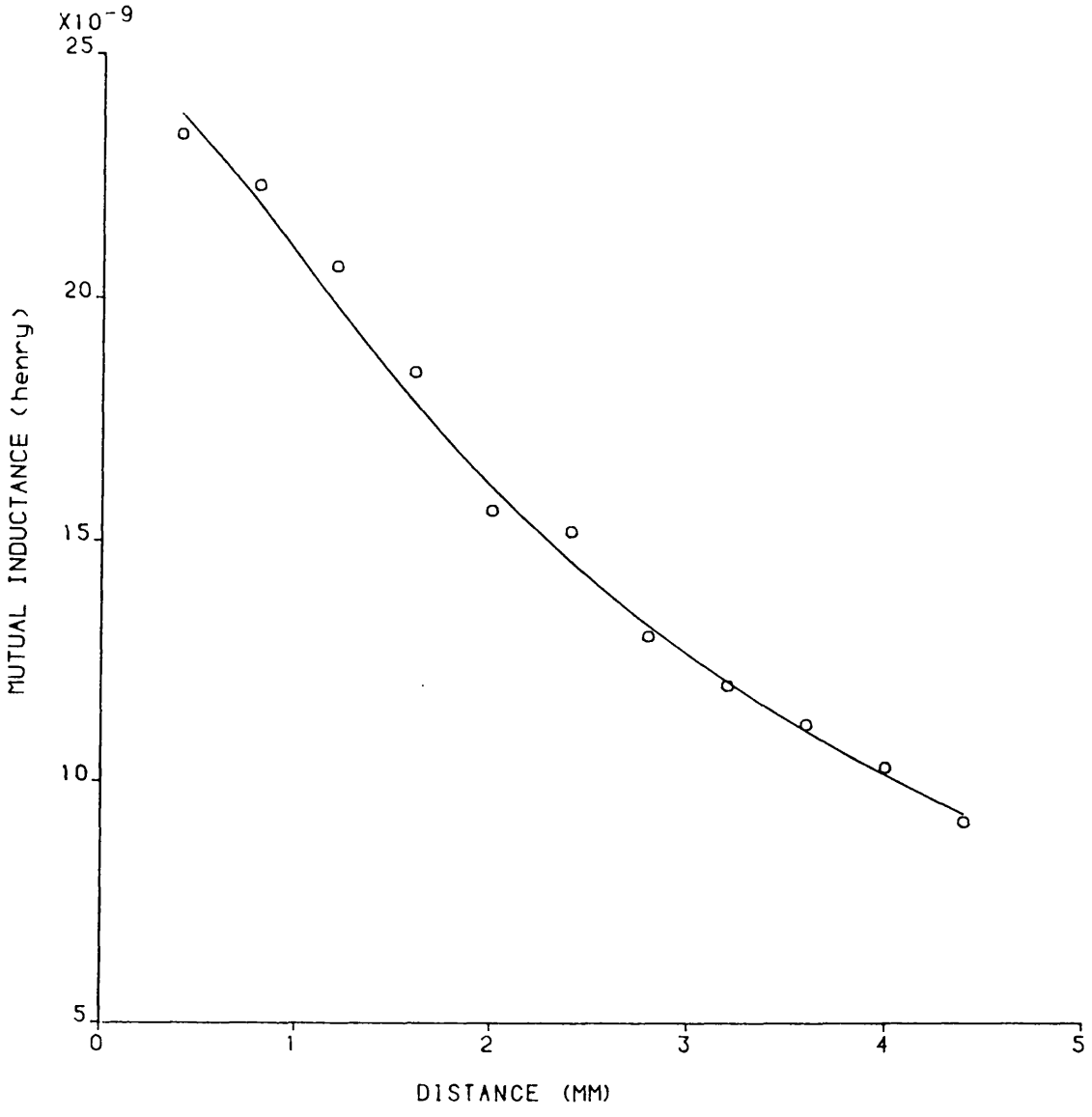

Fig.4.11: Mutual inductance between two coaxial circular coils with different radii and length 0.4 mm

a = 8.2 mm
A = 9.2 mm

——— Analytical method

o o o Grover method

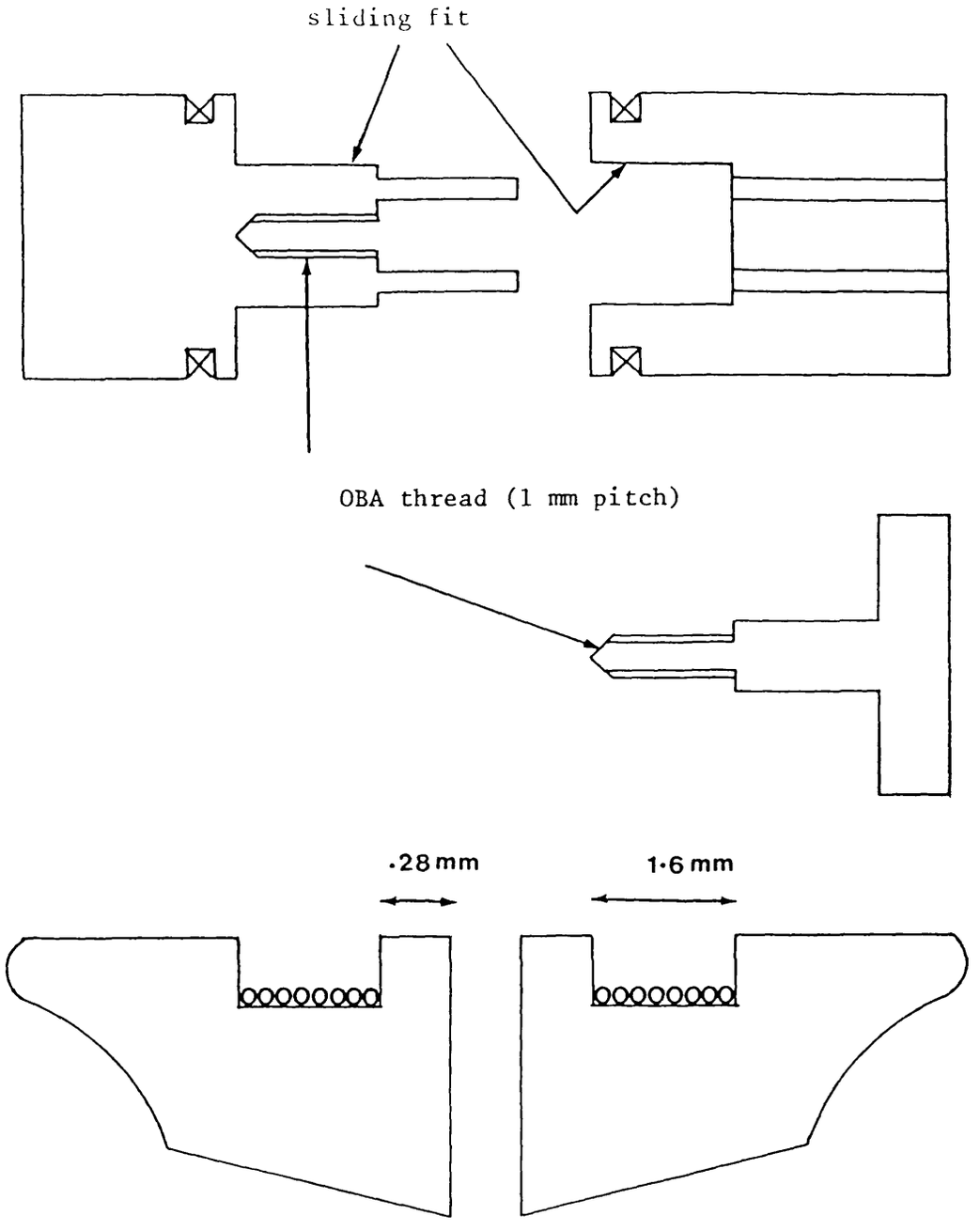

Fig.4.12: Nylon former

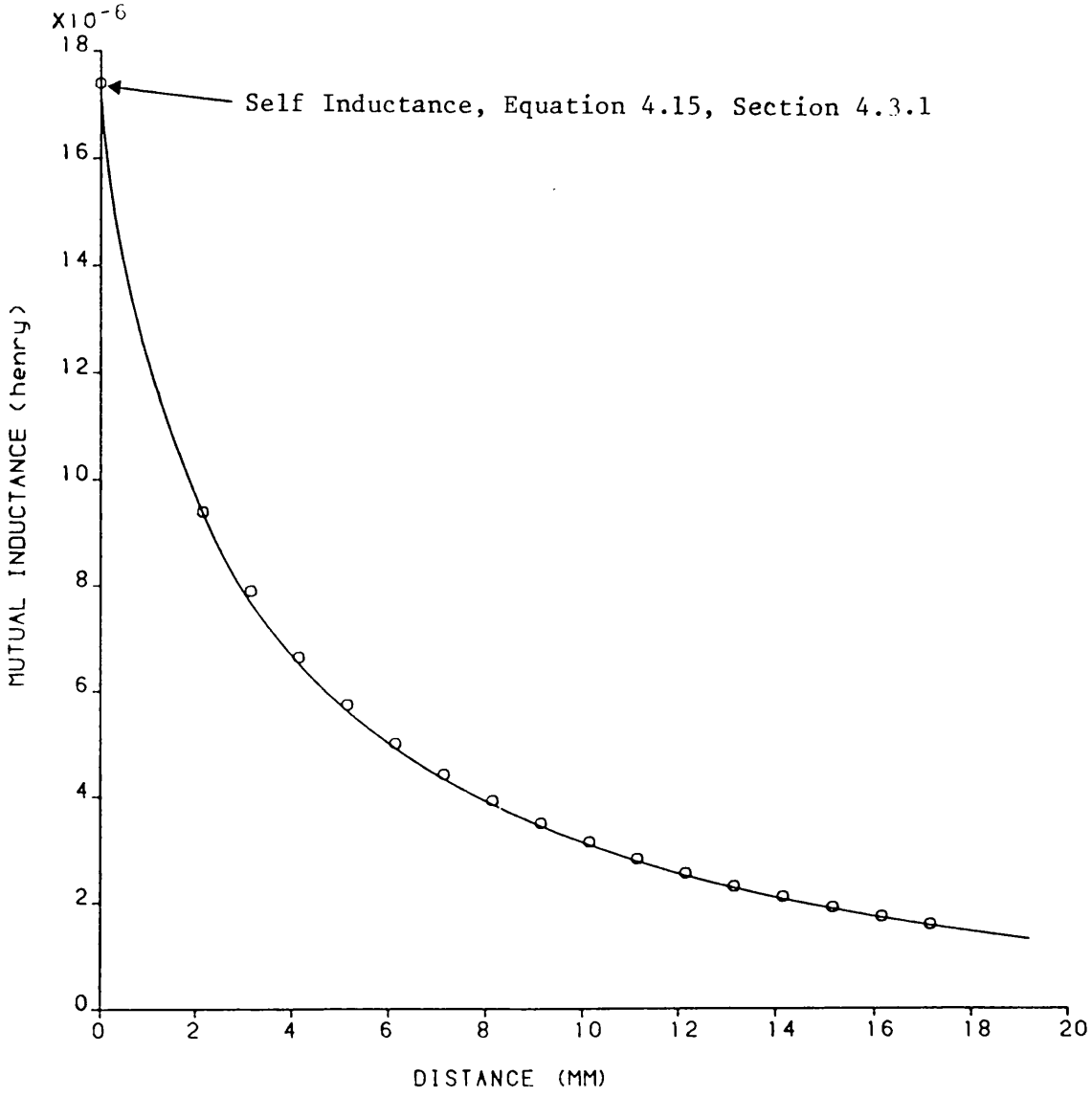

Fig.4.13: Mutual inductance between two circular filament with equal diameter
D = 31.6366 mm

——— Computed results

o o o Experimental results

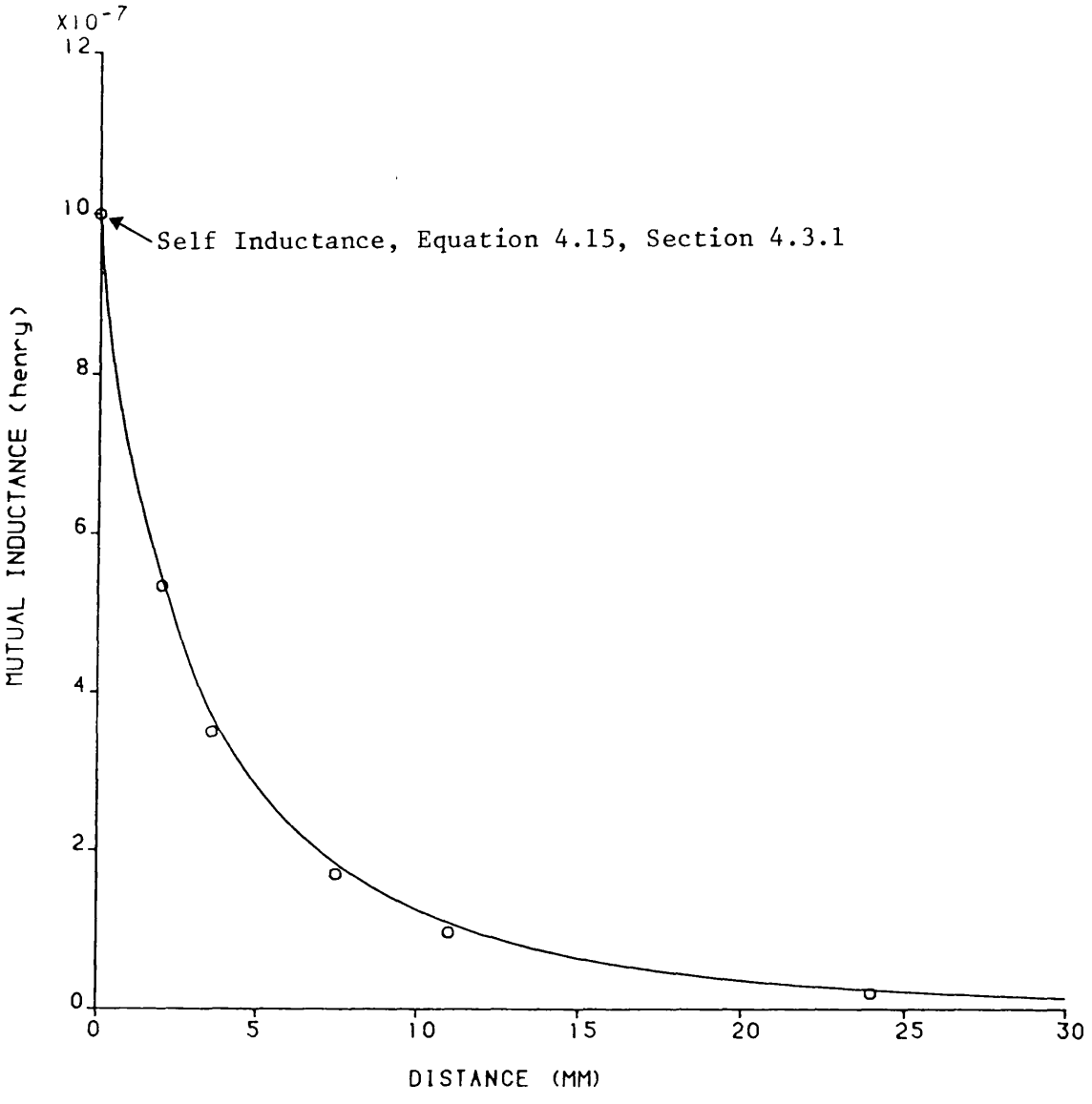

Fig.4.14: Mutual inductance between two circular filament with equal diameter

D = 20.131 mm

——— Computed results

o o o Experimental results

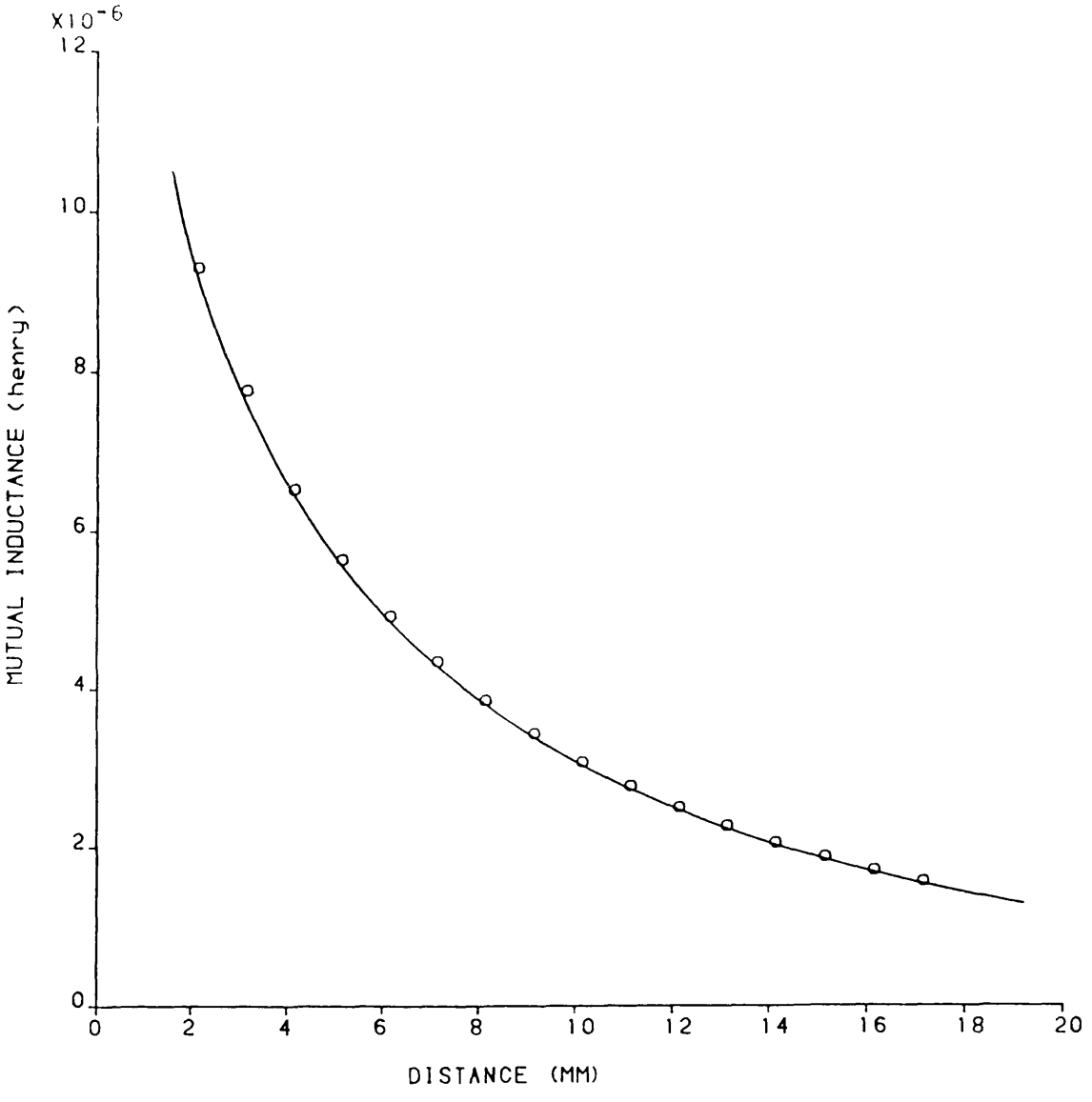

Fig.4.15: Mutual inductance between two coaxial circular filament

D_1 = 30.277 mm

D_2 = 31.6366 mm

——— Computed results

o o o Experimental results

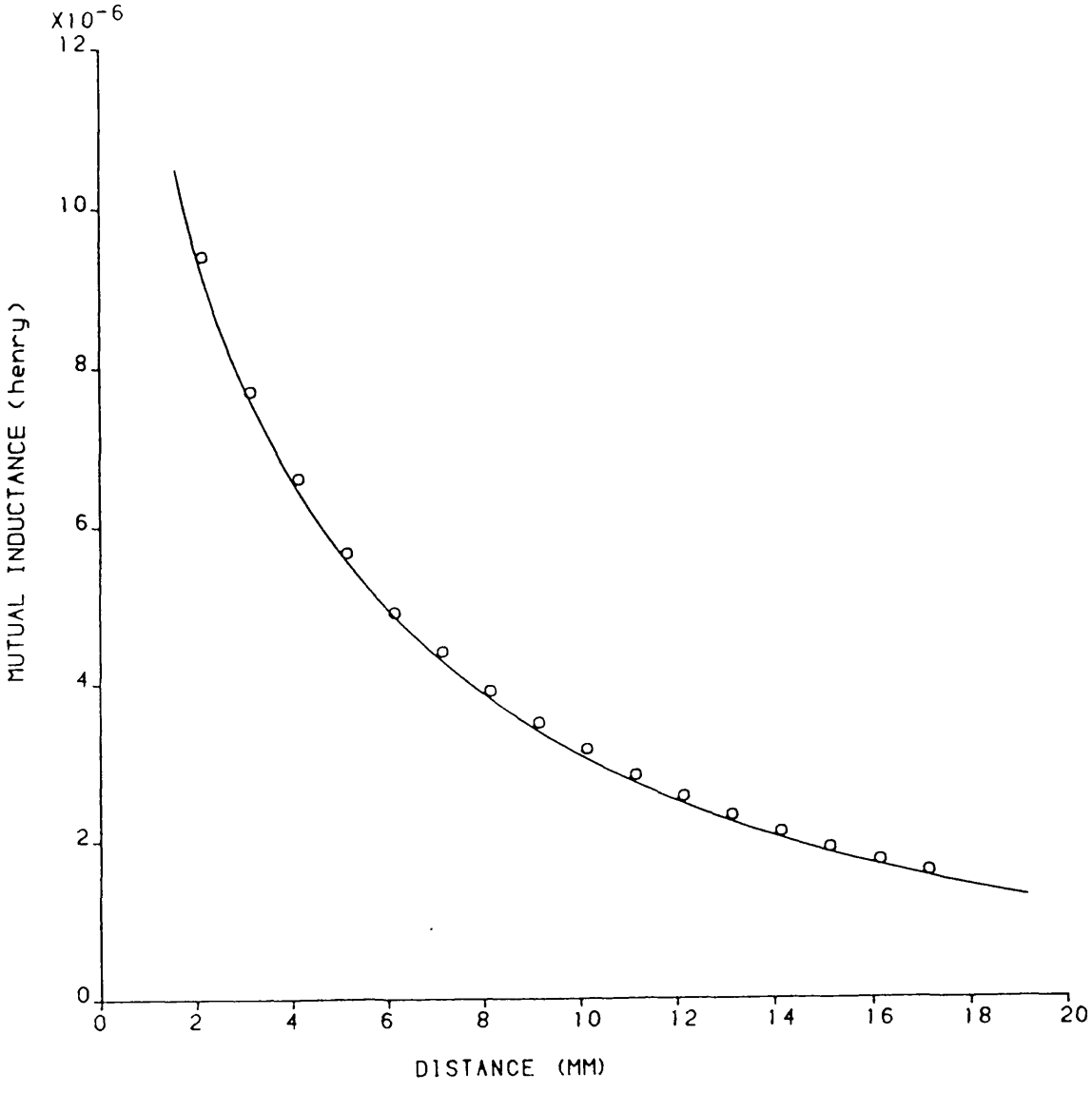

Fig.4.16: Mutual inductance between two coaxial circular filament

D_1 = 30.63 mm

D_2 = 31.6366 mm

——— Computed results

o o o Experimental results

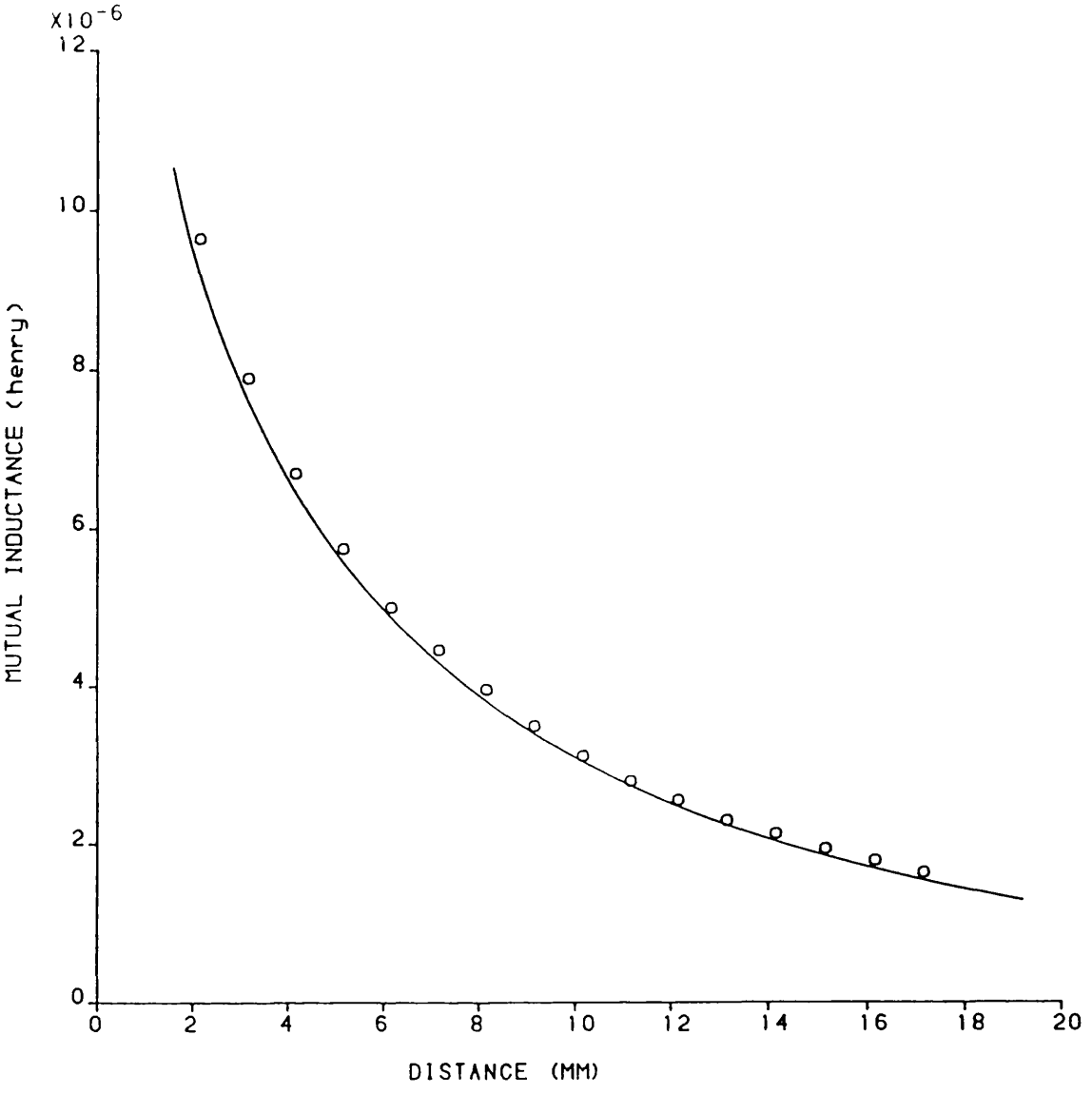

Fig.4.17: Mutual inductance between two coaxial circular filament

D_1 = 31.115 mm

D_2 = 31.6366 mm

——— Computed results

o o o Experimental results

CHAPTER FIVE

EVALUATION OF THEORETICAL AND EXPERIMENTAL RESULTS

5.1 Introduction

The previous two chapters have dealt with theoretical methods for computing the current distribution, and hence loss, in foil conductors used in both air-cored inductors, and transformers. The present chapter uses these methods to produce results for comparison with measurement.

Two air-cored, foil wound inductors are considered together with one transformer that has a foil wound secondary. In view of the fact that these problems are under investigation from the switched-mode power supply standpoint, the frequency range of 20 kHz to 100 kHz has been used for the main study, although computed results outside this range have also been produced in order to indicate trends.

Experimental measurement of losses of this type presents severe problems. The technique used for all loss measurements in this thesis is described in detail in Appendix A2. Briefly however it is a "power method", and not a "Q factor" type of method. The component under test is excited through an impedance matching transformer from sine-wave oscillator and power amplifier. The voltage and current are monitored and stored on a digital storage oscilloscope (DSO) capable of sampling up to 20 points per microsecond. The data is extracted from the DSO memory via an IEEE bus and read into the microcomputer. This multiplies instantaneous values of V and i to

obtain power, (and performs other calculations), so that average power, R_{ac}/R_{dc} etc. may be calculated.

Each of the experimental examples is described in turn below, together with supporting computations.

5.2 Foil-wound, Air-cored Inductor: Example 1

The sample inductor is illustrated on Figure 5.1(a). It consists of 5 turns of foil 12.5 mm wide by 0.073 mm thick with inner and outer diameters at 16.4 mm and 18.2 mm respectively. It has a dc resistance of 5.64 mΩ at 35°C and a dc inductance of 0.332 μH.

A direct comparison of results is given on Figure 5.2. It can be seen that while measured results are higher than computed results the general trend coincides and on average the computed results underestimate the total loss by around 10% (perhaps, more severely, the precision with which the additional loss due to non-uniform distribution of current is computed, should be considered - on this basis computed loss is some 30% less than measured).

While not greatly accurate therefore these results show some consistency, bearing in mind the complexities of both theory and experiment.

The computed results used the method described in Chapter Three, section 3.3 where each layer was treated individually. The number of notional filaments into which each layer should be subdivided in order to produce adequate results was established empirically from results plotted in Figure 5.3.

At 100 kHz each layer was divided into some 30 filaments which produce a basic set of some (150 x 150) simultaneous equations to be solved. This number can be halved by the use of symmetry.

R_{ac}/R_{dc} is a resulting parameter which may be measured by means of total power loss. But this is produced by non-uniform current distribution which is not simple to measure. Computed results are readily produced from the model however and some of these are illustrated in Figures 5.4, 5.5, 5.6 and 5.7. Figures 5.4 to 5.6 illustrate the current distribution in each layer of the five turn conductor at the frequencies 25 kHz, 50 kHz and 100 kHz respectively. They show a relatively small variation in current from one layer to the next, as might be expected in an inductor where the actual thickness of winding, 0.9 mm, is relatively small compared to the mean radius, 8.7 mm. Figure 5.7 compares the current distribution in the inner layer of the coil for the same three frequencies when the same total current is flowing in each case. It shows an increasing non-uniformity with frequency towards the edge of the foil, but remains relatively constant over the middle region of the conductor. The distribution of current at 100 kHz is particularly severe and this general pattern has also been shown by Mullineux[1].

Bearing in mind the relatively small variation in current distribution from one layer to the next, as seen in the above figures, the small "winding thickness/coil radius" ration, it might be thought possible to model the inductor as a single layer of filaments, situated at the mean coil radius and each consisting of five turns. This was done theoretically. Firstly the reduction in the number of equations is not as great as might be expected because

the foil had to be subdivided into a greater number of notional filaments to achieve stable results.

This is illustrated in Figure 5.8 which should be compared with Figure 5.3. At 100 kHz some 160 filaments were used, compared to about 30 per layer for the five layer case. The computed results for R_{ac}/R_{dc} are included in Figure 5.2. It can be seen that the results are clearly wrong in magnitude and general trend. It may be noted that these results were computed by two methods.

First the method of Chapter Three was applied to a single layer, i.e. the same computer program that produced the results for the five layer model losses used for single layer model with five turns per filament. Second, the equations of Murgatroyd[2] were programmed separately and were checked by inserting his data and producing his results. Both methods produced the identical results shown on Figure 5.2. The current distributions were also calculated and are shown on Figure 5.9. These do not demonstrate quite the sorts of shape that were found with the five layer model. At 100 kHz especially there is substantial difference, as shown in Figure 5.10. These results seem to make it clear that it is important to model each layer of a foil inductor separately, even when it might appear, from visual inspection, that this might not be strictly necessary.

While experimental results were restricted to the range 20 kHz - 100 kHz (the power amplifier was ac coupled and 20 kHz was its lowest reliable operating frequency) computed results were obtained over the range 1 kHz to 100 kHz in order to add some perspective to the study. These results are shown in Figure 5.11 plotted with both a linear and

logarithmic frequency axis. These display a generally well-known form. The variation of inductance with frequency is also shown here, which varies much less with frequency than resistance. This again is a well known effect. It appears from Figure 5.11 that frequencies up to about 5 kHz are effectively dc for the present choke configuration. This is supported by Figure 5.12 when current distribution against frequency is shown. The value of R_{ac}/R_{dc} is included for each of these distributions in order that visual relationship between current distribution and effective resistance can be seen.

It has been assumed so far that the current distribution varies across the width of the foil, but is constant through the thickness.

The general theoretical method is not restricted to this model. The foil may be assumed to consist of n thinner sublayers of copper rolled up together. Each sublayer is divided into filament coils in the usual way.

The number of equations and the length of each equation increases in proportion to the number of sublayer chosen. This technique therefore while taking into account quite fully non-uniform current distribution through the thickness of the foil, in practice leads to an undesirable increase in computing time. (The time to invert a matrix is almost exactly proportional to the cube of its order. If the foil is subdivided into just two sublayers therefore, the matrix inversion time increases by a factor of eight). Nevertheless the present example was subdivided into three sublayers in order to investigate the effect. In the present work the foil

thickness was 0.073 mm which is very small compared to the skin depth, if it means anything in the present context, at 100kHz of 0.216 mm. This probably indicates why subdivision into sublayers was not important. Under different conditions, thicker copper, higher frequencies, it might be much more important.

5.3 Foil-wound, Air-cored Inductor : Example 2

The second inductor tested and analysed consisted of ten turns of copper foil 0.073 mm thick and 30 mm wide. Its inner and outer diameters were 29.77 mm and 32.8 mm respectively. Its dc resistance at 22.5^{o}C was 8.21 mΩ, and its dc inductance was 2.08 μH. The inductor shape is sketched in Figure 5.1(b).

The general test and computational techniques were the same as for Example 1 in section 5.2 above, and the results are presented in a similar way.

Figure 5.13 provides the main comparison between measured and computed results for R_{ac}/R_{dc} over the frequency range 20 kHz to 100 kHz. It can be seen that the measured results are higher than computed results, as in Example 1 above.

The variation in computed values of R_{ac}/R_{dc} as the number of notional filaments is increased is shown in Figure 5.14. It can be seen that at 100 kHz some 65-75 filaments are needed for reasonable results, and in fact 70 filaments were used for all frequencies. R_{ac}/R_{dc} increases from about 1.5 at 20 kHz to 2.05 at 100 kHz indicating that the eddy currents due to radial flux components which cause the resulting non uniformity of current distribution are very

severe.

Computed values of this current distribution are shown for layer 1 (inner) 5 and 10 (outer) at frequencies 25 kHz, 50 kHz and 100 kHz in Figure 5.15, 5.16 and 5.17 respectively. The variation in current distribution is not great, although it increases with frequency, but the general shape becomes increasingly distorted with frequency as noted in Figure 5.6 for Example 1.

It is also apparent that there is not a gradual change in shape from layer 1 to layer 10, but for all three frequencies present layer 1 current distribution is intermediate between those of layer 5 and 10.

The current distributions for layer 1 at frequencies 25 kHz, 50 kHz and 100 kHz are compared in Figure 5.18, where the distribution scaled for the same total foil current. It can be seen here also, as for Example 1, that the current densities over a large central region of the foil is independent of frequency, only the distribution over the outermost 20% of the foil changes.

Computations were again made assuming that the 10 layer inductor consisted of a 'single layer' of 10 turns situated at the mean radius of the inductor. Computed values of R_{ac}/R_{dc} for this approximation are plotted for comparison of Figure 5.13 and can be seen to be worse than with other results. As with Example 1 therefore this approximation can be seen to be inadequate. Current distributions are compared on Figure 5.19 for a frequency of 100 kHz. There is no semblance of agreement between the 10 layer model and the one layer,

ten turn approximation. Computations were also made for the present example with the foil subdivided across its thickness into 2 sublayers. This was found to have a very small effect as discussed in section 5.2 above.

Computed results for Example 2 inductor for the frequency range 1 kHz to 100 kHz for both R_{ac}/R_{dc} and current distribution are shown in Figures 5.20 and 5.21 respectively. As with Example 1 inductor these demonstrate the expected trends with frequency.

5.4 Ferrite Cored Transformer: Example 1

A sample ferrite cored transformer was constructed which had a wire wound primary and a foil wound secondary. The purpose of this work was to demonstrate that the losses in the foil wound secondary of a ferrite cored transformer could be predicted using an air cored model, in which the primary and secondary ampere turns were equal and opposite. For this purpose therefore a primary winding was made so that eddy current loss in it was approximately zero, the loss in it therefore being calculated from its dc resistance. This was achieved by using a multistrand wire. The primary winding on an ETD44 core was 52 turns of wire consisting of 380 strands of 0.0508 mm (0.002 in) diameter wire. In the first instance a secondary winding using identical wires also of 52 turns was laid on the formers. This arrangement was put through a usual set of tests to calculate R_{ac}/R_{dc} in order to establish that it was close to unity. This also establishes that core losses are substantially zero. The total losses were measured using the technique described in Appendix A2, and the value so calculated was divided by the total dc copper loss. If R_{ac}/R_{dc} is unity therefore there is no eddy current loss in the

conductor and there is no core loss. The results are shown in Figure 5.22 for three test conditions. The primary and secondary windings were connected in series opposition, so that primary and secondary ampere turns were identically zero and measurements were made with and without the core in position. It can be seen that there is no significant difference and that R_{ac}/R_{dc} is quite close to unity. The results were repeated with the secondary winding short circuited and again the measured values of R_{ac}/R_{dc} are close to one. Under this last condition primary and secondary ampere turns are not necessarily the same, but measurements indicated that they differed by less than 1%. Clearly short circuited tests without the ferrite core in position would have no meaning in the present context, and were not undertaken.

These preliminary results suggest that losses other than dc copper losses in the primary winding may be neglected, and give some idea of the precision achieved by the experimental method.

Following this work, the secondary winding was removed, and replaced by 10 turns of copper foil of dimensions 30 mm wide, 0.073 mm thick. This was to be tested in the short circuited condition, as the option of connecting in series opposition, with 52 primary turns and 10 secondary turns not available. Although all due precautions were taken the actual short circuiting junction had a resistance that was significant compared to the dc resistance of the foil. To overcome this the voltage across the junction was monitored with sense wires and v and i across the termination were measured over the frequency range of interest so that its effective resistance, R_T, could be estimated. These results are shown in Figure 5.23, where it

can be seen that the termination resistance is just over 10% of the foil resistance. From the total loss measured by the experimental technique was subtracted the $i^2_pR_{dc}$ of the primary winding and $i^2_sR_T$, the termination loss in the secondary foil. i_s was assumed to be related directly to i_p via turns ratio in the usual way. The remaining loss was assumed to be in the foil, and R_{ac}/R_{dc} for the foil was calculated by dividing this net loss by the $i^2_sR_{dc}$ of the foil. Results of measurements and computations are shown in Figure 5.24.

The two sets of measurements show the difference made by allowing for the resistance of the short circuiting termination of the foil secondary. It is clear that there is very close agreement between measured and computed results. It is unfortunate however that the effect under examination is not very pronounced for these test conditions, nor does it change significantly with frequency. Nevertheless the close agreement gives a measure of confidence in the proposed technique. Work continues to apply the method to transformer in which R_{ac}/R_{dc} is more severe in the foil.

It might be emphasised at this point that the losses in a foil wound secondary of a ferrite cored transformer have been calculated from a model which assumes the ferrite is not present, the only necessary condition in this model is that the primary and secondary ampere turns are equal in magnitude and opposite in sense.

Figure 5.25, 5.26 and 5.27 illustrated computed current density distribution across the inner, 'middle' (layer 6) and outer layer of the foil secondary at 25 kHz, 50 kHz and 100 kHz respectively. It

can be seen in general that the current distribution is almost uniform across 80% of the width of the foil but increases sharply at the edge. This effect is most pronounced in the outer layer and at higher frequencies. The average current density is also indicated in each case.

5.5 Conclusion

The method proposed for computing losses in foil conductors used both in air cored inductors and ferrite cored transformers has been tested by comparing two experimental inductors and one experimental transformer with computed results. It has been shown that the multilayer model predicts the behaviour of a multiturn inductor quite well, and that a single layer, multiturn approximation does not appear to be suitable. The computed results underestimate the measured values and this is the usual position in loss calculations. This form of model therefore seems in principle to be satisfactory, although further refinements could probably be achieved. The transformer example also showed a good level of agreement between measured and computed losses. Further examples would be desirable in order to establish the validity of the model over a wider range of conditions. However the results obtained so far are optimistic. The use of an air cored model to predict the behaviour of a ferrite cored transformer is an interesting concept but appears to be satisfactory. If conditions are discovered where this model is no longer satisfactory then the main structure of the computer model is unchanged, only the calculation of self and mutual inductances needs modification. This might typically involve the use of a finite element field programme, to take into account presence of ferrite. 'TOSCA' which was shown in Chapter 2 to behave satisfactorily could

be used for this. However, all these methods involve the use of a large amount of computer time.

5.6 Reference

1. Mullineux, N., Reed, J.R. and Whyte, I.J.: "Current distribution in sheet- and foil-wound transformers", Proc.IEE, Vol.116, No.1, January 1969, pp.127.

2. Murgatroyd, P.N. and Walker, N.J.: "Frequency-dependent inductance and resistance of foil conductor loops", Proc.IEE, Vol.12, No.5, May 1977, pp.493-496.

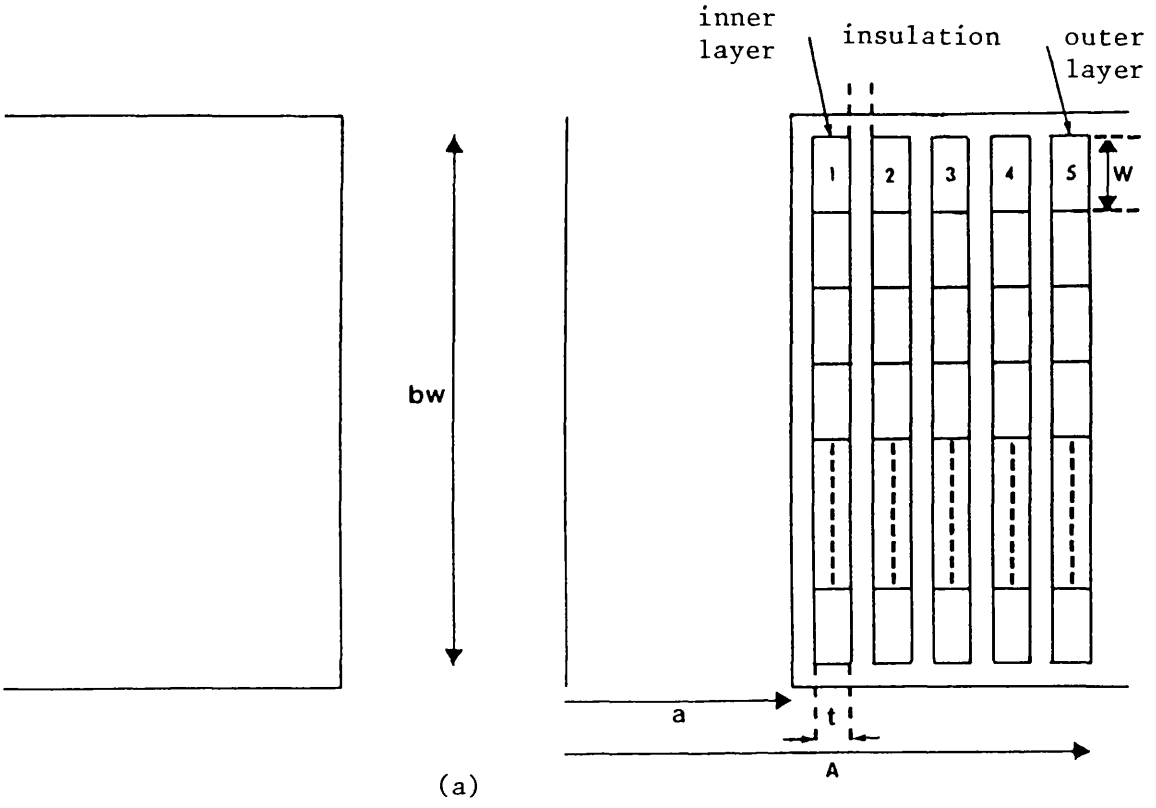

(a)

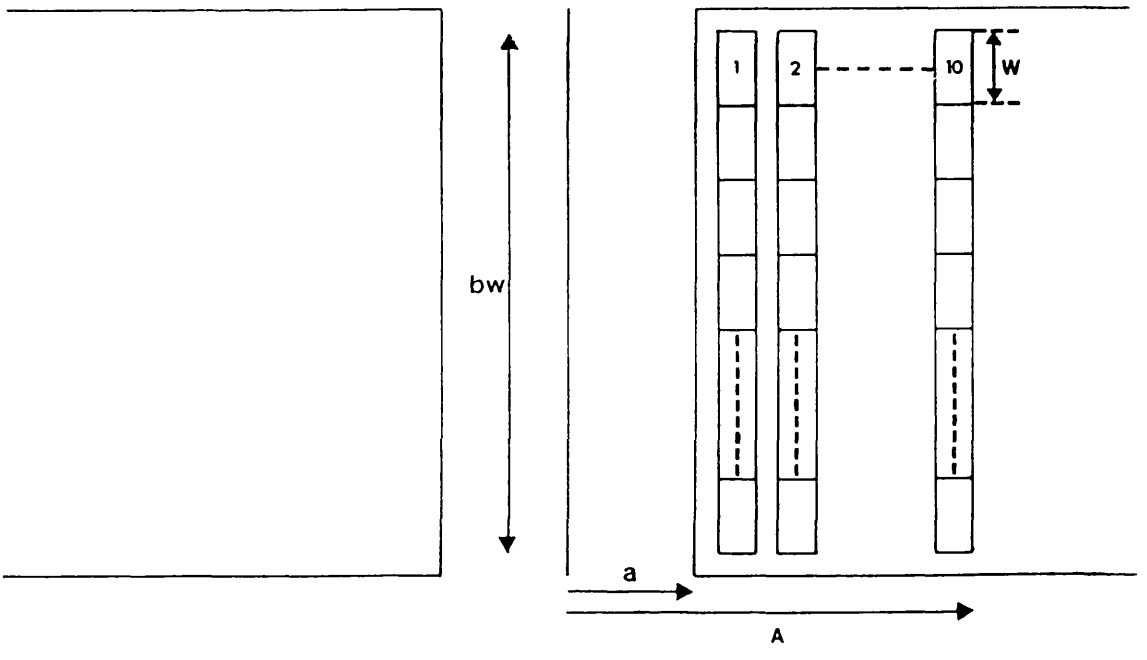

(b)

Fig.5.1: (a) Example 1 with 5 layer and bw = 12.5 mm
(b) Example 2 with 10 layer bw = 30 mm

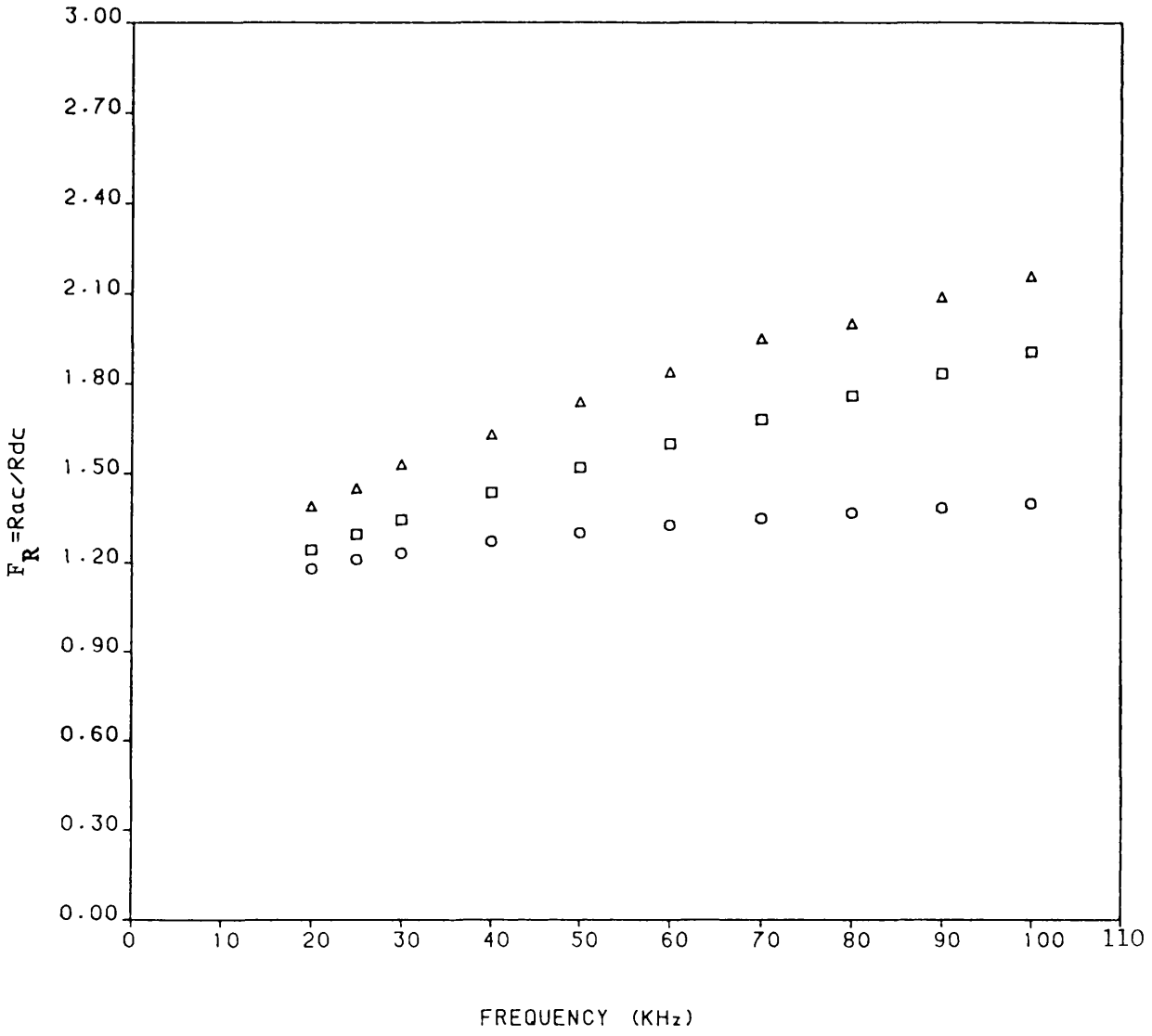

Fig.5.2: Comparison between the computed and measured results. Example 1

Δ Δ Δ Δ Measured results

□ □ □ □ Computed results, 5 layers

o o o o Computed results, single layer, 5 turns

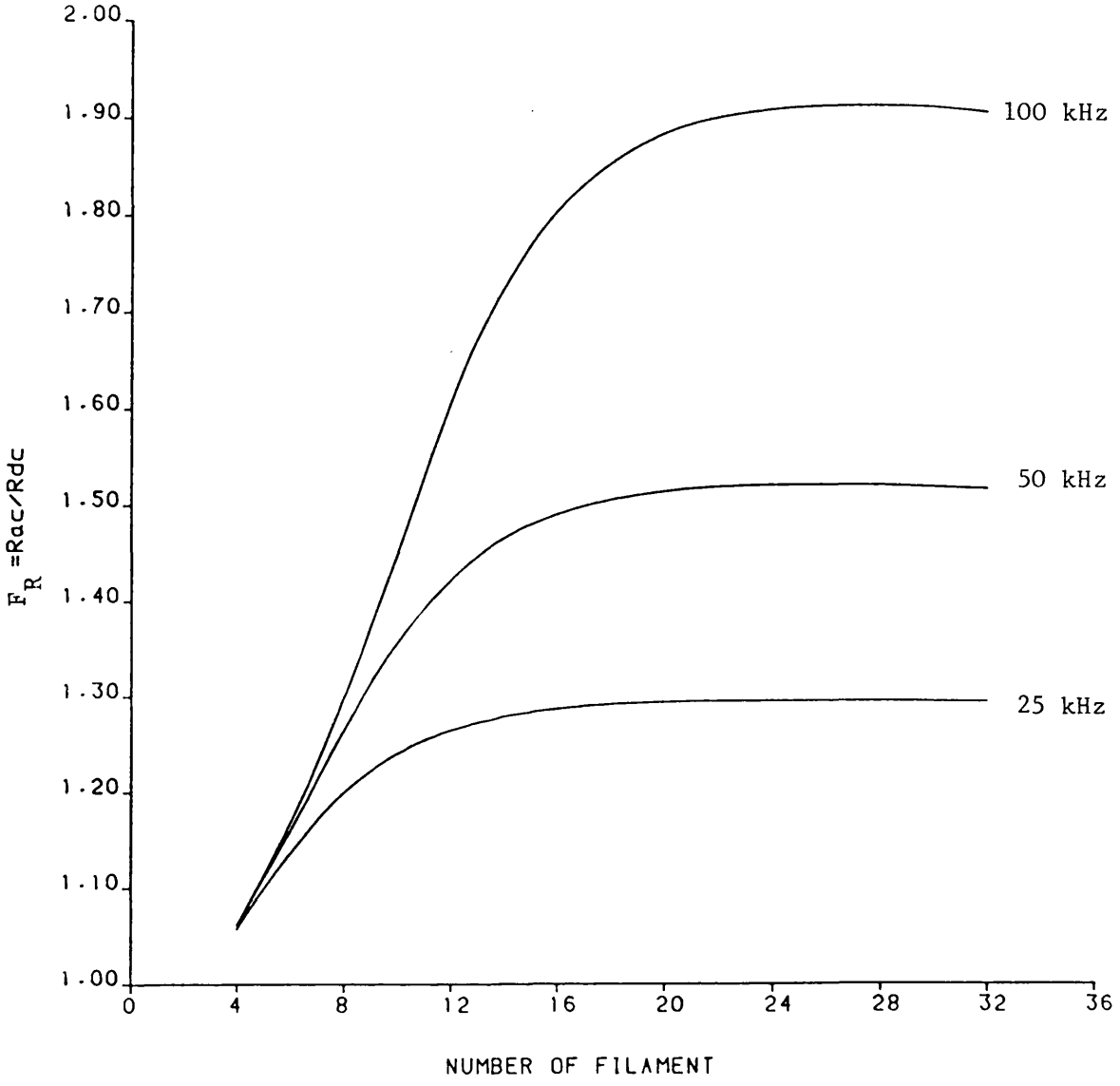

Fig.5.3: The variation of R_{ac}/R_{dc} with the number of filament at a given frequency. Example 1.

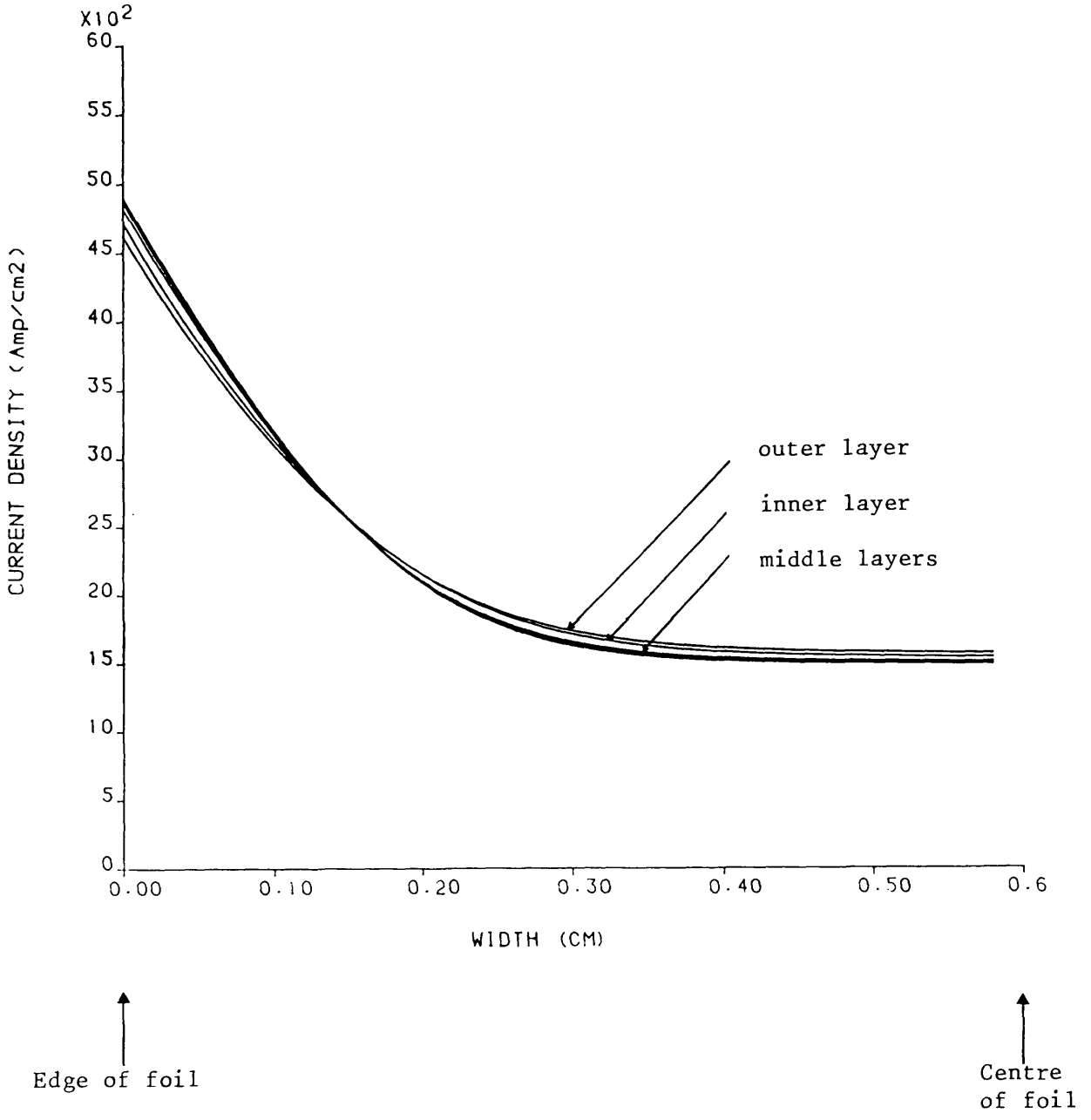

Fig.5.4: Current-density distribution
Example 1
f = 25 kHz

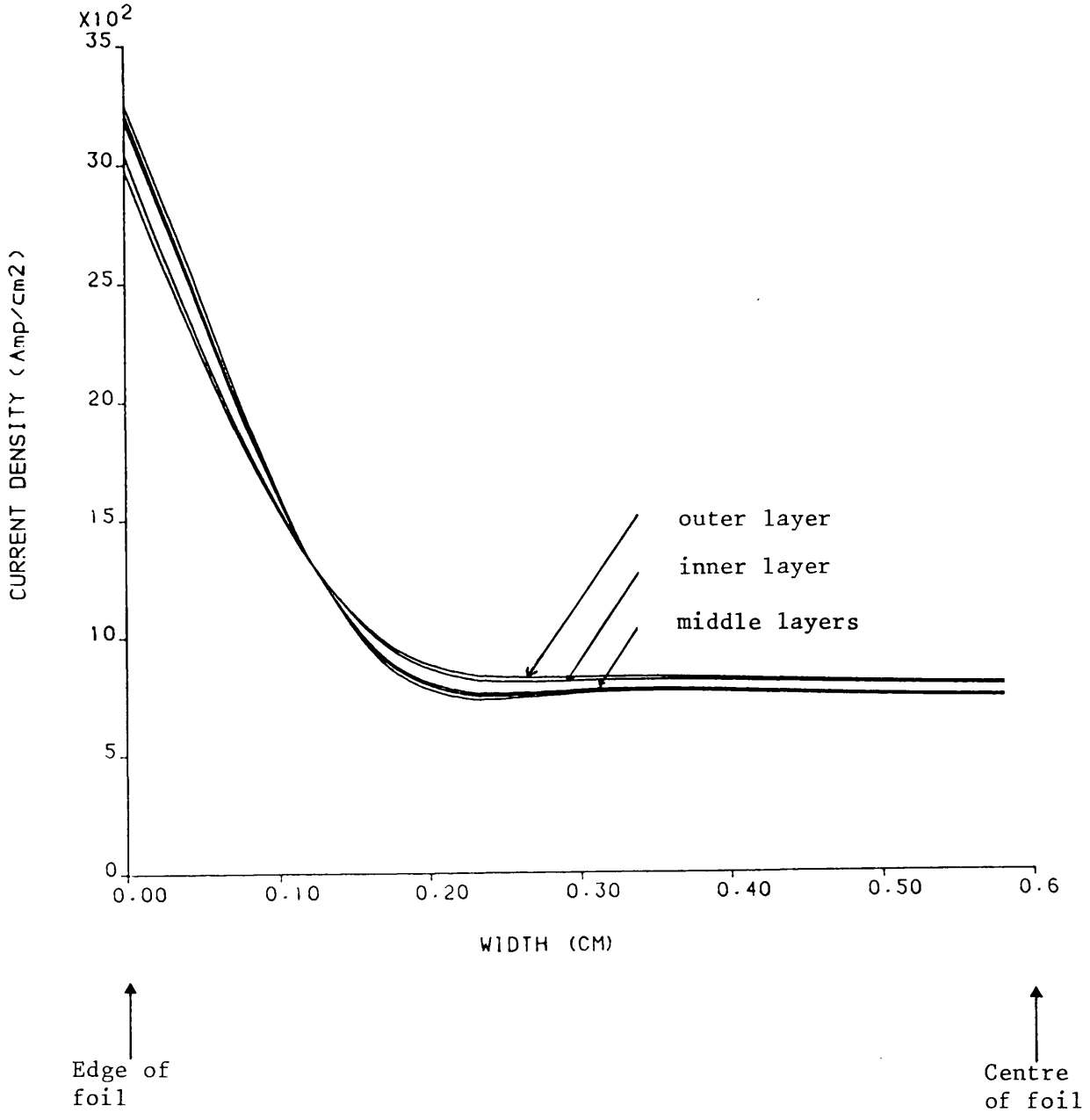

Fig.5.5: Current-density distribution
Example 1
f = 50 kHz

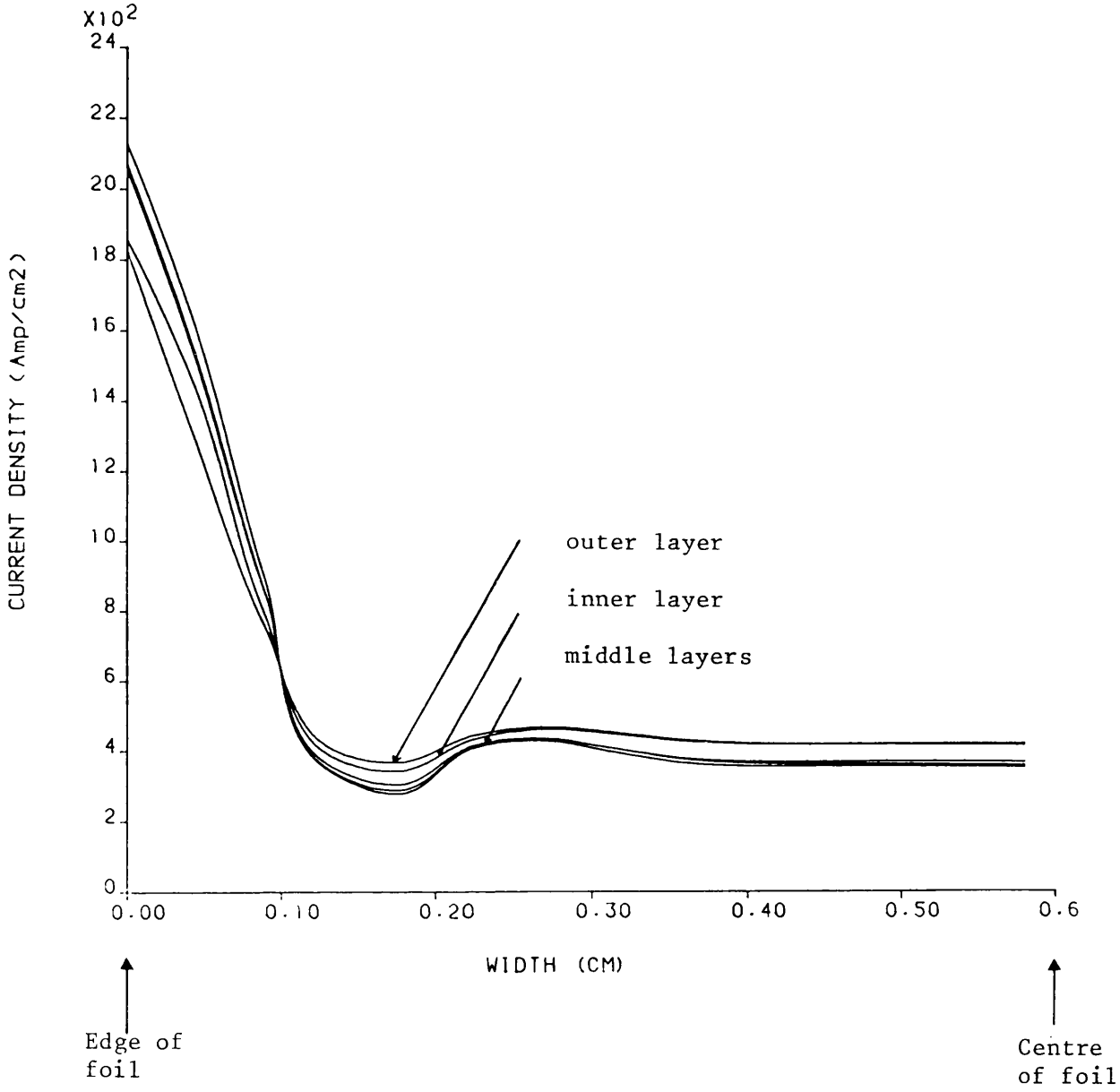

Fig.5.6: Current-density distribution
Example 1
f = 100 kHz

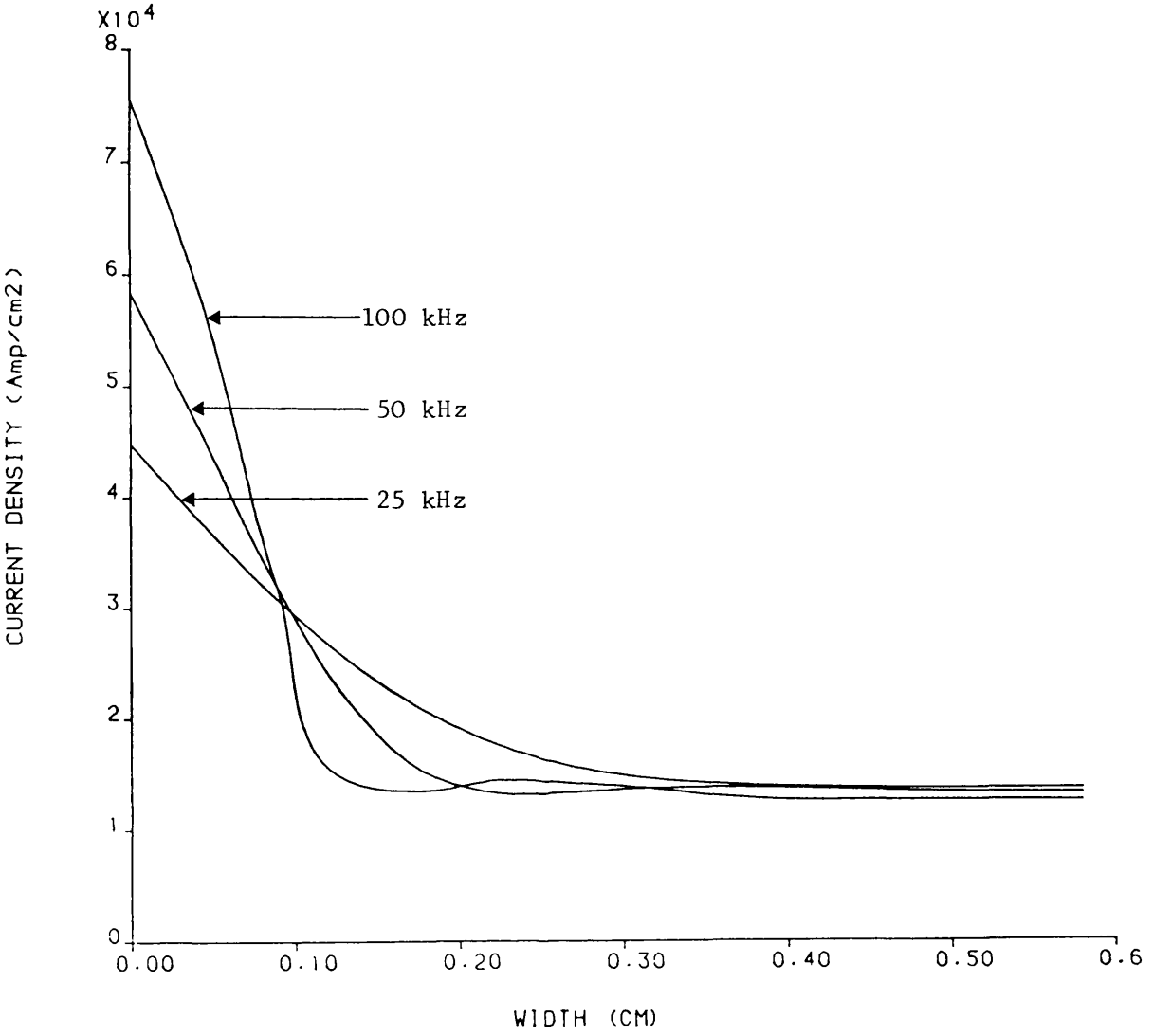

Fig.5.7: Current-density distribution
Example 1

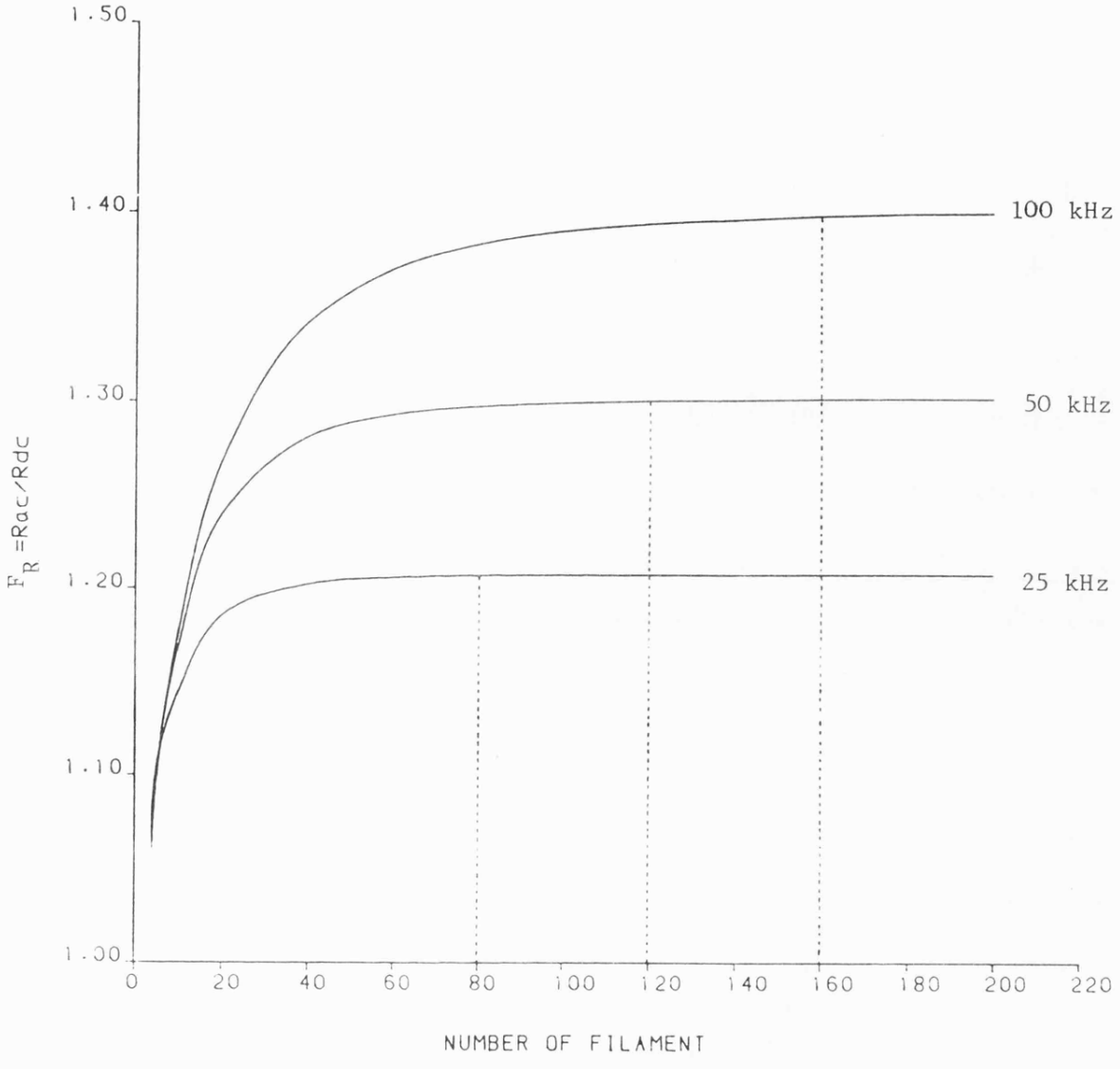

Fig.5.8: The variation of R_{ac}/R_{dc} with the number of filaments at a given frequency
Single layer, 5 turns

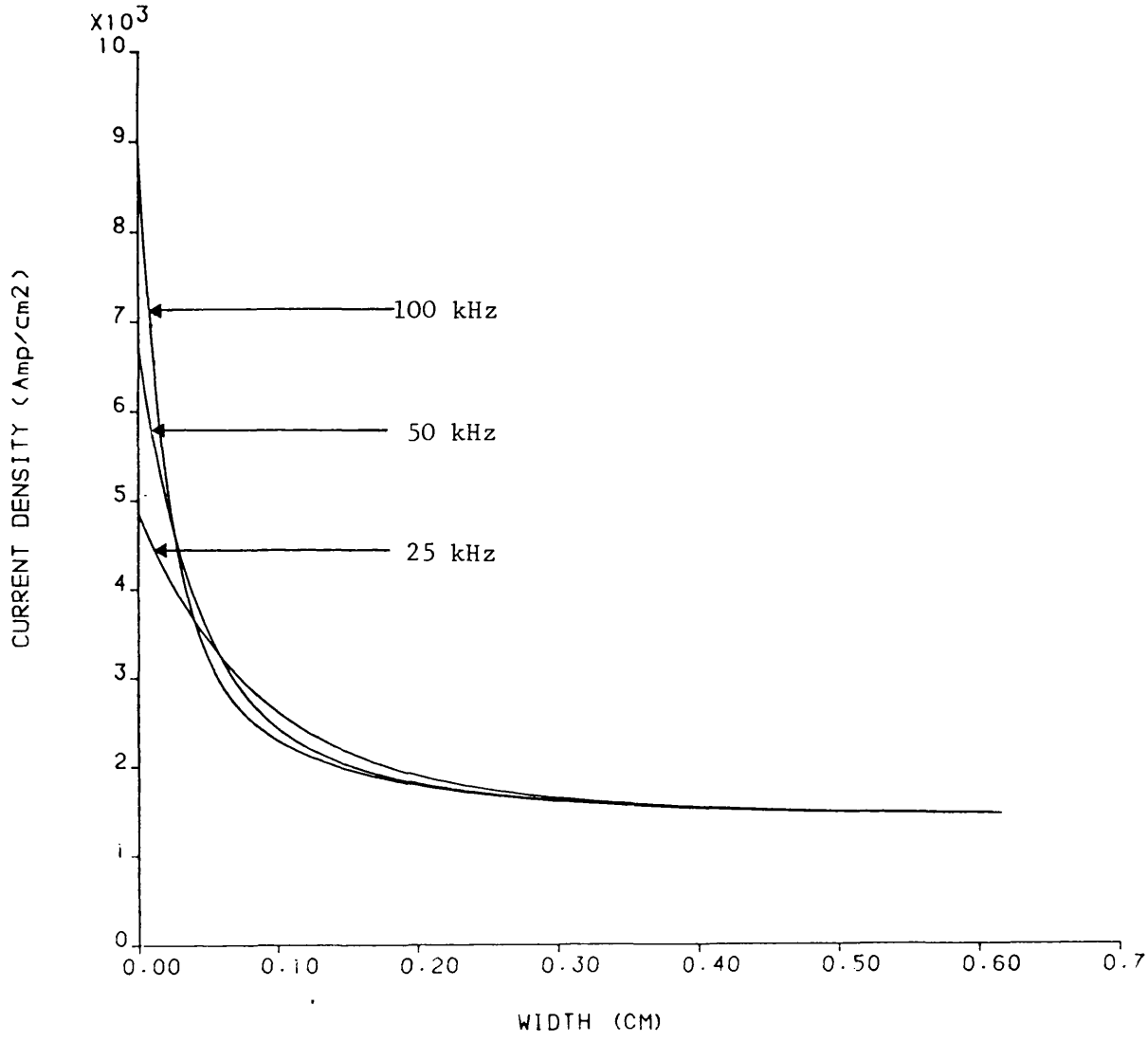

Fig.5.9: Current-density distribution
Single layer, 5 turns

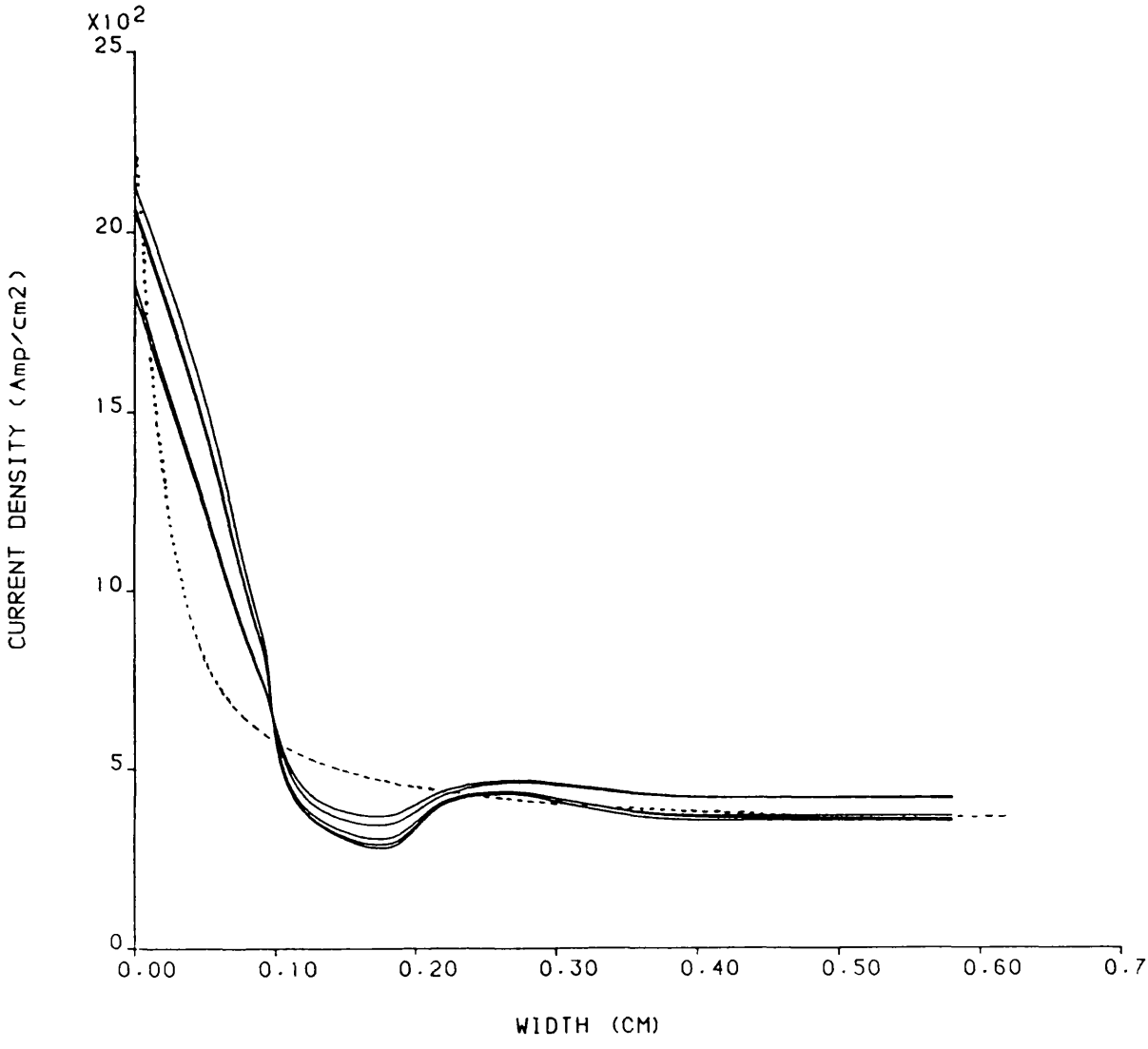

Fig.5.10: Comparison between the current-density distribution
f = 100 kHz

——— five layer. Example 1

. . . single layer 5 turns

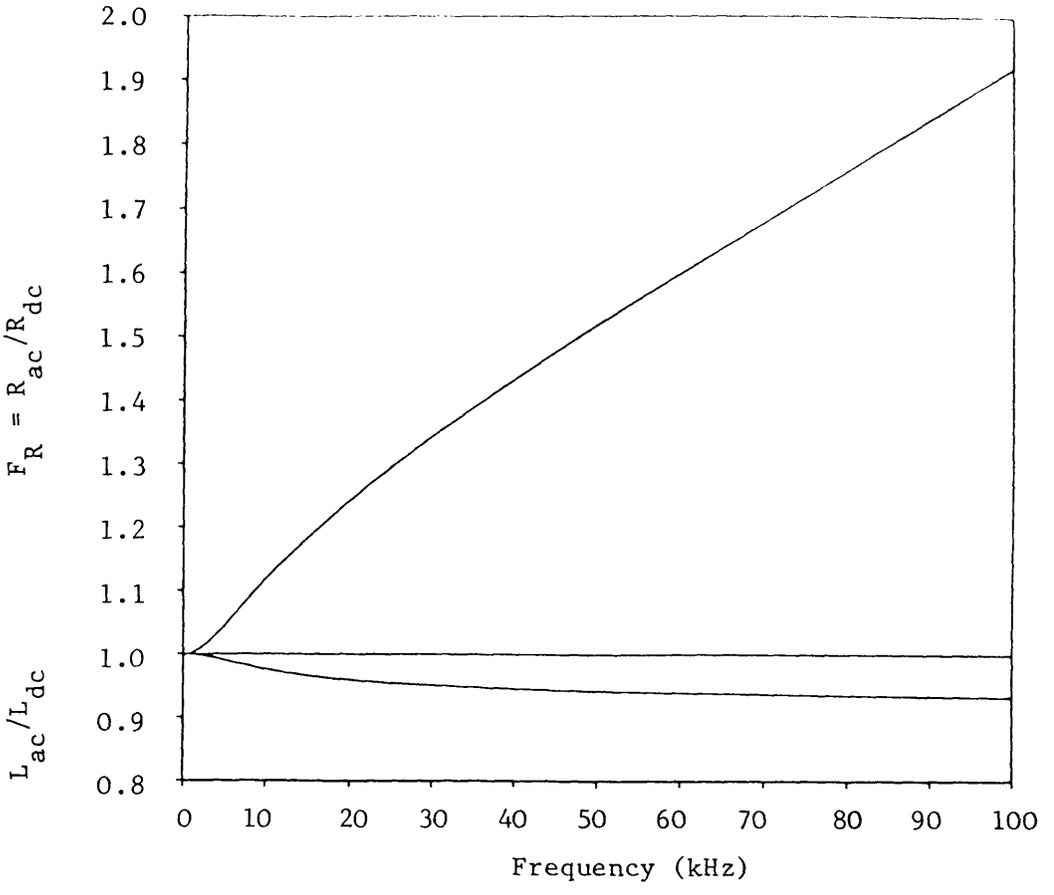

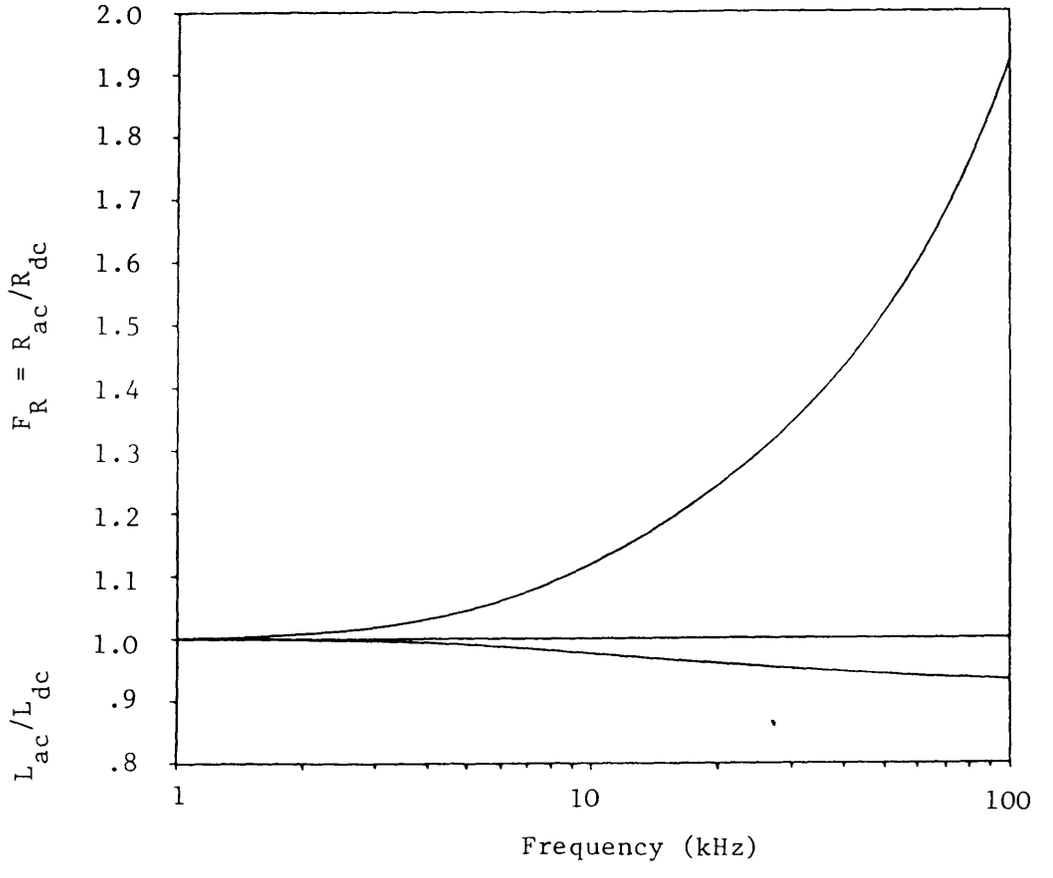

Fig.5.11: Variation of R_{ac}/R_{dc} and L_{ac}/L_{dc} with frequency
Example 1

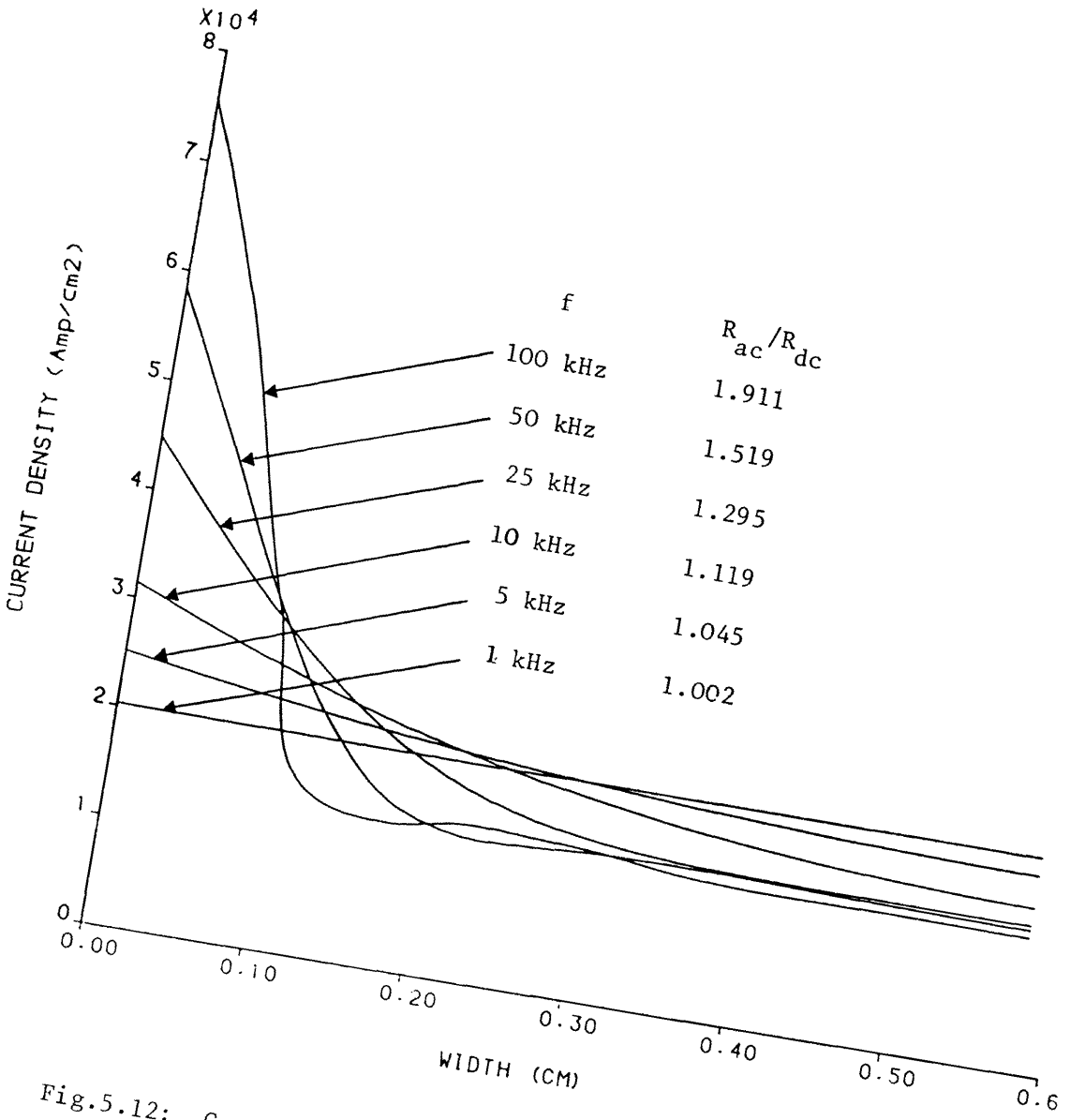

Fig.5.12: Current-density distribution at different frequencies Example 1

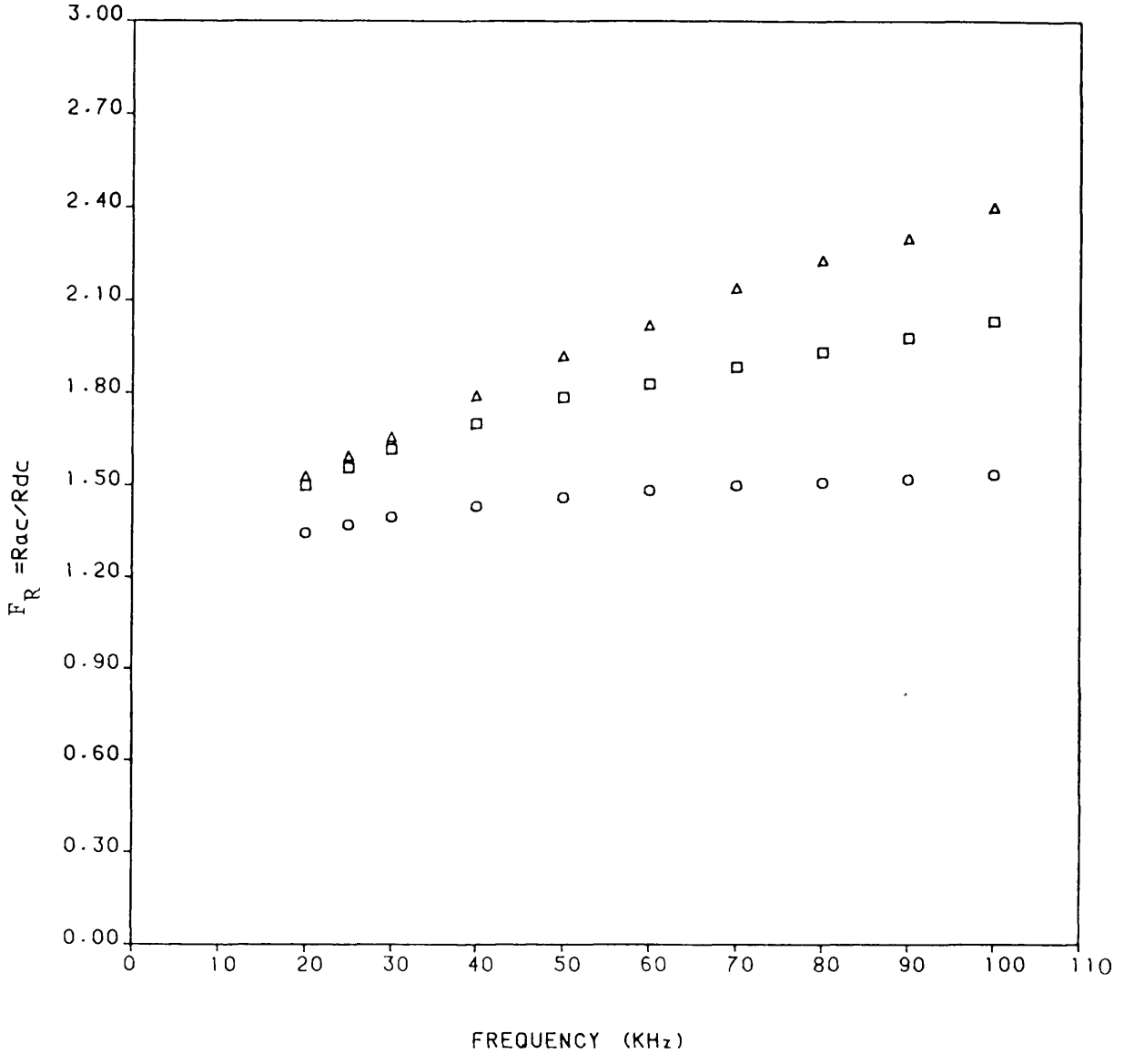

Fig.5.13: Comparison between the computed and measured results

Δ Δ Δ Δ Measured results

□ □ □ □ Computed results 10 layers

o o o o Computed results single layer 10 turns

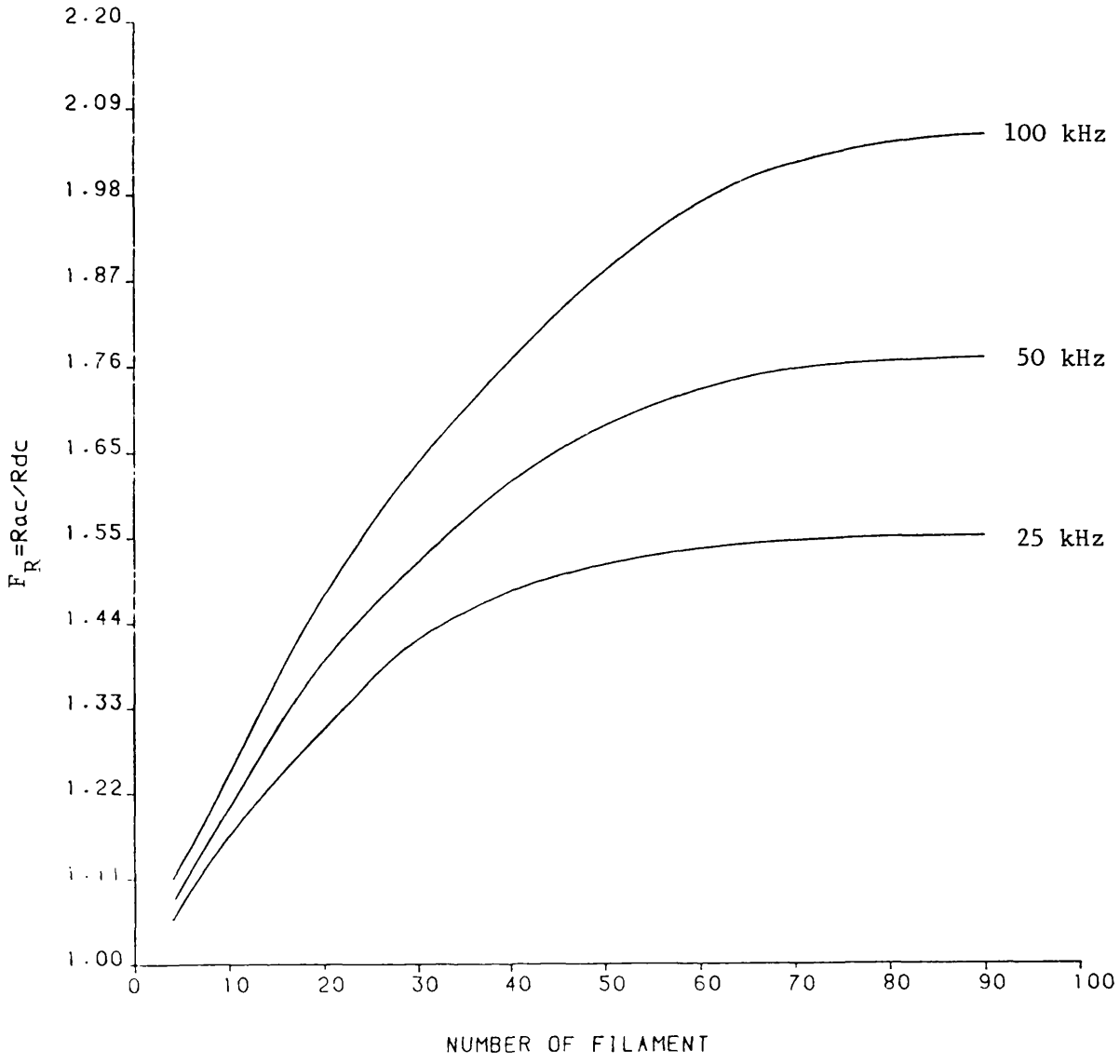

Fig.5.14: Variation of R_{ac}/R_{dc} with the number of filament at a given frequency
Example 2

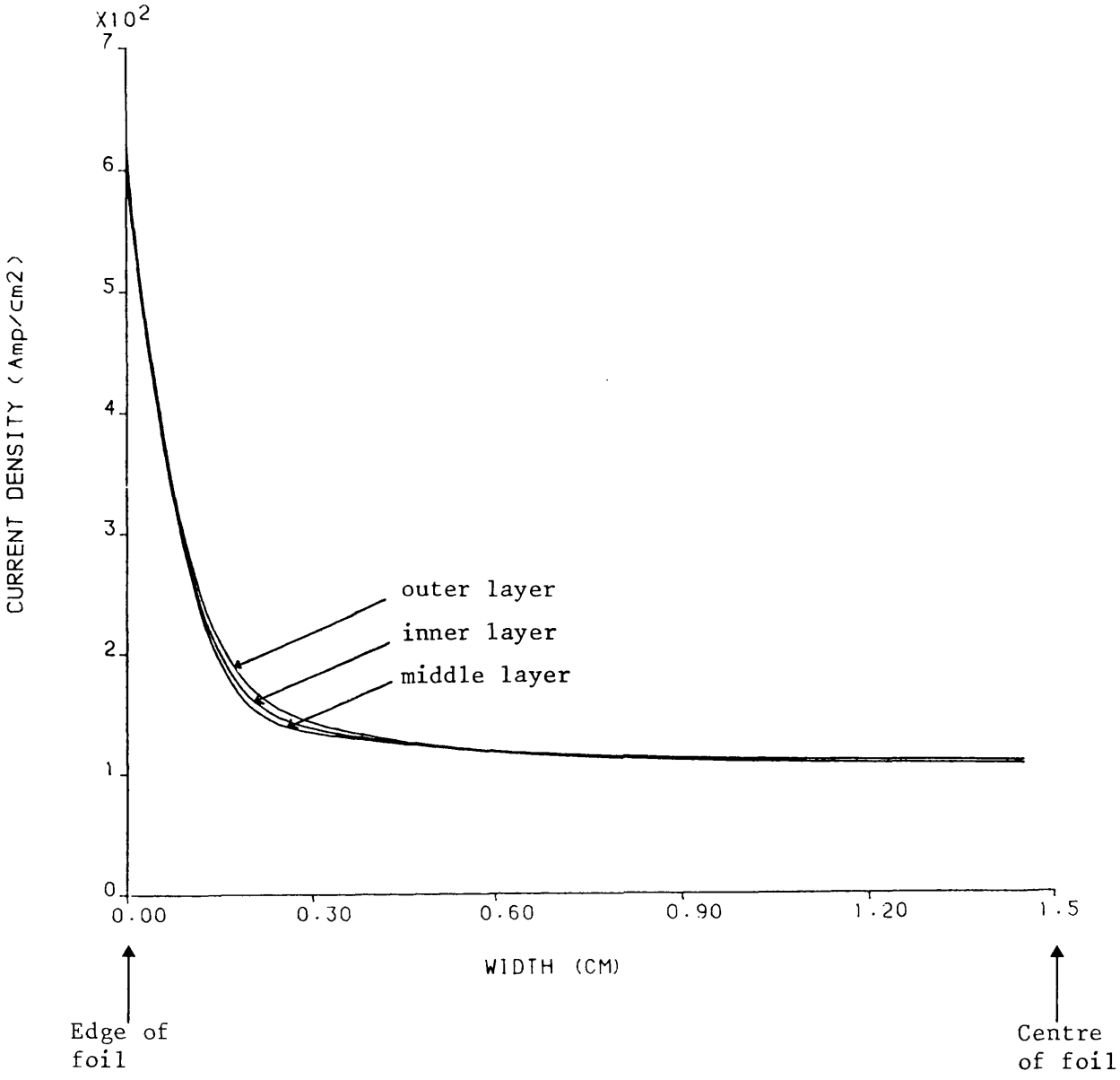

Fig.5.15: Current-density distribution
Example 2
f = 25 kHz

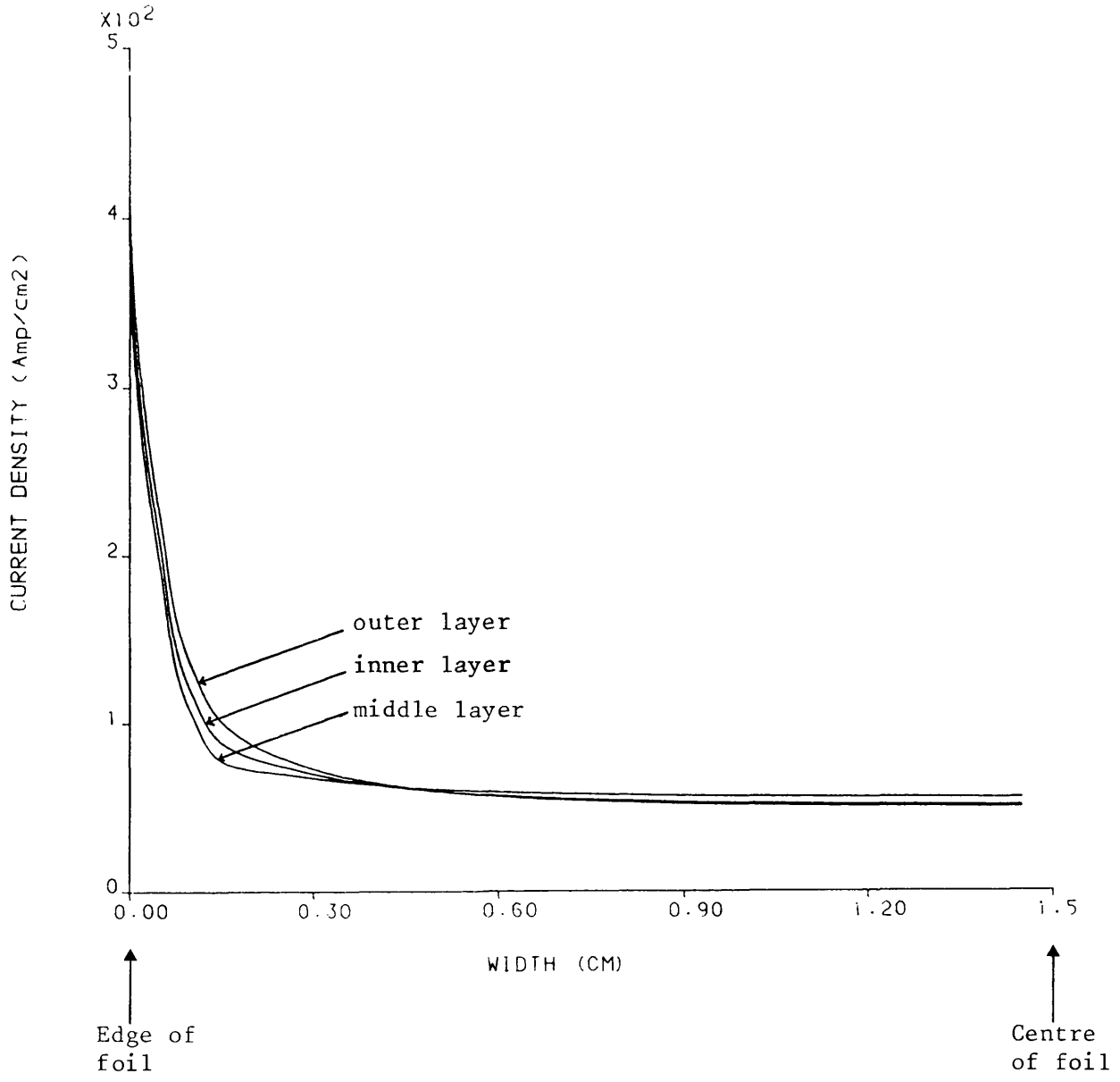

Fig.5.16: Current-density distribution
Example 2
f = 50 kHz

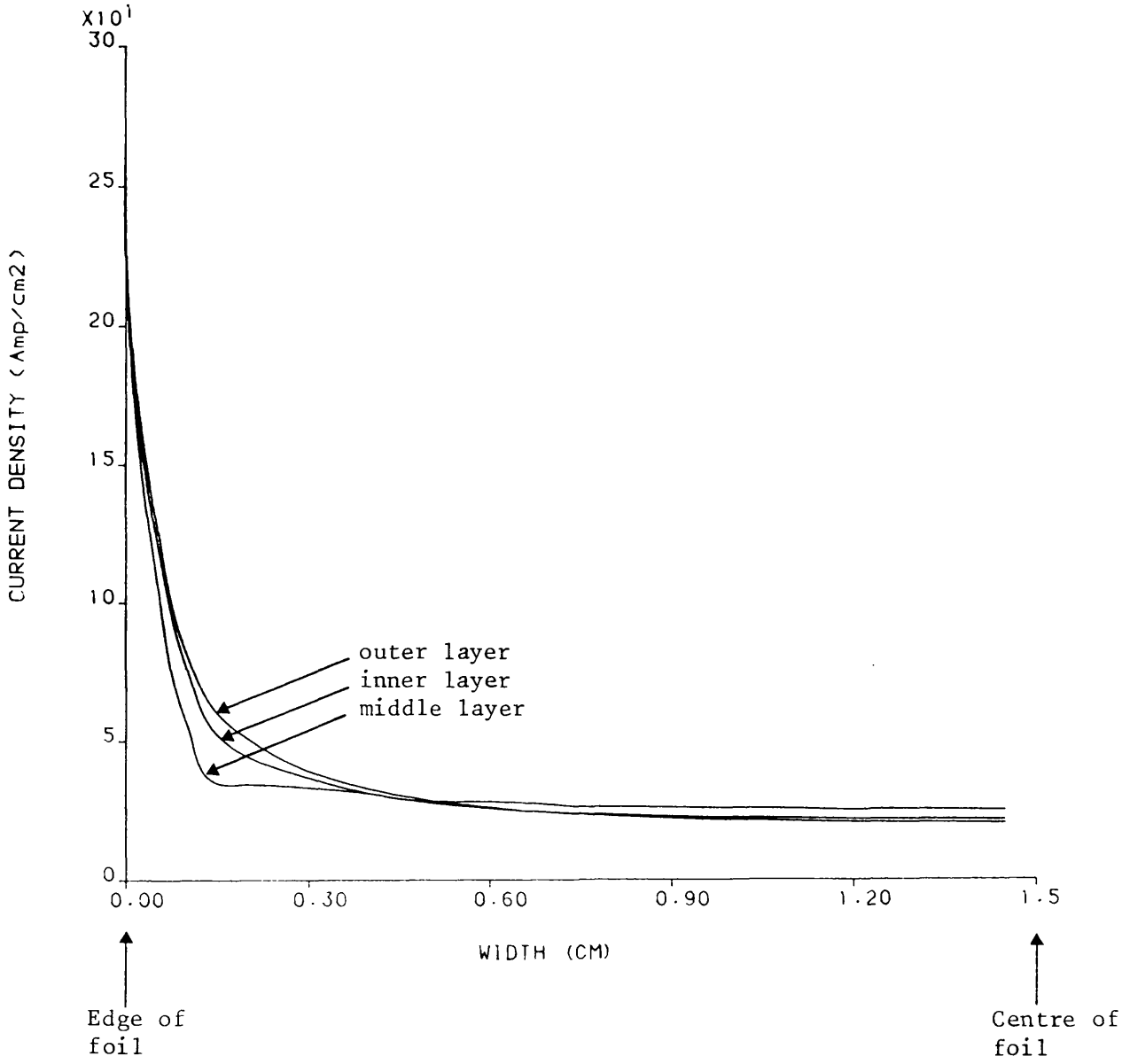

Fig.5.17: Current density distribution
Example 2
f = 100 kHz

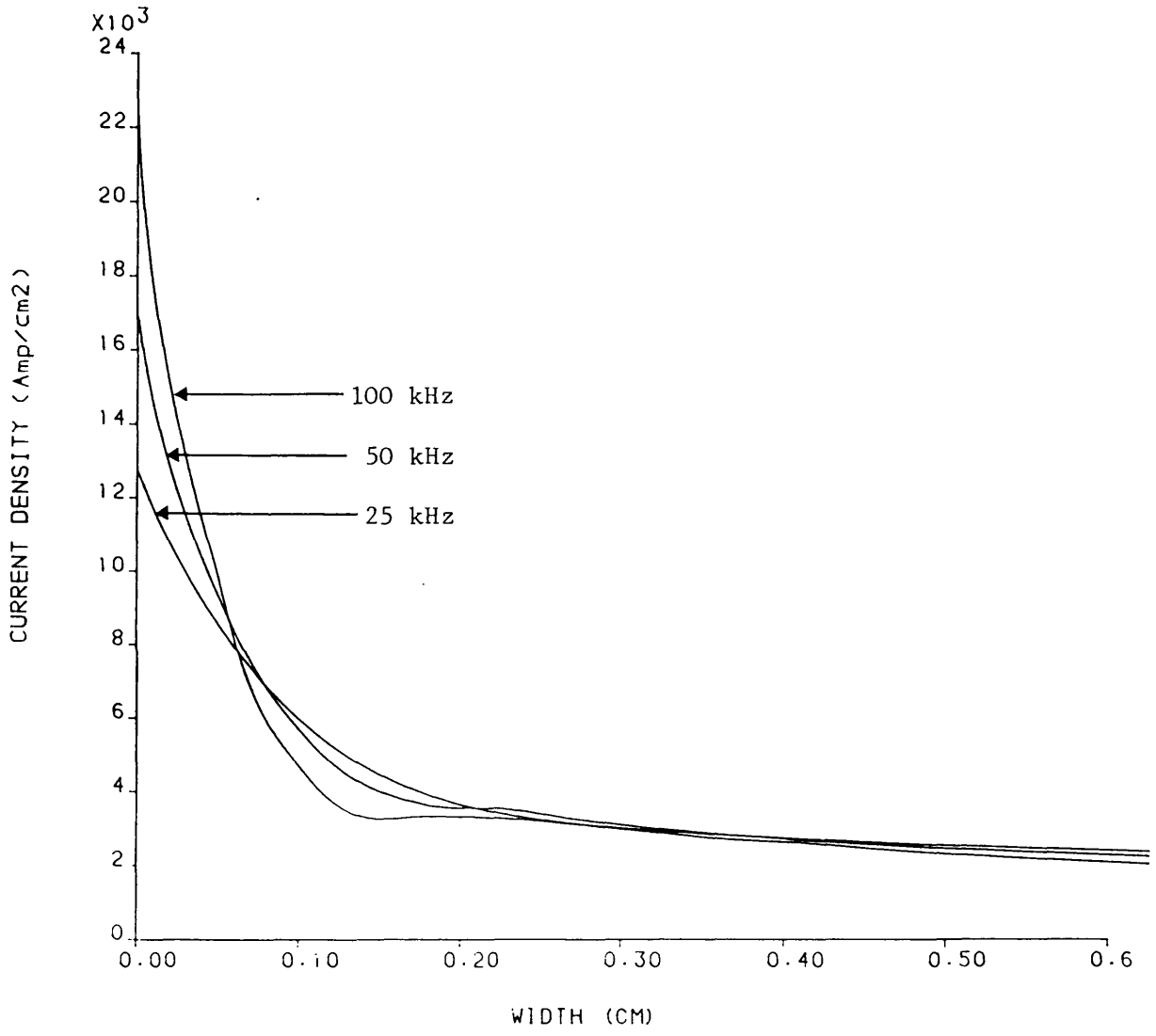

Fig.5.18: Current-density distribution
Example 2

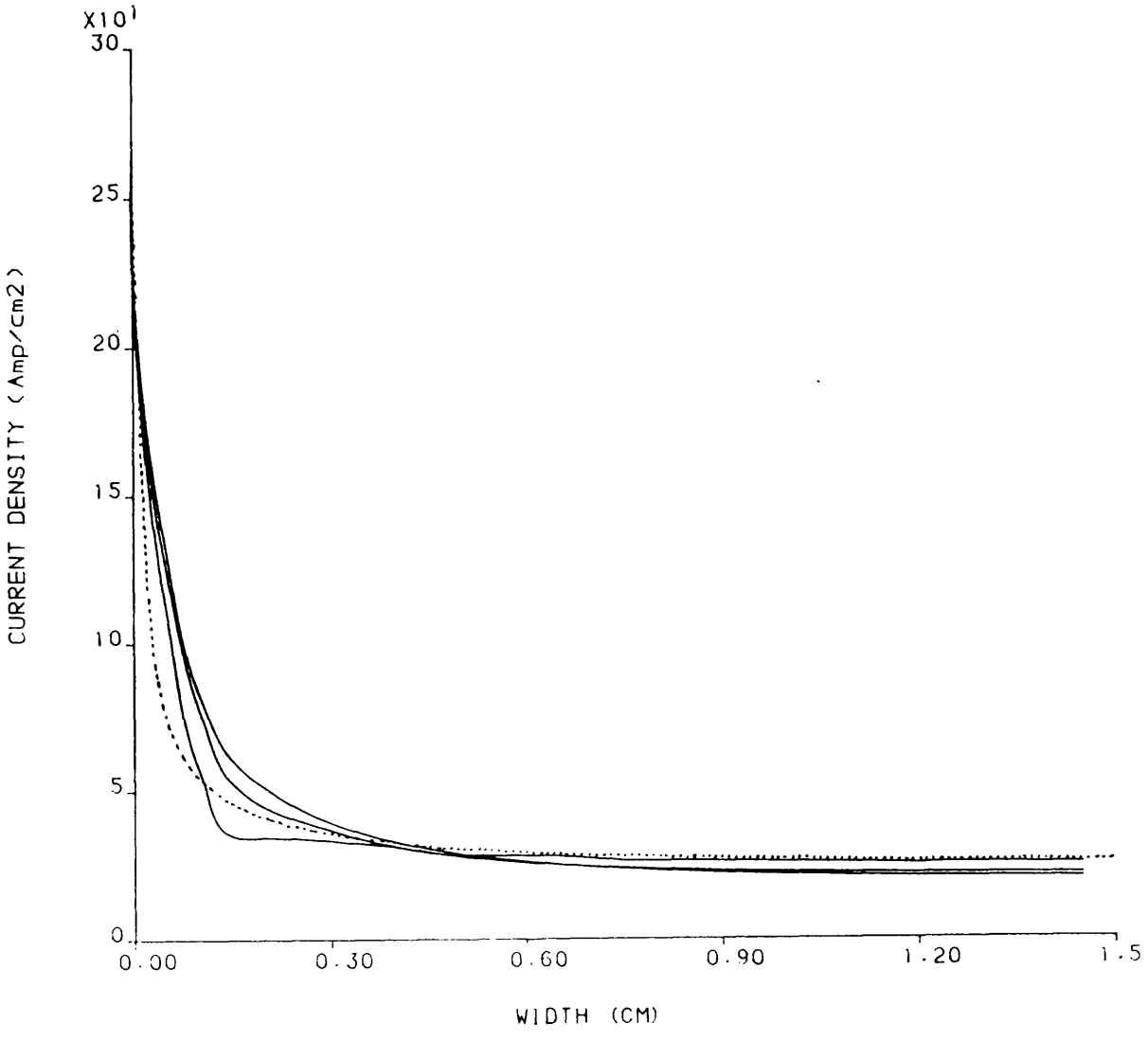

Fig.5.19: Comparison between the current density distribution
f = 100 kHz

——— Ten layers. Example 2

. . . Single layer 10 turns

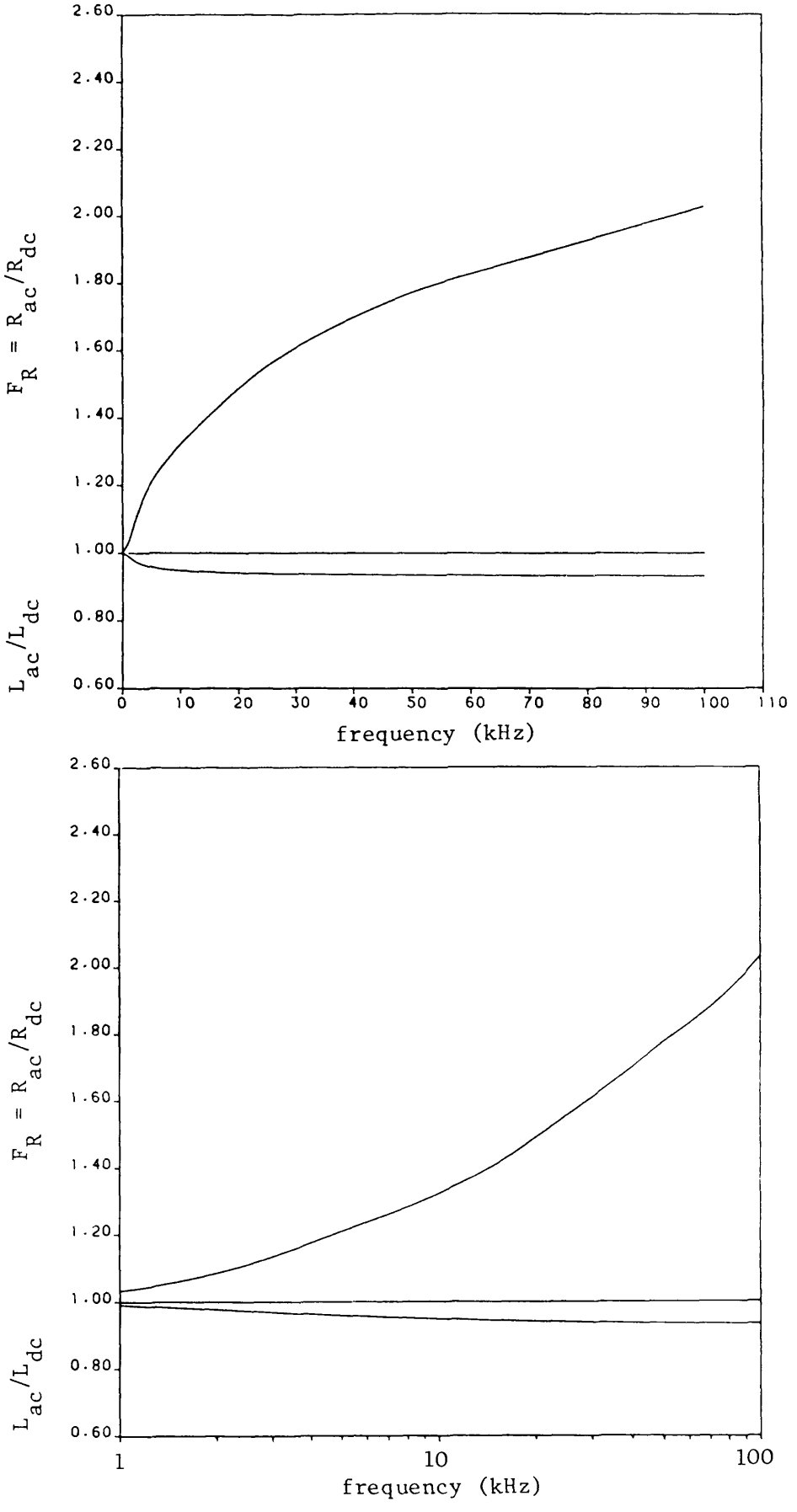

Fig.5.20: Variation of R_{ac}/R_{dc} and L_{ac}/L_{dc} with frequency
Example 2

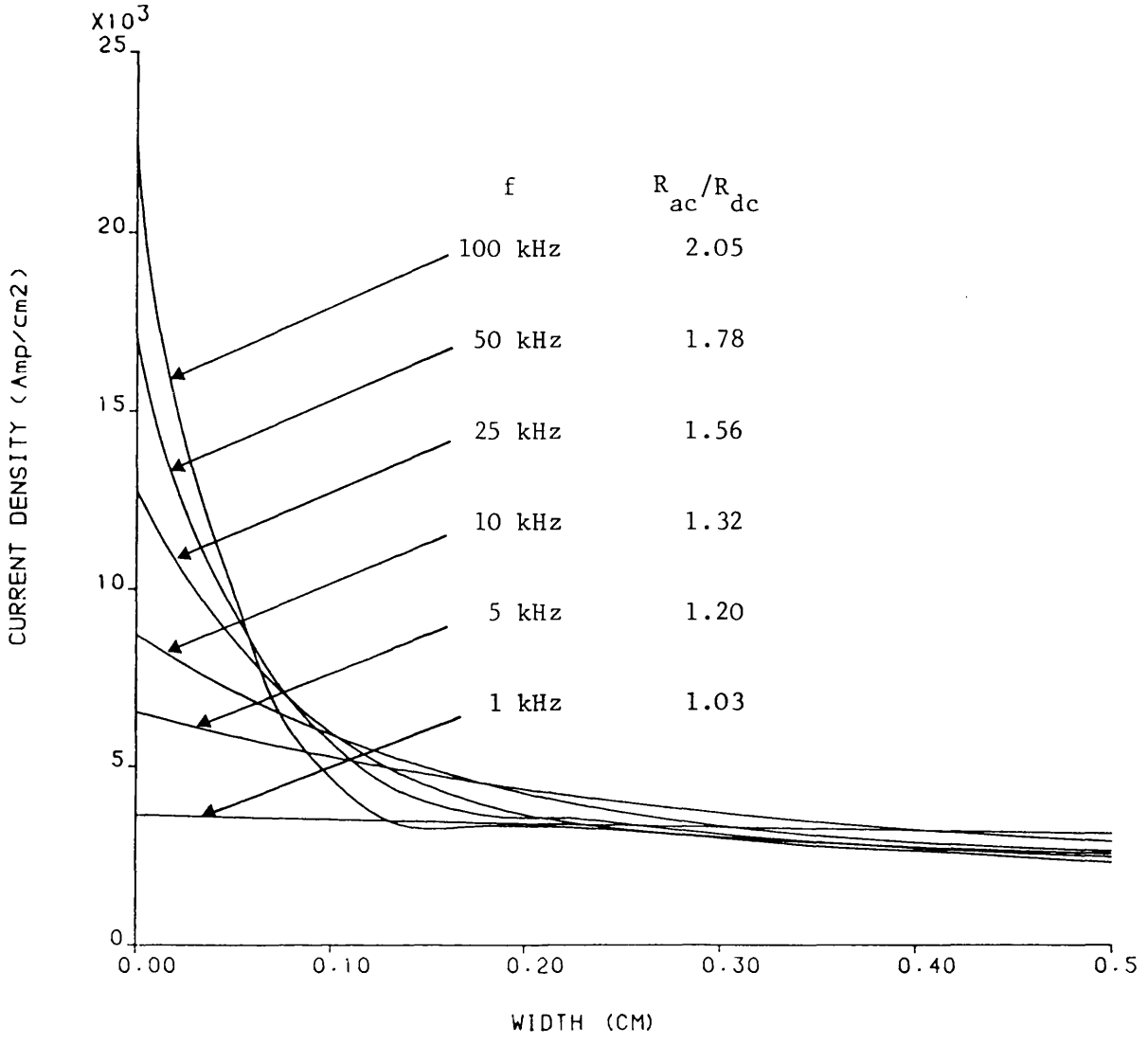

Fig.5.21: Current-density distribution at different frequencies
Example 2

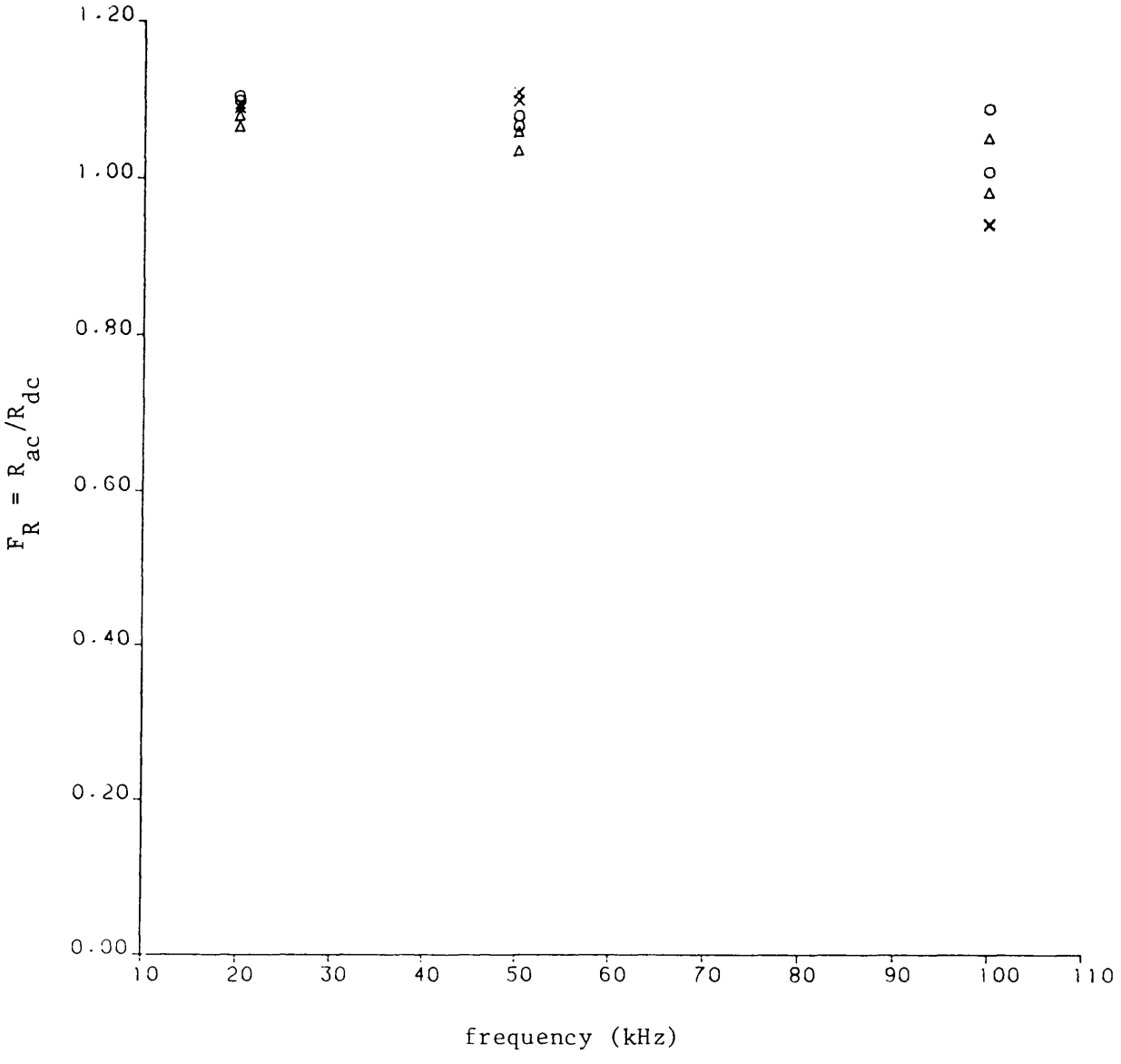

Fig.5.22: Losses in transformer winding

Δ Winding in series opposition with core

o Winding in series opposition without core

x Secondary winding short circuited with core

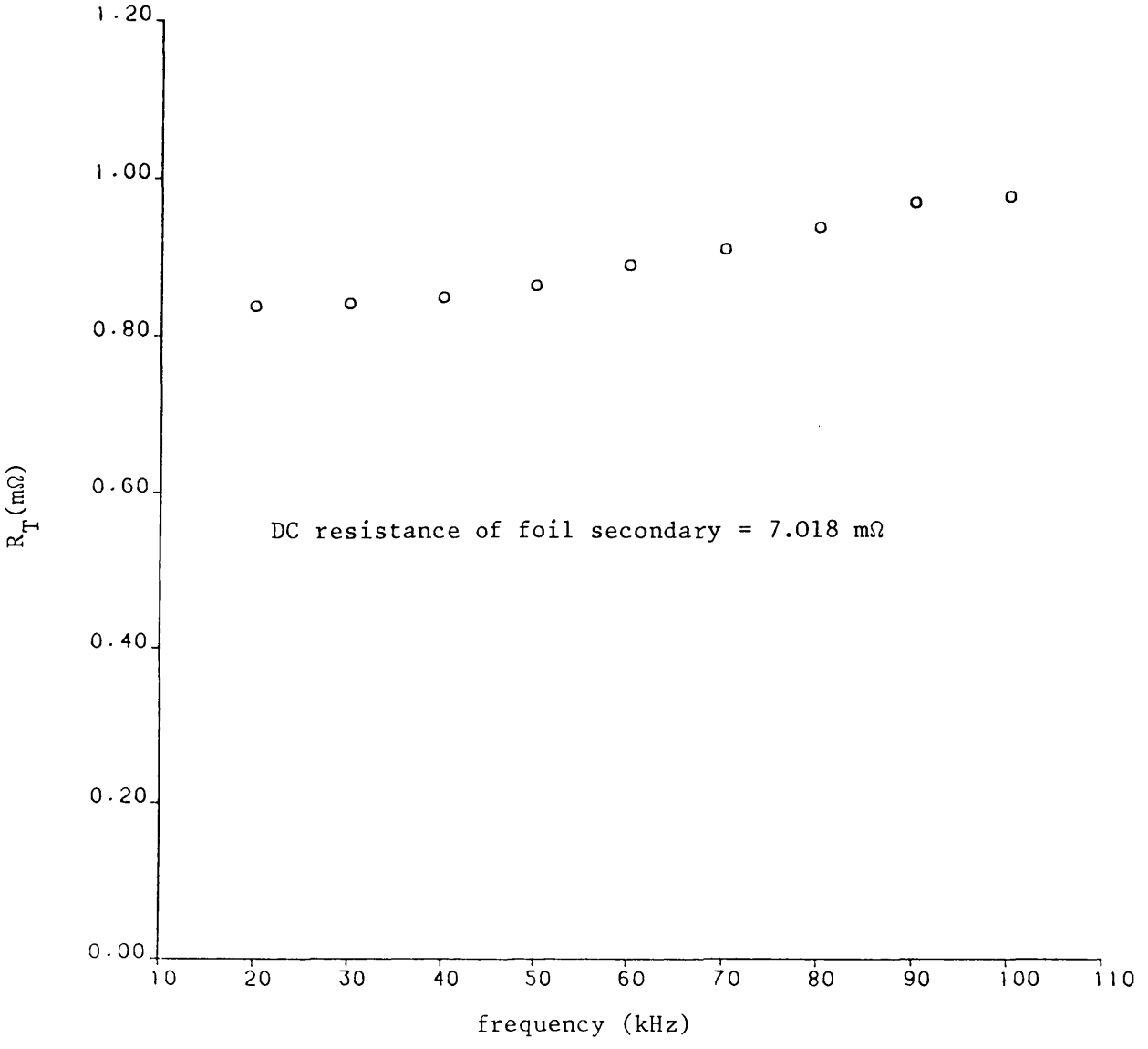

Fig.5.23: Variation of effective resistance, R_T, with frequency

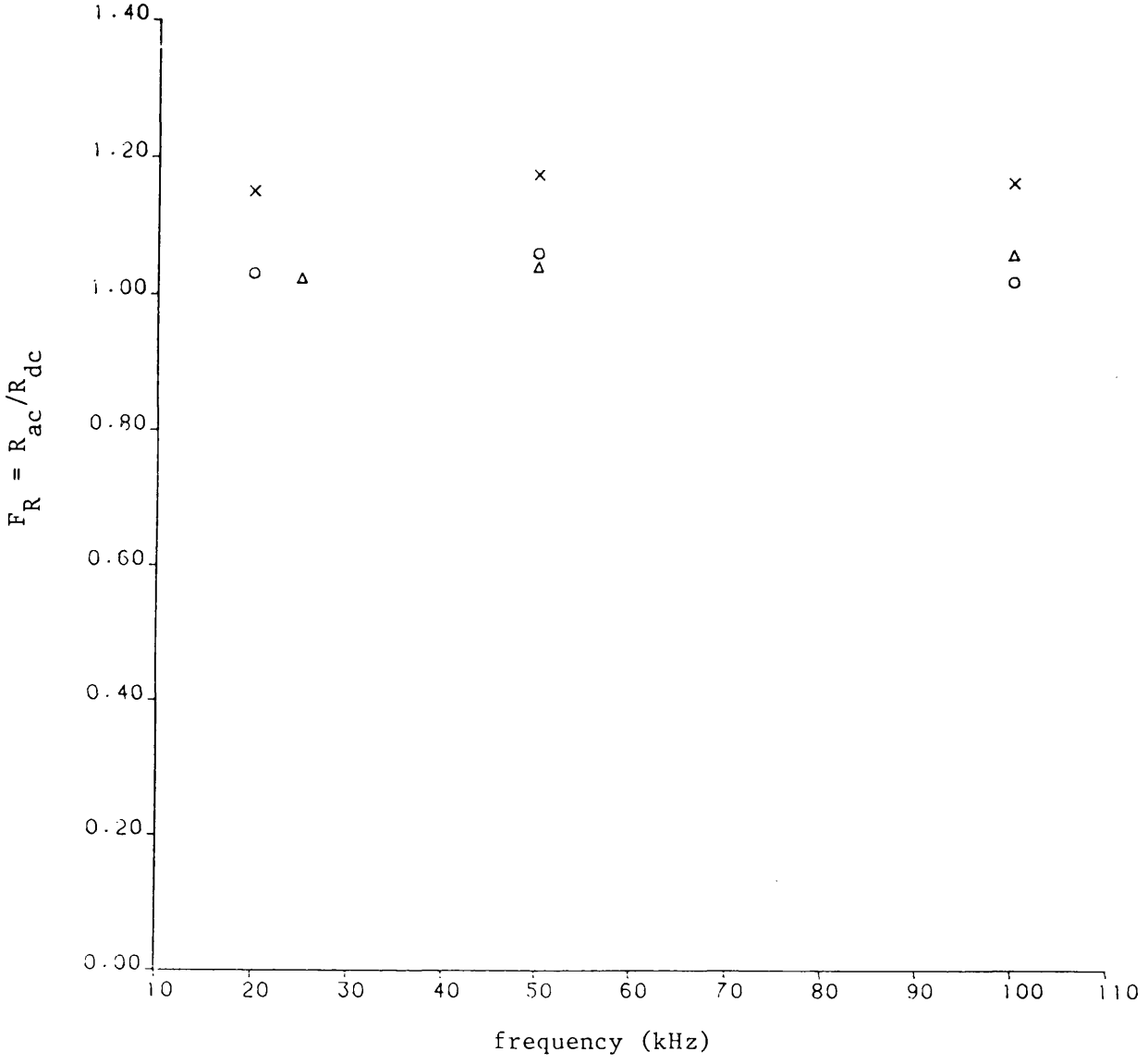

Fig.5.24: Variation of R_{ac}/R_{dc} with frequency

x Measured, without allowance made for termination loss

o Measured, with allowance made for termination loss

Δ Computed

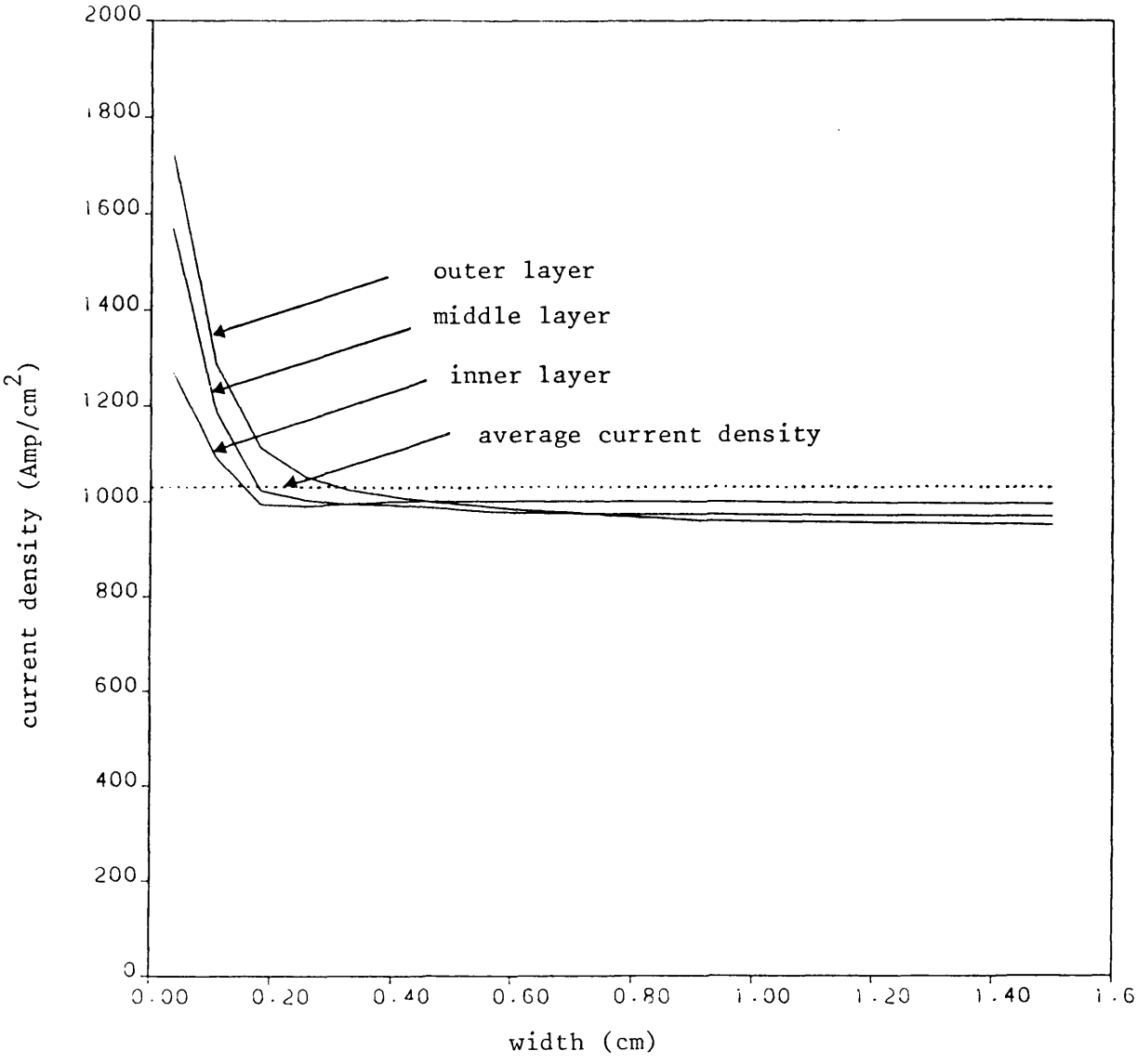

Fig.5.25: Current density distribution
f = 25 kHz
Transformer example 1

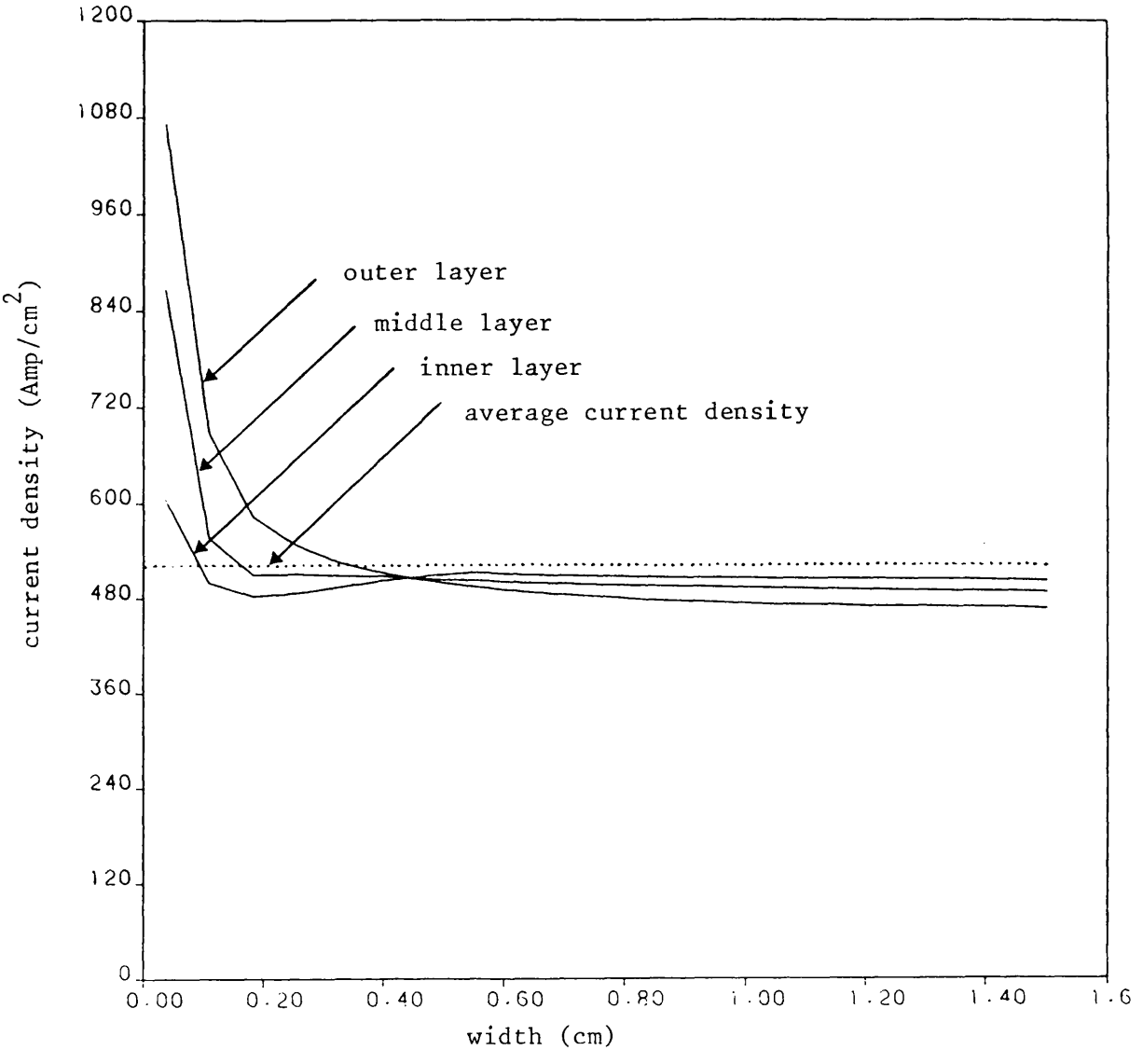

Fig.5.26: Current density distribution
f = 50 kHz
Transformer example 1

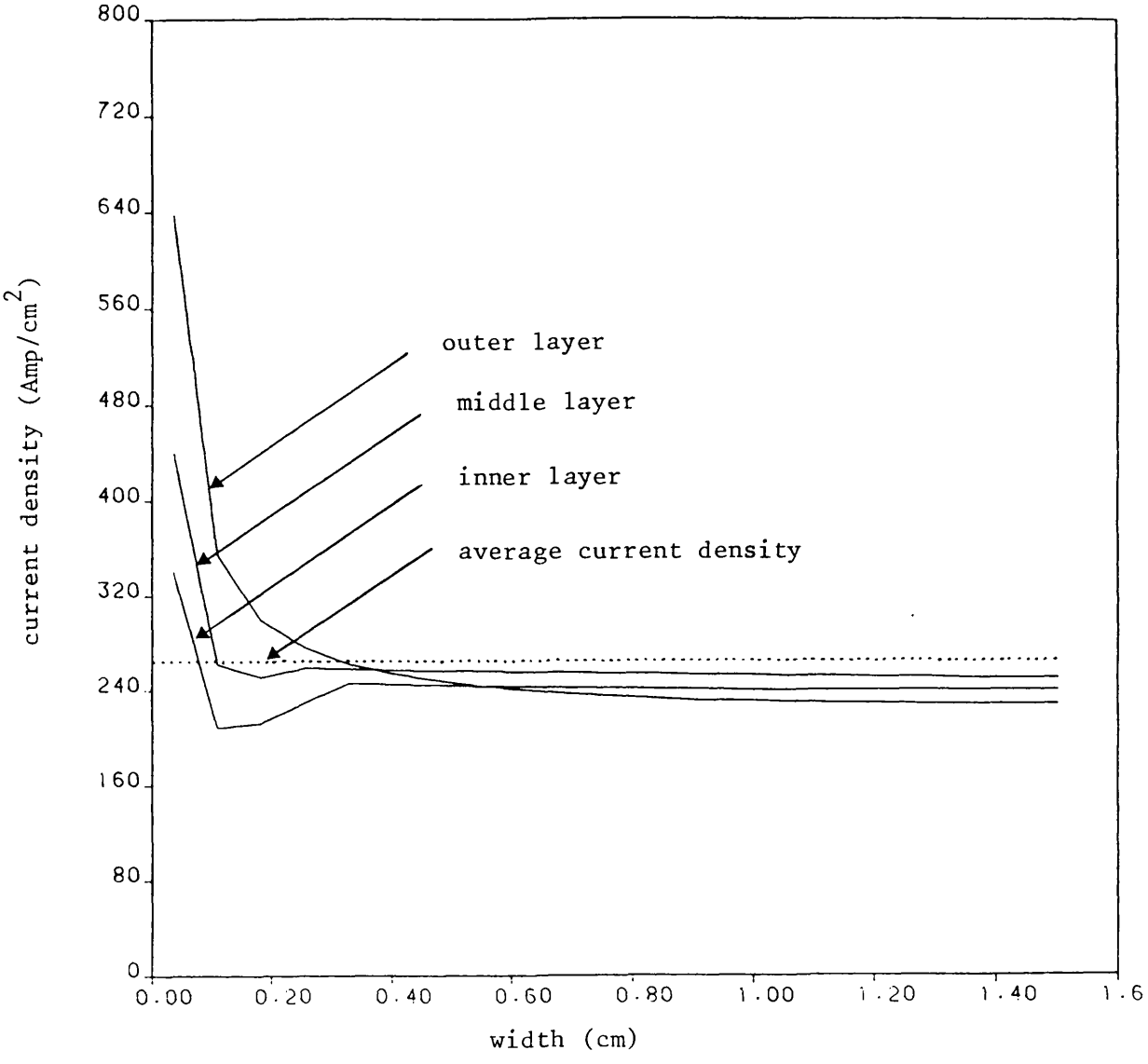

Fig.5.27: Current density distribution
f = 100 kHz
Transformer example 1

CHAPTER SIX

LOSSES IN FERRITE CORES

6.1 Introduction

The total loss produced in a wound ferrite component is the sum of the losses in the windings, the so-called 'copper losses', and the loss in the core. The copper losses, especially with regard to high frequency effects, have been given some consideration in the preceding part of this thesis. The present chapter describes a preliminary investigation of losses in the ferrite cores. The work is largely experimental, although fully supported by predictions from existing formulae, and is concerned mainly with the effect on core loss of square wave, rather than sinusoidal excitation. Two types of core were used for the work, the FX3750 (EC70/24/17) and the ETD44. They are both designed for switched-mode power supply applications and are made of the new low loss ferrite grade 3C8.

The two mechanisms for loss production in cores are hysteresis loss and eddy-current loss. The present understanding[1,2] of these loss mechanisms as they occur in ferrite cores is summarised briefly below.

i) Hysteresis loss

Hysteresis loss is caused by the magnetic properties of the ferrite material. When a cyclic variation of B and H occurs in the material an amount of energy dependent on the hysteresis loop area is dissipated in the ferrite i.e. hysteresis loss, per unit volume P_h, is given by

$$P_h = \oint H \, dB \qquad 6.1$$

This magnetic energy is converted to heat which dissipates in the crystal lattice of the material and is permanently lost. In magnetically soft material, such as soft ferrite the hysteresis loss is relatively small. Equation (6.1) above is difficult to apply, and the empirically based formula, attributed to Steinmetz[2] is more useful, i.e.

$$P_h = K_h . f^x . B_{max}^y \qquad 6.2$$

where

K_h is the Steinmetz coefficient

f is frequency

and B_{max} is maximum flux density

x and y are empirical exponents. x varies from about 1.1 at 10 kHz to 1.6 at 100 kHz. An average value of 1.3 over the range 10–100 kHz may be acceptable[1]. The fact that hysteresis loss is not simply proportional to frequency is due to distortion of internal fields in the ferrite by eddy-currents in the material. The exponent y is typically 2.5 for the 3C8 ferrite[1]. The specific hysteresis loss in equation 6.2 above is independent of core shape and size. In a core designed for uniform flux density loading throughout, then the total loss, P_H, is clearly:

$$P_H = P_h . V \qquad 6.3$$

where V is the total core volume. In cases where uniform flux density loading does not occur, such as in the FX3750, then each portion must be treated separately and

$$P_H = \Sigma P_h . V \qquad 6.4$$

Figures 6.1 and 6.2 illustrate calculated values of specific hysteresis loss, P_h, against frequency and flux density.

ii) Eddy current loss

Eddy-current loss is caused by the eddy-currents driven in a conducting material by the voltages induced by alternating fluxes. In general eddy currents at high frequencies produce a screening effect on the middle of the core with the flux being concentrated towards the outer skin. In ferrites the resistivity is so great that these effects are in fact quite small.

For the simplest case, when reaction fields do not modify the applied field, and this is approximately valid in the present conditions with the high resistivity ferrite material, then it can be shown[2] that specific eddy current loss, P_e is given by

$$P_e = \frac{\pi}{4} \frac{1}{\rho} f^2 B_{max}^2 A_e \qquad 6.5(a)$$

which is usually written in the form

$$P_e = 0.8\ f^2 B_{max}^2 A_e \qquad 6.5(b)$$

where

f is the frquency

B_{max} is the maximum flux density

A_e is the cross sectional area

and ρ is approximately 1.0 Ω.m for 3C8 ferrite

The total eddy curernt loss, P_E, is therefore

$$P_E = P_e.V \qquad 6.6$$

where V is the total volume.

The most important point about equations 6.5 is that they show the dependence of eddy-current loss on the variables involved, i.e. proportional to (frequency)^2 and (flux density)^2, and inversely

proportional to resistivity.

6.2 Calculated core losses

The total core losses, i.e. hysteresis loss and eddy-current loss were calculated for the FX3750 and ETD44 cores using the relationships 6.2 and 6.5 above. Sketches of these cores are shown in figures 6.3 and 6.4, and the dimensions and physical characteristics are given in Table 6.1 below.

While the ETD44 is designed for uniform flux density throughout its volume, the FX3750 has larger end limbs than strictly necessary for magnetic reasons, in order to contain the grooves for clamping screws. The flux density in these limbs is therefore lower than in the centre pole and this was taken into account in the calculations. Figure 6.5 shows both hysteresis loss and eddy-current loss for the FX3750 versus peak flux density and for 25, 50 and 100 kHz. It is clear that eddy-current loss is relatively small in this frequency range.

Total losses, hysteresis and eddy-current are shown for the FX3750 in Figure 6.6 versus flux density and for 25, 50 and 100 kHz.

	FX3750 (a)	ETD44 (b)	Unit
Main dimension:			
a	70.0	44.0	mm
b	16.4	14.9	mm
d_1	44.5	33.1	mm
d_2	16.4	14.9	mm
h_1	34.5	22.3	mm
h_2	22.75	16.5	mm
Core details (per pair):			
Total ferrite volume	55600	18000*	mm^3
Centre pole volume (V_{cp})	9600	5700*	mm^3
Back and leg volume (V_b)	46000	12300*	mm^3
Centre pole area (A_{cp})	211.0	175.0*	mm^2
Minimum centre pole area (A_{cpmin})	201.1	-	mm^2
Total back and leg area ($2A_b$)	386.0	175.0*	mm^2
Mean turn length ($\ell\omega$)	95.0	75.0*	mm
Magnetic characteristics:			
Magnetic path length=ℓe)	144	103	mm
Magnetic path area (A_e)	279	175	mm^2
Magnetic volume (V_e)	40100	18000	mm^3
Core factor (c_1) =$\ell e/A_e$	0.514	0.588*	

Table 6.1: Dimensions and design data for

a) FX3750 core
b) ETD44 core

* These quantities were calculated from prototype cores and were not obtained from a data sheet.

Core losses can therefore be controlled by varying flux density and frequency. From Figure 6.6 it appears that for a given core size reduced loss can be achieved in a transformer by running at a higher frequency and at a proportionally lower flux density. Thus approximately if frequency is doubled, say, then flux density can be halved and this results in lower total losses. This may be deduced from equation 6.2 for hysteresis loss, which dominates total loss, where the exponent for B_{max} is 2.5 while the exponent for the frequency is 1.3.

Figures 6.7 and 6.8 give loss components and total loss versus flux density and frequency for the ETD44 core. These show the same general trends as the FX3750 results, in particular the eddy-current loss is small compared to the hysteresis loss. In absolute terms the total loss in the ETD44 for any given set of conditions is about one-third that of the FX3750, and is a direct consequence of the smaller core volume (FX3750 - 55600 mm^3, ETD44 - 18000 mm^3).

6.3 Experimental results

A number of different sets of experimental results for core losses were obtained and they are described and discussed below. The experimental method used to obtain them is described in Appendix A2. The purpose of the test was to look at the variation of core loss with a number of parameters, such as temperature, core sample and excitation waveform and to compare these results with predictions using the methods of 6.1 above.

6.3.1 FX3750: Core losses with sinusoidal excitation at 25°C

The sets of FX3750 cores were selected at random and subjected to core loss measurements at an ambient temperature of 25°C. The results, for 25 kHz and 50 kHz excitation in Figure 6.9 show a relatively small variation from one sample to another, although the spread of results seems to be greater at the higher frequency. Bearing in mind the precision with which predictions might be made, these results suggest that variability of core loss from one sample to another is not a consideration that needs to be taken into account, by means of 'worst case' type designs.

6.3.2 FX3750: core losses with sinusoidal excitation at 100°C

The usual maximum design temperature for ferrite transformers is 100°C and this is assumed to prevail at the centre pole. For design purposes, losses at this temperature are therefore required. This was therefore undertaken by immersing the three sets of cores of the previous experiment in boiling water, and, after allowing time for steady temperatures to be achieved, repeating the core loss measurements. These results are shown in Figure 6.10. It can be seen that the generally small spread in loss results from one sample to another is maintained at the higher temperature.

Also shown on Figure 6.10 are the results presented on the Mullard Data Sheet which were derived empirically, and predictions using the method of section 6.1 above. There is a considerable degree of agreement between all three sets of results. The Mullard Data Sheet results tend to be slightly optimistic, however, in that they appear to underestimate slightly the core losses.

The predictions on the other hand tend to overestimate the losses slightly and would therefore be useful aids in the design process. The most worrying area is the predictions at 50 kHz at high flux densities where the degree of overprediction is increasing.

It is apparent that for most applications either predictions or loss data results will be adequate.

6.3.3 FX3750: Variation of core losses with temperature

The results for core 2 have been extracted from Fig.6.9 and Fig. 6.10 above and plotted together on Figure 6.11 to show the change in loss with temperature. It can be seen that variation is relatively small, generally less than 10% although at 50 kHz and at high flux densities the spread is greater.

A precise knowledge of operating temperature is therefore not critical in estimating core losses. (This contrasts with copper loss where resistance changes by approximately 40% per 100^{o}C change in temperature).

6.3.4 ETD44: Core losses with sinusoidal and square wave excitation

At the time of performing the work under discussion the ETD44 was one of a new series of SMPS cores for which only one sample was available, provided by Mullard Ltd. Comparable tests on a number of cores was therefore not possible. Neither had loss data been provided for it. Tests on this core were therefore performed to establish empirically the level of losses to be expected with it, and these tests were undertaken with both sinusoidal and square wave voltage excitation.

The square waves were produced by a purpose built single phase inverter of the outline configuration shown in Figure 6.12.

Power field effect transistors were used as the switching devices in order that the square wave was as ideal as possible, the switching times of the devices being very short, around 100 ns. Also, the centre-taped supply produced by the capacitor chain ensured that a dc component could not be applied to the core, due to switching asymmetry of the devices. It is particularly easy for this to occur at high switching frequencies and would cause unreliable results because of asymmetric flux density excursions around the BH loop.

Figures 6.13, 6.14 and 6.15 illustrate results for 25 kHz, 50 kHz and 100 kHz respectively. The basis of equivalence between the experimental results for sinusoidal and square wave excitation was that the peak flux density should be the same for both cases.

This is translated into voltage amplitudes for the two waveforms in the manner described below.

$$\text{As} \quad V = N\frac{d\phi}{dt}$$

$$\phi = \frac{1}{N}\int V\,dt$$

For the sinusoidal case $v = \hat{V}\sin\omega t$

$$\therefore \quad \phi = -\frac{1}{N}\,\frac{\hat{V}}{\omega}\cos\omega t$$

$$\therefore \quad \hat{\phi} = \frac{\hat{V}}{\omega N} \qquad 6.7$$

where

$\hat{V}$ is the peak sinusoidal voltage

ω is the angular frequency

N is the number of turns

For the square wave case

$v = V$ in any square wave half cycle

$$\therefore \quad \phi = \frac{1}{N} \int v \, dt$$

$$\therefore \quad \phi = \frac{VT}{N}$$

$$\phi = \frac{VT}{4N} \qquad 6.8$$

where T is the square wave period.

$\therefore$ For equivalence of maximum flux and flux density

$$\frac{\hat{V}}{\omega N} = \frac{VT}{4N}$$

As $\omega = 2\pi f$ and $T = \frac{1}{f}$

$$\frac{\hat{V}}{2\pi f N} = \frac{V}{4Nf}$$

$$\hat{V} = \frac{\pi}{2} \cdot V \qquad 6.9$$

It is clear that for the range of frequencies covered by the test results in Figure 6.13, 6.14 and 6.15, the losses with sinusoidal and square wave excitation are substantially similar, if the basis of equivalence described above is used. This is thought to be because the losses are predominantly hysteresis losses, so the maximum flux density obtained is more important than the actual shape of the waveform. It is interesting to note that the losses with

sinusoidal excitation are actually greater than the losses with square wave excitation, by some 5% - 10% and this result is generally maintained over the frequency range. This is thought to be due to the small eddy-current contribution to the total losses. The actual time variation of flux or flux density is sinusoidal for the sinusoidal excitation case and triangular for the square wave case. According to the equivalence suggested above the peak value of the triangular wave is equal to the peak value of the sinusoidal wave.

Eddy-current would normally be calculated harmonically, i.e. by taking each harmonic component in turn, calculating the appropriate losses and summing to obtain the total loss, providing the system was linear, which in the present case assumes that saturation effects are insignificant. To perform a harmonic analysis of the triangular flux waveform we may start with the well known square wave

$$v = \sum_{n=1,\ldots\text{odd}}^{\infty} \frac{4V}{\pi n} \sin n\omega t$$

$$\therefore \quad \phi = -\frac{1}{N} \sum \frac{4V}{\pi n} \frac{1}{n\omega} \cdot \cos n\omega t$$

$$\therefore \quad \hat{\phi}_n = \frac{4V}{\pi n^2 \omega N} \qquad 6.10$$

Comparing ϕ_1 with sinusoidal flux of equation 6.7 above we have that

$$\frac{\hat{\phi}_1}{\hat{\phi}} = \frac{4V}{\pi\omega N} \Big/ \frac{\hat{V}}{\omega N}$$

$$= \frac{4}{\pi} \frac{V}{\hat{V}}$$

but $\dfrac{V}{\hat{V}} = \dfrac{2}{\pi}$

$$\therefore \quad \frac{\hat{\phi}_1}{\hat{\phi}} = \frac{8}{\pi^2} \qquad 6.11$$

The fundamental component of the triangular waveform is clearly the most important, because harmonics decrease in amplitude with the square of the harmonic order, equation 6.11, and the amplitude of the fundamental is some 80% of the sine wave fundamental. Hence the slightly lower total loss with square wave excitation than with sinusoidal excitation.

Also shown on Figures 6.13, 6.14 and 6.15 are the measured square wave excitation losses, adjusted for a basis of equivalence that the fundamental amplitude of the square wave voltage waveform was equal to the sinusoidal voltage waveform. This clearly gives no basis of equivalence and is in any case inconsistent with the argument given above.

The results of Figures 6.13, 6.14 and 6.15 are summarized in Figure 6.16 where the relative loss levels of the frequency range 20 kHz - 100 kHz can be seen. It is clear that the calculated losses provide a reasonable basis for prediction with both excitation waveforms, providing that peak flux is used in the calculations.

6.4 Conclusions

This chapter has described an investigation of the losses in ferrite cores. A number of different sets of experimental results were obtained. Measurements were carried out using both sinusoidal and square wave excitation. Calculations were carried out using the equations recommended by a Philips publication[2].

A consistent trend is clear, that the losses with sinusoidal excitation are slightly greater, by 5% - 10%, than square wave losses.

Predictions by the accepted method[2] are reasonably close to sets of measurements, although they tend to underestimate losses at lower frequencies and at lower flux densities.

The method of calculating the losses are suitable over the practical range of operating frequency, for both sinusoidal and square wave excitation, providing that the peak flux is taken as the basis of comparison. However, bearing in mind the complexity of the mechanism producing the losses, and the empirical nature of the exponents used in the calculations, extrapolation to conditions outside those considered, especially frequency, would have a limited confidence factor unless supported by suitable experimental evidence.

6.5 References

1. Snelling, E.C.: "Ferrite for Inductors and Transformers", Research Studies Press Ltd., Letchworth, Hertfordshre, England, 1983.
2. Bracke, L.P.M.: "High frequency ferrite power transformer and choke design, part 2: switched-mode power supply magnetic consideration and core selection", Electronic Components and Materials (Philips Publication), September 1982.

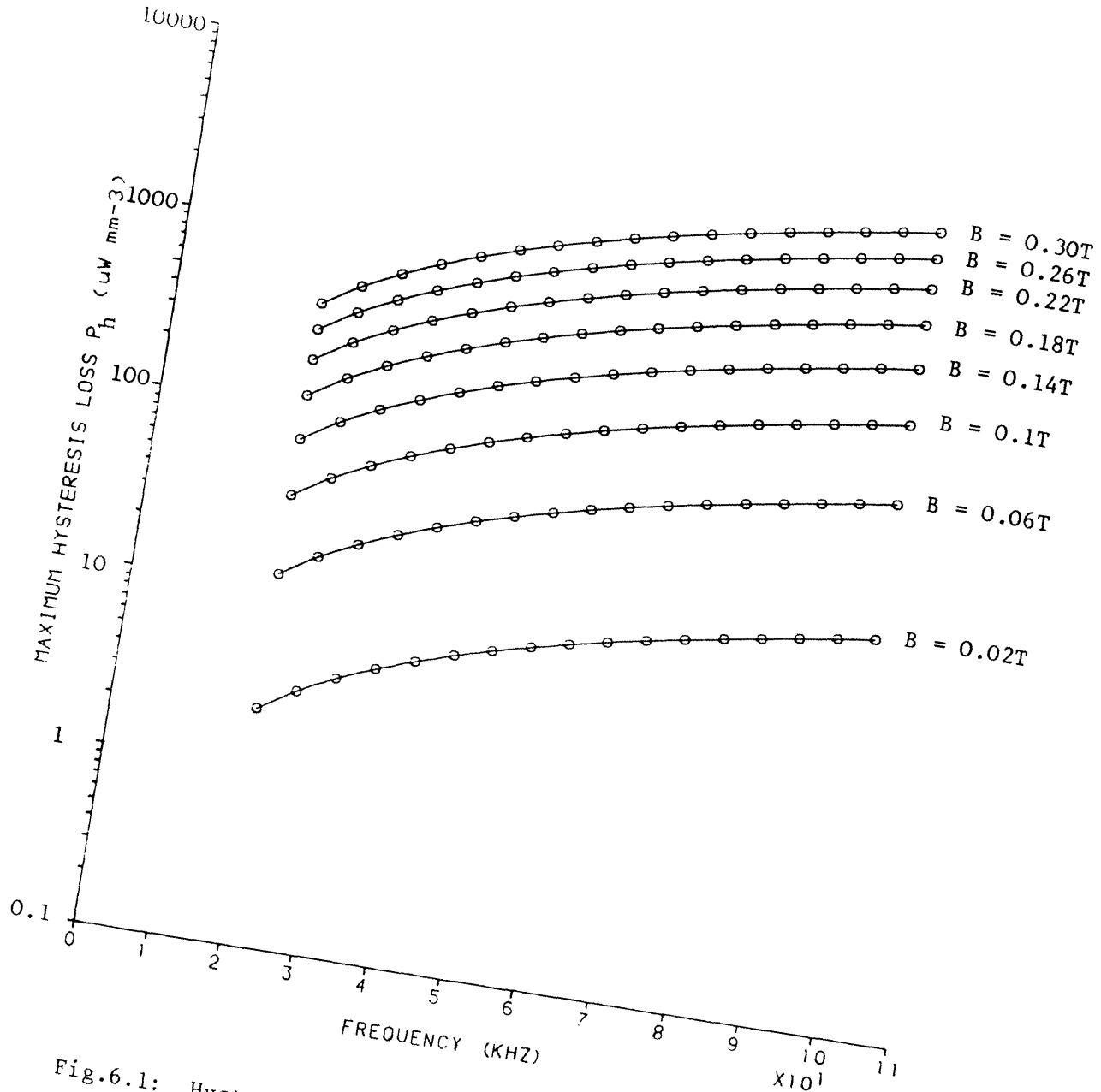

Fig.6.1: Hysteresis loss density as a function of frequency for ferrite material (3C8)

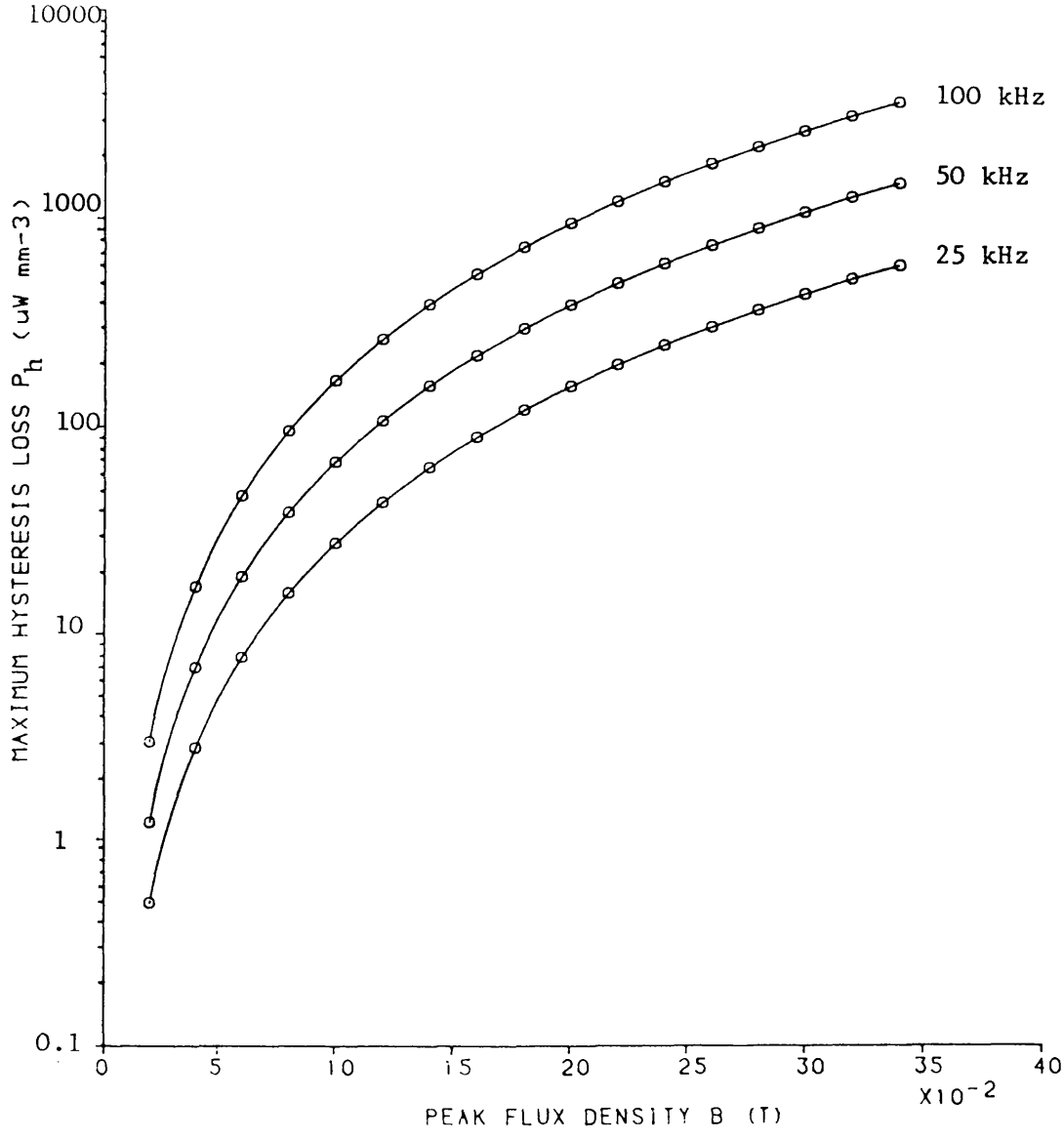

Fig.6.2: Hysteresis loss density as a function of peak flux density $\hat{B}$ for ferrite material

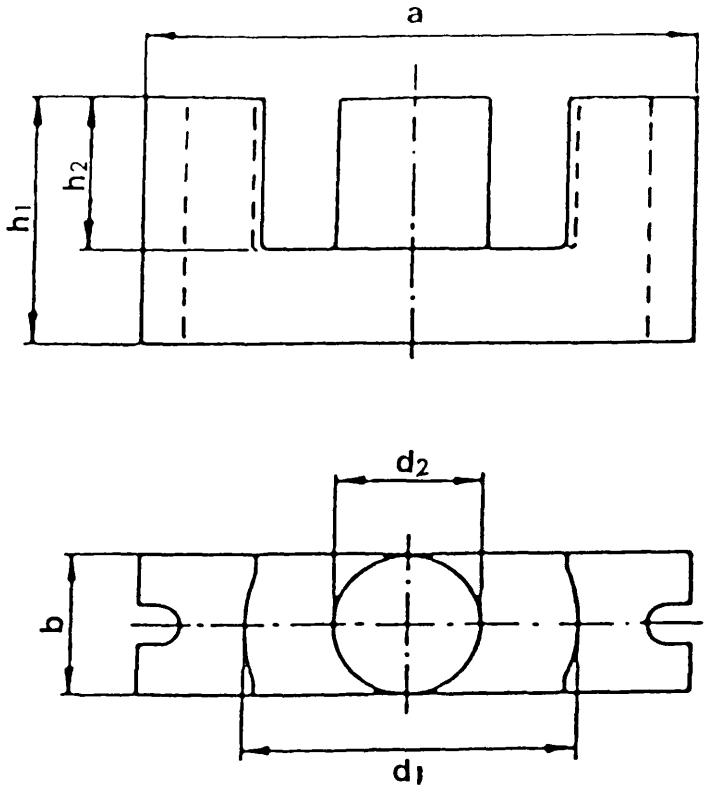

Fig.6.3: Dimensions of fully-wound FX3750 core

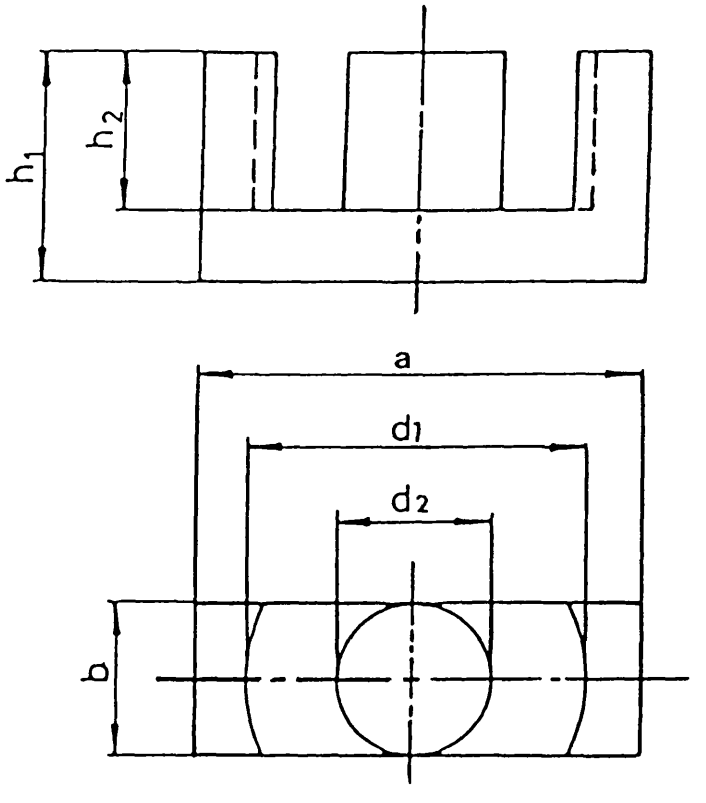

Fig.6.4: Dimensions of fully-wound ETD44 core

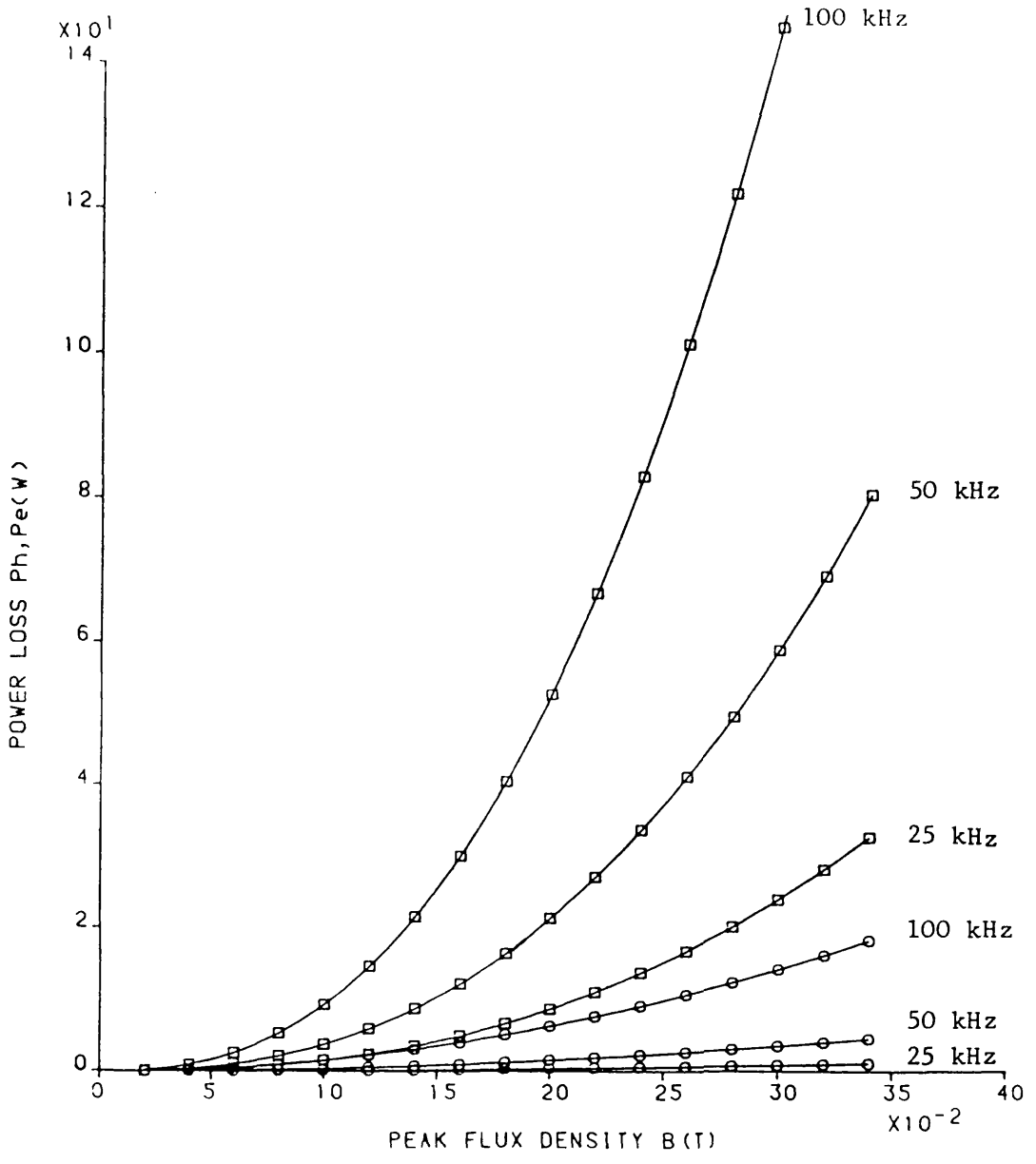

Fig.6.5: Hysteresis and eddy-current losses for FX3750 core

⊡—⊡—⊡ hysteresis loss

o—o—o eddy-current loss

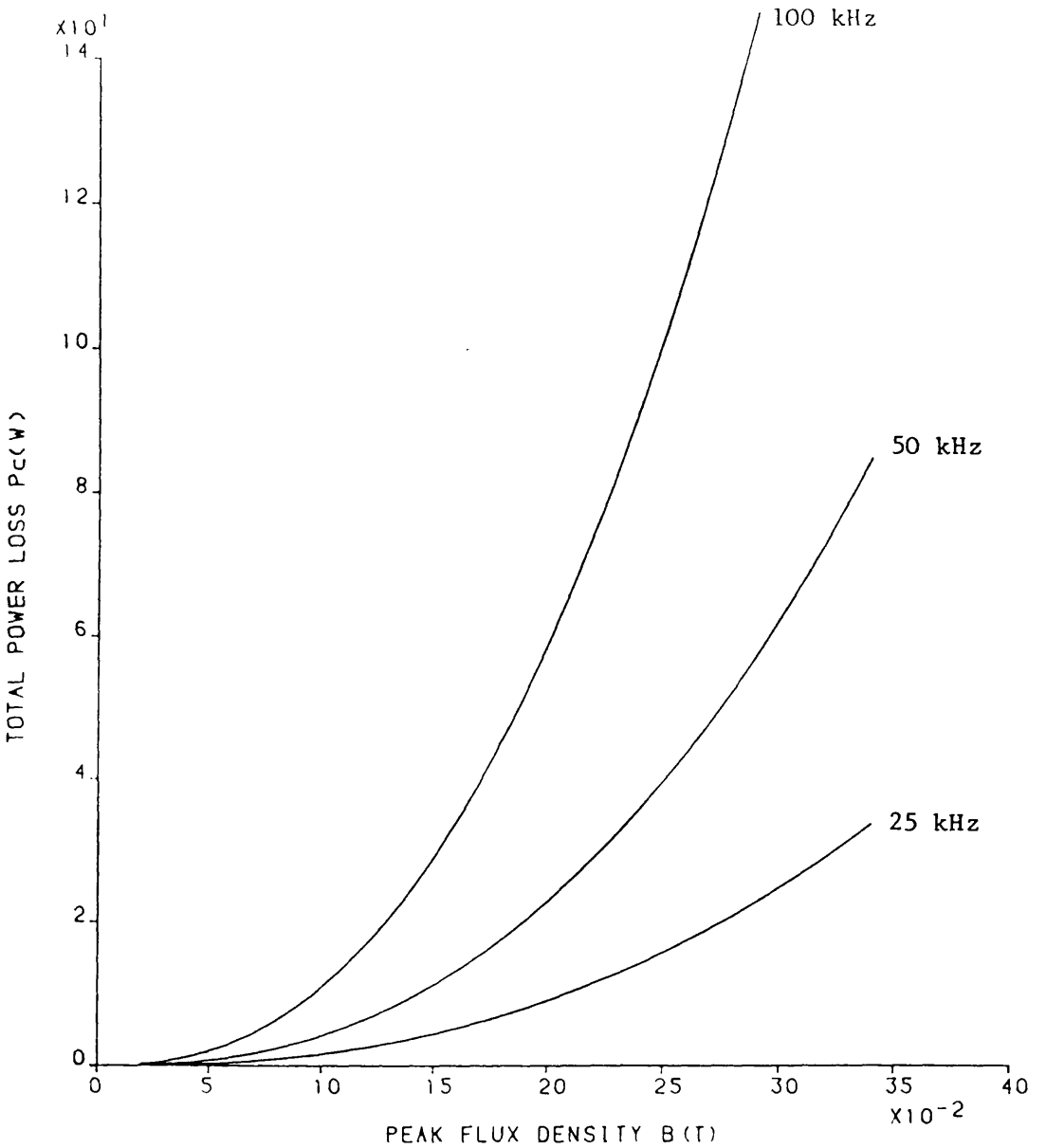

Fig.6.6: Total core losses for FX3750 core

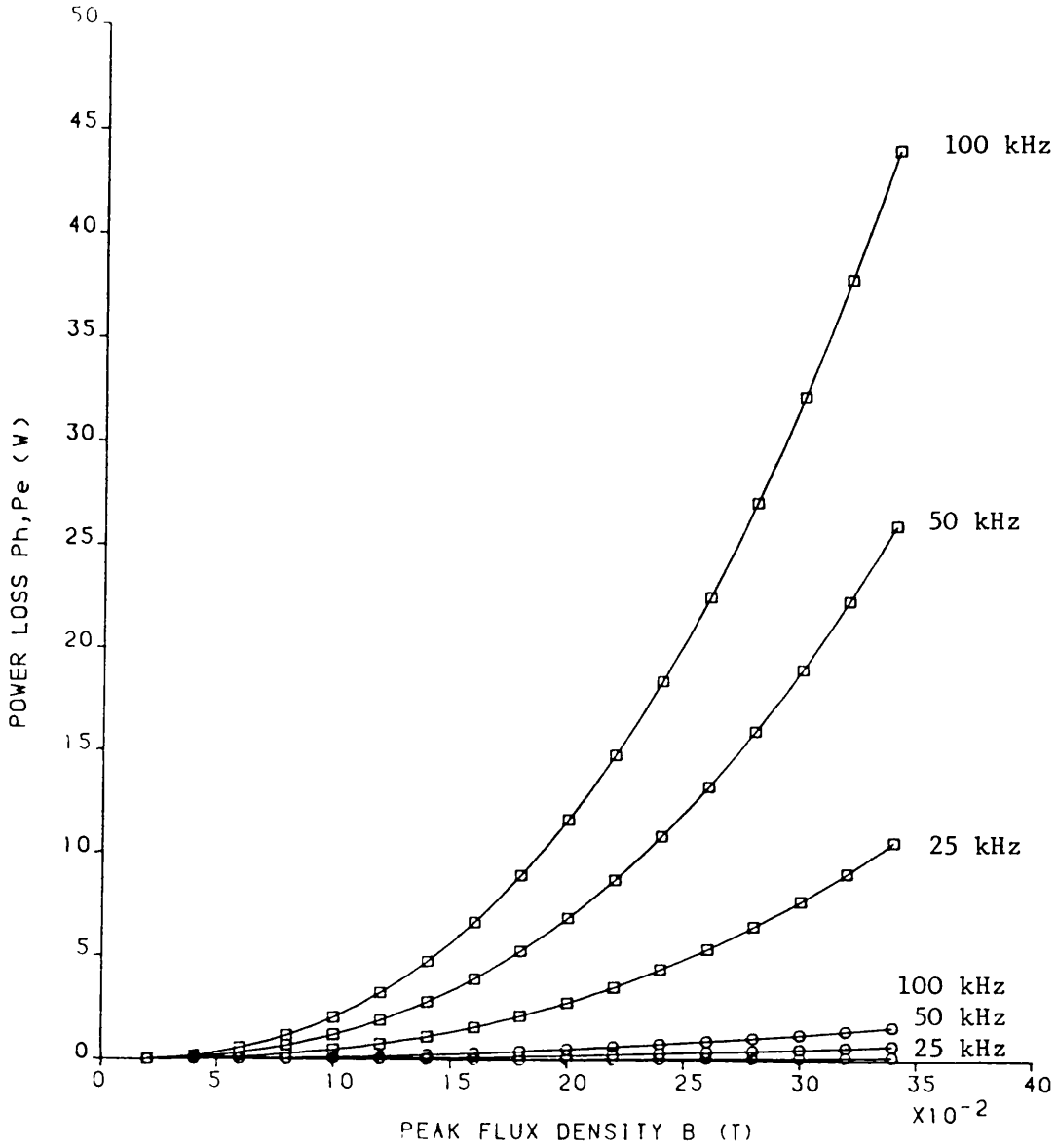

Fig.6.7: Hysteresis and eddy-current losses for ETD44 core

⊟⊟⊟ hysteresis loss

⊙⊙⊙ eddy current loss

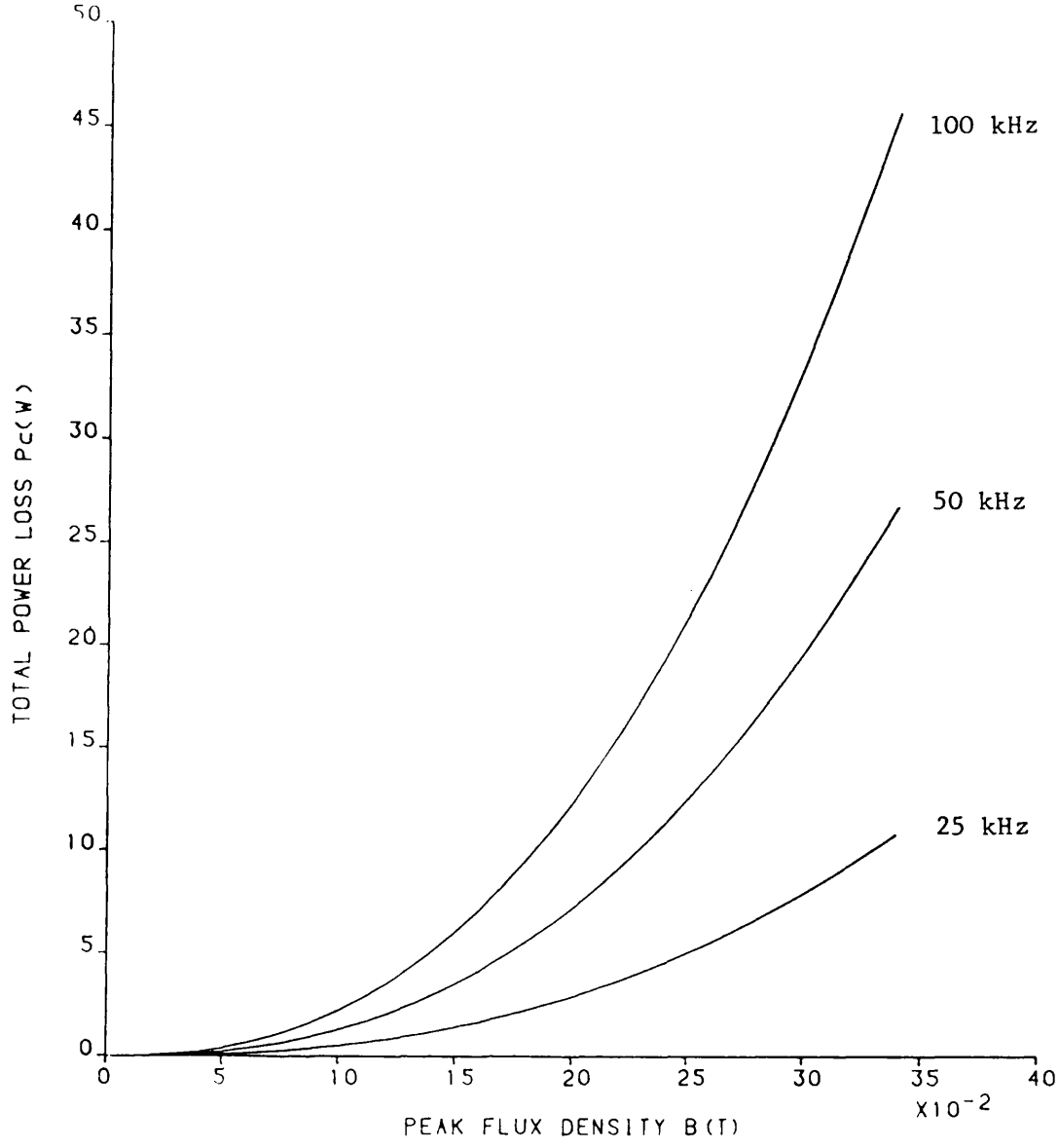

Fig.6.8: Total core losses for ETD44 core

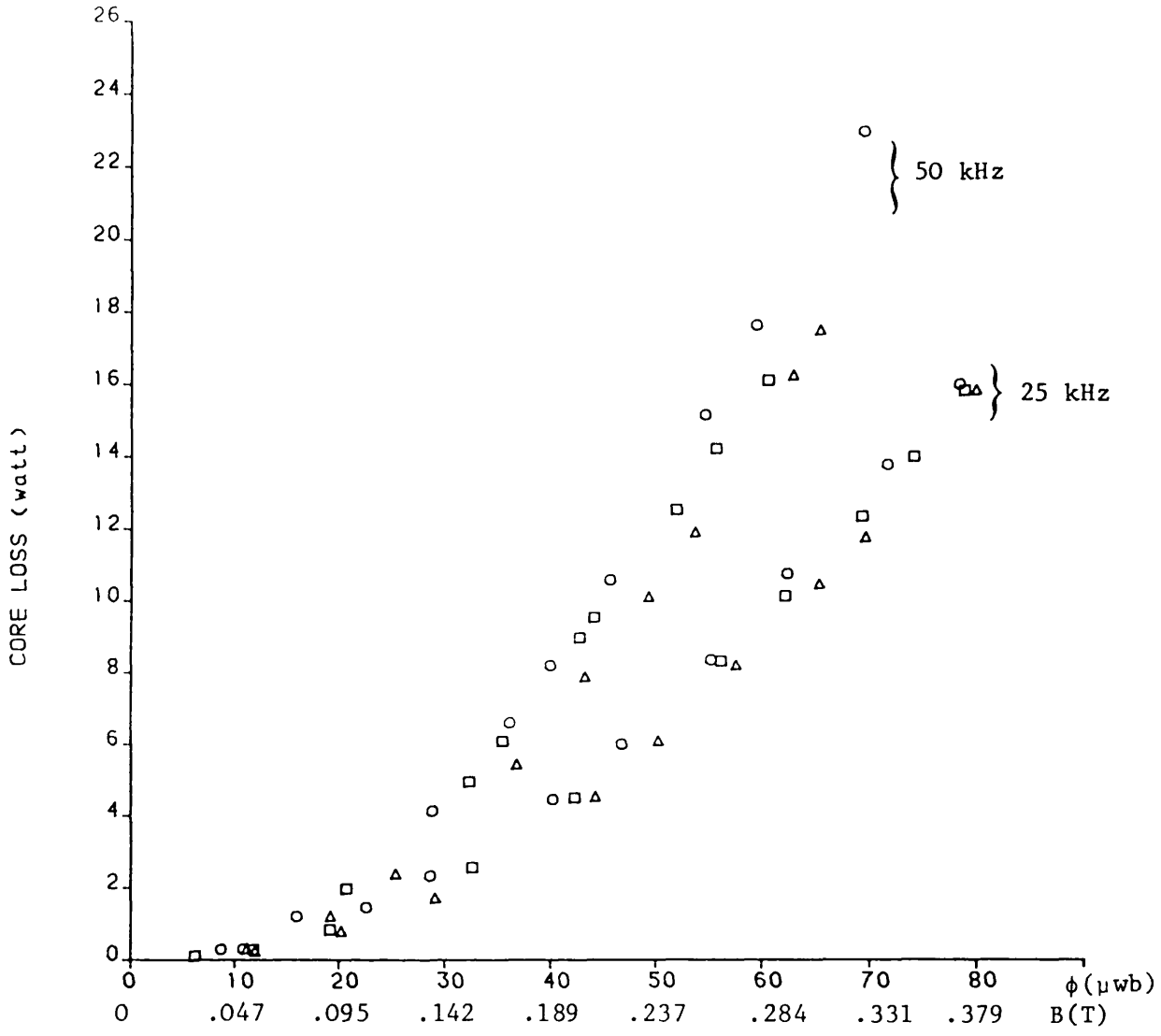

Fig.6.9: FX3750: core losses with sinusoidal excitation at 25°C. Results for three sets of cores selected at random core1 (o), core2 (□), core3 (Δ)

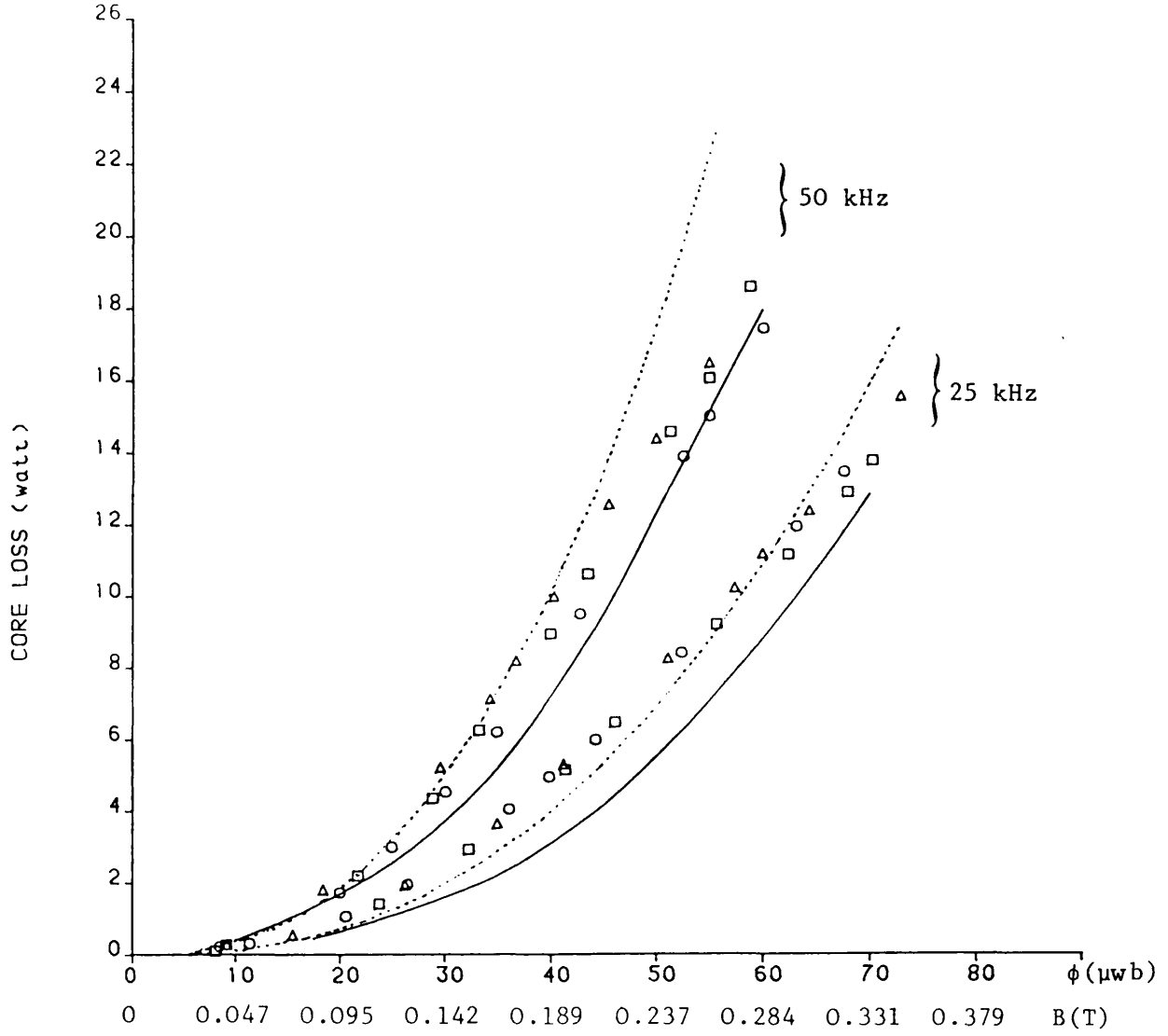

Fig.6.10: FX3750: core losses with sinusoidal excitation at 100°C
Results for three sets of cores selected at random
core1 (o), core2 (□), core3 (Δ)

——— Mullard data sheet results

. . . Calculated results using Equations 6.4 and 6.6

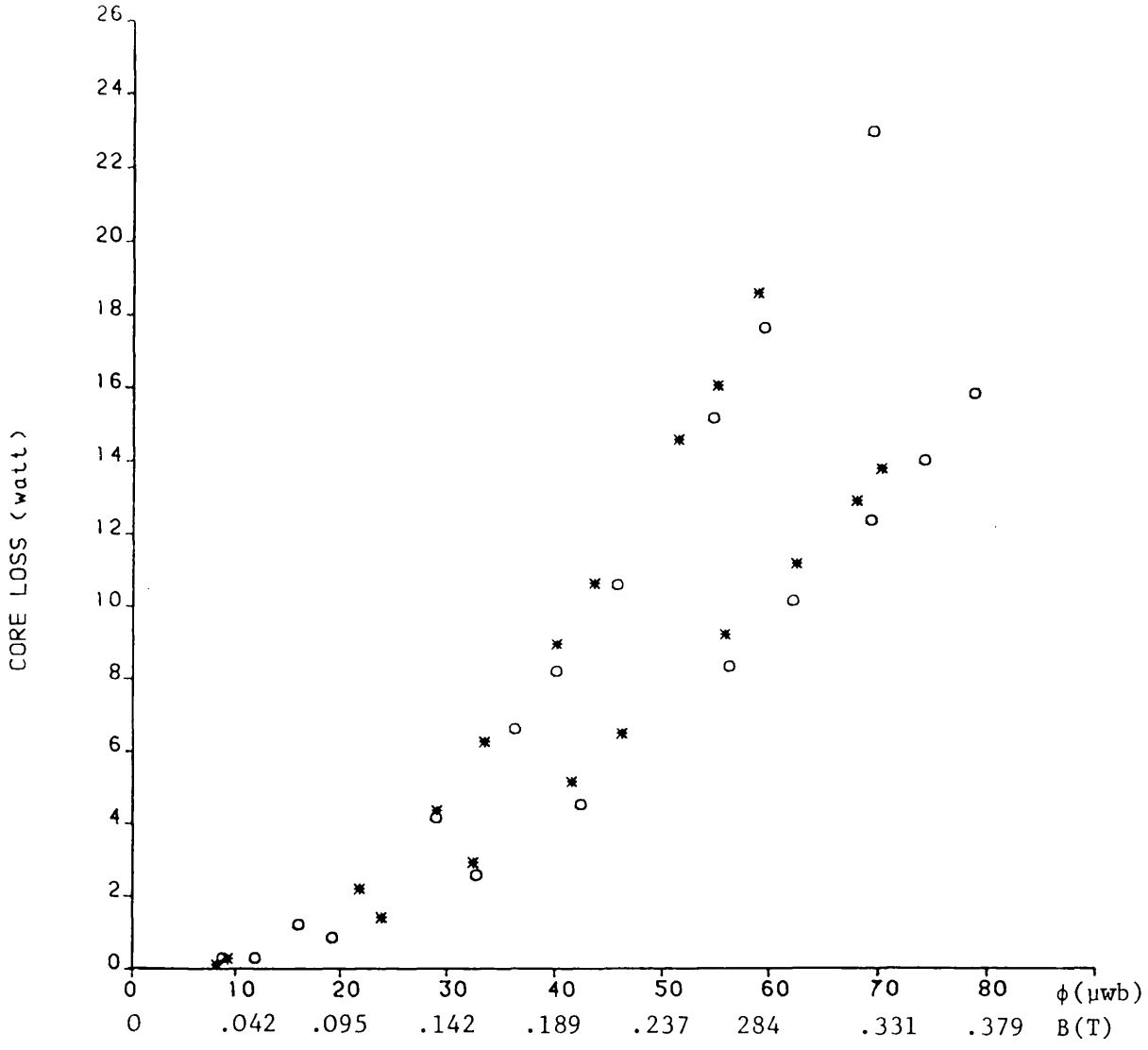

Fig.6.11: FX3750: Variation of core losses with temperature. sinusoidal excitation

core 2 o 25°C

* 100°C

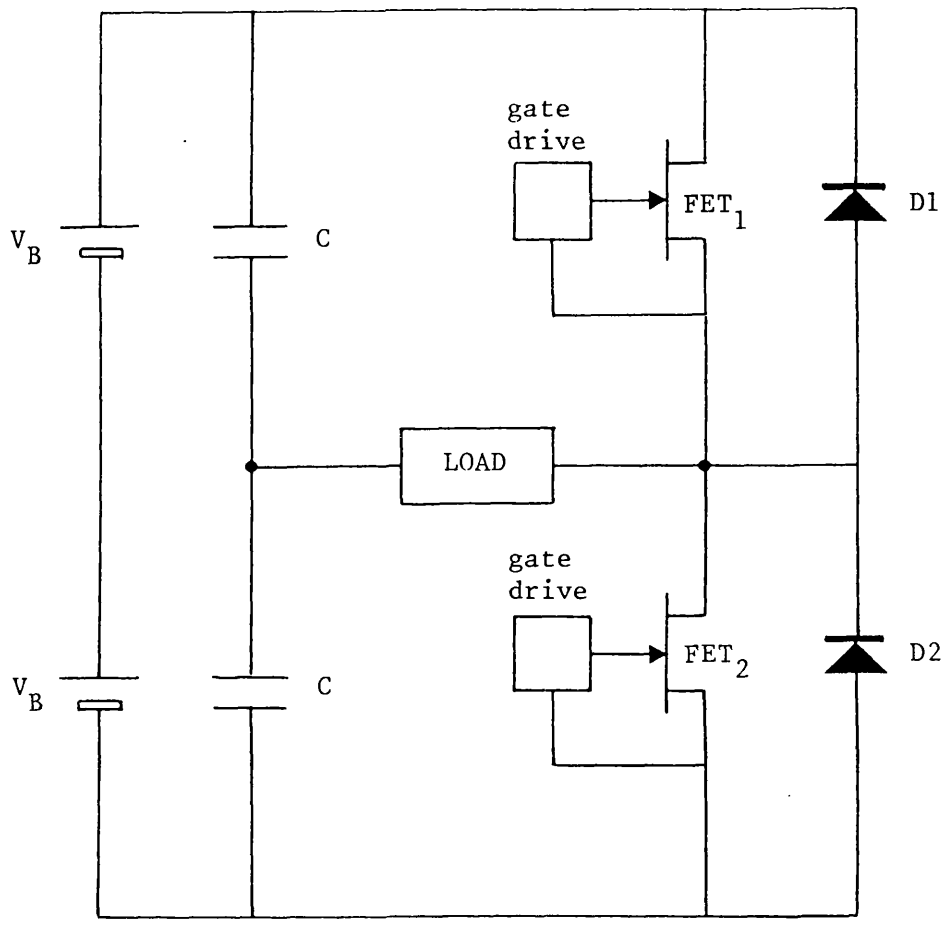

Fig.6.12: Configuration of single phase inverter

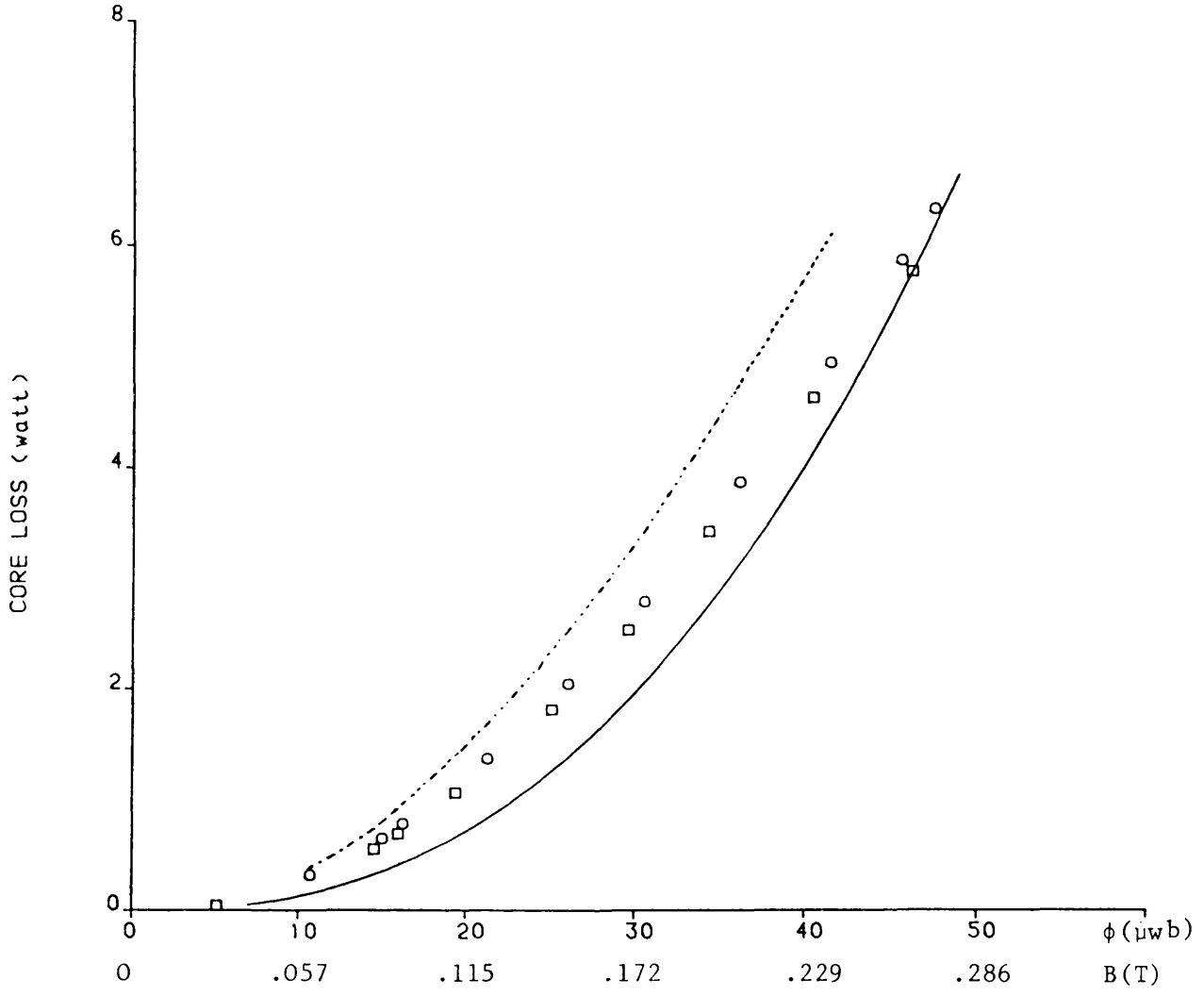

Fig.6.13: ETD44: core losses at 25°C, 25 kHz

o o o o sinusoidal excitation

□ □ □ □ square wave excitation

——— predictions

. . . . square wave excitation losses plotted against amplitude of fundamental

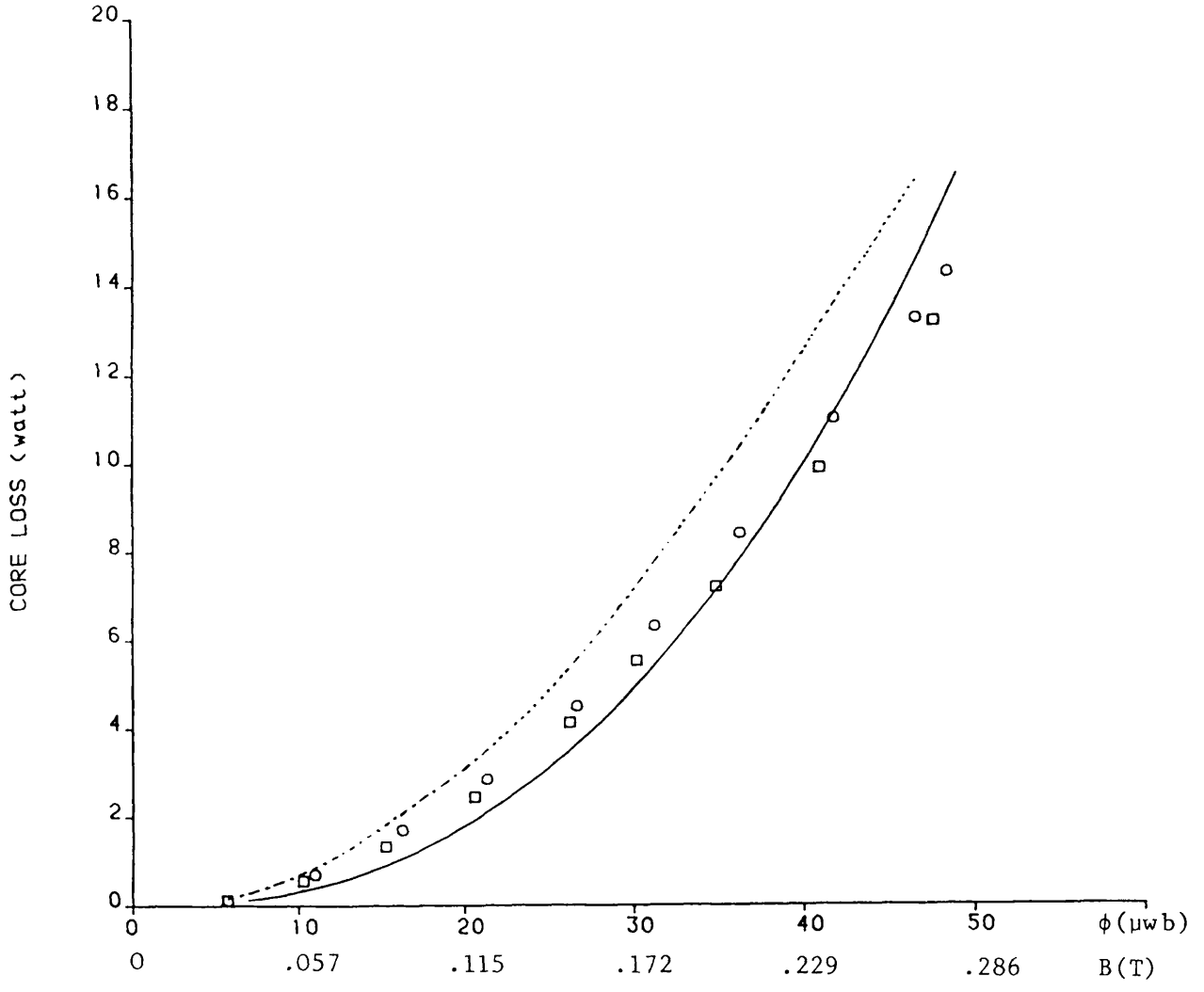

Fig.6.14: ETD44: core losses at 25°C, 50 kHz

o o o o sinusoidal excitation

□ □ □ □ square wave excitation

——— predictions

. . . . square wave excitation losses plotted against amplitude of fundamental

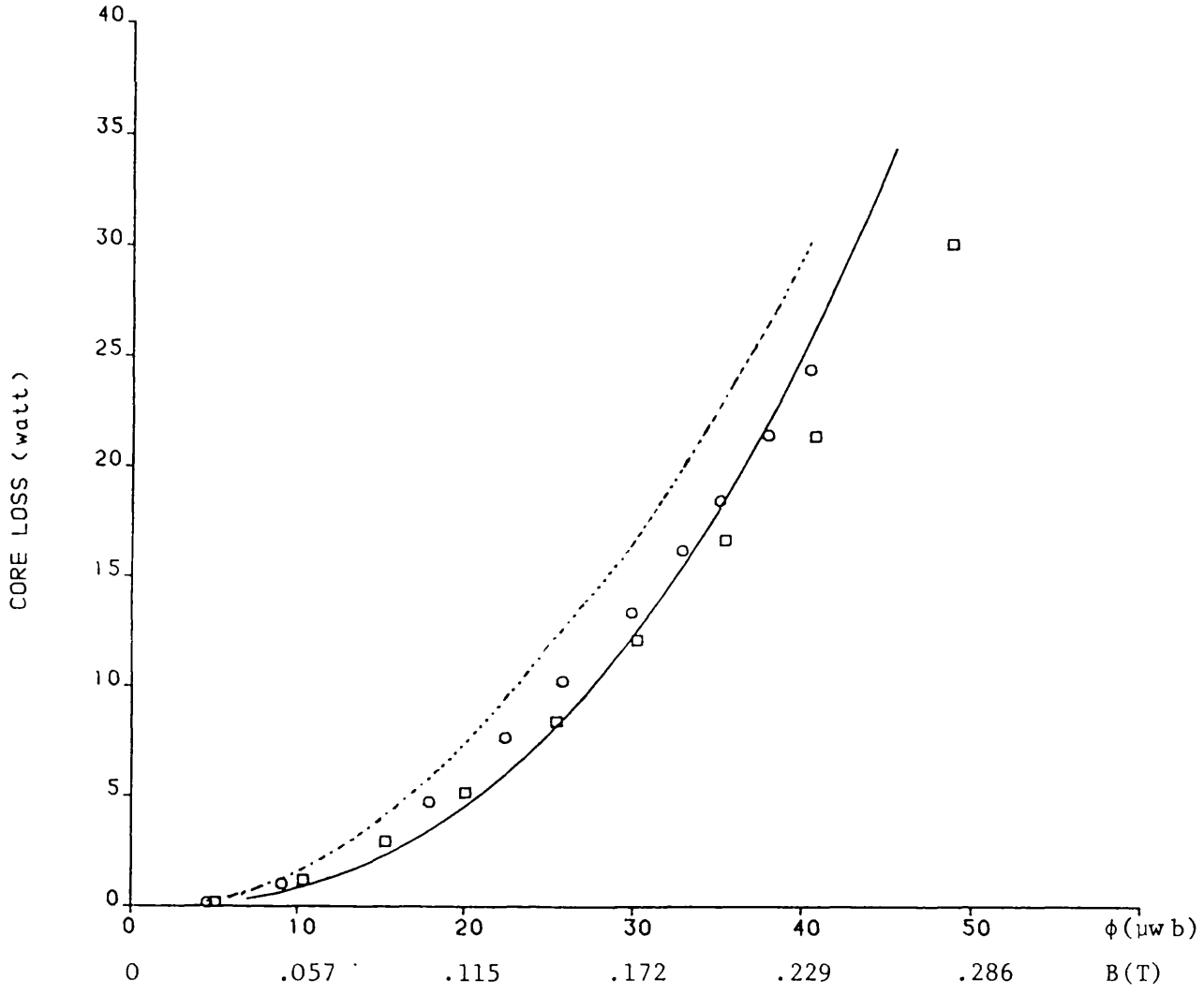

Fig.6.15: ETD44: core losses at 25°C, 100 kHz

o o o o sinusoidal excitation

□ □ □ □ square wave excitation

——— predictions

. . . . square wave excitation losses plotted against amplitude of fundamental

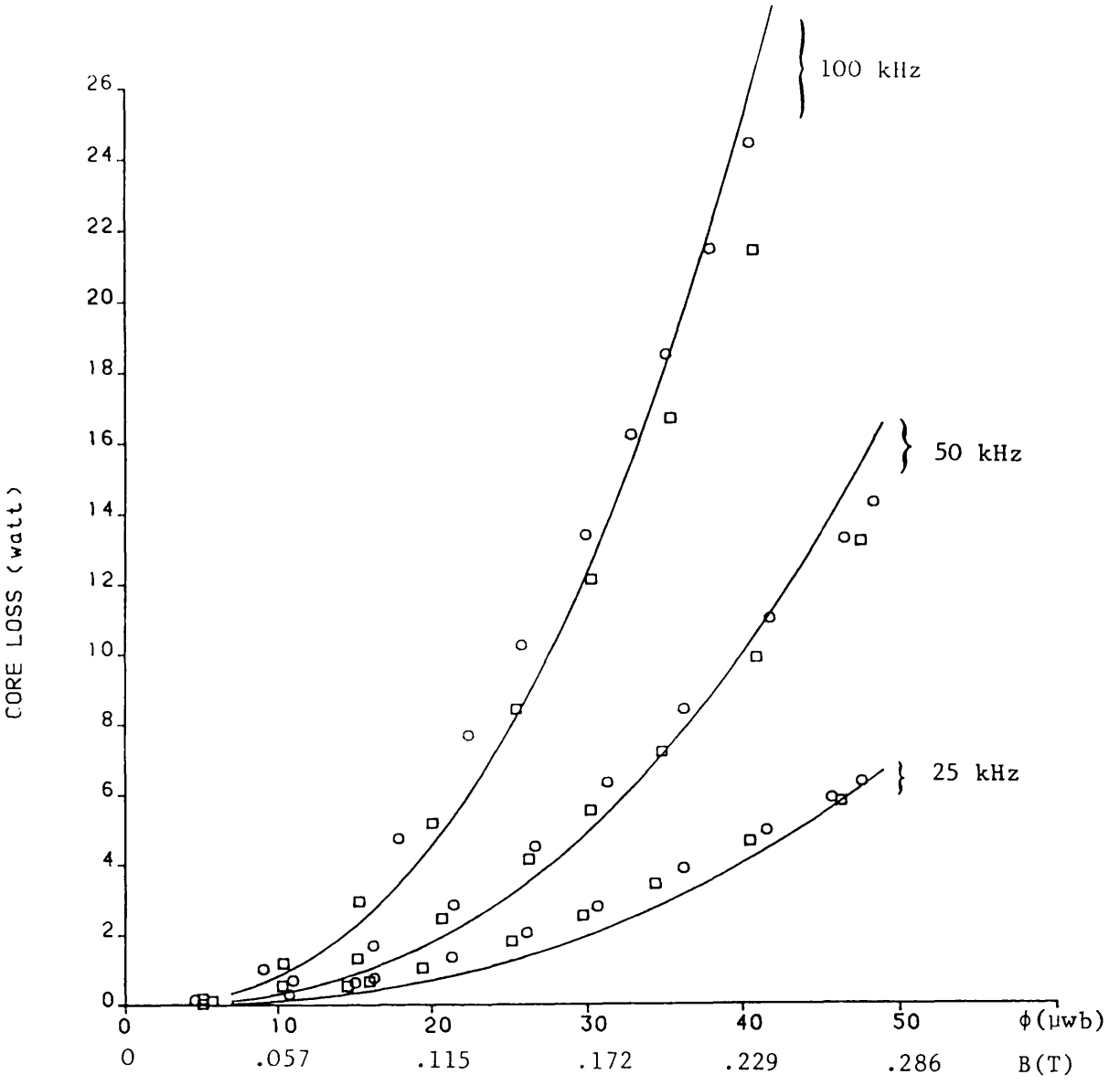

Fig.6.16: ETD44: core losses with sinusoidal and square wave excitation ($25^{o}C$)

o o o o sinusoidal excitation

□ □ □ □ square wave excitation

——— predictions

CHAPTER SEVEN

CONCLUSIONS

In recent years there has been a great increase in the use of switched-mode power supplies (SMPS) for all types of equipment. These supplies operate at high frequencies, typically 20 kHz to 100 kHz, and all use inductors and transformers, for filtering, voltage insulation and voltage transformation.

There is in general a need for greater understanding of these wound components in order that improved designs can be produced. The work presented in this thesis has defined and examined a few of the electromagnetic problems of wound components. Chapter 2 used 'TOSCA', a three dimensional magnetostatic finite element computer package to compute the fields in and around typically ferrite cores. Experimental measurements demonstrated that this technique was reliable.

The leakage fields were given particular attention because they are mainly responsible for eddy-current losses which increase the total copper loss in the windings at high frequencies. A number of points of interest were noted. First, the leakage fields can be reduced in the expected way by using 'sandwich' windings rather than 'simple' windings. Secondly, radial leakage fields are of the same order of magnitude as axial leakage fields. Although radial leakage fields are normally neglected in these types of analysis for the reason that they are not too important when round conductors are

used, they are obviously significant with foil or strip type conductors and are responsible for current in these conductors to be concentrated towards the outer edges. Thirdly, in a transformer, where primary and secondary ampere-turns are very nearly equal and opposite, the leakage fields are almost independent of whether the ferrite core is present or not.

This led to the idea, which was explored in Chapter 3 that conductor eddy current losses are approximately the same whether or not the ferrite core is present provided primary and secondary ampere-turns are the same. This was established to be the case for both round wire and foil conductors. It therefore allowed a coupled circuit model for foil conductors to be developed in which the conductors were assumed to be in air. This considerably simplifies the calculation of self and mutual inductances. The coupled circuit model used the normal technique of subdividing the foil conductor into thin circular coaxial filament coils, which were sufficiently small so that current density in them could be assumed to be uniform.

In view of the very large number of equations that has to be solved a formal method of solution was developed. This used the set of canonical equations, together with a connection, or transformation matrix which contained information about the interconnection of the separate circuits. It was shown how multiturn air-cored foil wound inductors and transformers with foil wound secondaries could be handled by the same technique, the only difference from one model to another being the transformation matrix.

Chapter 4 studied alternative methods of calculating the self and mutual inductance of circular coaxial filament coils in air. It was found that the Maxwell, the analytical method was most reliable, by comparing results with measurements.

Chapter 5 presented, measured and computed results for R_{ac}/R_{dc} for two examples of air-cored multiturn foil wound inductors and one transformer example with a foil wound secondary. It was shown in each case that the agreement is quite close, although further work with a wider range of examples would help to increase confidence in the method.

Chapter 6 was concerned with a different aspect of ferrite components, namely the loss in the ferrite core itself, especially under non sinusoidal excitation conditions. It was shown that there was no great variability of loss from one core to another, or with temperature between 25°C and 100°C. Also that equations for hysteresis and eddy current loss could be used with care over a restricted range of frequency and flux density, providing that suitable values of empirical constants and exponents were applied.

The loss with sinusoidal and square wave excitation was found to be approximately the same providing that the peak flux density was taken to be the basis of comparison. It is clear that the electromagnetic problems associated with the change of high frequency wound components are very severe and there is scope for much further work in this field.

APPENDIX A1

DESCRIPTION OF 3D STATIC ELECTROMAGNETIC/ELECTROSTATIC ANALYSIS 'TOSCA' PACKAGE

A1.1 Introduction

TOSCA is a program which uses the finite element method for the solution of partial differential equations in regions with prescribed boundary conditions. TOSCA uses a combination of the total and reduced scalar potentials of three dimension non-linear static electromagnetic field problems. The total scalar potential is one that represents the total field, e.g. $H = - \nabla\psi$[1].

Reduced potential must be used in regions where the currents are non-zero, total potential can be used elsewhere.

The two types of potential are exactly coupled at any interface by the field continuity conditions.

A1.2 Formulation of the defining equations

A1.2.1 Basic equation of non-linear magnetostatics[1]

The classical problem of magnetostatics field theory starts with the set of Maxwell's equations describing the non-linear magnetostatic field.

$$\text{Div } B = 0 \qquad \text{A1.1}$$

$$\text{Curl } H = J \qquad \text{A1.2}$$

where B is the magnetic induction, H the field intensity and J the current density, which is a known function. The magnetic induction and the field intensity are related by a constitutive equation of the form

$$B = \mu(H)(H - H_C) \qquad \text{A1.3}$$

where μ is the material permeability, for non-linear problem μ is a function of H and in general it may be a tensor. H_C is the material coercive field. In 'soft' magnetic materials the coercive field intensity is normally assumed to be zero, 'hard' magnetic materials e.g. permanent magnets, have a non-zero coercive field intensity.

A1.2.2 Derivative of the magnetic scalar potential

If in region of space

$$\text{curl } H = 0 \qquad \text{A1.4}$$

then H can be represented as the gradient of a scalar potential

$$H = -\nabla\psi \qquad \text{A1.5}$$

The scalar potential ψ whose gradient gives the total field will be called the total scalar potential.

If in the region of space

$$\text{curl } H \neq 0$$

the field at a point is expressed as the sum of the field (H_s) from current sources and (H_m) the field from induced magnetization sources.

$$H = H_m + H_s \qquad \text{A1.6}$$

H_m can be represented as the gradient of a scalar potential (the reduced scalar potential)

$$H_m = -\nabla\phi \qquad \text{A1.7}$$

The reduced scalar potential (ϕ) is given by the volume integral

$$\phi = \frac{1}{4\pi} \int_{\Omega j} \frac{M.|r - r'|}{|r - r'|^3} \, d\Omega j \qquad \text{A1.8}$$

The field H_s can be evaluated for any prescribed currents by evaluating

$$H_s = \frac{1}{4\pi} \int_{\Omega j} \frac{J \times |r - r'|}{|r - r'|^3} \, d\Omega j \qquad \text{A1.9}$$

where J is the current density and $|r - r'|$ is the distance from the field point r and the source point r' and Ωj is volume containing currents.

From equations (A1.1) and (A1.3), therefore

$$B = \mu_o \mu (H_s + H_m)$$

$$B = \mu_o (\mu H_s - \mu \nabla \phi)$$

$$\text{Div} \frac{B}{\mu_o} = - \text{Div } \mu \nabla \phi + \text{Div } \mu H_s = 0$$

or

$$\text{Div } \mu \nabla \phi = \text{Div } \mu H_s \qquad \text{A1.10}$$

and

$$\nabla \mu \nabla \phi - \nabla \mu H_c = \rho \qquad \text{A1.11}$$

where ρ scalar volume charge.

These equations are coupled by

$$\mu_1(- \nabla \psi - H_c).n = \mu_2(H_s - \nabla \phi).n \qquad \text{A1.12}$$

and

$$- \nabla \psi.t = (H_s - \nabla \phi).t \qquad \text{A1.13}$$

at an interface between total and reduced potential volumes.

Where n,t are normal and tangent direction in order to give the best possible results reduced potential volumes should have constant permeability therefore equation A1.10 reduced to

$$\nabla^2 \phi = 0 \qquad \text{A1.14}$$

These equations are solved by using the Galerkin and Weighted residuals procedures. These procedures are applied independently to the reduced and total potential regions and the residual, expressions

are then combined by requiring weight continuity across the interface and imposing the continuity boundary conditions. In TOSCA the basic finite-element used is the iso-parametric brick with either 8 or 20 nodes. The user is allowed to specify fixed potential, normal derivative and periodicity boundary conditions and the method allows specification of volume charge density in electrostatics and permanently magnetised materials for magnetostatic problems.

TOSCA's facilities and features are extensively given in the 'TOSCA User Guide'[2], however a summary is provided below.

A1.3 The SCARPIA pre-processor (data preparation)

The SCARPIA pre-processor, which works in the PRIME computer at the Rutherford Appleton Laboratories, enables users interactively to prepare the formatted data set required by the TOSCA analysis program. The philosophy of the pre-processor is that, since most 3D structures can be divided by a series of planes to give similar section geometries, then it is possible to perform the reverse proces, namely, defining a 2D geometric profile and extending in the 3rd dimension to produce a solid object.

The user builds up a geometric profile in the first plane (termed the "base plane") from quadrilaterals, modelling both material and whatever surrounding air space is required, and then extends from the base plane in the normal direction to a series of planes (called "mesh planes") containing the same connectivity of quadrilaterals as the base plane but allowing variation of profile by movement of the vertices of the quadrilaterals.

When defining the base plane, the user must take care to provide sufficient quadrilaterals to define all the variations of geometry in any other mesh plane, change in material may also be specified in each 'block plane' (i.e. a section of material lying between two mesh planes).

The user is then able to define boundary conditions, current-carrying conductors and magnetic material properties in the model and display all or part of it to check that geometry material and boundary conditions are all correct.

If the user requires to change block subdivision, materials or boundary conditions this is easily possible.

When the user is satisfied with model the TOSCA data can be generated. Additional information on output requirements and periodicity conditions must be supplied at this stage.

There are (17) commands available to the user, which may be divided into (3) broad categories: data generation, file handling and program administration. All commands may be abbreviated to the first 4 characters of their name as follows:

COMMAND TYPE	NAME
Data generation commands	DEFIne MODIf COIL@COND BHDA DISPlay EDIT CLEAr OUT3
File handling commands	READ ATTAch WRITe DELEte CNAMe LIST
Program administration commands	DEVIce HELP END

To obtain further information on any command e.g. Purpose, parameters etc, see 'TOSCA User Guide'[2].

A1.4 Analysis program

The program is launched to run on the central IBM computers. The IBM version of the analysis at RAL is limited to about (10-11) thousand nodes for 8-node bricks, or 4-thousand nodes with 20-node bricks. The IBM 3081 can solve 11.000 nodes in 1.75 Mbytes. Maximum core is 5 Mbytes, this allows approximately 22.000 nodes with quadratic elements.

Approximate times for analysis at RAL are

nodes	run-type	solution CPU time (minutes)
1000	linear	0.5
1000	non-linear	1.5
4000	linear	6
4000	non-linear	15
8000	linear	15
8000	non-linear	45

These times are only average as the requirement is strongly dependent on the number of conductor elements, the number of interface nodes, and the number of field calculations.

A1.5 The post-processor (POSTTOSCA)

The post-processor has been written to interactively give the user a limited amount of information on results from the TOSCA analysis. It permits the user to examine fields, scalar potential, permeability/permittivity and particle trajectories in (2) and (3) dimensions within the output meshes given to the analysis code. However, it is not possible to display the associated geometry and, consequently, interpretation of the results produced may be difficult.

There are 13 commands in the post-processor which may be subdivided into 3 categories: result file processing, file handling and program administration (similar to SCARPIA). The commands are:

Command Type	Names
results file processing	LOAD GETB GETVal MAB SHOW TRACk DISPlay CLEAr
file handling	ATTAch LIST
program administration	DEVLcs END

All commands may be abbreviated to their first 4 characters. If it is required to use the same command consecutively more than once, it is sufficient to only give the altered parameters. A list of the parameters for each commands are given by 'TOSCA user Guide'[1].

A1.6 References

A1.1 Simkin, J. and Trowbridge, C.W.: "Three-dimensional non-linear electromagnetic field computations, using scalar potentials", Proc.IEE, Vol.127, Pt.B, No.6, November 1980.

A1.2 Armstrong, A.G.A.M., Riley and Simkin, J.: "TOSCA User Guide", 3D Static Electromagnetic/Electrostatic Analysis Package, Version 3.1, May 1982.

APPENDIX A2

EXPERIMENTAL METHOD FOR POWER LOSS MEASUREMENT

All power loss measurements, both core loss and ac copper loss were undertaken by one general method, the equipment for which is illustrated in Figure A2.1. The heart of the technique is a digital storage oscilloscope (DSO), a Nicolet, Explorer II, type 2090-II. It is a two channel instrument which is capable of sampling at up to 20 points per microsecond on both channels. The DSO was equipped with an IEEE bus so that all stored data could be transferred to a microcomputer Commodore, a CBM Model 8032. The sample under test was fed from a power amplifier via a transformer which was used for impedance matching, but also ensured that dc was not applied to the test sample. The principle of the method was to store v and i for the sample under test, then read their values into the microcomputer, multiply them to obtain instantaneous power, and average over a cycle to derive average power.

The method is essentially quite simple, but the highly inductive nature of most loads - the power factor angle was typically between 85^{o} and 88^{o} - meant that considerable care had to be taken with measurements. Apart from the usual experimental precautions, two effects were found to be significant. First, all measurements were carried out at a known temperature, at which the ac resistance of the coils were known. In addition the raw experimental data v and i were used to calculate the fundamental Fourier component from which power calculations were subsequently made.

This removed the effect of any dc offset due to the DSO and removed a possible source of phase error between the two waveforms.

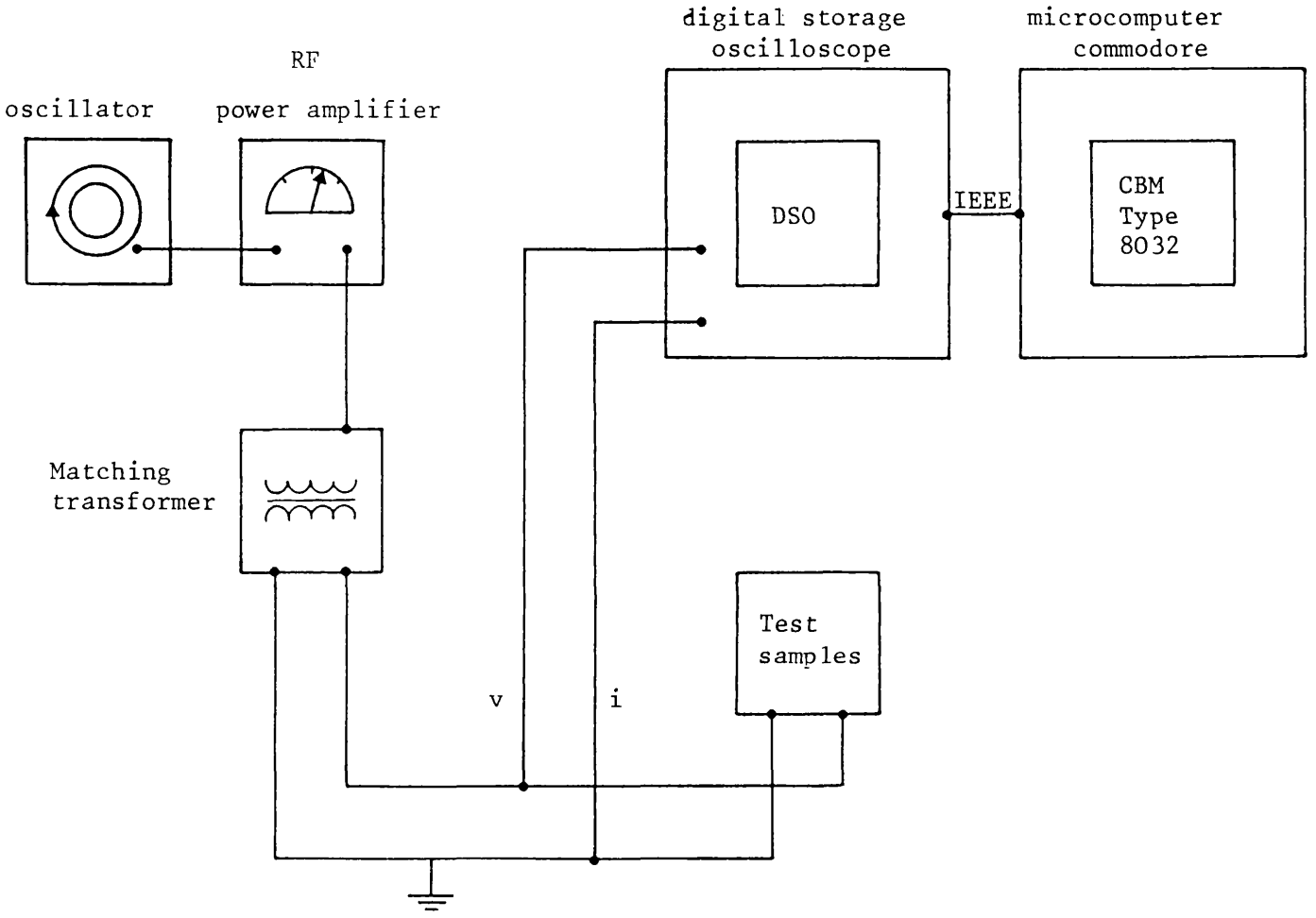

Fig.A2.1: Block diagram of experimental set up

APPENDIX A3

Directory of Computer Programs

Name	Thesis Reference		Description
	Chapter	Section	
1. Dowell	3	1	Calculation of the transformer winding losses using Dowell's method
2. Strip	3	1	Calculation of R_{ac}/R_{dc} and L_{ac}/L_{dc}, single layer Murgatroyd's method
3. Maxtot	3	1	Calculation of R_{ac}/R_{dc} and L_{ac}/L_{dc}, single layer Formal method
4. Inductor1	3	2,3	Calculation of R_{ac}/R_{dc}, single layer inductor. Formal method with even symmetry
5. Maxmutual	4	2.1	Calculation of mutual inductance for coaxial filament coils/ equation 4.3 using elliptic integral
6. Maxmodf	4	2.1	Calculation of mutual inductions using Rosa and Cohen equation (Series method Equation 4.8)
7. Grovertbl1	4	2.2	Calculation of mutual inductance using tabulated method and tables as in Grover's book, chapter 11
8. Grovertbl5	4	2.4	Calculation of mutual inductance of coaxial circular coils of finite cross section, using Grover's book, Chapter 15
9. Inductor	5	2,3	Calculation of the losses (R_{ac}/R_{dc}) in inductor of multilayer with even symmetry
10. Transformer1	5	4	Calculation of the losses in transformer secondary winding Example 1